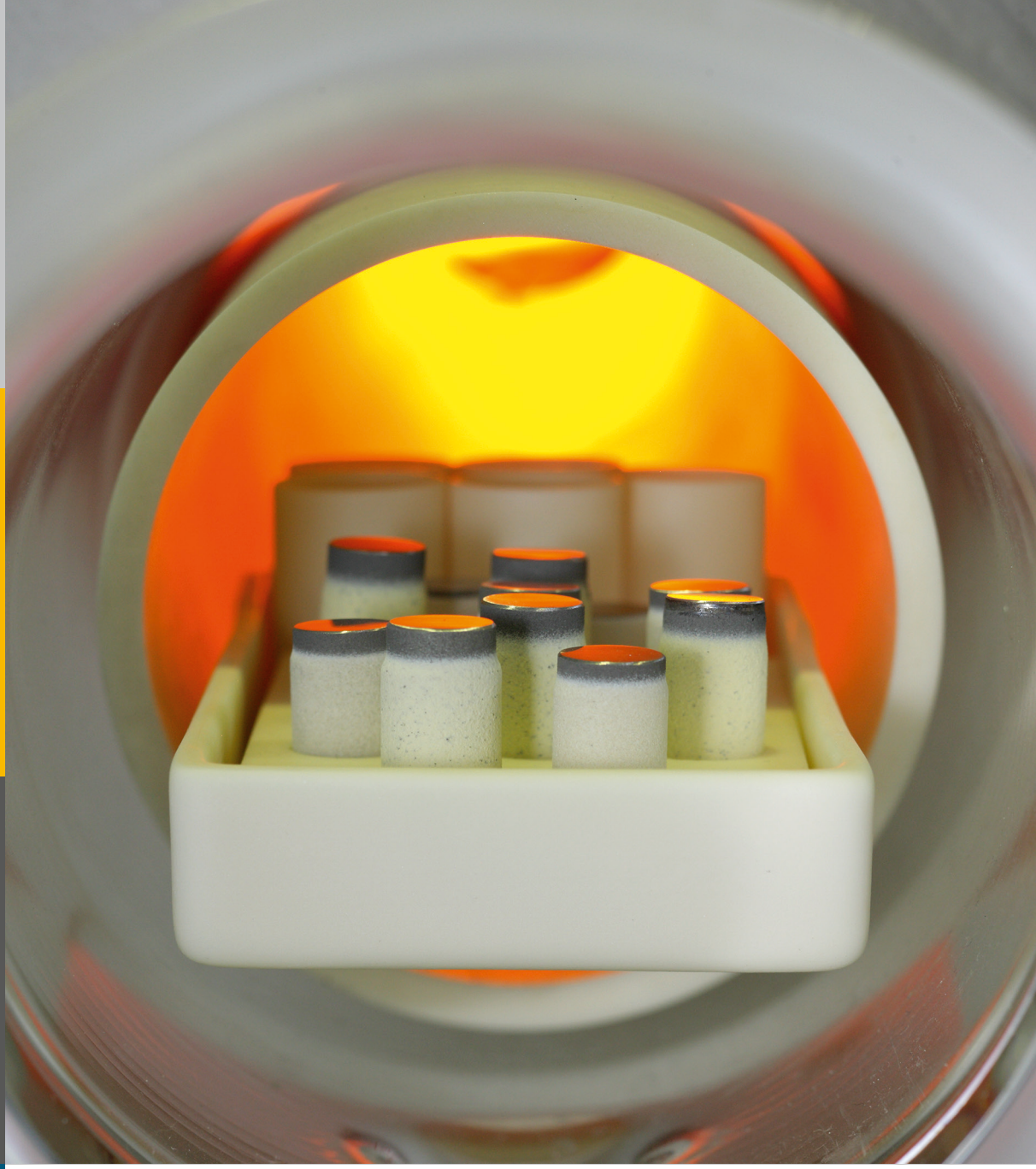

High Temperature Corrosion of Alloys and Coatings in Gas-Turbines Fired with Hydrogen-Rich Syngas Fuels

Wojciech Nowak

JÜLICH
FORSCHUNGSZENTRUM

Member of the Helmholtz Association

Schriften des Forschungszentrums Jülich
Reihe Energie & Umwelt / Energy & Environment Band / Volume 239

Forschungszentrum Jülich GmbH
Institute of Energy and Climate Research (IEK)
Microstructure and Properties of Materials (IEK-2)

High Temperature Corrosion of Alloys and Coatings in Gas-Turbines Fired with Hydrogen-Rich Syngas Fuels

Wojciech Nowak

Schriften des Forschungszentrums Jülich
Reihe Energie & Umwelt / Energy & Environment Band / Volume 239

ISSN 1866-1793 ISBN 978-3-95806-012-8

Bibliographic information published by the Deutsche Nationalbibliothek.
The Deutsche Nationalbibliothek lists this publication in the Deutsche Nationalbibliografie; detailed bibliographic data are available in the Internet at http://dnb.d-nb.de.

Publisher and Distributor: Forschungszentrum Jülich GmbH
Zentralbibliothek
52425 Jülich
Tel: +49 2461 61-5368
Fax: +49 2461 61-6103
Email: zb-publikation@fz-juelich.de
www.fz-juelich.de/zb

Cover Design: Grafische Medien, Forschungszentrum Jülich GmbH

Printer: Grafische Medien, Forschungszentrum Jülich GmbH

Schriften des Forschungszentrums Jülich
Reihe Energie & Umwelt / Energy & Environment, Band / Volume 239

D 82 (Diss. RWTH Aachen University, 2014)

ISSN 1866-1793
ISBN 978-3-95806-012-8

The complete volume is freely available on the Internet on the Jülicher Open Access Server (JuSER) at www.fz-juelich.de/zb/openaccess.

Abstract

One of the possible ways to reduce the CO_2 emissions from coal fired power plants is to use a H_2-rich syngas in the gas turbine as a fuel which is realized in the Integrated Gasification Combined Cycle (IGCC). However, burning syngas results in higher amount of water vapour in the turbine environment compared to the turbines operating on e.g. natural gas.

In the present studies the effect of water vapour on the oxidation behaviour of three material groups used in stationary gas turbines was investigated, including:

1. A polycrystalline Ni-base superalloy Rene 80, which is representative of a chromia forming alloys;
2. An alumina forming, Re-containing MCrAlY coating, and
3. APS-TBC systems based on Rene 80 and having the same MCrAlY as the bondcoat.

The three materials types were tested mainly at 1050°C, however, some experiments were also performed at higher temperatures: 1080°C and 1120°C in various atmospheres including those based on Ar-O_2 and synthetic air with various water vapour contents.

The results obtained for Rene 80 in Ar-O_2 based atmospheres showed that water vapour addition had only a minor effect on the scale composition and growth rate. However, in the synthetic air based atmospheres water vapour addition suppressed internal Ti nitridation. After longer exposure times (over 1000 h at 1050°C) higher material loss was observed in the H_2O-containing synthetic air, which might be related to evaporation of Cr, Mo, W oxyhydroxide species.

During exposure of Rene 80 B-incorporation into the oxide scale as $BCrO_3$ was found, which resulted in a depletion in the 2 mm thick bulk alloy from 92 wt. ppm to about 5 wt. ppm already after 20 h at 1050°C, which corresponds to the B-reservoir depletion of approximately 90%.

The results obtained during MCrAlY coating exposure revealed no major effect of H_2O at slow heating rate of 10K/min. In contrast at a faster heating rate of 90 K/min the water vapour promotes initially formation of a metastable alumina, which rapidly transforms into stable α-alumina after a few hours of exposure.

The testing of APS-TBC systems showed that addition of water vapour into the synthetic air resulted in TBC-lifetime shortening. For systems with relatively flat HVOF bondcoat, the lifetime shortening might be correlated with decreased thermally grown oxide (TGO) adherence. The lifetime shortening of APS-TBC's with VPS and HVOF+APS-flashcoat was not related to an increased growth kinetics of the TGO. For the latter two systems the lifetime shortening by water vapour is likely to be correlated with an effect of water vapour on crack propagation in the ceramic topcoats. Therefore detailed studies of ceramic powders and sprayed YSZ topcoats after various exposure times were carried out. Differences in yttrium distribution as well as in chemistry and the amount of monoclinic phase between two studied YSZ powders and corresponding topcoats were found. Low Temperature Degradation i.e. enhanced transformation from tetragonal to monoclinic zirconia in the presence of water vapour at temperature below approximately 400°C during cooling might be a mechanism responsible for the APS-TBC lifetime shortening in the water vapour containing gas.

The bondcoat roughness profile was found to be an important factor for the APS-TBC lifetime, independent of the test atmosphere. A new method for bondcoat roughness profiles

description was proposed based on fractal analysis. The results obtained using the latter approach revealed that the TBC system with HVOF+APS-flashcoat possesses a higher "microroughness" of the bondcoat surface profile than that of the studied VPS-bondcoat, which might explain a longer lifetime of the former TBC-system. In order to obtain a sufficiently long lifetime it is, however, necessary to carefully control the optimized APS-flashcoat spraying parameters. The flashcoat sprayed with a slightly different (non-optimized) set of parameters failed by breakaway oxidation causing very short TBC-lifetime.

Kurzfassung

Eine Möglichkeit zur Reduzierung der CO_2-Emissionen von kohlebefeuerten Kraftwerken ist der Kombi-Prozess mit integrierter Vergasung (Integrated Gasification Combined Cycle, IGCC). Dieser Prozess nutzt H_2-reiches Synthesegas als Brennstoff für Gasturbinen. Die Verbrennung von Synthesegas führt zu einem höheren Anteil an Wasserdampf in der Turbine im Vergleich zu Turbinen die beispielsweise Erdgas verbrennen.

In der vorliegenden Arbeit wurde der Einfluss von Wasserdampf auf das Oxidationsverhalten von drei Werkstoffgruppen, die in stationären Gasturbinen Verwendung finden, untersucht. Diese beinhalteten:

1. die polykristalline Ni-Basis Superlegierung Rene 80, als Vertreter chromoxidbildender Legierungen;
2. eine Aluminiumoxid bildende, Re-haltige MCrAlY-Schicht und
3. APS-TBC Systeme auf der Basis von Rene 80, wobei die gleiche MCrAlY-Schicht als Haftvermittlerschicht verwendet wurde.

Die drei Materialklassen wurden hauptsächlich bei 1050°C untersucht. Einige Versuche wurden außerdem bei 1080°C und 1120°C durchgeführt. Es wurden verschiedene Atmosphären verwendet, u.a. solche aus Ar-O_2-Mischungen und synthetische Luft, jeweils mit verschiedenen Gehalten an Wasserdampf.

Die Ergebnisse für Rene 80 in Ar-O_2-Atmosphären zeigten, dass Wasserdampf nur einen geringen Einfluss auf Zusammensetzung und Wachstumsrate der Oxide hatte. In Atmosphären auf Basis synthetischer Luft hingegen, führte die Zugabe von Wasserdampf zur

Unterdrückung interner Nitrierung von Ti. Nach längeren Auslagerungszeiten (über 1000h bei 1050°C) wurde höherer Materialverlust in wasserdampfhaltiger synthetischer Luft beobachtet. Dies könnte mit der Verdampfung von Cr, Mo, W Oxyhydroxiden in Zusammenhang stehen.

Während der Auslagerung von Rene 80 wurde B in die Oxidschicht eingebaut. Dies geschah in Form von $BCrO_3$ und führte zur Verarmung in den 2mm dicken Proben. Bereits nach 20h bei 1050°C sank der B-Gehalt von 92ppm auf etwa 5ppm, was einer Verarmung des B-Reservoirs von etwa 90% entspricht.

Die Auslagerung der MCrAlY-Schichten zeigte, dass bei langsamen Heizraten von 10K/min, Wasserdampf keinen deutlich sichtbaren Effekt hatte. Bei schnelleren Heizraten von 90K/min hingegen, begünstigt Wasserdampf zunächst die Bildung von metastabilem Aluminiumoxid. Dieses wandelt sich nach einigen Stunden Auslagerung in stabiles α-Aluminiumoxid um.

Die Untersuchung von APS-TBC-Systemen zeigte, dass die Zugabe von Wasserdampf zu synthetischer Luft die Lebensdauer der Wärmedämmschicht vermindert. Bei Systemen mit relativ flacher HVOF-Haftvermittlerschicht könnte die Lebensdauerminderung mit einer schlechteren Haftung der Oxidschicht zusammenhängen. Die verkürzte Lebensdauer von APS-TBCs mit VPS und HVOF+APS-Flashcoat stand nicht im Zusammenhang mit einer erhöhten Kinetik des Oxidwachstums. Bei den beiden letztgenannten Systemen steht die durch Wasserdampf hervorgerufene kürzere Lebensdauer vermutlich mit einer Beeinflussung der Rissausbreitung durch den Wasserdampf in Zusammenhang. Deshalb wurden detaillierte Untersuchungen der keramischen Pulver und YSZ-Schichten nach verschiedenen Auslagerungszeiten durchgeführt. Unterschiede in der Y-Verteilung, der chemischen Zusammensetzung und des Anteils monokliner Phase in zwei untersuchten YSZ-Pulvern und daraus hergestellten Schichten wurden gefunden. Eine mögliche Ursache für die kürzere

Lebensdauer von APS-TBC-Systemen in wasserdampfhaltigen Gasen, könnte die Niedertemperaturumwandlung von tetragonalem zu monoklinem Zirkonoxid in Gegenwart von Wasserdampf unterhalb von etwa 400°C während des Abkühlens sein.

Es wurde festgestellt, dass die Rauigkeit der Haftvermittlerschicht ein wichtiger Faktor für die Lebensdauer der APS-TBCs ist, und zwar unabhängig von der Versuchsatmosphäre. Basierend auf Fraktalanalyse, wurde eine neue Methode zur Beschreibung der Rauhigkeitsprofile von Haftvermittlerschichten vorgeschlagen. Die mittels dieses Ansatzes erzielten Ergebnisse zeigen, dass TBC-Systeme mit HVOF+APS-Flashcoat eine höhere "Mikrorauigkeit" des Oberflächenprofiles der Haftvermittlerschicht aufweisen als solche mit VPS-Haftvermittlerschicht. Dies könnte die höhere Lebensdauer ersterer TBC-Systeme erklären. Um eine ausreichende Lebensdauer zu gewährleisten, ist es notwendig die optimierten Spritzparameter der APS-Flashcoats sorgfältig zu kontrollieren. Ein Flashcoat welches mit geringfügig veränderten (nicht optimierten) Parametern gespritzt wurde, versagte bereits nach sehr kurzer Zeit durch Breakawayoxidation.

Acknowledgments

I would like to express my gratitude to Prof. L. Singheiser for the supervision of my PhD Thesis. Many thanks to Dr D. Naumenko and Prof. W.J. Quadakkers, who help me a lot with their expertise, understanding, patience, and permanent support of this work.

I am grateful to my colleagues in the Institute for Energy and Climate Research (IEK) of the Forschungszentrum Julich GmbH, for carrying out the oxidation experiments (H. Cosler, R. Mahnke and A. Kick and M. Borzikov), SEM analysis (Dr E. Wessel, Dr D. Grüner), XRD analyses (M. Ziegner) and metallographic investigations (V. Gutzeit, J. Bartch and M. Felden).

To all the colleagues in the High Temperature Corrosion Group: Joanna Żurek, Aleksandra Jałowicka, Leszek Niewolak, Paweł Huczkowski, Tomas Hüttel, Laura Garcia Fresnillo, Anton Chyrkin, Rishi Pillai, Vladimir Shemet, Hänsel Michael, Elham Hejrani, Ran Duan and Martin Schiek for the great time and their helpful discussions during my studies.

The financial support of the European Union (Collaborative Project: FP7-239349 with acronym: H2-IGCC) is also gratefully acknowledged.

To my family, especially my lovely wife and our daughter for being my motivation as well as for their constant support and patience during this time.

1 Introduction:

1.1 Energy demand and requirements of environmental protection

The global energy demand between 2011 and 2035 is predicted to increase by more than 70%. The fossil fuel share in power generation declines from 68% in 2011 to 57% in 2035, but will still be dominating and furthermore increase [1, 2] (**Figure 1.1**). **Figure 1.2** shows percentage contribution of various types of energy sources in total electric power generation worldwide in 2013 [3].

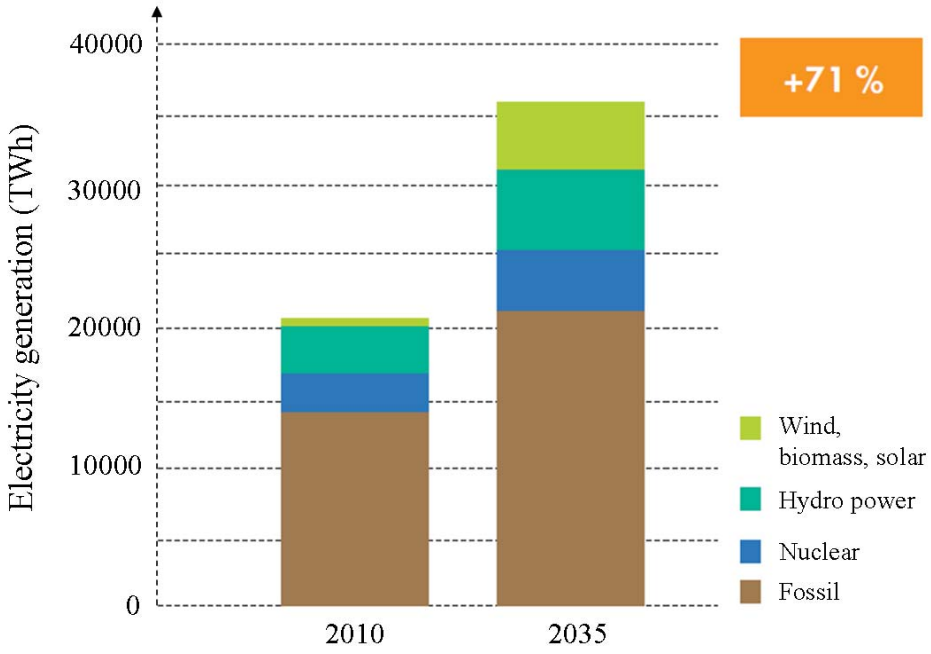

Figure 1.1 Expected growth in electricity generation in 10^9 kWh worldwide [2]

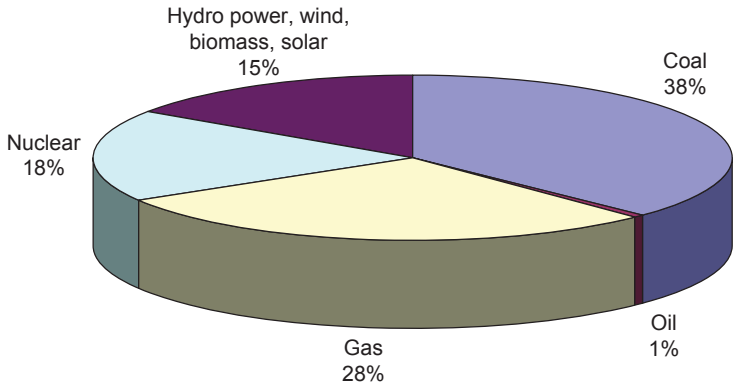

Figure 1.2 Percentage contributions in power generation by using different resources in 2013 worldwide [3]

The energy sector is considered to be a source of two-third of global greenhouse-gas emission (primarily CO_2). According to the European Council plan a target of 20% CO_2 emission reduction needs to be achieved by 2020 [1]. One of the most promising technologies to decrease the CO_2 emissions by fossil fuel fired power-plants is an Integrated Gasification Combined Cycle (IGCC) plant combined with carbon capture and storage (CCS). This type of power plants uses hydrogen-rich syngas as a fuel for the gas turbine. For syngas a wide variety of coal grades, biomass, petroleum coke, etc. can be used. The major component of syngas is H_2 [4]. **Figure 1.3** shows a schematic of an IGCC power plant with CO_2 capture technology. In this plant the oxygen is separated from nitrogen in air and used in the gasifier. The gasification process produces raw syngas, which is in the next steps cleaned from fly ash, sulphur. The CO is converted into CO_2 by shift reaction and finally CO_2 is sequestrated. Purified syngas can be mixed with natural gas or burned alone in the gas turbine [4]. Hot exhaust gas of the gas turbine is used in a heat recovery steam generator which feeds a steam turbine. Both gas and steam turbine are involved in electricity generation. Thereby the overall efficiency of the Combined Cycle (CC) plant is greatly increased as compared to the single gas turbine plant.

Combustion of H_2-rich syngas implies that the gas turbine components will be operating in environments containing higher amounts of water vapour than in the gas turbines burning natural gas. Gas turbines operating on H_2-rich syngas produce very low NO_x emissions [5]. However, due to the energy consuming gasification and CO_2 capture processes, the overall efficiency of the IGCC power plants is decreased compared to conventional CC-plants. To compensate the efficiency losses a higher operating temperature of the gas turbine is an option.

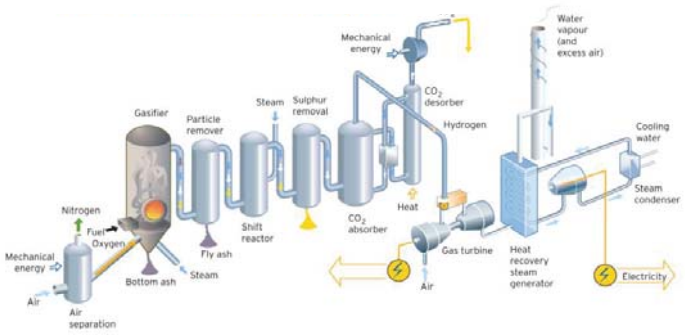

Figure 1.3 Schematic of IGCC power plant with CO_2 capture and storage technology [6]

1.2 Gas turbine materials

One of the main components of an IGCC power plant is the gas turbine, which converts thermochemical energy into mechanical energy according to the Joule-Brayton cycle, which consists of four processes:

- air compression in the compressor of a gas turbine (adiabatic process),
- burning mixture of air and fuel in the combustion chamber (isobaric process),
- expansion of gases to turbine blades (adiabatic process), and
- heat exhaust out of the gas turbine (isobaric process).

An advanced gas turbine used in modern power plants is shown in **Figure 1.4**.

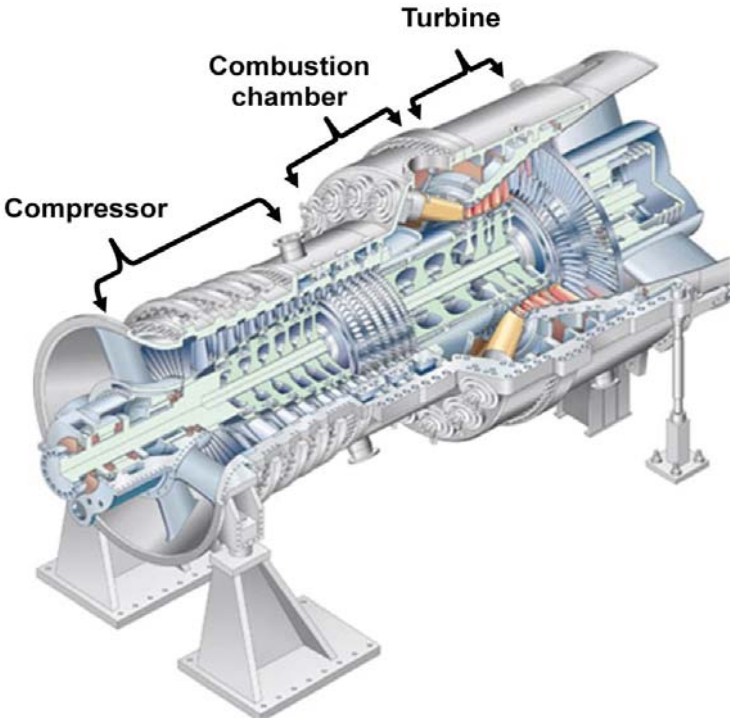

Figure 1.4 Gas turbine – SIEMENS SGT5-8000H (375 MW simple cycle, 570 MW combined cycle) [7].

The gas stream undergoes three processes: compression, combustion and expansion. Compressed to high pressure in a multistage compressor, air is moved to the combustion chamber to be mixed with the fuel and combusted to produce high pressure exhaust gas. The extremely hot exhaust gas is released to the expansion stage (turbine) where it passes through several stages of blades and vanes on a shaft driving power generator. The temperature of the exhaust gas entering the turbine (turbine inlet temperature) can be around 1200°C to 1400°C.

The materials used in the gas turbines should fulfil a number of requirements such as: suitable ductility at low temperature, high creep strength and high oxidation resistance at a wide range of operating temperatures, environments and loading conditions.

In the combustion chamber heat resistant alloys are used as construction material, such as wrought Ni- or Co-based superalloys (e.g. Haynes 188 or Hastelloy-X). In the turbine section usually cast nickel- and cobalt-based superalloys such as Rene 80 or MARM-509 as well as directionally solidified and single crystal alloys (e.g. PWA 1483) are used for blades and vanes [8]. In the hotter parts of the turbine section an oxidation resistant coating, typically MCrAlY (M=Ni, Co), is required for oxidation/corrosion-protection of the superalloys. The components facing the highest (turbine inlet) temperatures are internally cooled and, in addition to MCrAlY, are coated with a ceramic Thermal Barrier Coating (TBC).

In the following chapter the compositional and microstructural features of the three material types: Ni-base superalloys, MCrAlY coatings and TBC-coating systems are discussed in detail.

1.2.1 Ni-base superalloys

In the colder end of the turbine section (material temperatures of below 800°C) usually cast Ni-based superalloys are used without coatings. These alloys can be used in load-bearing applications at temperatures of about 80% of their melting temperatures [9], which is much higher than that of many other constructional materials. The excellent mechanical properties of Ni-based superalloys are achieved by their microstructure: a thermodynamically stable face-centered cubic (FCC) matrix with combination of precipitation strengthening and solid solution hardening. The first superalloys developed at the end of 1940's such as NIMONIC 80A were wrought materials with a relatively small fraction of the γ'-Ni_3Al intermetallic strengthening phase which was stabilized by Ti addition. In order to increase high temperature strength the formation of γ'-precipitates was increased by higher Ti and Al contents resulting

in the development of cast Ni-base superalloy components. The high temperature oxidation resistance relies on the formation of a protective oxide scale, which is obtained by additions of chromium and aluminium [9]. In general, Ni based superalloys contain, apart from Ni a combination of up to ten alloying elements. Typically cast Ni-based superalloys contain 5 – 15 wt. % Cr, up to 8 wt. % Al and Ti, Co in the range between 5 – 15 wt. % and minor alloying elements such as boron, zirconium magnesium and carbon [9]. Other alloying additions such as tungsten, molybdenum and niobium result in solid solution strengthening as well as carbide formation. Advanced Ni-base superalloys contain higher Al (5-6 wt. %) and lower Cr (6-8 wt. %) contents to promote formation of γ'-Ni_3Al thereby increasing creep rupture strength and to avoid formation of brittle Topologically Close Packed (TCP) phases [10, 11].

Grain boundaries are known to be easy paths for diffusion processes which results in reducing resistance of the material to creep deformation [11]. Reducing the grain boundary density in the superalloys results in improvement of their creep resistance at high temperatures. Therefore directionally solidified as well as single crystal superalloys have been developed recently (**Figure 1.5**) [10]. The newest single crystal superalloys can be operated at temperatures as high as 1100°C, which is much higher than the operating temperature of about 750°C for the first wrought superalloys developed in the 1940's [12]. **Figure 1.6** shows microstructures of polycrystalline, directionally solidified and single crystal materials.

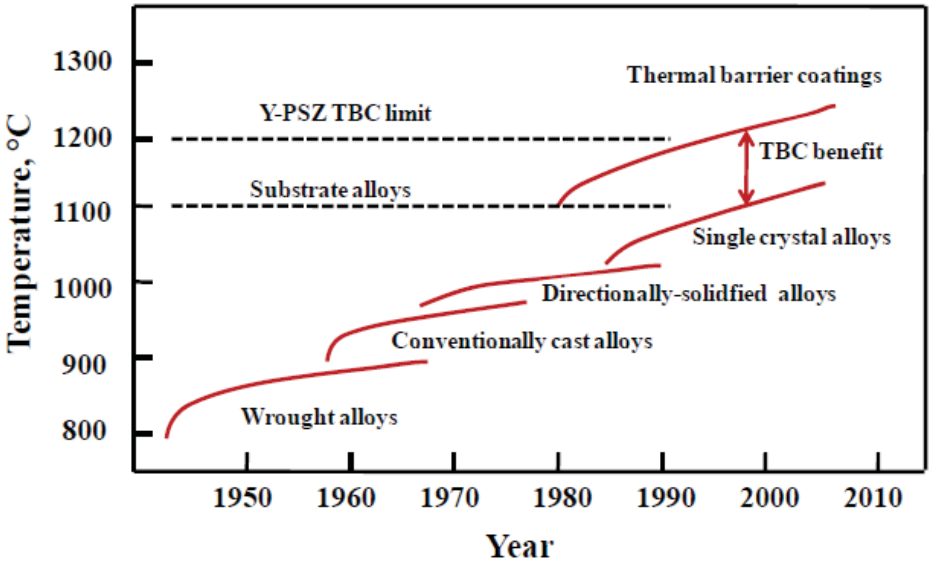

Figure 1.5 Alloy and coating development for gas turbine blades and used turbine gas inlet temperature [10]

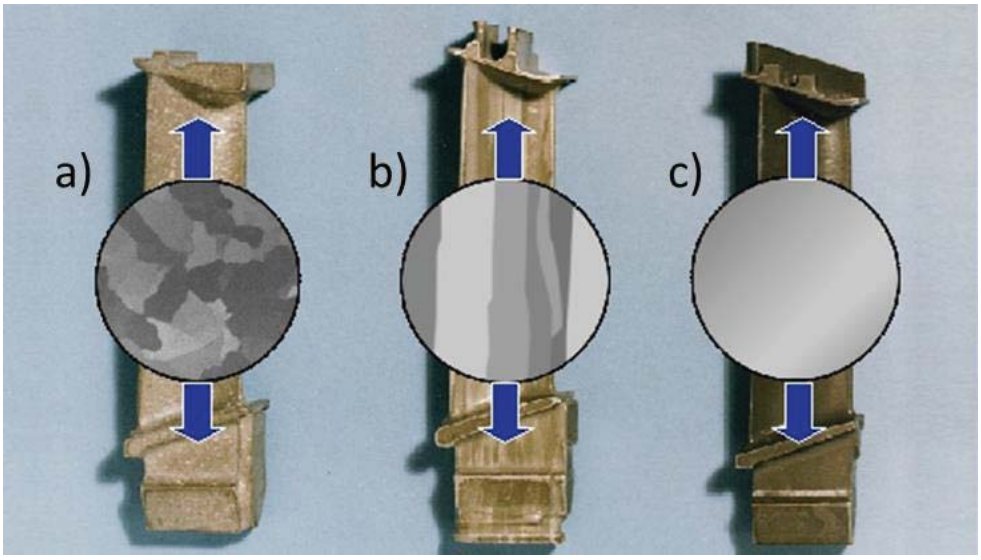

Figure 1.6 Comparison of macro- and microstructures in a) polycrystalline, b) directionally solidified and c) single-crystal turbine blades of Ni-base alloys [10]

Uncoated superalloys are usually used in the last turbine stages. In the turbine section with higher temperature above approximately 800°C the oxidation resistance of the superalloys is not sufficient and application of high oxidation resistant coatings is necessary.

1.2.2 Oxidation resistant coatings

MCrAlY coatings, where M represents Ni and/or Co, are commonly used for oxidation protection of turbine components. During exposure at high temperature the MCrAlY coatings possess an ability to form a dense, slowly growing and adherent alumina scale, which effectively protects the underlying metal components from rapid oxidation/corrosion degradation. This type of coatings usually contains 15-25 wt.% Cr, 10-15 wt.% Al and an addition of yttrium in the range between 0.2-0.6 wt% for improvement of the oxide scale protective properties, in particular adherence. Other additions include Si, Hf and Re [13].

At temperatures above 1000°C the microstructure of the MCrAlY coatings consists of β-NiAl intermetallic phase in a matrix of γ-Ni solid solution (with Co, Cr, Re). The γ-phase is responsible for ductility of the coating and the β-phase is a reservoir of Al to form the protective alumina scale. During oxidation, a phase transformation from β-NiAl to γ-Ni is commonly observed due to Al consumption for the formation of the protective α-Al_2O_3 scale. It needs to be noticed that at lower temperatures (below 1000°C) the microstructure of MCrAlY coatings may be far more complex and also formation of γ' as well as α-Cr and sigma phases is often observed depending on the coating composition [14]. This effect is discussed in more detail in chapter 3.4. To stabilize γ+β microstructure in the coating commonly Co is added.

MCrAlY coatings can be deposited by different methods, including: electron-beam physical vapour deposition (EB-PVD) [15], vacuum plasma spraying (VPS) [16], low pressure plasma spraying (LPPS) [17], air plasma spraying (APS) [18] or high velocity oxy-fuel spraying (HVOF) [19].

1.2.3 TBC systems

In the hottest part of the gas turbines the turbine inlet temperature exceeds 1200°C. For such severe service conditions the Ni-base superalloy components are internally cooled and are additionally coated with ceramic thermal barrier coatings (TBC's). A state of the art TBC system consists of a ceramic top coat, which typically is yttria stabilized zirconia (7-8 wt. % Y_2O_3), over a metallic bondcoat (usually MCrAlY). Both of these layers are applied on top of the superalloys. During service a thermally grown oxide (TGO) based on Al_2O_3 is formed at the interface between the topcoat and bondcoat.

The material used for the ceramic topcoat should have a relatively low coefficient of thermal conductivity for significant temperature reduction across the coating. The coefficients of thermal expansion (CTE) for the topcoat, bondcoat and base metal should be similar to reduce thermal stresses during temperature cycling. The material used as a bondcoat should possess a high aluminium content to provide high oxidation resistance due to formation of an oxide scale based on α-Al_2O_3. Another important factor is good chemical compatibility of the bondcoat with the superalloys in order to suppress interdiffusion between the materials which may cause formation of pores or brittle phases such as TCP. **Figure 1.7** shows macro images of a TBC coated, internally cooled turbine blade and a schematic showing the temperature distribution across the TBC-system.

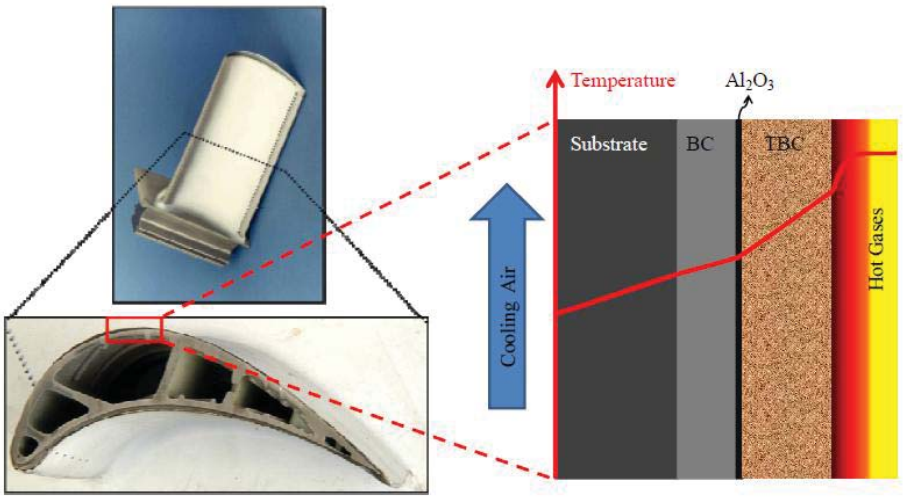

Figure 1.7 TBC-coated turbine blade, its cross-section and schematic of temperature gradient in TBC cross-section (reproduced from Ref [7])

As mentioned above the state of the art material used for the topcoat is YSZ. Yttria stabilized zirconia has a very high melting point, thermal conductivity (value between 0.8 and 1.9 W/mK depending on the microstructure and mol fraction of yttria) [20] and a relatively high coefficient of thermal expansion (CTE) with a better match to the metallic material than many other high strength ceramics. The CTE values obtained for 6-8 wt. % Y_2O_3-doped zirconia are in the range 9-11.5·$10^{-6}K^{-1}$ which is very close to the CTE of superalloys (12-14·$10^{-6}K^{-1}$). Finally, a major advantage of YSZ is its high fracture toughness.

For the application in the gas turbine components YSZ is stabilized by 6-8 wt. % of Y_2O_3. This composition is relatively stable during high temperature exposure. In addition, YSZ containing 6-8 wt.% Y_2O_3 has a lower Young's modulus than pure zirconia, resulting in reduced stresses induced by CTE mismatch between YSZ and other components of the TBC-system upon temperature change [21].

A number of ceramic materials with potential to be applied as ceramic topcoats have been investigated, however none of the alternative materials was found to perform better than YSZ [22, 23, 24, 25]. Some of the studied materials show e.g. higher temperature stability and/or lower thermal conductivity; however, they typically have a lower fracture toughness and/or a lower coefficient of thermal expansion which leads to faster topcoat failure.

Deposition of ceramic topcoats [26, 27] is commonly carried out using two methods: Electron-Beam Physical Vapour Deposition (EB-PVD) [28, 29] and Air Plasma Spraying (APS) [30, 31]. The similarity in vapour pressures of ZrO_2 and Y_2O_3 allow deposition by APS as well as EB-PVD. An advantage of the EB-PVD deposition method is a very smooth surface of the component, which in jet engine application has benefits with respect to aerodynamics [20]. Also, cooling holes are not covered during the process. In the deposition by the EB-PVD process the coating is obtained by condensation of a vapour on the substrate. Therefore a columnar structure of the coating can be observed (**Figure 1.8 a**)). To obtain a regular columnar structure with a minimum of growth defects a flat surface of the bondcoat is necessary. The columnar structure of the TBC clearly differs from the structure obtained after topcoat deposition by APS (**Figure 1.8 b**)).

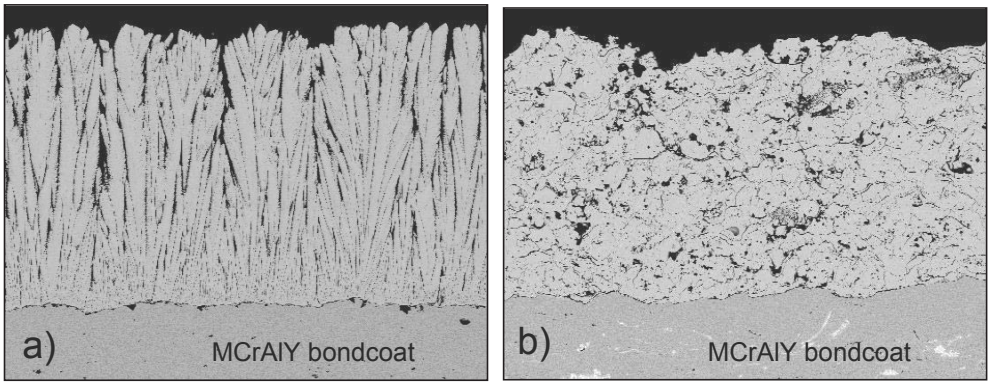

Figure 1.8 Microstructure of yttria stabilized zirconia TBC's deposited by a) EB-PVD, b) APS (SEM cross-sections)

The APS deposition method is based on melting and accelerating particles of YSZ powder in a plasma jet generated by an ionised gas such as Ar. Thereby molten powder particles are sprayed onto the substrate. The molten particles hit the surface, become flattened and very rapidly solidify. This process produces intersplat voids (porosity of about 10–20 vol. %) which reduce the thermal conductivity and increase the strain tolerance of the topcoat. Because of the microstructural features related to the APS deposition process characteristic adhesion between the sprayed topcoat and bondcoat is primarily mechanical, and therefore a rough bondcoat surface is necessary. In addition, both APS and EB-PVD are line-of-sight processes and the coating cannot be deposited by this method on inner surfaces of components with complex shapes, such as internally cooled turbine blades. Because of the above described production related differences in the coating microstructures the coefficient of thermal conductivity for the two types of topcoats differs: for EB-PVD coating it is in the range of 1.5-1.9 $W \cdot m^{-1}K^{-1}$ while for those sprayed by APS it is between 0.8-1.1 $W \cdot m^{-1}K^{-1}$ [32].

2 Degradation of gas turbine components due to high-temperature oxidation

2.1 General remarks

Several potential degradation modes of GT-components exist e.g. mechanical or thermo-mechanical fatigue, particle erosion, low temperature “down-time” corrosion during extended plant shut-offs etc. In the present work uncoated Ni-based superalloys, overlay coated alloys and TBC systems have been investigated with emphasis put on their high temperature oxidation in dry and water vapour containing atmospheres thus addressing possible differences in degradation modes for components of stationary gas turbines using conventional or syngas based fuels.

2.2 Thermodynamic considerations

An oxidation reaction between a metal (M) and oxygen (O_2) can be written as [33]:

$$M_{(S)} + O_{2(g)} = MO_{2(S)} \tag{2.1}$$

The driving force for this reaction (the Gibbs free energy of oxide formation) for defined pressure and temperature is given by the following equation:

$$\Delta G = \Delta G^0 + RT \ln\left(\frac{a_{MO_2}}{a_M p_{O_2}}\right) \tag{2.2}$$

where:

ΔG^0 - Standard Gibbs free energy,

R - gas constant,

T - temperature,

a_M and a_{MO_2} - activity of metal and oxide respectively,

p_{O_2} - oxygen partial pressure

Under these conditions the second thermodynamic law states that:

$\Delta G < 0$ - spontaneous reaction expected

$\Delta G = 0$ - system in a state of equilibrium

$\Delta G > 0$ - reaction thermodynamically impossible

Under thermodynamic equilibrium $\Delta G = 0$ the standard Gibbs free energy can then be obtained from the equation:

$$\Delta G^0 = -RT \ln\left(\frac{a_{MO_2}}{a_M p_{O_2}}\right) \tag{2.3}$$

If the activities of M and MO_2 are considered as unity like in the case of a pure metal and pure oxide, the equation (2.3) reveals the oxygen partial pressure at which metal and oxide can coexist, i.e. the dissociation pressure of the oxide, can be expressed by the following equations:

$$p_{O_2} = \exp\left(-\frac{\Delta G^0}{RT}\right) \tag{2.4}$$

The value of the dissociation pressure may be obtained from the Ellingham/Richardson diagram (**Figure 2.1**), i.e. a plot of standard free energies for the formation of oxides as a function of temperature. Thermodynamically more stable oxides posses lower dissociation pressures. The dissociation pressures increase with increasing temperature meaning that the thermodynamic tendency of a metal to oxidise decreases with increasing temperature.

From **Figure 2.1** it is clearly visible, that the iron, nickel or cobalt oxides (which elements are commonly a matrix for high temperature alloys) are significantly less stable than the oxides of the alloying additions forming protective oxide scales (e.g. Al, Cr, Si). This means that from the thermodynamic point of view oxidation of Cr and Al is promoted which is the basis of the alloys design philosophy for obtaining oxidation protection.

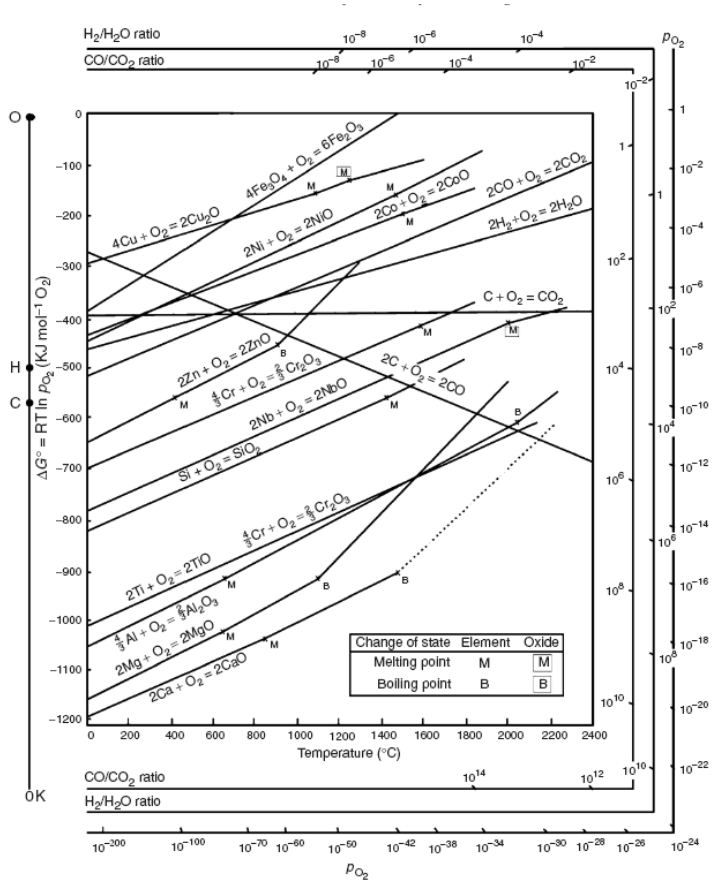

Figure 2.1 Ellingham-Richardson diagram for standard free energies of formation for selected oxide formation per mole of oxygen [34]

2.3 Oxidation kinetics

During exposure at high temperature oxidation products start to form at the interface between a metal and the surrounding atmosphere. After formation of a continuous oxide scale the two reactants become separated, and the reaction rate is controlled by the solid state diffusion of the reactants through the oxide. The mechanism of oxide scale growth was described by Wagner [12, 34, 35] and applies only for the case of lattice diffusion. **Figure 2.2** schematically shows the mechanism of oxide scale growth: metal cations and oxygen anions migrate through the scale in opposite directions and consequently gradients in metal activity

and oxygen partial pressure are established across the scale. The metal and the oxygen activities at both interfaces are controlled by the equilibria with the gas atmosphere and the metal, respectively.

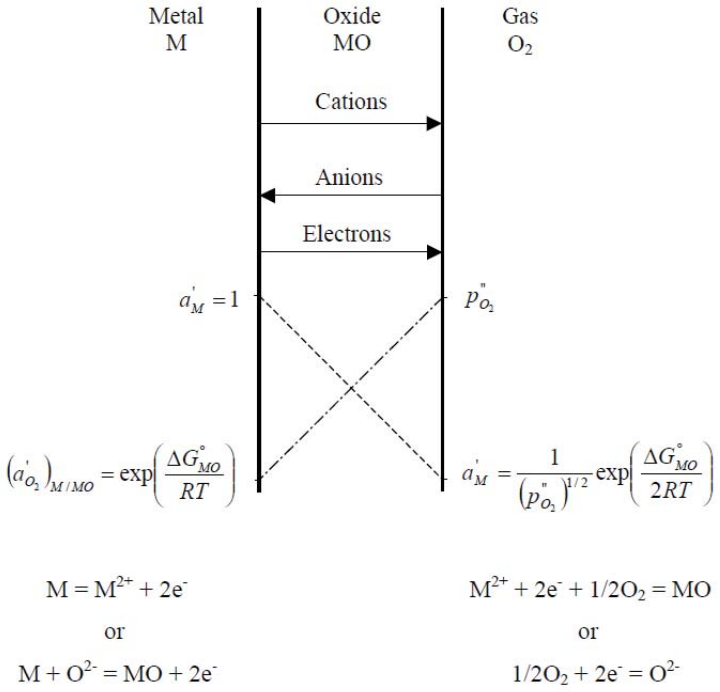

Figure 2.2 Scale formation according to Wagner's model [12, 34, 35]

Considering an oxide scale growing via cation transport, the outward cation flux $j_{M^{2+}}$ is equal and opposite to the inward flux of cation vacancies j_{V_M} [35]. According to Fick's first law of diffusion:

$$J_{M^{2+}} = const\frac{dx}{dt} = D_{V_M}\frac{C''_{V_M} - C'_{V_M}}{x} \tag{2.6}$$

where:

x - oxide scale thickness,

D_{V_M} - diffusion coefficient for cation vacancies,

C''_{V_M}, C'_{V_M} - vacancy concentrations at the scale-gas and scale-metal interfaces respectively.

Integrating equation (2.6) and noting that $x = 0$ at $t = 0$ leads to the common parabolic rate law:

$$x^2 = 2k \cdot t \tag{2.7}$$

where $k = D_{V_M} \frac{C''_{V_M} - C'_{V_M}}{const.}$ (2.8)

The parabolic rate law correctly describes the oxidation kinetic only if the following assumptions made by Wagner [34, 35] are fulfilled:

(1) The oxide layer is a compact and perfectly adherent scale,

(2) Migration of ions or electrons across the scale is the rate-controlling process,

(3) Thermodynamic equilibrium is established at the metal-scale and the scale-gas interfaces,

(4) The oxide scale shows only small deviations from stoichiometry and, hence, the ionic fluxes are independent of position within the scale,

(5) Thermodynamic equilibrium is established locally throughout the scale,

(6) The scale is thick compared to the distances over which space charge effects (electrical double layer) occur,

(7) Oxygen solubility in the metal can be neglected

If any of these assumptions is not fulfilled, different types of scaling rate may occur. One of the most technologically important oxide scales is α-Al_2O_3 which forms on alloys and coatings such as MCrAlY at high temperature as described above [34]. Formation of protective α-Al_2O_3 often follows subparabolic kinetic, given by the following equation:

$$x = k' \cdot t^{n} \tag{2.10}$$

where the n value is in the range $0.33 \leq n \leq 0.5$ [34].

The reason for deviation from the parabolic kinetics is that α-Al_2O_3 scale growth occurs not via lattice diffusion but rather via oxide grain boundaries in a scale with a columnar structure. The grain boundary density was frequently observed to decrease with increasing scale thickness due to the columnar microstructure of the oxide scale [36, 37, 38].

The high temperature oxidation kinetics of metals and alloys is often experimentally determined using weight change measurements; then equation (2.7) may be written in the form:

$$(\Delta m)^2 = k_w \cdot t \tag{2.11}$$

where Δm is the area specific weight gain e.g. in $mg \cdot cm^{-2}$.

3 Aims and outline of the present studies:

Using purified hydrogen rich syngas as a fuel in gas turbines operating in IGCC power plants with CO_2 capture results in higher amounts of water vapour in the service environments. Increased operating temperature of the gas turbines is necessary to compensate the efficiency losses due to the gasification and capture processes. These changed service parameters require wide knowledge about the oxidation behaviour of the materials used for components in gas turbines, including superalloys, MCrAlY-coatings as well as TBC systems, which need to operate in water vapour containing gases at high temperature. Studies of the effect of water vapour on the oxidation behaviour of selected superalloys are available in literature; however studies about the effect of water vapour on MCrAlY-coatings and TBC systems are very limited. Moreover, there is no agreement in the available literature concerning the water

vapour influence on the oxidation behaviour of TBC systems and the parameters affecting TBC life. Moreover, there are many studies available on the EB-PVD TBC systems but far less for the APS TBC systems, in spite of the fact that the latter are state of the art systems in modern gas turbines.

First, an extensive evaluation of information available from literature about water vapour effect on oxidation behaviour of four material groups: 1 - chromia-forming alloys, 2 - alumina-forming alloys, 3 - MCrAlY coatings and 4 - TBC systems, will be presented.

Then investigation are carried out on the oxidation behaviour of three main groups of materials used in stationary gas turbines , i.e., Ni-base superalloys, MCrAlY-coatings and TBC-systems, in atmospheres with various water vapour contents. First, commercially available Ni-based superalloy, polycrystalline Rene 80, which is commonly used as base materials in the hottest section of the gas turbines, was studied. The second material group is a free standing, Re-containing MCrAlY. Specimens which were tested include ground and rough, free standing coatings.

The studies with uncoated superalloys and MCrAlY-coatings include short-time oxidation tests using a thermobalance in Ar-O_2-H_2O and synthetic air – H_2O with various oxygen and water vapour contents. Additionally long-time (up to 2000 hours) discontinuous exposures in laboratory air with and without intentionally added water vapour at 1050°C were carried out.

The third group of the examined materials were APS TBC systems. A number of APS TBC coated samples with MCrAlY bondcoats deposited by VPS, HVOF as well as with bondcoat surface roughness profile of the HVOF bondcoat improved by a special APS technology were

examined. In addition to the influence of BC-roughness profile the effect of ceramic topcoat porosity on APS TBC lifetime was investigated.

The TBC-systems were subjected to an accelerated cyclic test (2 hour cycles) at 1120˚C to qualify the coatings systems for the long-time discontinuous tests (100 hour cycles) estimating the influence of water vapour, which were performed at 1050˚C till the TBC failure.

4 Scale formation on Ni-base alloys and coatings systems:

4.1 General background

One of the major requirements for an extended lifetime of gas turbine components is the formation of a protective (slow growing and adherent) oxide scale on the surface of superalloys and/or coatings. For obtaining optimum protection the oxide scale should cover the alloy surface. The oxide scale can only be protective if the Pilling-Bedworth Ratio , i.e. the ratio between the volume of formed oxide and the volume of metal consumed for its formation is larger than 1. However, if the PBR is much larger than two, then high growth stresses in the oxide scale may occur which lead to oxide scale cracking and spallation.

Considering the growth rate of the oxide scales shown in **Figure 4.1**, the formation of Al_2O_3 or Cr_2O_3 scales is the most desirable from the view point of slow growth kinetics. Therefore, as mentioned in **chapter 1.2.1** Cr and Al alloying additions are present in the superalloys chemical compositions.

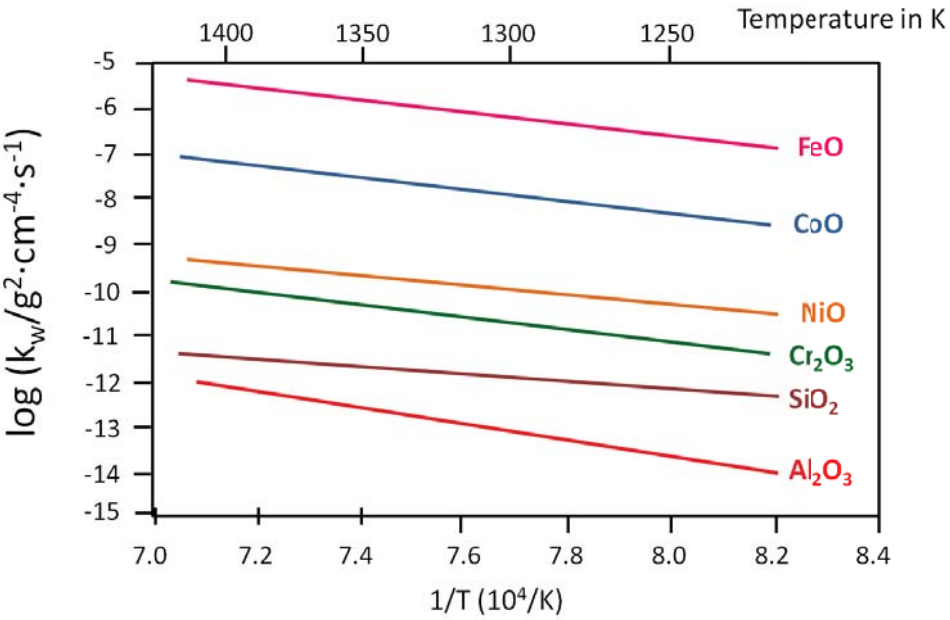

Figure 4.1 Parabolic rate constants for the growth of various oxide scales as a function of reciprocal temperature (reproduced from [34])

Early studies related to the oxidation properties of ternary NiCrAl model alloys revealed three types of oxidation behaviour (**Figure 4.2** [35, 39]):

(I) formation of an external NiO scale with internal Al_2O_3/Cr_2O_3 precipitates in the sub-surface zone,

(II) formation of an external Cr_2O_3 scale with internal Al_2O_3 precipitates,

(III) formation of an external Al_2O_3 scale.

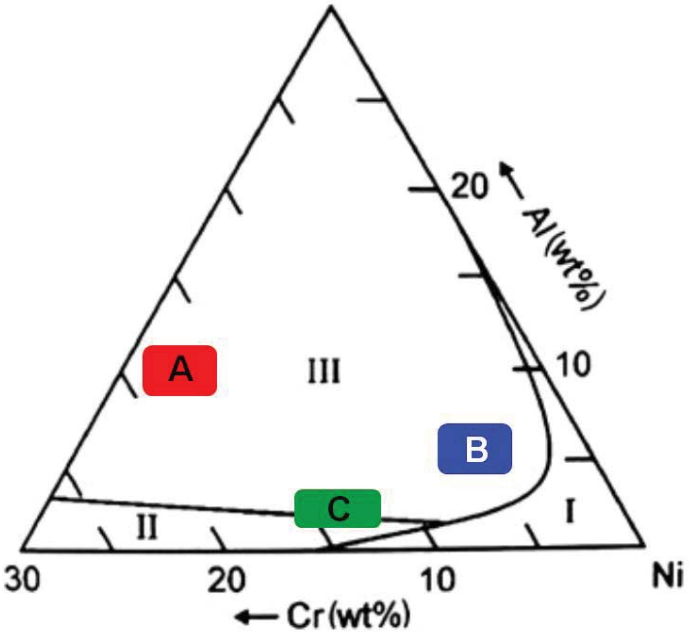

Figure 4.2 Oxidation map for ternary NiCrAl alloys during isothermal exposure in air at 1000 -1100°C. Area I: external NiO + internal oxidation of Cr and Al. Area II: external Cr_2O_3 + internal Al_2O_3 formation. Area III: external Al_2O_3 formation [35]. Locations of material groups used in the present studies are also shown: A – MCrAlY, B – cast Ni-base superalloys with 6-8 wt.% Cr and 5-6 wt.% Al, e.g. CMSX-4, CM247, C –cast Ni-base superalloys with 12-16 wt.% Cr and 3-4 wt.% Al, e.g. Rene 80, PWA 1483.

The Ni-base superalloys used in gas turbines could be chromia formers, e.g. Rene 80, IN 738, or (marginal) alumina formers such as PWA 1483 or CMSX-4. MCrAlY coatings can be considered as stable alumina formers with large Cr and Al-reservoirs. In the following chapter the oxidation behaviour of chromia and alumina forming materials and the effects of water vapour in the operating atmospheres relevant for the H_2-rich syngas will be described.

4.2 Oxidation behaviour of chromia forming alloys in the presence of water vapour

In numerous materials used at high temperatures, e.g. stainless steels or wrought Ni-base superalloys, oxidation protection is achieved by formation of a protective chromia surface scale. However, a number of investigations have shown that the oxidation behaviour of chromia forming alloys may be strongly affected by the presence of water vapour in the oxidizing atmospheres.

4.2.1 Effect of the test atmosphere on the chromia scale growth mechanisms

Pure chromium oxidation was extensively investigated by the research group in Julich (Quadakkers et al. [40], Michalik et al. [41] and Hänsel et al. [42, 43]). For pure chromium oxidized in Ar-H_2-H_2O faster oxide scale growth rate and a better adherence was found than in dry Ar-O_2 atmosphere. Oxide scale buckling and void formation at the scale/metal interface was far less pronounced in Ar-H_2-H_2O than in Ar-O_2. The authors proposed that void formation is suppressed due to the change of the oxide scale growth mechanism from outward to predominantly inward transport. Also formation of chromia blade-shaped oxide was found on pure chromium exposed in Ar-H_2-H_2O by Quadakkers et al. [40] and Hänsel et al. [42, 43]. This phenomenon was correlated with formation of hydroxyl species in water vapour containing atmospheres.

The growth rates of the oxide scales on binary Ni-25Cr alloys obtained during oxidation in water vapour containing gas (Ar-7%H_2O) were found by Essuman et al. [44] to be higher than in dry atmosphere (Ar-20%O_2). In spite of the smaller growth rate, formation of voids and pores was observed in the dry atmosphere. The oxide scale formed under wet conditions was

compact and well adherent to the substrate. Zurek et al. [45] found that for a binary Ni-25Cr alloy chromia scales formed in Ar-H_2-H_2O grew faster, but the scale adherence was better than those in Ar-O_2. The authors correlated both phenomena with the differences in scale microstructure. The oxide grain size was much finer in Ar-H_2-H_2O than in Ar-O_2 and the predominant transport process in the chromia scale changed from nearly exclusive outward growth in Ar-O_2 to substantial inward growth in Ar-H_2-H_2O as verified by tracer experiments.

Essuman et al. [46, 47] oxidized Fe-Cr (10 and 20 wt.% of Cr) alloys at 900°C in Ar-O_2 and Ar-H_2-H_2O. In both atmospheres formation of a chromium rich scale was observed, however the growth rate obtained for the alloy exposed in the water vapour containing gas was greater than in dry gas. It was proposed that water vapour may affect the oxidation behaviour not only by volatilization or by modifying transport process and void formation in the oxide scale, but also by affecting transport process in the alloy [47].

Increasing oxidation rate for Ni-base superalloys such as Hastelloy X, Haynes 230, Inconel 625 and Inconel 718 in wet atmosphere was found by England and Virkar [48, 49]. The authors exposed the alloys in air in the temperature range of 800 – 1100°C [48] and in wet hydrogen at temperatures between 700 and 1100°C [49]. At 800°C the authors found the oxidation rates in wet hydrogen to be higher by a factor varying between 8 and 30 compared to air, while at 1100°C the effect of water vapour decreased and the growth rate in wet hydrogen was higher than in dry air by a factor of 1.5 to 13.

The papers mentioned above compare the behaviour of chromia-forming alloys in low-pO_2 (Ar-H_2-H_2O) and high-pO_2 (Ar-O_2 or air) atmospheres. However several authors investigated chromia forming alloys in high-pO_2 (Ar-O_2) with and without water vapour. An increasing effect of water vapour on the chromia scale growth was observed by Henry et al. [50] during

oxidation of pure chromium at 900°C. The chromia scale growth rate was higher in Ar-15%H_2O than in Ar-15%O_2. The higher chromium oxide scale growth rate was explained by the smaller ionic radius of OH^- (95 pm) compared with the radius of O^{2-} (140 pm). Thereby it was speculated that the lattice diffusion transport of the OH^- species through the scale should be faster than that of oxygen. Similar to the results of other authors it was also observed that the oxide scale adherence was improved in the water vapour containing atmosphere.

Hultquist et al. [51] oxidized pure chromium at 900°C. The measured chromia scale growth rate was double in the oxygen atmosphere containing 2% H_2O compared with dry oxygen. Also improved adhesion of the oxide scale was observed for chromium oxidized in water vapour containing gas. Better adhesion of the oxide scale was proposed to be related to a greater fraction of the scale growth occurring at the metal-oxide interface.

4.2.2 Effect of H_2O on selective oxidation of Cr

Essuman et al. [44] found that water vapour addition in Ar–O_2 mixtures tends to suppress protective scale formation for ‘‘borderline” alloy Ni–10Cr with the result that an alloy which forms a protective chromia base scale in dry Ar–O_2 may form a rapidly growing, non-protective oxide in Ar–O_2–H_2O. This detrimental effect of water vapour was partly explained by enhanced Cr depletion due to formation of volatile Cr-species. However, indications were found that the enhanced tendency for Cr to become internally oxidized is an additional, perhaps dominating factor which explains the experimental results. Additionally, the authors found that the detrimental effect of water vapour strongly depends on the oxygen partial pressure in the gas. Lowering the pO_2 decreases the growth rate of the non-protective oxide NiO, which on the basis of oxidation theory, decreases the critical Cr content required for

protective scale formation. A change from protective to non-protective behaviour by water vapour addition was found more likely in a high-pO_2 (e.g. Ar–20%O_2), than in a low-pO_2 gas (e.g. Ar–1%O_2).

Othman et al. [52] studied FeCr alloys (5, 17 and 25wt.% Cr) in Ar-5%O_2-20%H_2O, Ar-20%O_2-5%H_2O, Ar-10%H_2-20%H_2O and Ar-20%O_2 at 700°C. Higher growth rates for Fe-17Cr and Fe-25Cr were obtained in Ar-5%O_2-20%H_2O, Ar-20%O_2-5%H_2O than in Ar-20%O_2. The alloy containing 9% Cr failed by breakaway oxidation in the water vapour containing gases. In the low oxygen partial pressure gas (Ar-10%H_2-20%H_2O) alloys Fe-17Cr and Fe-25Cr formed an outer protective chromium oxide scale while Fe-9Cr showed internal oxidation of Cr. The authors found coarsening in chromia grain sizes with increasing H_2O/O_2 ratio. Additionally, in Ar-10%H_2-20%H_2O whisker formation was observed.

Bin Ani et al. [53] investigated Fe-Cr alloys in dry and humid atmospheres. The obtained results showed that transition from internal to external oxidation occurs at 8 mass % Cr and 12 mass % Cr in dry and humid environments, respectively. The authors found that in the presence of water vapour the oxygen permeability increased by a factor of 1.4 compared to that in dry gas. It was also concluded that dissolved hydrogen possibly enhances the transport of oxygen along the metal/oxide internal precipitate interfaces.

4.2.3 Effect of H_2O in the atmosphere on Cr_2O_3-evaporation

Chromium evaporation from the surfaces of chromia forming alloys at high temperatures is a well known effect which was extensively investigated e g. by Opila et al. [54, 55] in high pO_2-gas, e.g. wet air. Chromium oxide can evaporate according to the following reactions:

$$\frac{1}{2}Cr_2O_{3(s)} + \frac{3}{4}O_2 \rightarrow CrO_{3(g)} \quad (3.1)$$

$$\frac{1}{2}Cr_2O_{3(s)} + H_2O_{(g)} + \frac{3}{4}O_{2(g)} \rightarrow CrO_2(OH)_{2(g)} \quad (3.2)$$

$$\frac{1}{2}Cr_2O_{3(s)} + \frac{1}{2}H_2O_{(g)} + \frac{1}{2}O_{2(g)} \rightarrow CrO_2(OH)_{(g)} \quad (3.3)$$

In the temperature range below 1500°C the predominant process is reaction (3.2) [54].

Deodeshmukh [56, 57] tested several Ni- and Fe-based alloys in air with 10% H_2O at 760°C and 871°C. For many chromia forming alloys the authors found weight-loss (in spite of the fact that no spallation occurred). The authors concluded that the latter fact is an indication that the dominant mode of degradation is chromia vaporization [56]. The authors investigated also Cr consumption during long term exposures in air 10% H_2O at 760°C and 871°C. It was found that measured Cr-consumption is in good agreement with the theoretical chromium vaporisation rate calculation proposed by Young and Pint based on classical gas transport theory [57].

Holcomb [58] investigated reactive-evaporation rates of chromia in stainless steels and Ni-based alloys. The author claimed that not only temperature, but also factors such as amount of water vapour in oxygen or air, gas flow rate and the pressure of the gases, has a detrimental effect on the rate of chromia evaporation. It was also mentioned that chromium evaporation is expected to be an important factor which might substantially increase the oxidation rates of Ni-based alloys due to faster Cr depletion by evaporation. Chromium evaporation is less important for ferritic and austenitic steels due to their relatively high oxidation rate with respect to the evaporation rates.

Pujilaksono at al. [59] investigated the oxidation behaviour of pure chromium in dry O_2 and O_2+10%H_2O at 600 and 700°C. On the surface of specimen oxidized under wet conditions formation of blade-shaped crystals was observed. This effect was not visible after dry gas exposure. The authors correlated this phenomenon with vaporisation of volatile species such as $CrO_2(OH)_2$.

4.3 Oxidation behaviour of alumina forming superalloys

According to **Figure 3.2** the compositions of cast Ni-base superalloys such as e.g. PWA 1483, IN792 and CMSX-4, CM247 lie in respect to oxide scale formation relatively close to the boundaries between Al_2O_3/Cr_2O_3 and Al_2O_3/NiO respectively. Therefore the above materials can be classified as "marginal alumina formers". Typically, an alumina scale forms after an extensive transient oxidation period and its formation can be adversely affected by experimental (service) conditions, such as lower temperature, more aggressive test gas, etc.

4.3.1 Effect of H_2O on transient oxide formation

Maris-Sida et al. [60] investigated several Ni-based alumina forming superalloys (e.g. Rene N5, PWA1484, Ni-8Cr-6Al) at 1100°C in dry air and air containing water vapour. It was found that water vapour strongly enhanced spallation of the oxide scale during cyclic oxidation. The authors concluded that the reason for this effect is a decrease in fracture toughness of the alloy/alumina interface by water vapour. In addition water vapour was found to promote the transient oxidation regime (formation of Ni-rich oxides such as spinels). After long-term exposure spinel formation on top of the alumina scale was found in both atmospheres, however this effect was much more pronounced in water vapour containing

atmosphere. The authors proposed that water vapour could possibly enhance α-Al_2O_3 cracking and spallation compared to the dry atmosphere. Another explanation could be that spinel formation via outward diffusion of Nickel and Chromium could be accelerated by water vapour.

Onal et al. [61] studied the oxidation behaviour of Ni-based superalloys in dry and wet (0.3 atm. H_2O) air at temperatures between 700 and 1100°C. It was found that for alumina forming alloys water vapour adversely affects the selective oxidation of aluminium. The authors concluded that suppression of external oxidation of aluminium may be the result of a more rapid growth of the transient oxides caused by the presence of water vapour. Another finding was enhanced spallation of the alumina scale in the water vapour containing environment.

4.3.2 Effect of H_2O in the test gas on the scale adherence

Cyclic oxidation at 1100°C of alumina forming Ni-base superalloys and coatings in dry and wet air was performed by Janakiraman et al. [62]. The authors found that for alloys oxidized in water vapour containing gases the weight losses were increased by a factor of 2 to 4 compared to dry air. However, this effect was not observed for alloys which showed extremely adherent oxide scales. Enhanced spallation was observed for alloys in which after exposure in dry atmosphere damage in the formed alumina scale was found. It was proposed that water vapour causes a phenomenon similar to stress corrosion cracking at the Al_2O_3-alloy interface during cyclic oxidation.

Spallation of the alumina scale was widely investigated by Smialek [63, 64]. The author investigated alumina forming alloys as well as TBC systems (further discussed in **chapter**

3.5) as well as oxide scale spallation in wet atmosphere and correlated it with so called desktop spallation (DTS) and moisture-induced delayed spallation (MIDS) respectively. In both proposed mechanisms moisture has been postulated to serve as a source of interfacial hydrogen embrittlement. Hydrogen, in this particular case, is derived from reaction with aluminium in the alloy at an exposed interface.

4.4 Oxidation behaviour of MCrAlY alloys and coatings

4.4.1 Effect of MCrAlY-coating composition and microstructure on oxidation resistance

A substantial number of investigations on materials containing high amounts of Al and Cr such as MCrAlY (M = Ni, Co) has been carried out.

MCrAlY materials used in gas turbines need to possess not only an excellent oxidation resistance at elevated temperature but also a high fatigue resistance due to cyclic thermal stresses in the turbine components. It is known that the fatigue behaviour is governed by the ductility and strength of the coating which is reached by additions of Co and Re. The influence of addition of Co and Re on MCrAlY microstructure was investigated e.g. by Achar et al. [65] and Täck [66]. It was concluded, that Co stabilizes the γ+β two-phase microstructure thereby suppressing transformation from ductile γ to a brittle γ'+α-Cr at T<1000°C which is associated with a volume change and deteriorated oxide scale adherence [65, 66]. It was also observed that Re addition, in spite of improving fatigue resistance, has a negative influence on ductility because it promotes the formation of brittle phases such as TCP-phases and α-Cr. Therefore, a compromise in the addition of Re needs to be obtained.

A similar effect of Re addition on the formation of brittle phases such as α-Cr, γ'-Ni_3Al and σ-(Co, Cr, Re) in a NiCoCrAlY-coating was found by Toscano et al. [67]. The mentioned phase formation is associated with a volume change and consequently an increasing of the coating CTE. Moreover, formation of those phases is expected to decrease ductility and thus lower the resistance against thermo-mechanical fatigue.

Quadakkers et al. [68] studied the oxidation behaviour of cast MCrAlY materials. The authors found improvement of alumina scale adherence by minor additions of yttrium. The proposed mechanism of improved alumina adherence proposed by the authors is formation of yttrium oxides and/or Y-aluminates as fingerlike precipitates which provides better bonding between the oxide scale and the MCrAlY. Also formation of different oxide scale morphologies on γ- and β-phases was observed: on the γ-phase a thin alumina layer with a spinel on top formed whereas on the β-phase needle shaped aluminium oxide formed, which was identified as metastable θ-Al_2O_3. Lan et al. [69] investigated the oxidation behaviour of CoNiCrAlY alloys without and with addition of Re. It was observed that addition of rhenium improved the oxidation behaviour of the coating by accelerating the transformation from θ-alumina to α-alumina.

4.4.2 Effect of manufacturing parameters on the MCrAlY-coating oxidation behaviour

Results obtained by many researchers showed that the oxidation behaviour of MCrAlY materials can be strongly affected by their manufacturing process. Investigations of MCrAlY coatings by Gil et al. [16, 70] showed that the yttrium distribution in the MCrAlY-coating is strongly affected by the base material composition and the manufacturing parameters. Of

equal importance are the Y-content, the surface roughness, the vacuum quality during MCrAlY powder gas-atomisation and especially the temperature regime and vacuum quality during diffusion heat treatment after spraying. It was found that different oxide scale morphologies formed on flat and on rough MCrAlY surfaces. Moreover, differences in the oxide scales formed in concave and convex regions of rough coating have been found: in convex regions a thinner alumina scale formed than in the concave regions, where thicker alumina containing more Y-Al oxide pegs was present. The authors attributed this effect to an inhomogeneous Y-depletion which is faster in the convex regions of rough surface.

Gudmundsson et al. [71] observed that high yttrium concentrations can result in the formation of different types of Y-Al mixed oxide precipitates in the grain boundaries of the oxide scale. This precipitates were identified as $Y_3Al_5O_{15}$ (yttrium-aluminium-garnet YAG) and $YAlO_3$ (yttrium-aluminium-perovskite YAP).

Similar results were obtained by Nijdam et al. [72]. The authors observed a beneficial effect of mixed Y-Al oxide pegs on the scale adhesion. In contrast Braue et al. [73] observed that under certain conditions formation of the yttrium aluminates may be detrimental to the oxide scale adhesion, because of the different coefficients of thermal expansion of Al_2O_3 and yttrium aluminates.

An influence of manufacturing parameters on the distribution of reactive elements such as Y and Hf in the coating on oxidation behaviour was found also by Subanovic et al. [74]. The authors found that variation of oxygen partial pressure during VPS spraying and/or the subsequent vacuum heat treatment procedure significantly affects the yttrium and hafnium distribution in the coating. In coatings sprayed in high pO_2, both elements were tied up into oxide precipitates in the as-received condition. For these coatings early alumina spallation has

been found during oxidation tests. For the coatings sprayed at low pO_2 an "overdoping" effect occurred which leads to extensive Y and Hf incorporation into the scale resulting in accelerated scale growth rates and pronounced internal oxidation. Toscano et al. [75] found that not only the yttrium distribution is an important factor increasing oxide scale adherence but also the yttrium reservoir itself. The authors tested free standing MCrAlY coatings and found that, if the yttrium concentration has been decreased beneath a critical level, its positive effect on TGO adherence is lost. The authors concluded that the positive effect of yttrium on oxide scale adherence is correlated not only with the initial content, but also with the yttrium reservoir which is directly proportional to the coating thickness. Moreover it was found that yttrium transport occurred to be slower in CoNiCrAlY- than in NiCoCrAlY-coatings, which results in a better oxidation behaviour of the CoNiCrAlY-coating.

Toma et al. [76] examined the oxidation behaviour of free standing coatings deposited by HVOF at temperatures between 850 and 1050°C. The obtained results showed that the oxidation rates for HVOF deposited coatings were two times slower than for those deposited by VPS. The better oxidation behaviour in case of the HVOF sprayed coating were correlated with formation of fine Al_2O_3 and aluminium-yttrium mixed oxides dispersions formed during the spraying by HVOF. The authors assumed that these fine oxide precipitations hindered diffusion of various elements from the bulk material to the coating/gas interface during oxidation. Based on the obtained results the authors suggested that the HVOF process can be used as a technological alternative to the more expensive VPS coating deposition method.

Only few literature sources exist on the oxidation of MCrAlY-coatings in H_2O-containing gases. Subanovic et al. [77] studied the oxidation behaviour of free standing VPS MCrAlY coatings in Ar-20%O_2 and Ar-4%H_2-2%H_2O. The authors observed a lower growth rate for the MCrAlY-coating exposed in wet, low pO_2 atmosphere compared to dry, high pO_2-gas.

This was in accordance with earlier observations related to the oxidation behaviour of alumina forming FeCrAlY alloys [78]. For the coating exposed in Ar-4%H_2-2%H_2O also "blistering" of the coating was found. The authors correlated this phenomenon with hydrogen recombination in coating defects. It was suggested that hydrogen was produced at the scale/metal interface by reaction of water vapour with Y and Al from the coating.

4.5 Oxidation of TBC systems

4.5.1 EB-PVD TBC's

For the EB-PVD TBC systems with conventional MCrAlY bondcoats it was found that cracks usually initiate and propagate at the flat TGO/bondcoat interface. Toscano et al. [79] found longer lifetime of EB-PVD TBC systems exposed in Ar-4%H_2-2%H_2O than those exposed in air-2%H_2O. This was related to the slower growth rate of the alumina in the low pO_2-atmosphere resulting in an extended exposure time for obtaining the critical thickness to initiate scale spallation.

An effect of water vapour on the behaviour EB-PVD TBC systems was observed by Deneux et al. [80]. The addition of water vapour appeared to promote spallation after a critical number of cycles at 1150°C (170 cycles in this particular case). Moreover, it was shown that after a critical number of cycles water vapour present in ambient air after minutes or hours at room temperature also promotes spallation of TBC.

Water vapour in the atmosphere was shown to have an adverse effect on the EB-PVD TBC's lifetime. Smialek [64] found a so called "moisture-induced delayed spallation" (MIDS) of the

TBC. The author explained this phenomenon by weakening of the bondcoat/TGO interface by hydrogen embrittlement, which is derived from the water molecules or hydroxyl species.

Song [7] observed lifetime extension for EB-PVD TBC systems by minor additions of Zr to the bondcoat. Zr incorporation into the oxide scale allows faster oxygen diffusion via zirconia precipitates at the alumina grain boundaries. As a result of the local zirconia incorporation a more convoluted TGO/bondcoat interface forms and crack propagation is slower than that occurring at a flat TGO/bondcoat interface. However, precise control of Hf, Zr or Y-reservoir appeared to be very difficult. The authors also found a detrimental effect of high pO_2 in the water vapour containing atmosphere on the lifetime of EB-PVD TBC system with NiCoCrAlY bondcoat. The moisture-induced delayed spallation was proposed as an operating mechanism adversely affecting the Al_2O_3 scale adhesion.

4.5.2 APS TBC's

The mechanisms of governing failure EB-PVD and APS-TBC systems during cyclic exposure substantially differ [7]. In the APS-TBC systems cracks start to form usually on the hills of rough bondcoat surfaces and subsequently propagate through the topcoat. Therefore two important factors determining crack propagation, and thus the APS-TBC lifetime, were identified i.e., bondcoat roughness and topcoat porosity. Bondcoat roughness profiles strongly depend on the coating manufacturing method. Naumenko et al. [81] found that APS TBC systems are prone to formation of intrinsically inhomogeneous TGO-morphologies on the MCrAlY bondcoats. This phenomenon was attributed to a non-uniform Y and Al depletion as well as to the commonly observed repeated cracking and re-growth of the TGO. A similar effect was found by Tang [82].

Yamazaki et al. [83] investigated the influence of bondcoat roughness on the residual adhesion strength after thermal cycle fatigue. It was observed that for rough LPPS coating after cycle fatigue, the residual adhesion strength was higher than for the specimens with a relatively flat interface. Moreover, formation of microcracks within the TBC was found to be dependent on bondcoat roughness.

It was observed that the oxidation of Y by residual oxygen can occur during gas atomisation of the MCrAlY-powders or during the spraying process. The vacuum heat treatment of the MCrAlY-coatings after spraying also results in selective oxidation of Y at the surface. This phenomenon was found to be independent of the deposition method and was found in MCrAlY-coatings produced by VPS [74] as well as by EB-PVD [84, 85, 86]. The precipitate morphology, form and distribution of this Y-rich oxides depend on the time and temperature of heat-treatment as well as on the vacuum quality. The Y-oxide distribution prevailing in the MCrAlY-coating after the heat treatment was shown to have a significant effect on the growth rate and adherence of the alumina scale and consequently the lifetime of the TBCs [74, 84, 85, 86, 87].

Renusch et al. [88] proposed that Al depletion in the bondcoat after longer exposure time results in formation of non-protective oxides, e.g. spinel, which can provide sites for initiation and propagation of failure relevant cracks.

De Masi-Marcin et al. [89] proposed that linking of the micro-cracks within the APS topcoat finally results in TBC spallation. The cracks should penetrate the TBC above the concave regions of the rough bondcoat. Vaßen et al. [90] showed that in the early stages of exposure, i.e., if the TGO thickness is relatively small, the residual stress during cooling in the TBC systems in these areas is compressive, which hinders the crack linking. As the TGO grows

with time, a conversion of the residual stress from compressive into tensile occurs after a given time [91], which permits crack linking and failure. This means that the lifetime for APS TBC's can be much longer than the time for first TGO delamination at bondcoat hills.

Evans et al. [92] found in MCrAlY bondcoats deposited by APS formation of spinel due to a so-called "diffusion cell" effect, resulting from oxidation of individual MCrAlY powder particles during spraying. This leads to a hindering of the Al-flux from the bulk bondcoat towards the surface for alumina scale formation. Each of the solidified MCrAlY powder particles represents a "diffusion cell" which fails after relatively short exposure time by breakaway oxidation involving Ni and Co rich oxide formation resulting in rapid TBC failure.

It was also found that properties of the YSZ topcoat can play a significant role for the lifetime of the TBC systems. Helminiak et al. [93] studied the behaviour of high-purity, low-density (85%) APS TBC's with NiCoCrAlY bondcoat deposited by argon-shrouded plasma spraying. The obtained results showed that high purity YSZ topcoats are highly resistant to sintering and transformation from the metastable tetragonal phase into the equilibrium mixture of monoclinic and cubic phases. The porous topcoats also resulted in significantly enhanced durability during thermal cycling. The failure mechanisms of the APS TBC were found to depend on topcoat thickness, CTE of the substrate and the nature of the thermal exposure. Yasuda et al. [94] found that partially yttria stabilized zirconia can exhibit accelerated transformation from the tetragonal into the monoclinic phase in water vapour containing atmosphere depending on the Y-content and distribution in the ceramic.

Based on literature data an effect of water vapour in the test gas is less evident for APS-TBC systems than for the lifetime of EB-PVD TBC's. Some authors found an adverse effect of water vapour on the oxidation behaviour of APS-TBC systems. Rudolphi et al. [95] found (by

acoustic emission analysis) formation of cracks after immersion of specimens in water vapour. It was found that cracks were mostly accumulated at the YSZ topcoat and the TGO interface. The authors proposed a failure mechanism which assumes a weakening of the alumina bonds by aluminium hydroxide formation. Other authors found no substantial effect of water vapour on TBC lifetime (e.g. Song [7]).

5 Experimental:

5.1 Studied materials and geometry of the specimens

The materials investigated in the current study were: uncoated Ni-based superalloys, free standing coatings, MCrAlY-overlay coatings on Ni-based superalloys and APS TBC systems.

5.1.1 Chemistry of the materials

5.1.1.1 Ni-based superalloys

Ni-based polycrystalline superalloy Rene 80 was investigated. The commercial conventionally cast Ni-base superalloy Rene 80 was used in this study. Chemical analyses were performed by inductively coupled plasma – optical emission spectroscopy (ICP-OES) for most of the metallic elements and mass spectrometry (ICP-MS) for boron and zirconium after dissolution in aqua regia. The carbon analysis was performed by combustion in oxygen flow with subsequent quantitative infrared spectroscopy. The results in **Table 5.1** revealed that the analysed composition of the studied alloy batch was very similar to the nominal composition of Rene 80.

Table 5.1 Nominal and analysed* composition of Rene 80 in wt.% (reproduced from reference [96]).

	Cr	Co	Ti	Al	Mo	W	C	B	Zr
Nom.	14.0	9.5	5.0	3.0	4.0	4.0	0.17	0.02	0.03
An.	13.2	9.2	4.6	3.9	3.9	3.9	0.15	0.03	<0.01

* For all measured concentrations above 1% the uncertainty is +/- 3%, for the concentrations below 1% it is 10%.

5.1.1.2 MCrAlY coating

Table 5.2 shows the nominal and the measured chemical composition of the studied MCrAlY coating. The chemical analysis of the sprayed MCrAlY was performed using a free-standing coating. For this purpose a 4 mm thick layer was sprayed on a steel substrate and subsequently removed from the substrate using spark erosion. The specimens for the analysis were ground to remove pollutions from the surface, cut into small pieces and subsequently 200 mg of the sample was dissolved in a solution made of 3 ml HCl / 0.5 ml HNO_3 / 0.5 ml HF, filled up to 50 ml and then analysed by ICP-OES. For all measured concentrations above 1% the uncertainty is +/- 3%, for the concentrations below 1% it is 10%.

Table 5.2 Chemical composition of studied MCrAlY coating analysed by ICP-OES (in wt. %)

		Ni	Co	Cr	Al	Y	Re
MCrAlY	Nominal	Bal.	25.0	17.0	10.0	0.40	1.50
	Powder	Bal.	24.6	17.0	10.4	0.23	1.29
	Coating sprayed by HVOF	Bal.	24.9	16.8	10.3	0.24	1.34

5.1.1.3 YSZ powders for ceramic topcoats of TBC systems

The investigated TBC systems consisted of Rene 80 as the base material with the above mentioned bondcoat and a ceramic topcoat sprayed by APS using two commercially available YSZ powders: AMPERIT® 827.773 by H.C.Starck and METCO YSZ 335M by SULZER METCO. 100 g of the above mentioned powders in the as-received were dissolved in 2 g

ammonium sulphate and 4 ml H_2SO_4 and filled up to 100 ml and analysed using ICP-OES. The chemical analysis of both YSZ powders is given in **Table 5.3**. The chemical analyses revealed that all of the studied materials the compositions were very similar to the nominal ones. For all measured concentrations above 1% the uncertainty is +/- 3%, for the concentrations below 1% it is 10%.

Table 5.3 Chemical compositions of the ceramic YSZ powders analyzed by ICP-OES (Zr, Y, Hf) and ICP-MS for the rest of elements.

Powder	Elements (wt. %)									
	Zr	Y	Hf	Ti	Si	Na	Ca	Al	Fe	O
AMPERIT 827.773	66.1	6.0	1.6	0.05	0.04	<0.01	0.02	0.06	0.01	rest
METCO 335M	67.0	5.9	1.4	0.06	0.03	0.06	<0.01	<0.01	<0.01	

5.2 Specimens preparation

5.2.1 Ni-based superalloys (uncoated)

Coupons of 20 x 10 x 2 mm were machined from the as-delivered materials by spark erosion. Depending on the testing requirement for some specimens a hole with 2 mm diameter was drilled close to the short sample edge for suspension in the test environment. All the specimens were ground till 1200 grit surface finish using SiC-paper. **Figure 5.1** shows the standard specimens shape.

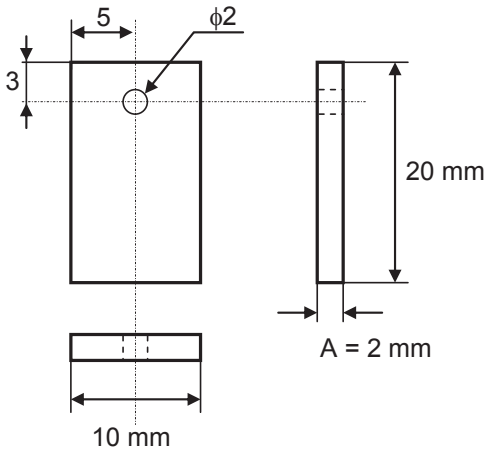

Figure 5.1 Standard specimen geometries used for testing of uncoated Ni-base alloys and free-standing MCrAlY-coatings

5.2.2 Free standing MCrAlY coating

A 3 mm thick MCrAlY layer was deposited by HVOF on a steel plate, and thereafter removed from the substrate using spark erosion. The eroded coating was heat treated (vacuum of 10^{-5} mbar according to the specification for Rene 80, that is: 1 hour at 1080°C and 12 hours at 870°C. The cooling rate was 10 K/min) and thereafter cut into specimens of 20 x 10 x 2 mm. One part of the specimens was ground on both sides to 1200 grit surface finish using SiC-paper. The second part of the samples was ground only from one side up to 1200 grit and the other side was retained with the rough, as sprayed surface. In the specimens for thermogravimetric tests a hole with 2 mm diameter was drilled for sample suspension (compare with **Figure 5.1**).

5.2.3 TBC specimens

TBC specimens were delivered as cylindrical rods with topcoats sprayed in segments (**Figure 5.2 a**)). The rods were cut into single specimens (**Figure 5.2 b**)) using a low speed saw.

All of the specimens were ultrasonically cleaned in ethanol prior to oxidation.

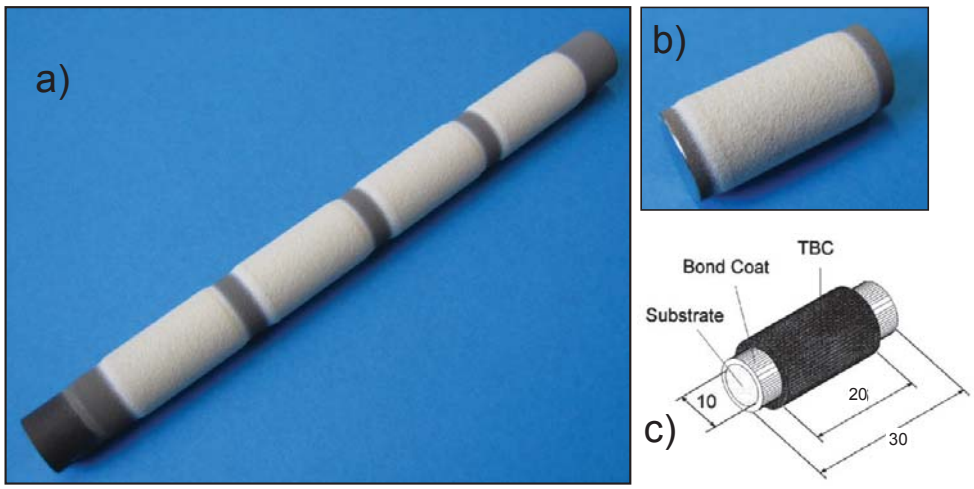

Figure 5.2 TBC systems in the as-delivered condition (a), after cutting into a single specimen (b) and schematic showing geometry and dimensions of TBC-specimen used for testing (c)

5.3 Oxidation experiments

Three different types of oxidation tests were carried out with the above mentioned specimens:

5.3.1 Isothermal and discontinuous oxidation

The discontinuous oxidation tests were performed at 1050°C in a tube furnaces with a heating rate of 10 K/min and a cooling rate of 2 K/min in two atmospheres:

- Synthetic air (N_2 + 21 % O_2)

- Synthetic air + 20% H_2O

During discontinuous exposure the furnaces were cooled down each 100 hours. The cooling was performed to approximately 70˚C in the test gas. This was necessary to prevent condensation of water vapour in the reaction tube in the wet atmosphere. At this temperature the specimens were kept for about two hours. Subsequently the furnaces were opened, the samples taken out and (after cooling down to room temperature) inspected and weighed. **Figure 5.3** shows the testing equipment and the sample holder for the discontinuous tests. **Figure 5.4** shows the temperature-time curve during one cycle.

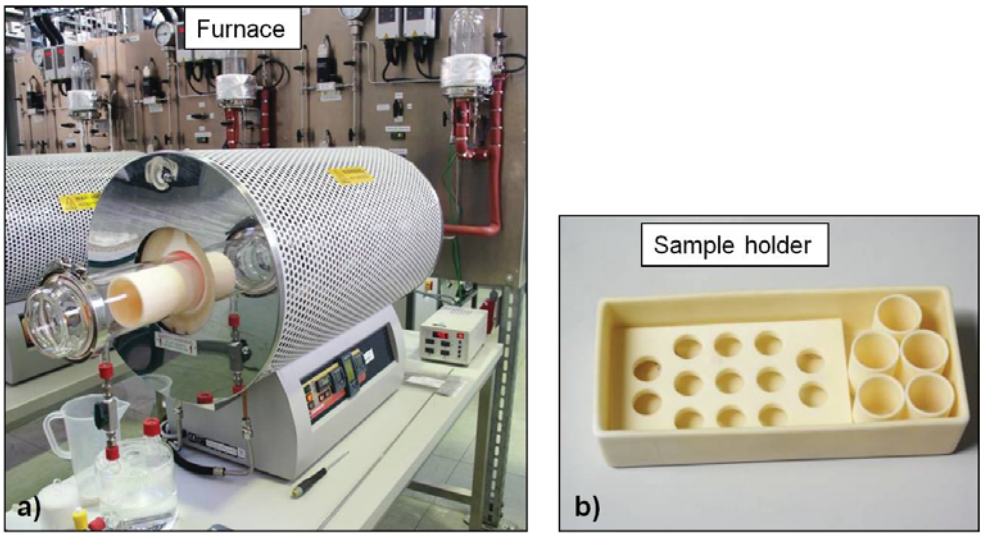

Figure 5.3 Testing equipment for discontinuous tests showing: a) furnace, b) sample holder

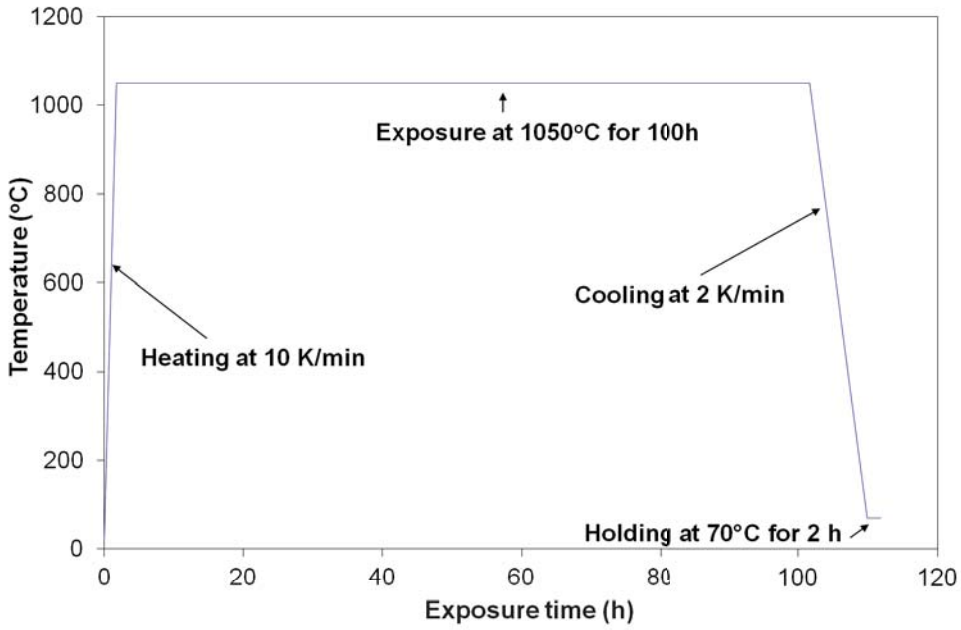

Figure 5.4 Temperature-time curve for one cycle of discontinuous oxidation

5.3.2 Accelerated cyclic oxidation tests

Accelerated cyclic oxidation tests were performed in laboratory air at 1120°C using automated rigs. The cycling consisted in moving the sample holder into the hot furnace for 2 hours. After this heating period the samples were moved out of the furnace automatically for 15 minutes during which intensive cooling was performed with pressurized air. The TBC specimens used for the lifetime measurement were inspected for failure daily (after each 18 hours hot time). Specimens were qualified as failed when the length of a macroscopically visible crack within the topcoat was longer than 5 mm.

5.3.3 Thermogravimetric (TG) experiments

For an accurate determination of the oxidation kinetics, thermogravimetric experiments [38] up to a maximum exposure time of 100 hours at 1050°C were carried out in six atmospheres:

- Ar – 1% O_2,
- Ar – 20% O_2,
- Ar – 1% O_2 + 7% H_2O,
- Ar – 20% O_2 + 7% H_2O,
- Synthetic air,
- Synthetic air + 7% H_2O.

The test facility was a TGA 92-16.18 SETARAM® thermobalance. The heating rate was 90 K/min, the cooling rate 10K/min and the gas flow rate 2 l/h.

5.4 Characterisation of oxidized specimens

The oxidized specimens were investigated using a variety of analytical techniques. These included glow discharge optical emission spectroscopy (GD-OES, GD Profiler HR, Horiba Jobin Yvon, France), plasma secondary neutral mass spectroscopy (SNMS, INA-5, SNMS Analyzer, SPECS GmbH, Berlin Germany), X-ray diffraction (XRD, D4 ENDEAVOR Diffractometer from Bruker AXS GmbH, Karlsruhe Germany in parafocussing Bragg-Brentano geometry), optical microscope Leica MF4 equipped with a digital camera ProgRes CFscan from Jenoptic and two scanning electron microscopes (SEM: - Merlin and – Supra 50VP from Zeiss Microscopy in Oberkochen, Germany). Both SEM's were equipped with energy dispersive X-ray analysis (EDX, Inca from Oxford Instruments).

Only selected specimens were analysed by GD-OES or SNMS. The elemental intensity versus sputtering time profiles were quantified into concentration versus depth profiles using the procedure described in references [97, 98].

For cross section analyses with optical microscopy and/or SEM the specimens after oxidation were mounted in epoxy resin. In order to obtain a better contrast between the oxide scale and the epoxy resin as well as to protect the oxide scale during cross section preparation, the oxidized Ni-based superalloys and overlay coated specimens were sputtered with a thin layer of gold and subsequently a Ni-coating was applied electrochemically from a $NiSO_4$ bath. A series of grinding and polishing steps followed with a final polishing using 0.25 μm granulation in SiO_2 solution.

5.4.1 Bondcoat roughness evaluation using fractal analysis

In order to describe the roughness profiles of bondcoats in the studied APS-TBC systems fractal analysis was used. Fractal analysis is a relatively flexible method for roughness profile evaluation, which has been applied to evaluate two dimensional roughness profile of flat ground surfaces [99], of cylindrical turned rods [100] as well as for three dimensional roughness descriptions of grit blasted metallic substrates [101, 102, 103]. The data used for fractal analysis in the mentioned publications are obtained from the roughness measurements using a standard profilometer with stylus [99, 100, 101, 102, 103]. However, it is possible to evaluate roughness by fractal analysis based on the surface profile data derived from microscopic analysis. Scott et al. [104] described dental microwear texture by fractal analysis using data obtained by a white-light scanning confocal imaging profiler. Briones et al. [105]

evaluated the surface roughness of bloomed chocolate based on results obtained using scanning laser microscopy. In the present study, fractal analysis was performed on the two dimensional bondcoat roughness profiles derived from metallographic cross sections.

5.4.2 Basics of fractal analysis

Fractal analysis is a mathematical method for describing self-similar objects. The basic concept is one of scale, which in this particular case is the apparent length of a surface profile, depends on the size of the device with which it is measured.

The definition of the relative length is given by the following equation:

$$L_R = \sum_i^N \frac{1}{\cos\theta_i} \frac{p_i}{L} \quad (5.1)$$

where:

L_R = relative length,

L = total projected length for all N virtual steps,

p_i = projected length for virtual step,

θ_i = angle between the normal to the nominal surface.

Relative length (L_R) as a function of scale length (r) plots were produced using the compass-method by measuring the apparent length of the profiles with progressively shorter rulers. For each measurement the length of the virtual rulers is kept constant and linear interpolation is used to locate the virtual steps between the sampling intervals in the profile [100] (**Figure 5.5 a**)).

As shown in **Figure 5.5 b)** the relative length as a function of scale length plots can be used to derive the following characteristic parameters describing the measured surface roughness profiles [99, 100, 101, 102]:

- *D* (Fractal Dimension): $D = 1 + |slope|$ (5.2)

- *LSFC* (Length-Scale Fractal Complexity): $LSFC=1000(D-1)$ (5.3)

- Relative Length at a given scale (L_R)

- Smooth-rough crossover (*SRC*)

More convoluted surfaces have higher values of *D*, *LSFC* and relative length at a given scale, whereas the value of *SRC* indicates the scale at which the roughness starts to prevail ((e. g.) on a mm-scale or μm-scale).

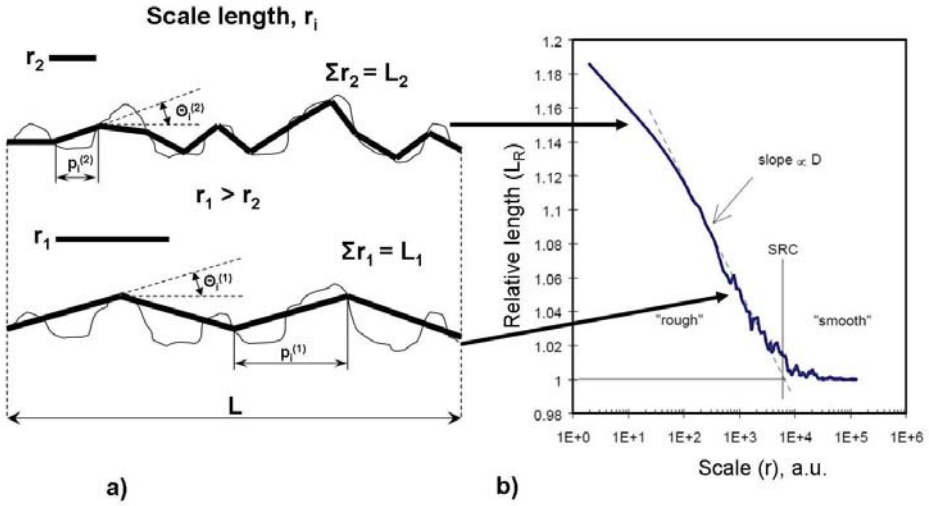

Figure 5.5 Schematic showing: a) roughness profiles description using different ruler length and b) typical plot obtained during fractal analysis of two dimensional surfaces (reproduced from Reference [99])

5.4.3 Procedure of bondcoat roughness evaluation using fractal analysis

The data used for the roughness evaluation were derived from the metallographic cross-section images of APS-TBC's in the as sprayed conditions. The procedure of roughness analysis included:

a) Image acquisition using an optical microscope,

b) Converting microscopic images into binary scale images (bondcoat – white and topcoat and mounting – black),
c) Digitalization of binary scale images into 2-D x-y data sets with constant x step,
d) Correction for cylindrical sample geometry using polynomial levelling algorithm (Alpha-step IQ software).

Four TBC systems with different bondcoats (HVOF BC, VPS BC + dense topcoat, VPS BC + porous topcoat and APS-flashcoat sprayed with parameter set II) were evaluated by fractal analysis using the commercial software Sfrax 1.0 [106].

Results and discussion

6 Oxidation behaviour of Rene 80

6.1 Short-term exposures of Rene 80

6.1.1 Oxidation kinetics

Figure 6.1 shows the mass changes of Rene 80 during oxidation up to 50 h in dry and water vapour containing, Ar-O_2 based gases as well as in synthetic air. The data show relatively small differences in the mass changes between the samples oxidized in the various atmospheres. The highest mass gain after oxidation for 50 h was found for the specimen oxidized in Ar-20%O_2-7%H_2O followed by (in decreasing order): Ar-20%O_2, Synthetic air, Ar-1%O_2 and Ar-1%O_2-7%H_2O. In spite of the fact that the measured mass changes are not very different, there are some variations in the instantaneous reaction rate after longer exposure times in the various atmospheres. This is apparent from **Figure 6.2** which shows k_w as a function of time plots calculated by local fitting of the mass gain curve with a parabolic law according to the procedure described in reference [38]. It can be observed that for all tested conditions, the k_w values decrease with time, reaching quasi-stationary regime after around 30 hours.

During oxidation up to 100 h the trend of mass gain was similar to that observed in the 50 h experiments (**Figure 6.3**). The obtained mass gain values after 100 h oxidation are in the range of 3.6 - 4.2 mg*cm^{-2}. In both the 50 and 100 hours experiments the instantaneous k_w values after longer exposure times seem to be lower for the Ar-1%O_2 based atmospheres than for the Ar-20%O_2 gases (**Figure 6.4**).

For the same atmosphere the reproducibility of the mass changes appeared to be good as could be seen by comparing the TG-curves after 50 and 100 h exposure showing only small

differences in the mass change after the same exposure time (compare **Figure 6.1** and **6.3**). The minor variations in the TG-curves for nominally the same conditions can be attributed to the unavoidable variations in the experimental and material parameters.

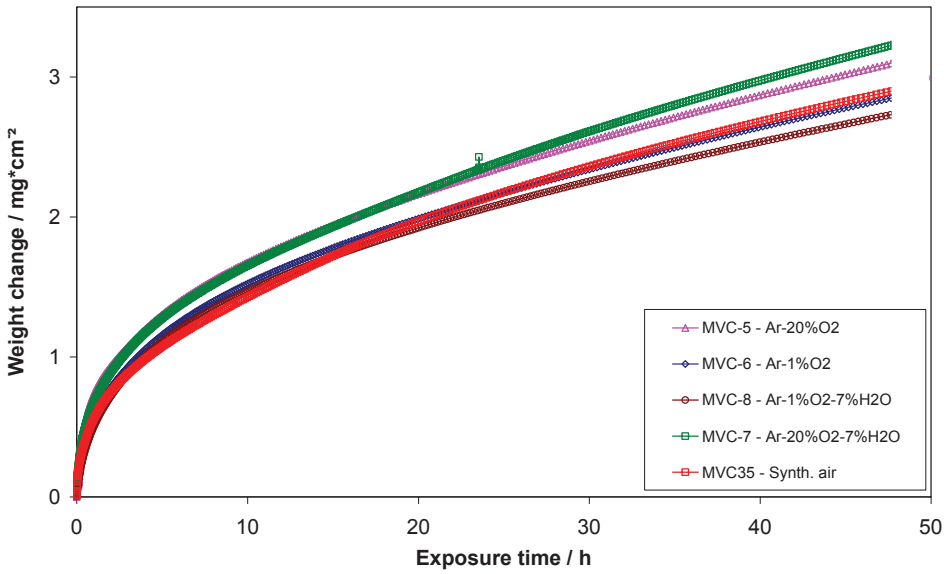

Figure 6.1 Mass changes during isothermal oxidation (TGA test) of Rene 80 at 1050°C up to 50 h in various atmospheres

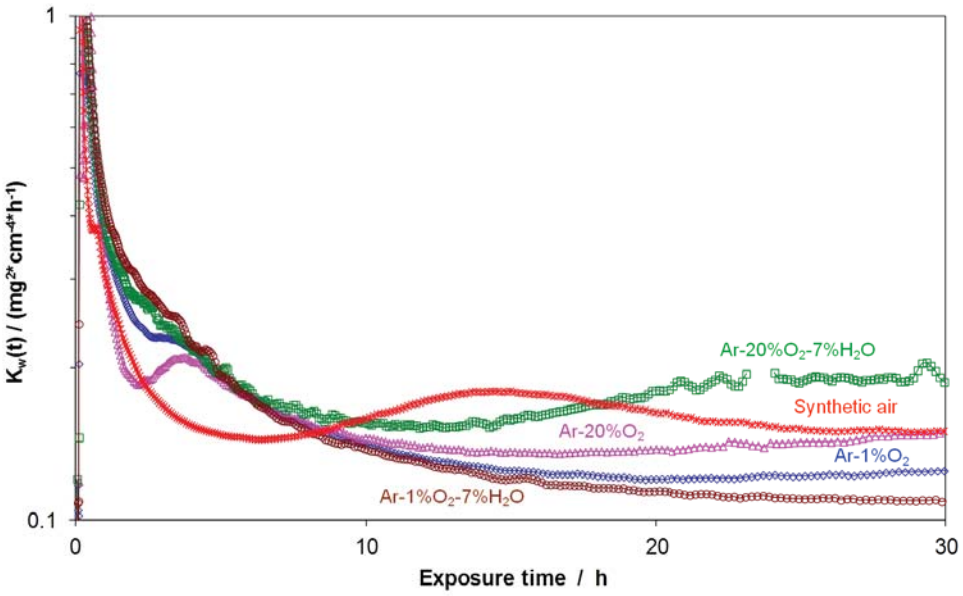

Figure 6.2 Instantaneous k_w as a function of exposure time obtained calculated from TG-data in Figure 6.1 (Rene 80 at 1050°C up to 50 h)

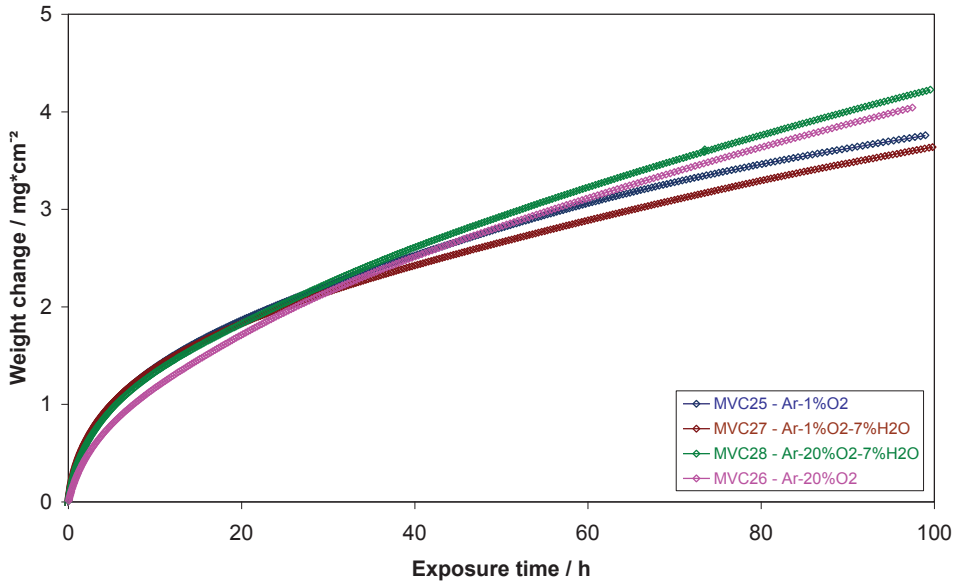

Figure 6.3 Mass changes during isothermal oxidation (TGA test) of Rene 80 at 1050°C up to 100 h

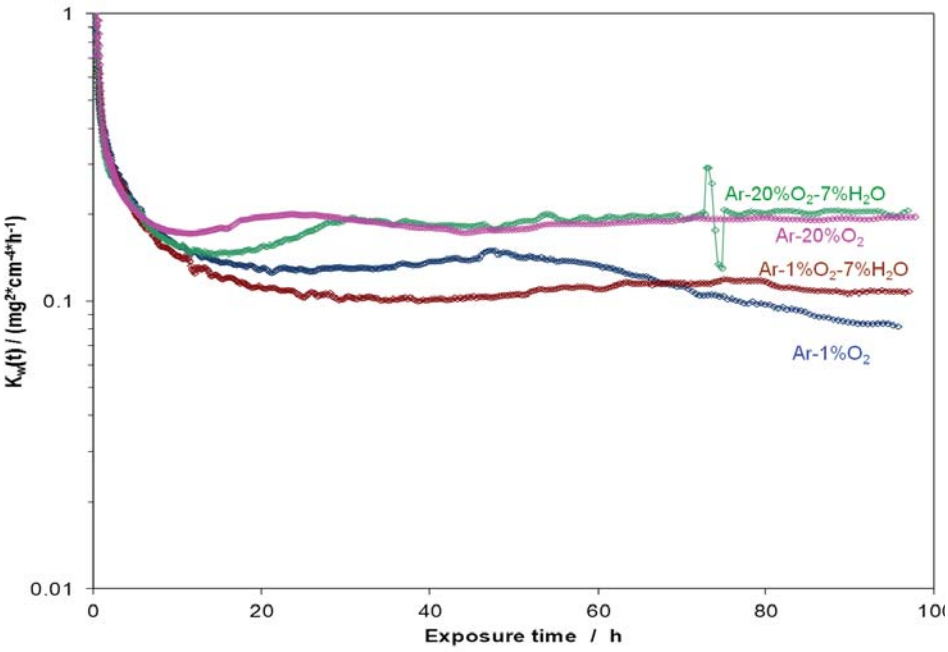

Figure 6.4 Instantaneous k_w as a function of exposure for data in **Figure 6.3** (Rene 80 at 1050°C up to 100 h)

6.1.2 Analytical studies of Rene 80

6.1.2.1 Early stages of oxidation; 1 hour exposures

To investigate the elemental distribution in the oxide scale and the sub-scale zone of the alloy GD-OES depth profiles were measured on the samples after 1 hour of oxidation (**Figure 6.5a – 6.5d**). All specimens were found to form Ti-rich oxide with small amounts of Co in the outer part of the scale. Below the outer Ti-oxide, chromium rich oxide formed and in the inner part of the chromium oxide a second enrichment of Ti is present. This Ti enrichment occurs in the scale regions where the concentration of Cr is still relatively high, which can be an indication of Ti/Cr mixed oxide formation. In addition, Al enrichment is observed beneath the Cr-rich oxide in all studied atmospheres. Also B enrichment was observed in the oxide scale formed in all studied atmospheres. The latter effect will be discussed in detail in **chapter 6.3**.

Figure 6.6 shows SEM cross-sections of Rene 80 after oxidation for 1 h. The oxide scales consist of outer continuous TiO_2, a Cr-rich oxide scale, Cr-Ti-mixed oxide in the inner part of the chromia scale and internal Al_2O_3 precipitates. For the specimens oxidized in water vapour containing atmospheres the oxide scale compositions are qualitatively similar to those in the dry gases. However, Ti is partly oxidized internally together with Al, which might be the reason why the inner Cr-Ti mixed oxide does not form a continuous layer in the wet gases (**Figure 6.7**). Moreover, the outer TiO_2 layers are thicker and more porous on the samples oxidized in the wet gases than in the dry gases.

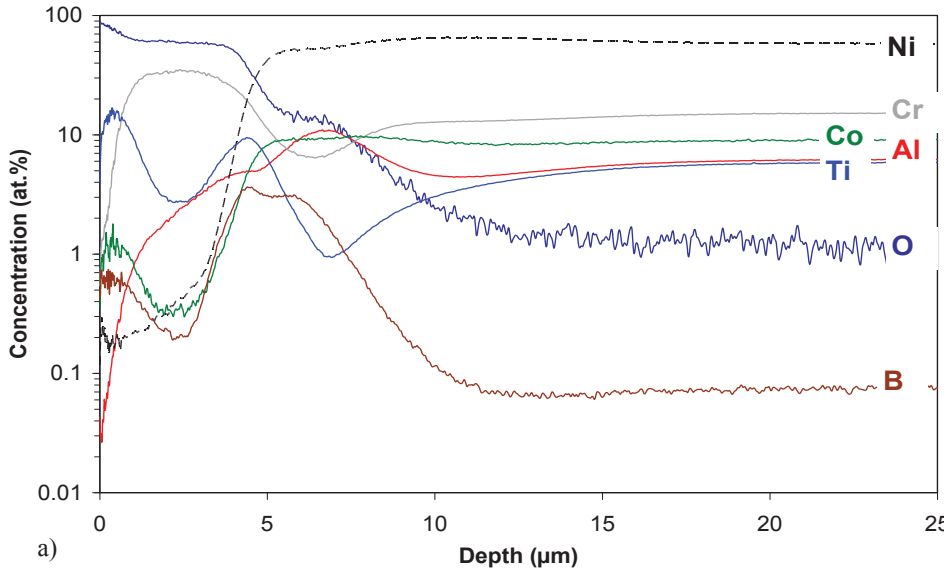

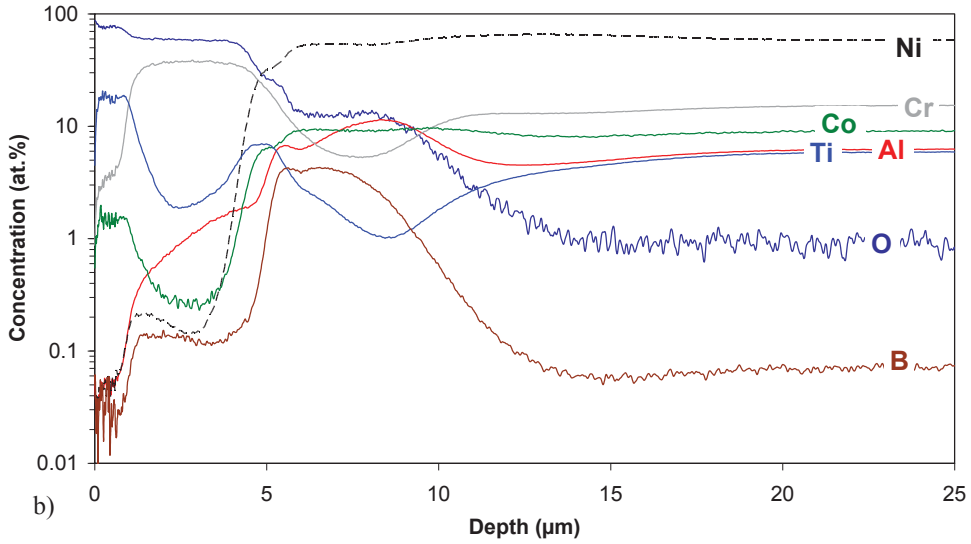

Figure 6.5 GD-OES depth profiles of Rene 80 after isothermal oxidation at 1050°C for 1 h in: a) Ar-1%O_2, b) Ar-1%O_2-7%H_2O, c) Ar-20%O_2, d) Ar-20%O_2-7%H_2O

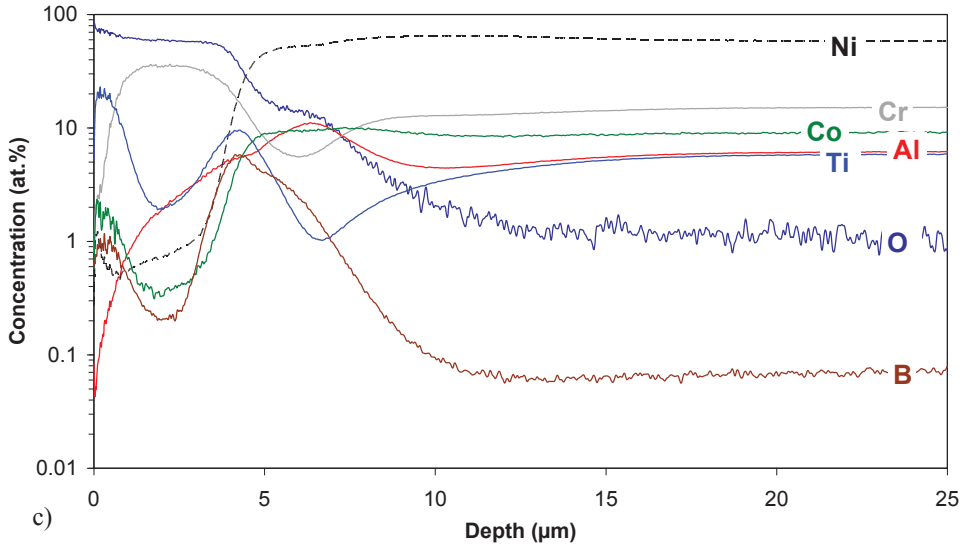

c)

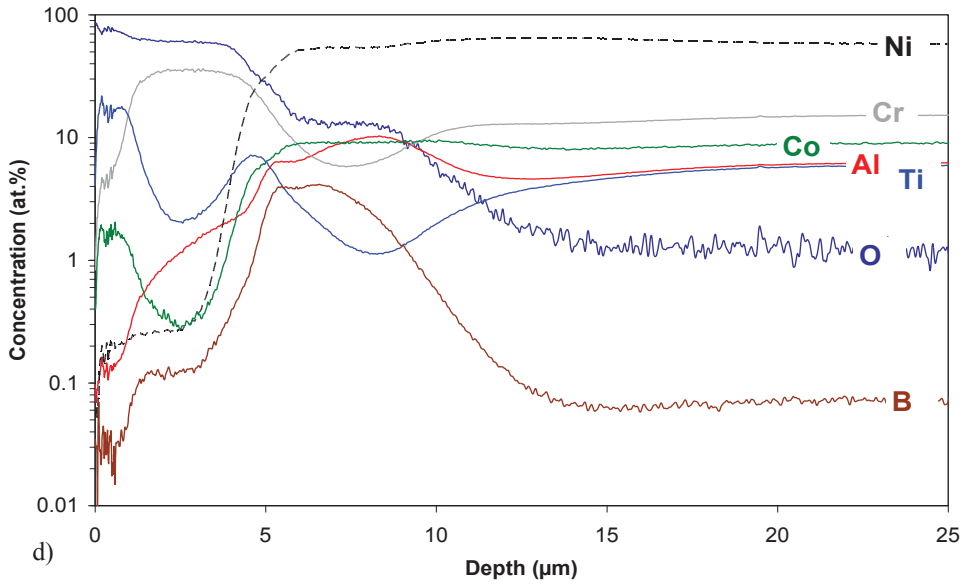

d)

Figure 6.5 Continued

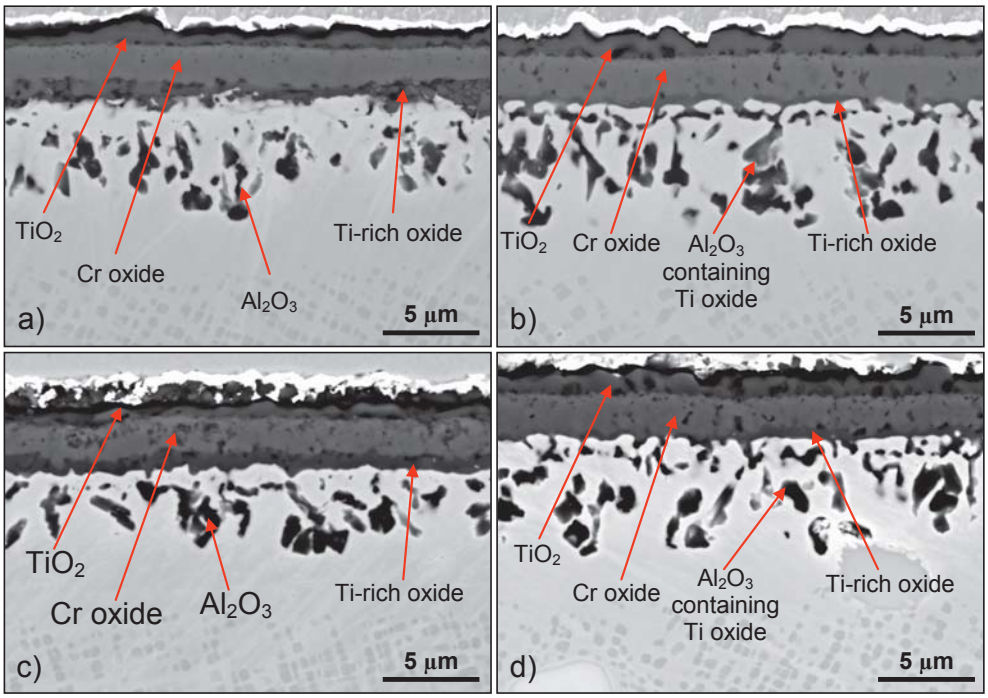

Figure 6.6 SEM BSE images of Rene 80 cross-sections after isothermal oxidation at 1050°C for 1 hour in: a) Ar-1%O_2, b) Ar-1%O_2-7%H_2O, c) Ar-20%O_2, d) Ar-20%O_2-7%H_2O.

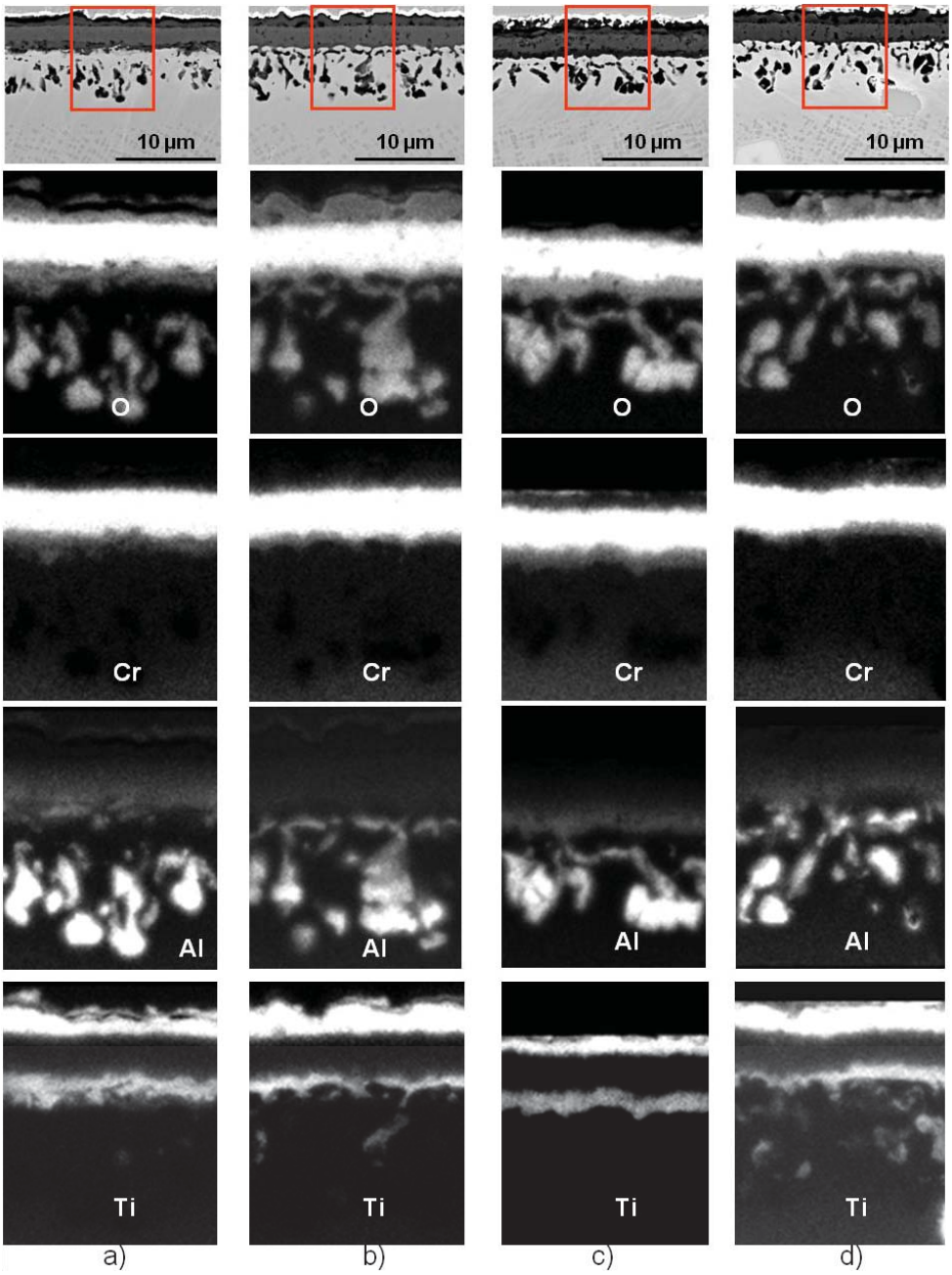

Figure 6.7 EDX elemental maps for Rene 80 isothermally oxidized for 1 hour at 1050°C in: a) Ar-1%O_2, b) Ar-1%O_2-7%H_2O, c) Ar-20%O_2, d) Ar-20%O_2-7%H_2O

6.1.2.2 Scale composition after 50 hour exposures

XRD analyses were performed on the samples oxidized for 50 h in all four studied atmospheres. The obtained results confirmed the presence of Cr/Ti mixed oxide after exposure in dry and wet atmospheres containing 1%O_2. The latter phase was identified as $CrTi_2O_5$. After exposure in the atmospheres with 20%O_2 this phase could not be found with XRD (**Figure 6.8**). After 50 h oxidation in the atmospheres with 1%O_2 the oxide scale composition is qualitatively similar to that after 1 hour exposure (compare **Figure 6.6** with **Figure 6.9**). However, in the SEM images at lower magnification (**Figure 6.9**) it can be observed that the inner Ti/Cr mixed oxide layer in the specimen oxidized in Ar-1%O_2 for 50 hours is not continuous. An important difference of the oxide scales after 50 hours exposure is substantial porosity, which was not observed after 1 hour. Based on **Figure 6.9 a**) and **b)** it seems that in the water vapour containing atmosphere the pores in the outer part of the scale are larger than the dry gas. In the inner part of the porous Cr oxide initiation of scale cracking can be observed (**Figure 6.10 b**).

In the specimens oxidized in the atmospheres with 20% oxygen no formation of Cr/Ti mixed oxide in the inner part of the oxide scale can be observed (**Figure 6.10 c**) and **d)**). However, in the SEM images at lower magnification (**Figure 6.9 c)** and **d)**) islands of mixed Cr/Ti oxides are visible and Ti-rich oxide particles embedded into the Cr oxide scale exist. It seems that the inner Ti/Cr-mixed oxide layer observed after 1 hour becomes unstable after 50 hours and the discrete Ti oxide particles after 50 hours originate from the Ti/Cr mixed oxide visible after 1h. A larger number of the latter particles is visible on the sample oxidized in dry atmosphere than that exposed in the wet gas.

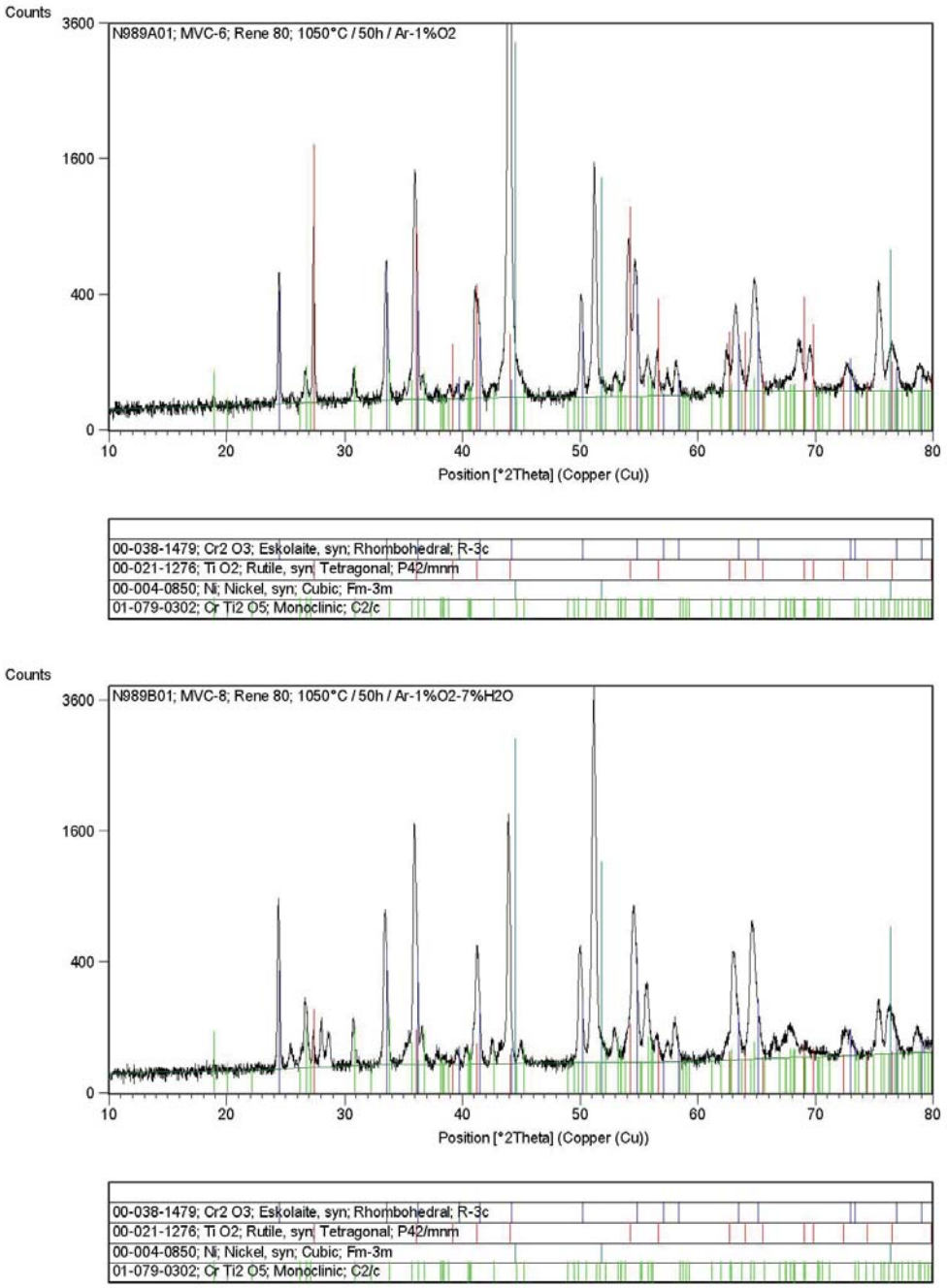

Figure 6.8 XRD patterns obtained from Rene 80 oxidized at 1050°C for 50 h in: a) Ar-1%O_2, b) Ar-1%O_2-7%H_2O, c) Ar-20%O_2, d) Ar-20%O_2-7%H_2O

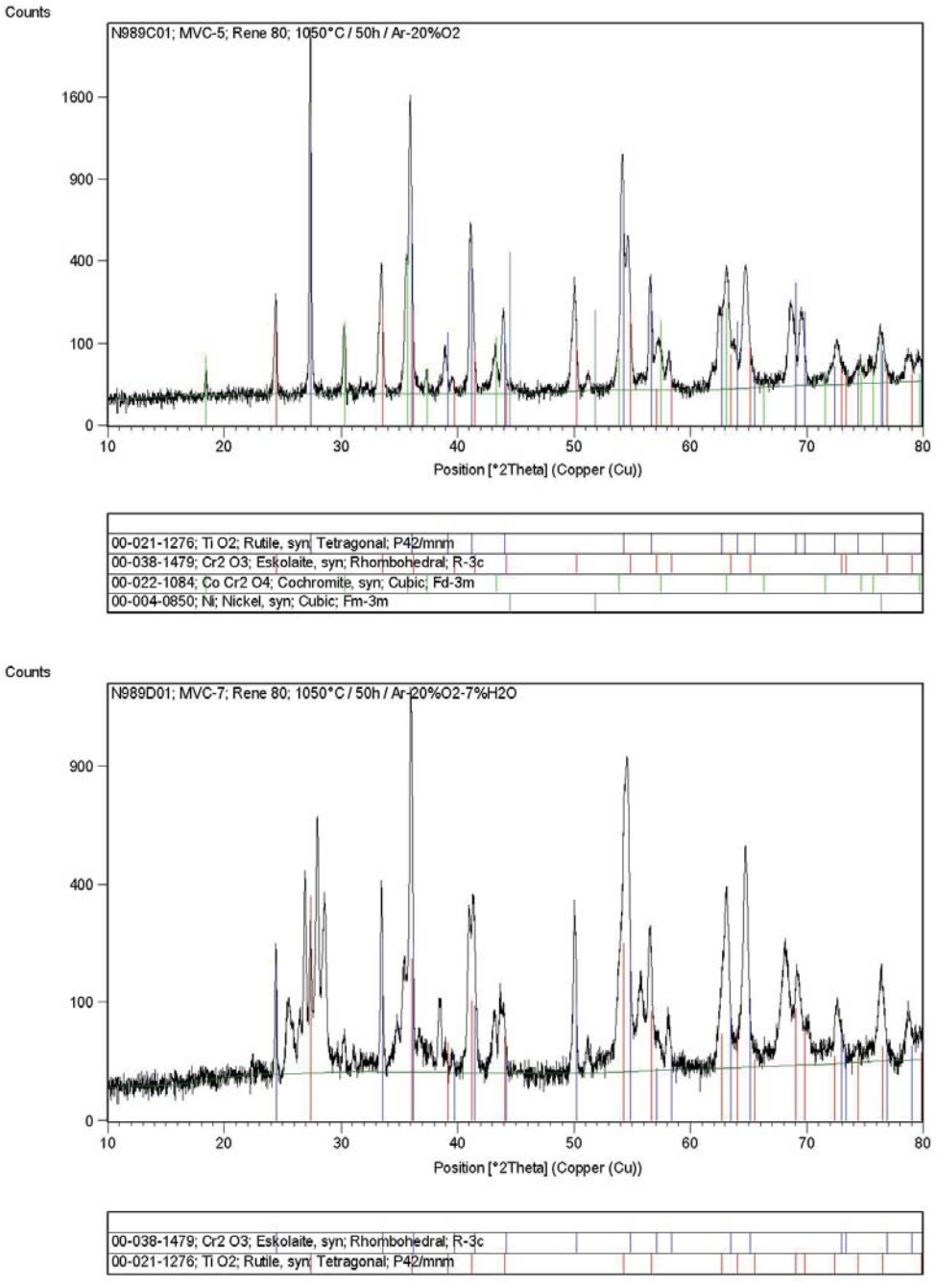

Figure 6.8 Continued

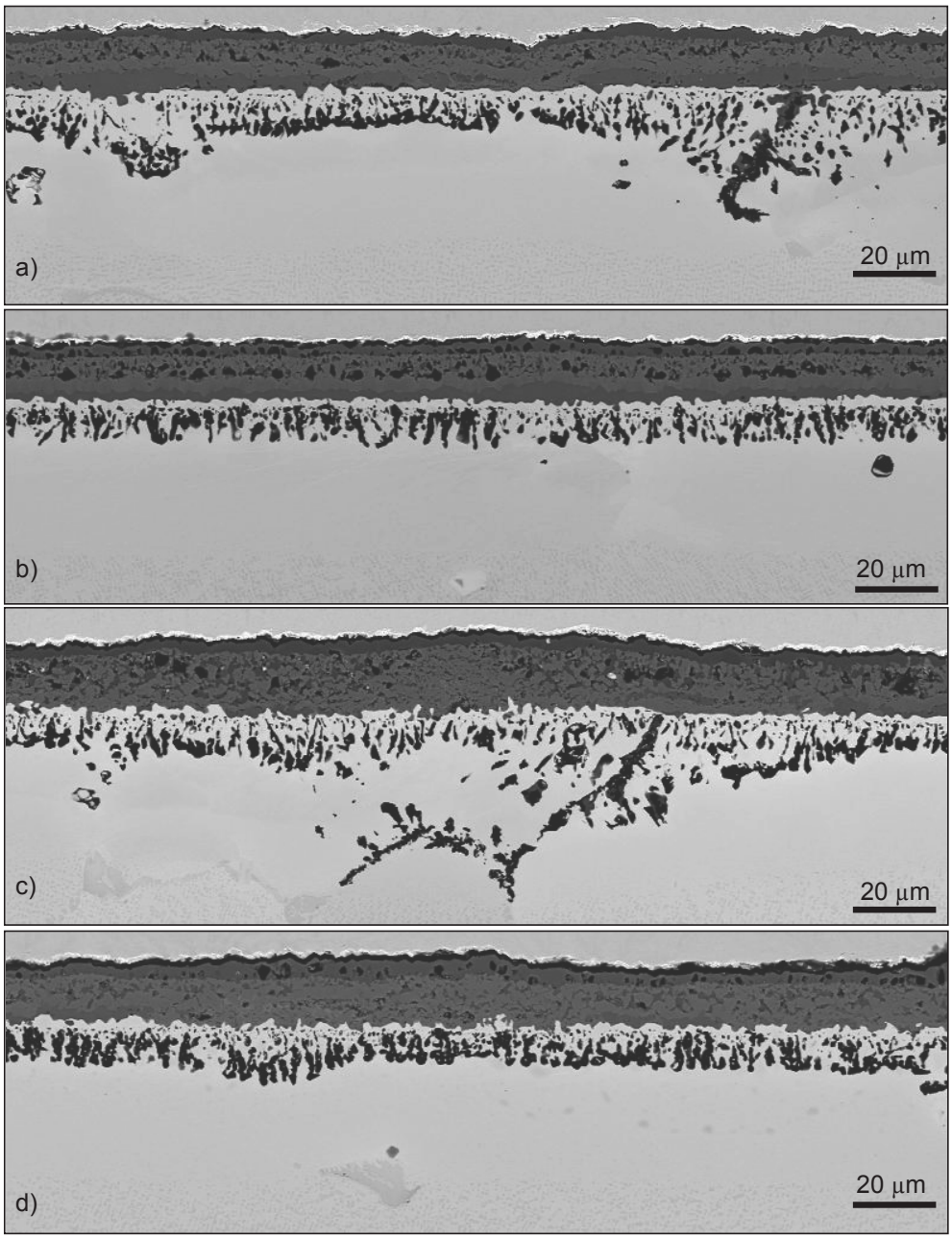

Figure 6.9 Overview SEM BSE images of cross-sections of Rene 80 after isothermal oxidation at 1050°C for 50 hours in: : a) Ar-1%O_2, b) Ar-1%O_2-7%H_2O, c) Ar-20%O_2, d) Ar-20%O_2-7%H_2O

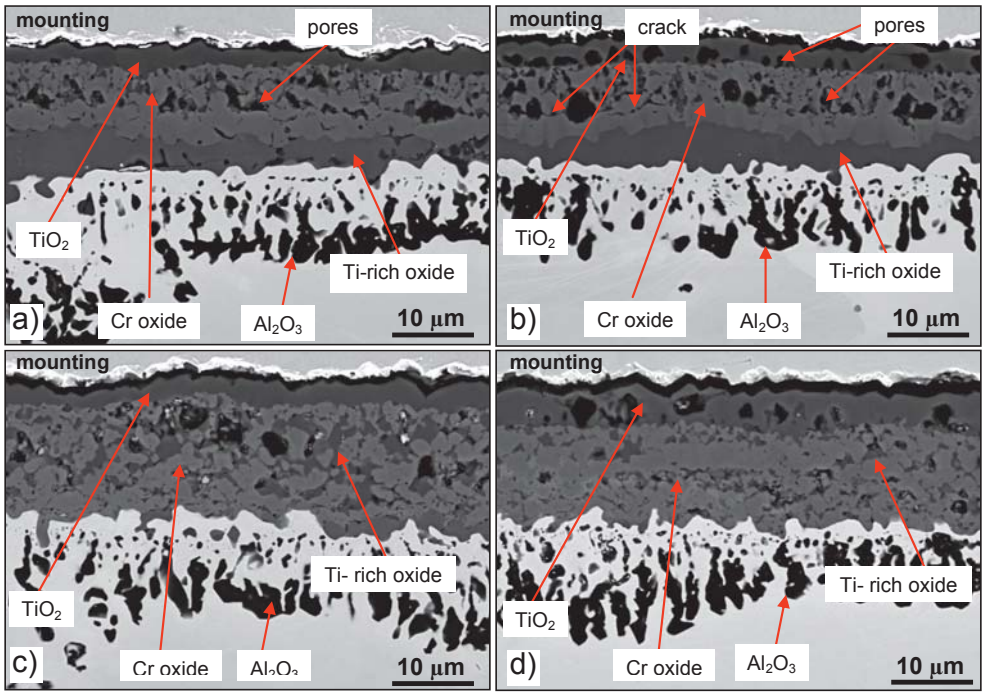

Figure 6.10 SEM BSE images of cross-sections of Rene 80 after isothermal oxidation at 1050°C for 50 hours in: a) Ar-1%O_2, b) Ar-1%O_2-7%H_2O, c) Ar-20%O_2, d) Ar-20%O_2-7%H_2O

6.1.2.3 Scale microstructure after 100 hours exposures

The cross sections of the samples after oxidation up to 100 h in Ar-1%O_2 with and without water vapour show oxide scale spallation exactly at the bottom of the outer porous oxide observed after 50 hours, but not at the oxide/superalloy interface (**Figures 6.11** and **6.12**). Also remnants of the inner Ti/Cr mixed oxide can be observed in both Ar-1%O_2 based atmospheres.

The cross sections of the samples oxidized in Ar-20%O_2 showed an outer titania scale and Ti-oxide precipitates embedded in the chromia scale. Therefore the scale morphology was similar to that observed after 50 hours. However, the number of Ti-oxide precipitates is larger for samples oxidized in dry than in wet gases. Also the extent of porosity in the chromia scale is larger for the specimen oxidized in dry atmosphere compared to the wet gas. Moreover, after 100 h exposure one can observe a roughening of the oxide/superalloy interface, which is stronger than after 50 hours exposure. Finally, the precipitates of internal Al-oxides are coarsened and locally have a tendency to grow together into a continuous layer. In some of these places local chromium oxide formation can be observed on top of the internal alumina well below the external chromia scale (**Figure 6.13a**).

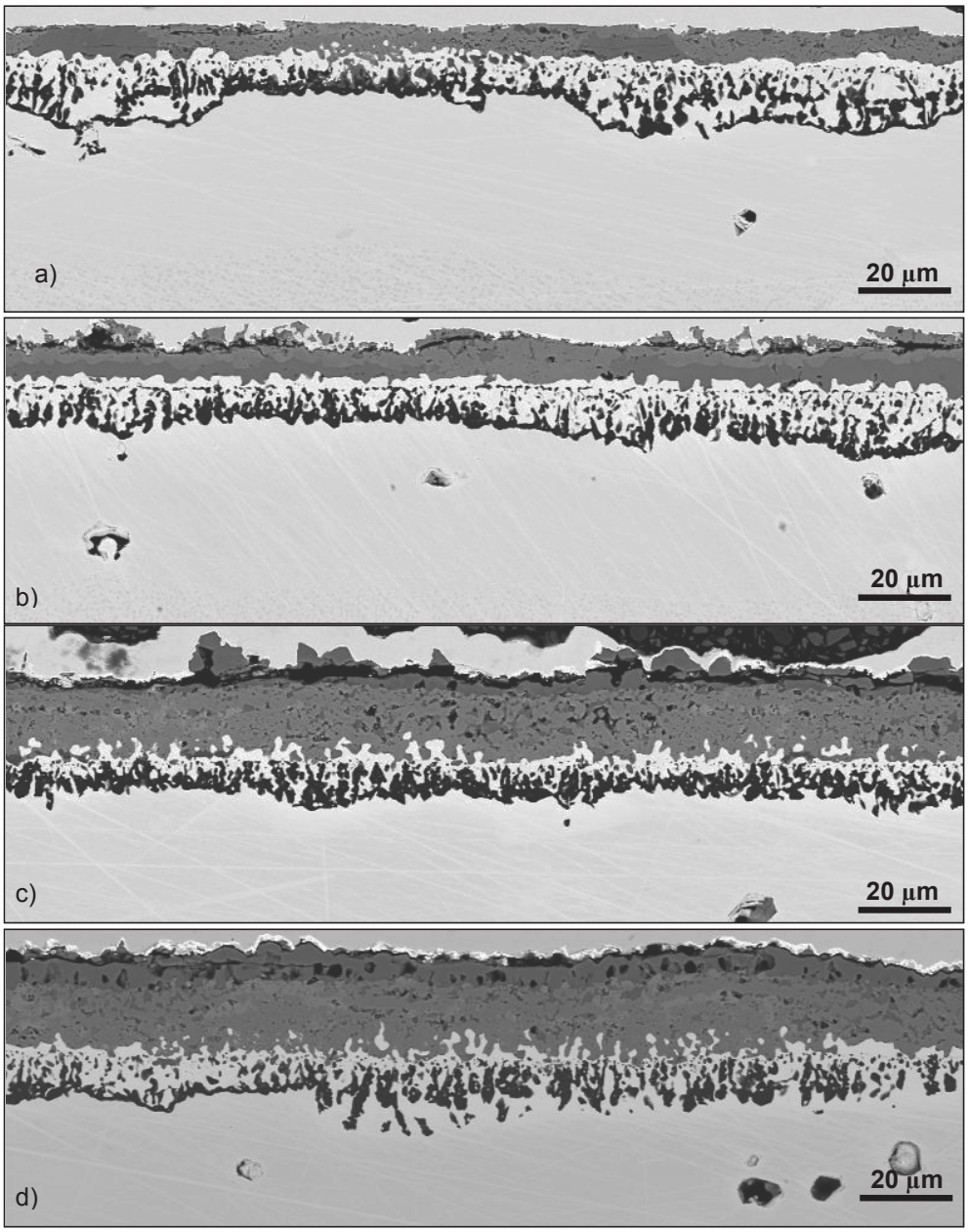

Figure 6.11 Overview SEM BSE images of cross sections for Rene 80 after exposure at 1050°C for 100 h in: : a) Ar-1%O_2, b) Ar-1%O_2-7%H_2O, c) Ar-20%O_2, d) Ar-20%O_2-7%H_2O

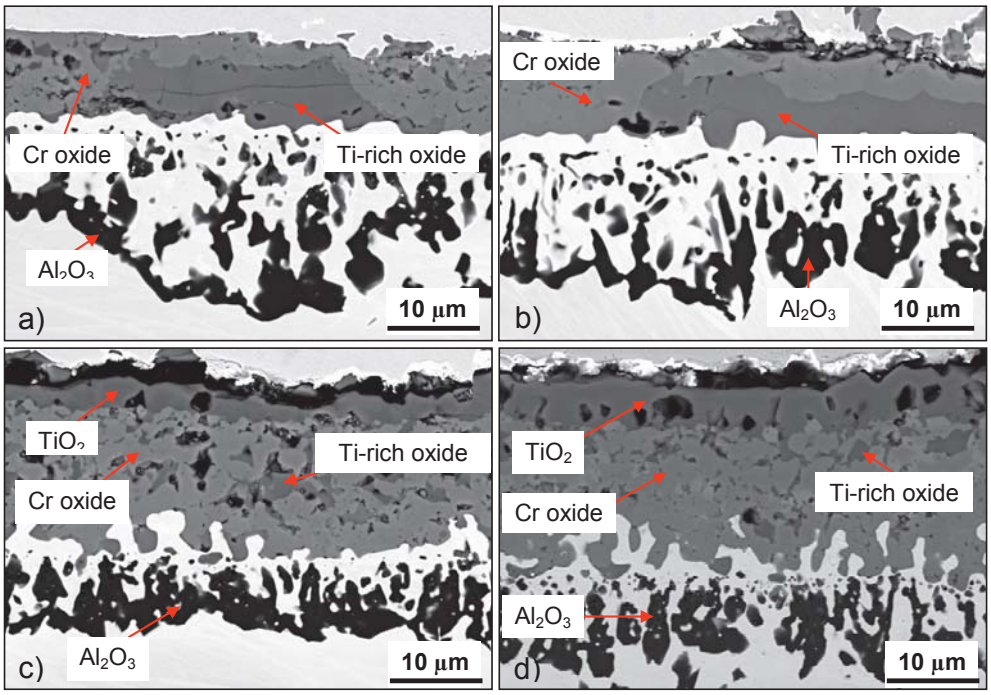

Figure 6.12 SEM BSE cross sections of Rene 80 after exposure at 1050°C for 100 h in: a) Ar-1%O_2, b) Ar-1%O_2-7%H_2O, c) Ar-20%O_2, d) Ar-20%O_2-7%H_2O

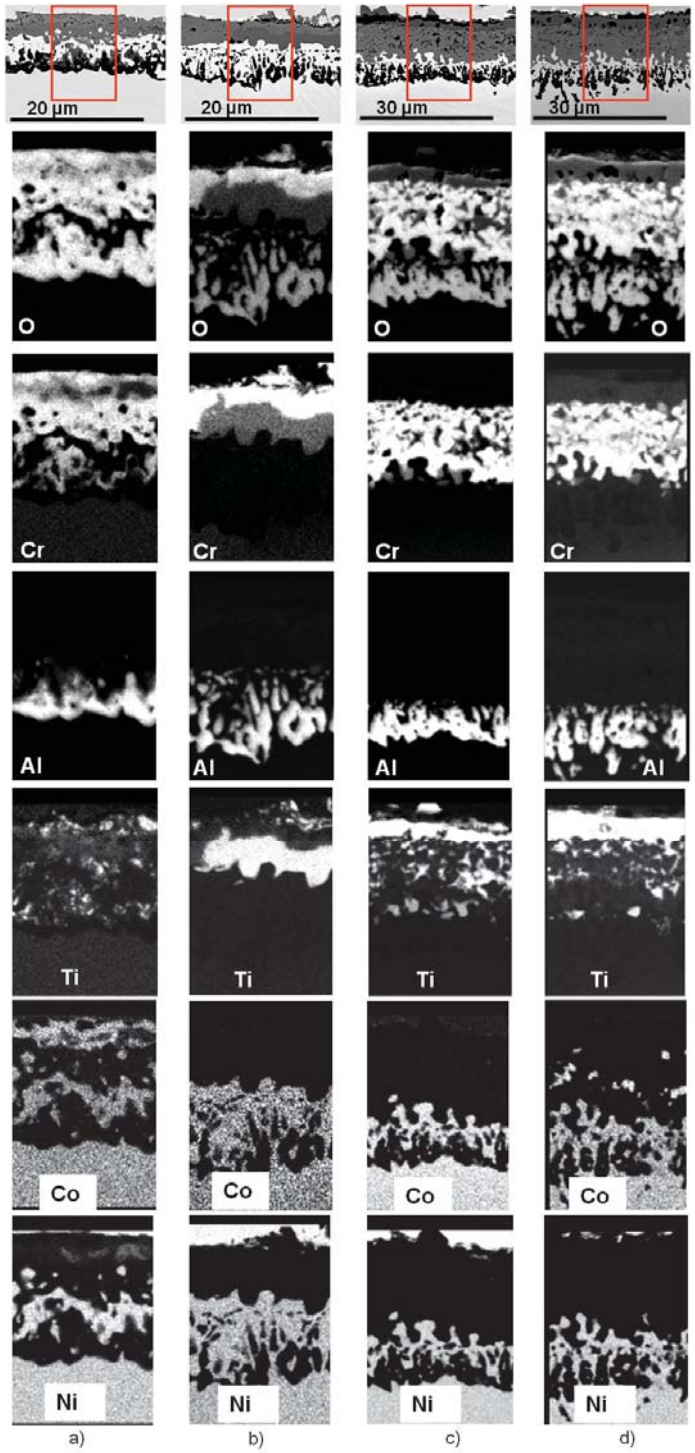

Figure 6.13 SEM EDX elemental maps from surfaces of Rene 80 oxidized for 100 hour at 1050°C in: a) Ar-1%O_2, b) Ar-1%O_2-7%H_2O, c) Ar-20%O_2, d) Ar-20%O_2-7%H_2O

6.1.3 Effect of H_2O on oxidation of Rene 80 in air based atmospheres

In addition to exposures in Ar-O_2 based atmospheres, isothermal exposures of Rene 80 were also performed at 1050°C in synthetic air and synthetic air + 7%H_2O for 50 h to study the effect of H_2O on the oxidation behaviour in N_2-based gases. Addition of 7% H_2O had no substantial influence on the mass change as well as on the $k_w(t)$ of Rene 80 (**Figures 6.14** and **6.15**). The GD-OES profiles in **Figure 6.16** reveal qualitatively similar scale compositions in the dry and wet synthetic air. The differences relate to a less extensive B enrichment in the oxide scale formed in wet gas as well as N-enrichment in the sub-scale regions of the sample exposed to dry gas. **Figure 6.17** shows a comparison of Rene 80 cross sections after oxidation in synthetic air and synthetic air + 7%H_2O. The oxide scale morphologies in **Figure 6.17** are similar to those found in Ar-20%O_2 based gases (compare with **Figure 6.10**). The specimen oxidized in dry synthetic air formed a thinner oxide layer with less Ti-oxide precipitates embedded in the chromia scale. Also the internal Al-oxide precipitates are coarser and have a larger tendency to coalesce leading locally to formation of a continuous layer in dry air. The latter observation might explain why there are slight differences in the oxide scale thickness between the dry and wet gases in **Figure 6.17** in spite of the fact that the mass change curves in **Figure 6.14** do not show substantial differences. Below the internal Al_2O_3 precipitates, particles of TiN are visible. The presence of TiN is in agreement with the nitrogen distribution in the respective GD-OES depth profiles (**Figure 6.16**).

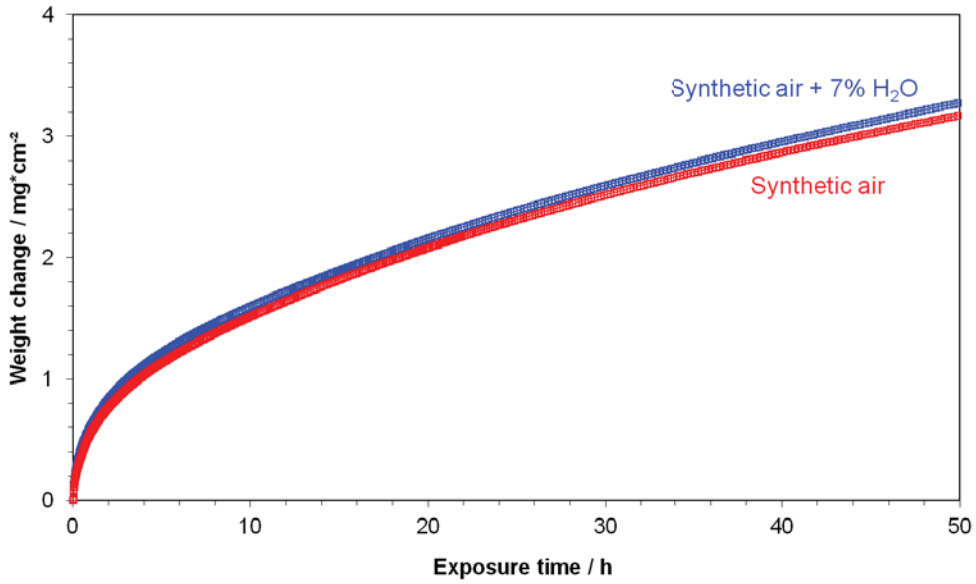

Figure 6.14 Mass changes obtained during isothermal oxidation (TGA test) of Rene 80 at 1050°C for 50 hours in studied atmospheres

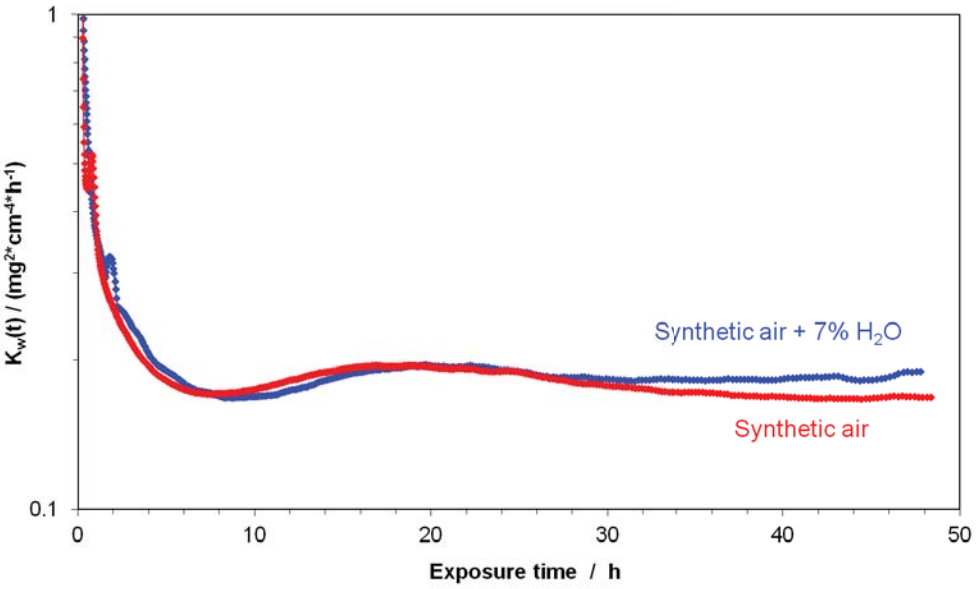

Figure 6.15 Instantaneous k_w as a function of exposure time for the data in **Figure 6.14**

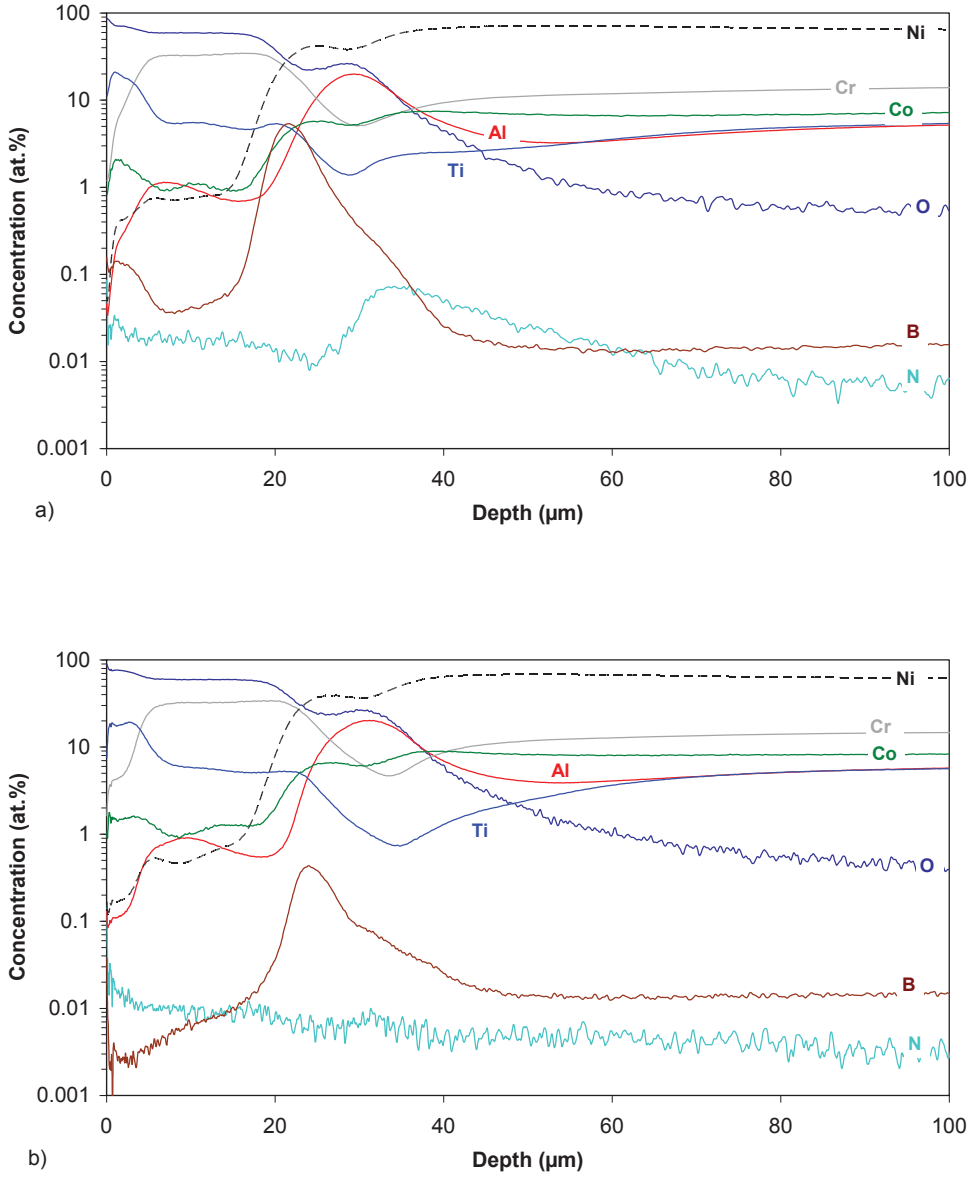

Figure 6.16 GD-OES depth profiles of Rene 80 oxidized at 1050°C for 50 h in: a) Synthetic air and b) Synthetic air + 7% H_2O.

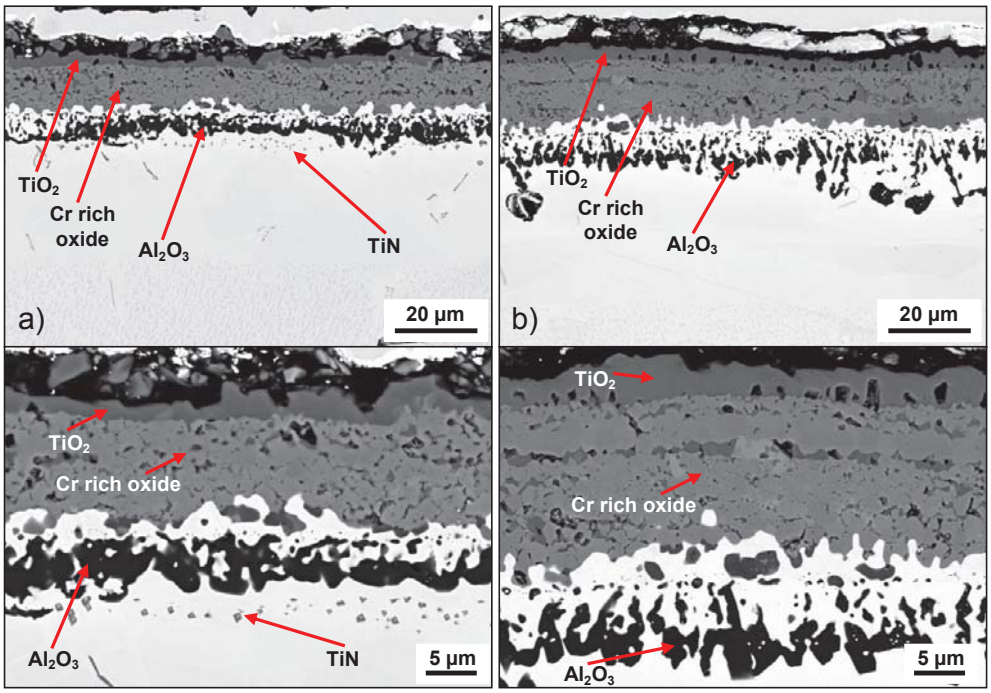

Figure 6.17 SEM cross sections of Rene 80 after isothermal oxidation at 1050°C for 50 hours in: a) Synthetic air, b) Synthetic air + 7%H_2O

6.2 Long-term exposure of Rene 80

6.2.1 Oxidation kinetics

Figure 6.18 shows mass change curves for Rene 80 one-side coated by MCrAlY overlay coating during discontinuous oxidation up to 2000 hours in synthetic air and synthetic air + 20%H_2O. The mass change curves show big mass losses which (based on **Figure 6.18**) started to occur after approximately 200 hours of exposure. The mass change curves show slightly larger mass loss after 2000 hours of exposure in water vapour containing atmosphere, although the effect is not very pronounced after shorter exposure times (up to approximately 1000 h).

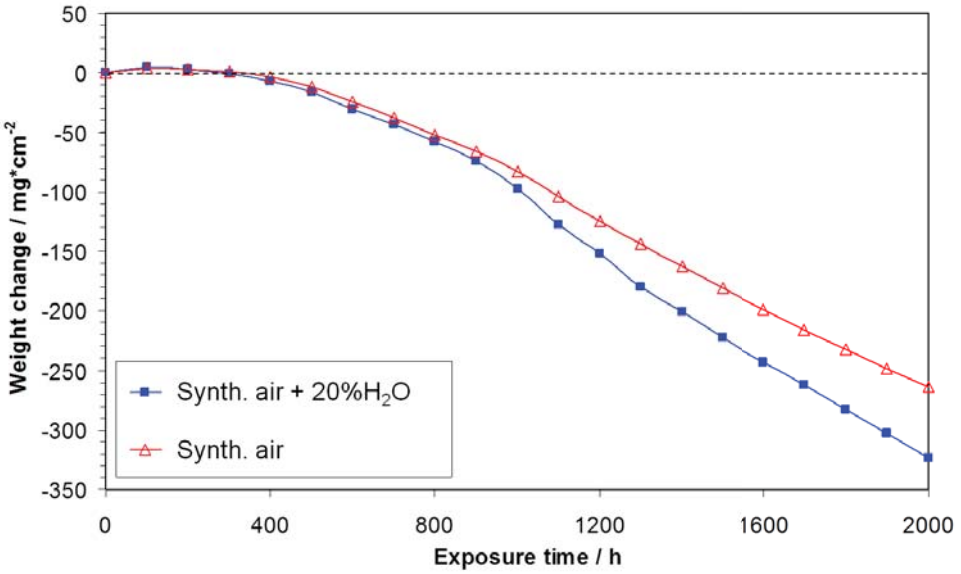

Figure 6.18 Mass changes of Rene 80 one-side coated with HVOF MCrAlY overlay coating obtained during discontinuous oxidation at 1050°C up to 2000 hours in synthetic air and synthetic air + 20%H_2O (Data related only to uncoated surfaces of the samples).

6.2.2 Microstructure features after long term oxidation

Figure 6.19 shows metallographic cross sections of Rene 80 one-side coated with MCrAlY after 100 hours of cyclic exposure in dry and wet air. The figures clearly show that the overall measured mass change is mainly caused by oxidation of Rene 80; the oxide scale formed on the base alloy is much thicker than that formed on the MCrAlY coating. Investigation of the uncoated part of Rene 80 revealed suppression of internal Ti nitridation by presence of water vapour after 100 hours of exposure (**Figure 6.20**). This is in agreement with the observations in **chapter 6.1.2**. The effect of H_2O on internal TiN formation might explain the differences in the composition between the outer parts of the oxide scales formed in dry and wet air (**Figure 6.20**). In the dry gas the outer oxide was mainly spinel, whereas in the wet gas it was mainly TiO_2. Images at lower magnification show that oxide scale spallation is more pronounced in dry than in wet gas, which is in good agreement with the mass change curves (**Figure 6.18**) showing that after 100 h oxidation the mass change obtained in dry atmosphere is slightly lower than that in wet. However, after longer exposure times the sample oxidized in wet atmosphere shows a higher mass loss than that in the dry gas. **Figure 6.21** and **Figure 6.22** show that the mass loss is mainly due to spallation and/or evaporation of the oxide scale formed on Rene 80.

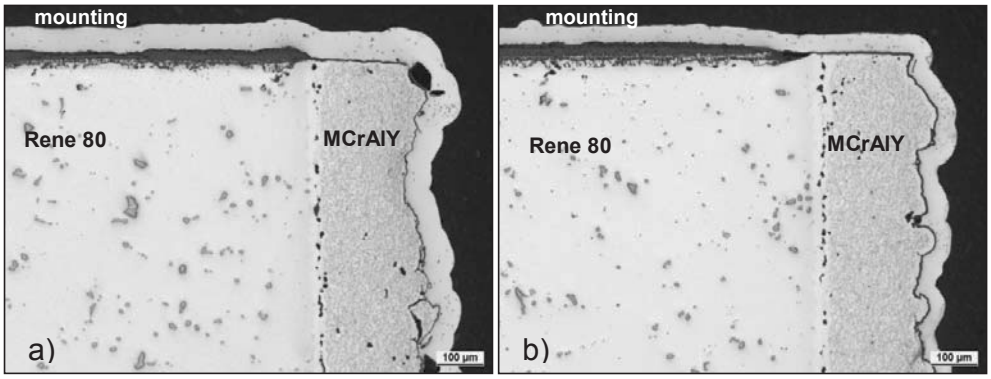

Figure 6.19 Metallographic cross sections of Rene 80 an one-side coated with MCrAlY, after oxidation at 1050°C for 100 hours in: a) synthetic air, b) synthetic air + 20%H_2O

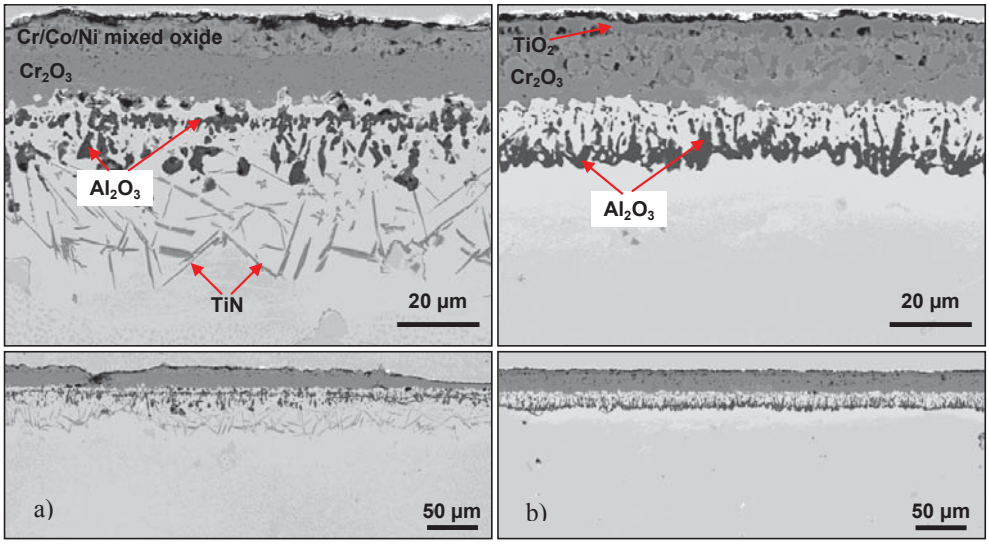

Figure 6.20 SEM cross sections of Rene 80 after discontinuous oxidation at 1050°C for 100 hours in: a) synthetic air, b) synthetic air + 20%H_2O

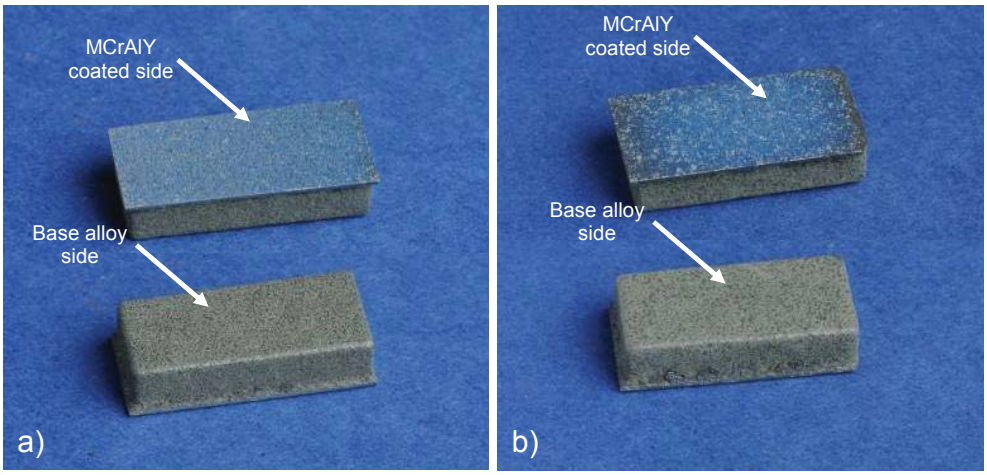

Figure 6.21 Macroscopic images of Rene 80 one-side coated with HVOF MCrAlY overlay coating after discontinuous oxidation at 1050°C up to 2000 hours in: a) synthetic air, b) synthetic air + 20%H_2O

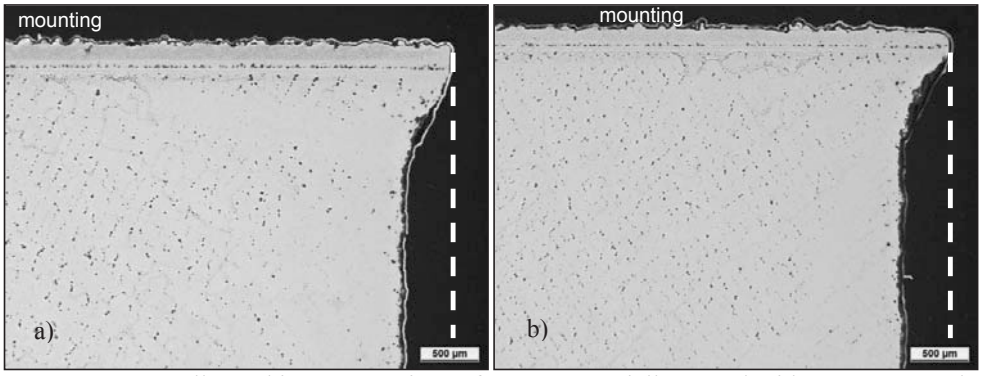

Figure 6.22 Metallographic cross sections of Rene 80 partially coated with HVOF MCrAlY overlay coating after discontinuous oxidation at 1050°C up to 2000 hours in: a) synthetic air, b) synthetic air + 20%H_2O. White dashed line indicates original specimens surfaces.

Cross sections of Rene 80 after 100 hours of discontinuous exposure in synthetic air and synthetic air + 20%H_2O (**Figure 6.20**) revealed an adherent oxide scale, whereby composition and morphology were similar to those formed on Rene 80 during exposure in Ar-O_2 based atmospheres (e.g. **Figure 6.10**). However, after 2000 hours the cross-sections of Rene 80 revealed substantial oxide scale spallation (**Figure 6.23**). Moreover, detailed SEM-studies showed also a completely different oxide scale composition (**Figures 6.24** and **6.25**) compared to that after exposure for 100 hours. SEM/EDX analysis after exposure for 2000 hours revealed that the outer part of the oxide scale consists mainly of Cr/Ti-mixed oxide while in the inner part of the chromia scale large amounts of W/Mo-rich oxides particles are found (**Figures 6.24** and **6.25**). This observation might be related to the repeated oxide scale spallation (indicated by the mass change curves (**Figure 6.18**) as well as in **Figure 6.23**) and associated Cr-depletion in the near-surface alloy region. The Cr-depletion might allow elements like W and Mo start to oxidize especially when the base-metal after spallation is exposed to the high temperature environment during the next cycle. This process might be enhanced by alloy recession with W/Mo accumulation in the sub-scale regions. In the lower part of the oxide scale W/Mo-rich oxides exist as a separate particles whereas in the outer part

of the oxide scale, where pO_2 is higher, Cr/Ti/Mo/W-mixed oxides are formed (**Figures 6.24** and **6.25**).

Based on the available results it is unlikely that the lower mass change in the H_2O containing gas (**Figure 6.18**) is strongly affected by $CrO_2(OH)_2$-evaporation. According to Mescher et al. [107] MoO_3 has in high pO_2 atmospheres a higher vapour pressure than $MoO_2(OH)_2$, while in the same conditions $(WO_3)_n$ species have much lower partial pressures; therefore volatilization is then dominated by $WO_2(OH)_2$. In low pO_2 atmospheres containing water vapour, Mo and W can form volatile oxyhydroxide by direct reaction with the metal [107].

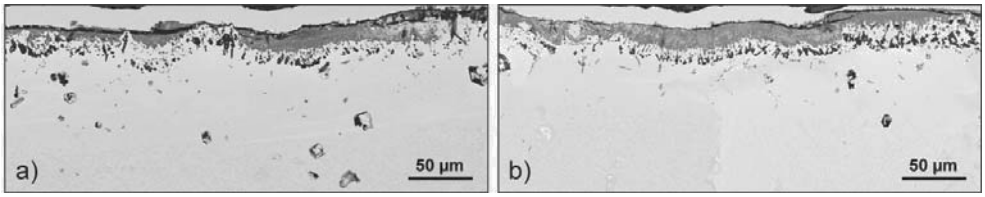

Figure 6.23 Cross sections of Rene 80 (SEM BSE images) after discontinuous oxidation at 1050°C for 2000 hours in: a) synthetic air, b) synthetic air + 20%H_2O

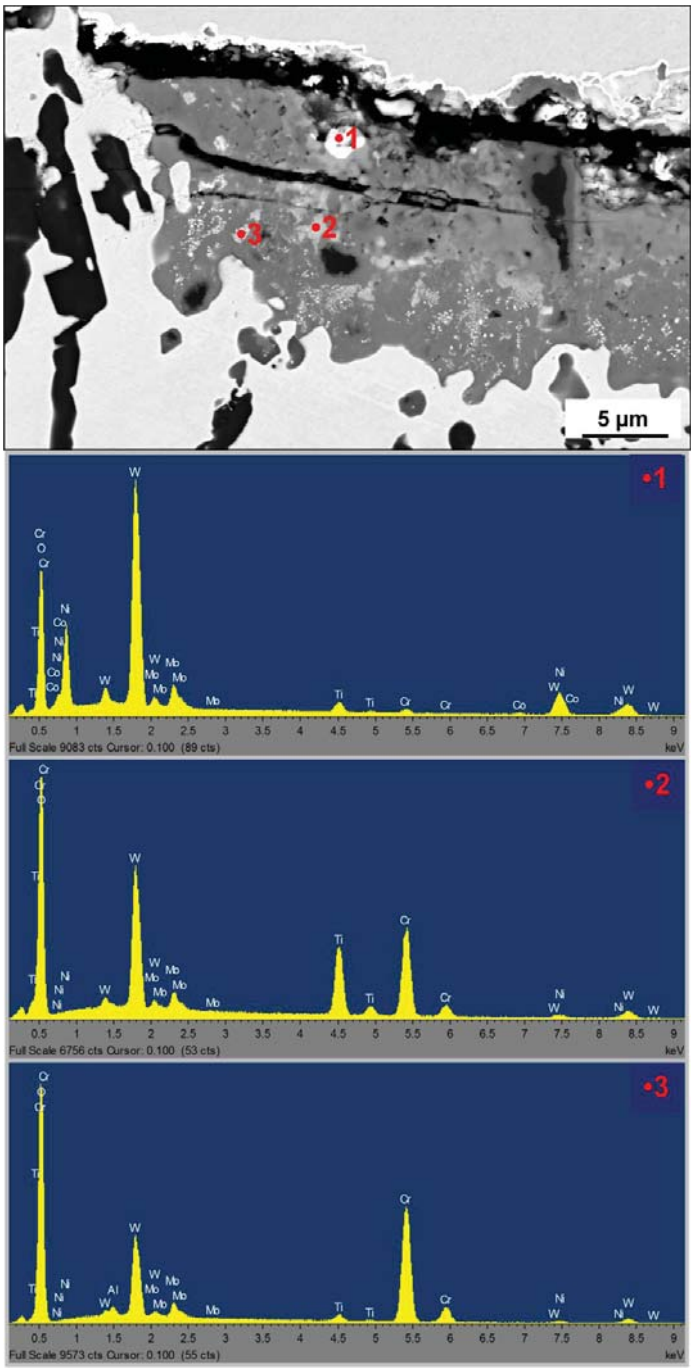

Figure 6.24 SEM BSE images and EDX spectra of Rene 80 cross section after discontinuous exposure at 1050°C for 2000 hours in synthetic air

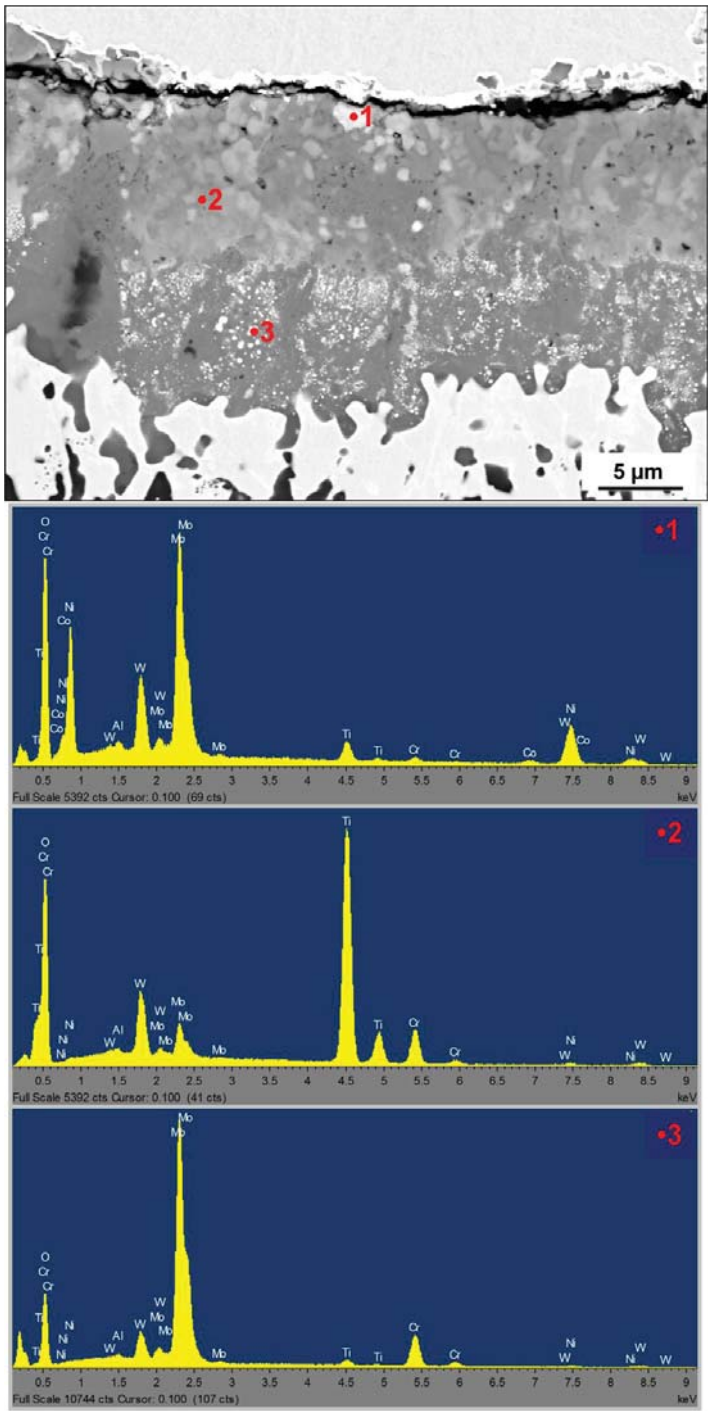

Figure 6.25 SEM BSE images and EDX spectra of Rene 80 cross section after discontinuous exposure at 1050°C for 2000 hours in synthetic air + 20%H_2O

6.3 Discussion of Rene 80 oxidation behaviour

6.3.1 General aspects of oxide scale formation on Rene 80

After short exposure times ($t \leq 100$ h) Rene 80 formed in dry and wet gases the oxide scales with similar compositions. In general, the scales consisted of an outer TiO_2, chromia, Ti/Cr-mixed oxide and internal alumina precipitates (e.g. **Figure 6.6**). **Figure 6.26** schematically shows the morphology of the oxide scale formed on Rene 80 during exposure in air. The oxide scale composition/morphology obtained in the present work are in good agreement with the literature data on scale formation on polycrystalline Ni-base alloys of similar compositions [108, 109]. The oxide scale morphologies observed in the SEM cross-sections are confirmed by GD-OES depth profiles (**Figure 6.5**).

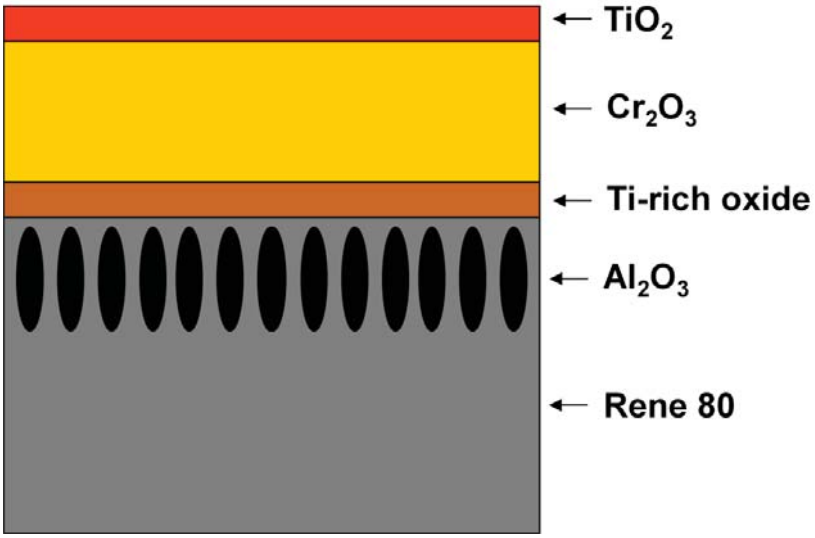

Figure 6.26 Schematic showing microstructure of the oxide scale formed on Rene 80 during oxidation in air.

The described morphology of the oxide scale formed on Rene 80 contradicts with the results obtained by Giggins and Pettit [39] on ternary Ni-Cr-Al model alloys (**Figure 3.2**). According to the oxidation map in **Figure 3.2** an alloy with 14% Cr and 3% Al (corresponding to the Cr and Al contents in Rene 80) should be an alumina former. However, as it has been recently shown [96] Ti promotes internal oxidation of aluminium by increasing the growth rate of the chromia scale. The dissolution of Ti into chromia by substituting Ti^{4+} for Cr^{3+}, thereby increasing the concentration of Cr-vacancies in the chromia scale [108] according to reaction (6.1):

$$3TiO_2(+Cr_2O_3) = 3Ti_{Cr}^{\cdot} + V_{Cr}^{'''} + 6O_O^x(+Cr_2O_3) \quad (6.1)$$

The high chromia growth rate in turn results in a lower Cr concentration at the oxide/metal interface according to the Wagner's treatment given by equation (6.2):

$$C_{Cr}^{i} = C_{Cr}^{0} - \frac{100M_{Cr}}{M_{alloy}} \frac{1}{2\phi} \left(\frac{\pi \cdot k_p}{D_{Cr}} \right)^{\frac{1}{2}} \quad (6.2)$$

where C^0 is the initial concentration of Cr in the alloy, M_{Cr} and M_{alloy} are the average molar mass of Cr (52 g/mol) and the alloy (62.7 g/mol), respectively, D_{Cr} is the interdiffusion constant, ϕ is the value of the Pilling-Bedworth ratio.

Figure 6.27 presents the oxide scale development on Rene 80 exposed at 1050°C with increasing exposure time in the Ar-O_2 based atmospheres. Based on **Figure 6.27** one can observe that the outer TiO_2 layer thickens with increasing time, which suggests that Ti seems to be transported through the Cr_2O_3 scale outwardly. It has been shown that elements like e.g. Mn can be transported through the chromia scale in ferritic steels (e.g. Crofer) [110] to form Mn/Cr-spinel on top of the chromia scale. The authors of [110] found that in Ar-H_2-H_2O this

spinel grows via grain boundary diffusion, while it grows by outward lattice diffusion of cations during air oxidation [111].

Outward diffusion of the reactive elements through the oxide scale was observed by Pint et al. [112]. The authors found that Reactive Elements (RE) such as Y, Zr, La, Hf and Ti segregate at the α-Al_2O_3 grain boundaries and at the alloy/oxide scale interface. The amount of segregants at the oxide scale grain boundaries near the gas interface increase with increasing exposure time until a critical level is reached and precipitates of the respective RE oxides begin to nucleate and grow. It iss claimed that this effect is the result of the outward transport of the elements from the alloy, through the external alumina scale, to the gas interface. The most likely driving force for this diffusion process iss claimed to be the oxygen potential gradient in the oxide scale.

Similar observations to those in [112] were made by Naumenko [78] and Meier et al. [113] with Y, Ti and Mg in FeCrAlY alloys whereby formation of mixed-oxide precipitates such as $Y_3Al_5O_{12}$, $Y_2Ti_2O_7$ and $MgAl_2O_4$ on top of the external alumina scale were observed.

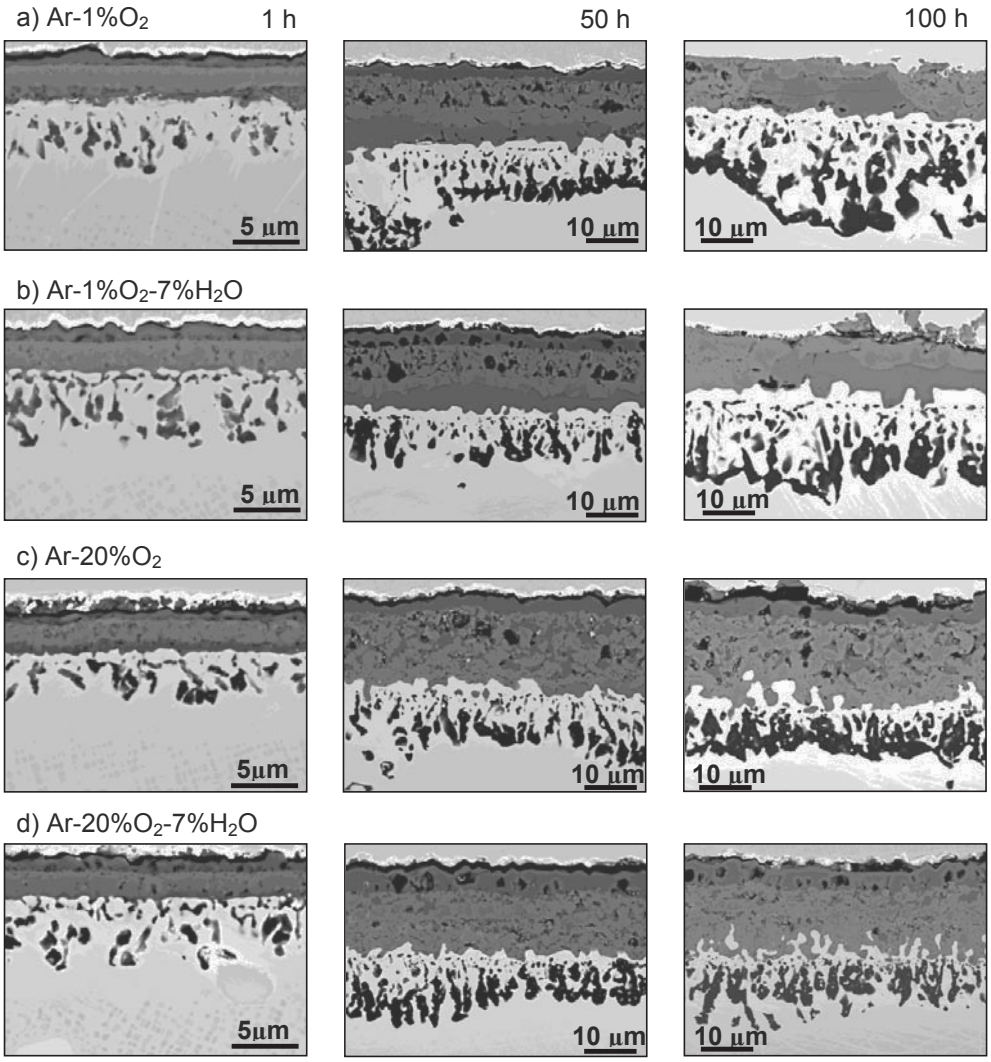

Figure 6.27 Cross sections showing development of oxide scales on Rene 80 as a function of isothermal exposure time at 1050°C in: a) Ar-1%O_2, b) Ar-1%O_2-7%H_2O, c) Ar-20%O_2, d) Ar-20%O_2-7%H_2O

The thermodynamic stability of Ti oxide (TiO: ΔG=-348.3 kJ/mol $O_2 \cdot K$) is higher than that of Cr_2O_3 (ΔG=-259.6 kJ/mol $O_2 \cdot K$). This means that Ti can in principle oxidize internally underneath the chromia scale. Indications for this effect were found after short exposure times (1hour) in Ar-O_2 based gases (**Figure 6.7**). In Rene 80, however, Al is oxidized internally which might reduce the oxygen solubility in the near-surface regions to the extent that large

amounts of Ti can be directly incorporated into the oxide scale, in other words its "internal oxidation" occurs at the scale/metal surface. This was observed in the SEM images of cross sections after longer exposure times (**Figure 6.13**). Ti-oxide is more stable compared to Cr-oxide, therefore Ti might be expected to oxidize beneath the chromia scale [12]. Such phenomenon was observed in some materials, such as in case of the ferritic steels e.g. Crofer 22APU [110].

The depth of internal Ti oxidation, X is given by equation 6.2 [34]

$$X = \left[\frac{2N_O^{(S)}D_O}{\nu N_{Ti}^{(O)}}t\right]^{\frac{1}{2}} \qquad (6.2)$$

where:

N_0 – oxygen solubility,

D_0 – oxygen diffusivity,

ν – valence of the metal in the oxide,

N_{Ti} – initial Ti concentration.

From equation (6.2) it can be seen that if N_O is very small then $X \rightarrow 0$ and Ti can be oxidized at the scale/metal interface.

After one hour of oxidation all samples had a relatively flat alloy / oxide scale interface. After longer exposure time (50 h) this interface became more convoluted. In cross sections after 100 h oxidation this phenomenon is easily visible, especially for the two atmospheres containing 20% oxygen. It seems that a higher oxygen content enhances the process of metal / oxide scale interface roughening. Formation of metal nodules in the scale was observed by Krupp and Christ [114, 115]. The authors explained this phenomenon by volume increase as a result of internal oxidation leading to outward metal flow. Rapp et al. [116] and Litz et al. [117]

showed that internal oxidation leads to a volume increase which causes plastic deformation of the base metal. Litz et al. [117] showed that during formation of internal Al_2O_3 from Al the volume increase can be in the order of 28%. From **Figures 6.11** and **6.12** it can be observed that the extent of the oxide/metal interface convolutions strongly depends on the morphology of the internal alumina precipitates: in the areas in which the latter locally forms a continuous layer, the interface becomes less convoluted. In contrast, above the discrete internal alumina precipitates the scale/alloy interface is more convoluted. This observation suggests that the level of convolutions depends on the flux of scale forming element (Cr) from the bulk superalloy towards the oxide scale.

Based on **Figure 6.27** Rene 80 exposed in Ar-20%O_2 based atmospheres showed more extensive convolution of the metal/oxide scale interface, than in Ar-1%O_2 based test gases especially after 100 hours of exposure (**Figure 6.27**). Moreover, an increased metal/oxide scale interface roughness with exposure time can be observed. A possible reason for the scale/metal interface roughening might be the Cr-depletion from the alloy. Coarsening of Al_2O_3 internal precipitates reduces the cross-section area of the alloy matrix available for Cr-diffusion thereby reducing the Cr-flux to the surface. This leads to a decrease in Cr-concentration at the scale/metal interface and a corresponding increase in the equilibrium oxygen activity. An increase in the oxygen activity promotes the transition from external to internal oxidation of Cr manifested by a wavy, convoluted chromia inner interface in **Figure 6.27**. The larger extent of the interfacial convolutions in Rene 80 exposed in high pO_2 gases might be related to the higher k_w (**Figure 6.4**) and, according to equation (6.2), a faster Cr-depletion.

Another effect associated with the coarsening of alumina precipitates is the Cr/Ni/Co/Ti-mixed oxide formation on top of the internal aluminium oxide precipitates after longer

exposure times (**Figure 6.13 a**), meaning local breakaway oxidation of the alloy above Al_2O_3 particles.

As mentioned above, an increase in the outer Ti-oxide thickness was observed between 1 and 50 hours of exposure, however no substantial difference in the thickness of the outer Ti-oxide layer was found between 50 and 100 hours of exposure, which might be related to Ti-depletion from the near-surface alloy regions. In the work of Cruchley et al. [109] a reduction in the growth rate of the chromia scale formed on Ni-base superalloy RR1000 with 15 Cr, 3.6 Ti, 3.0 Al (all in wt. %) was found after long exposure times in the temperature range between 600 - 900°C. This was attributed to Ti depletion from the sub-surface alloy regions.

6.3.2 Effect of pO_2 in the test gas on the oxide scale formation on Rene 80

Figure 6.27 shows that the microstructure and thickness of the oxide scale formed during 1 hour exposure of Rene 80 in Ar-1%O_2 looks very similar to that formed in Ar-20%O_2. This observation is confirmed by the GD-OES depth profiles (**Figure 6.5**). However, after 50 hours of exposure the oxide scale in the lower pO_2 gas featured formation of a Cr/Ti-mixed oxide at the scale/metal interface, which was not observed in high pO_2 gas. As mentioned previously, this Cr/Ti-mixed oxide layer was identified by XRD as $CrTi_2O_5$ (**Figure 6.8**). Formation of $CrTi_2O_5$ layer can be correlated with the results of Naoumidis et al. [118] (**Figure 6.28**) who found that this Cr-Ti mixed compound is stable in low pO_2 atmospheres but not in high pO_2 atmospheres. Indications for the presence of a $CrTi_2O_5$ layer was found also in Ar-20%O_2 after 1 hour but not after 50 hours exposure.

Essuman et al. [119] investigated in detail the influence of different pO_2 on the oxidation behaviour of NiCr alloys. One of the conclusions coming from this work was that the Ti solubility in the chromia scale depends on pO_2. As described in the previous chapter it was found that in both test atmospheres containing 1% oxygen internal Ti, Cr mixed oxide was still present as a semi-continuous layer after 50 h oxidation. In contrast, this layer is present only occasionally (**Figure 6.9**) after 50 h oxidation and after 100 h seems to be completely absent in the atmospheres containing 20%O_2. This observation indicates that the stability of the Cr/Ti-mixed oxide may depend on the oxygen partial pressure in the test atmosphere. Naoumidis et.al [118] showed that in the quasi-ternary, Cr-Ti-Mn oxide system different Cr, Ti oxides can be formed depending on pO_2 (**Figure 6.28**), whereby $CrTi_2O_5$ exists only in the low pO_2 gas.

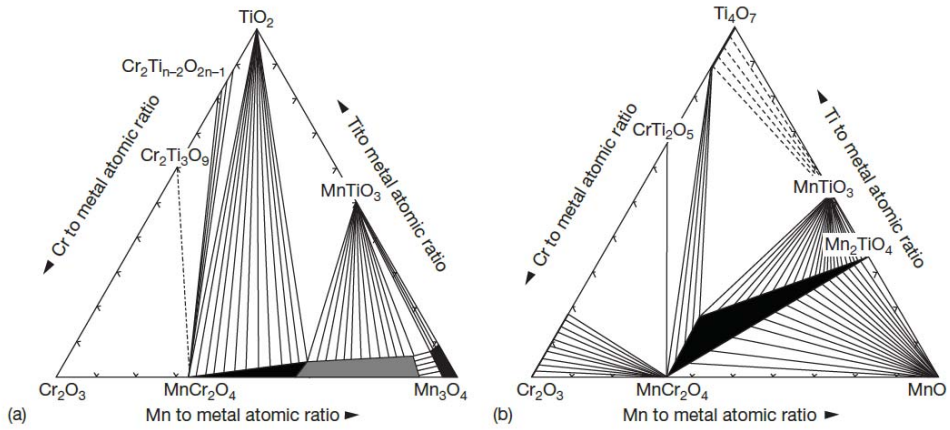

Figure 6.28 Phase equilibria in the quasi-ternary system: (a) Cr_2O_3–Mn_3O_4–TiO_2, after annealing at 1000˚C in air; (b) Cr_2O_3–MnO–Ti_4O_7 after annealing at 1000˚C in a gas with an equilibrium oxygen partial pressure of 10^{-21} bar. Reproduced from reference [118].

Figure 6.29 shows a schematic of a possible explanation for the formation and later dissociation of Cr/Ti-mixed oxide at the scale/metal interface. At the scale/gas interface the value of pO_2 is determined by the oxygen content in the oxidizing gas, however within the oxide scale pO_2 decreases and at the superalloy/oxide scale interface pO_2 is fixed by the

equilibrium reaction: $2Cr + \frac{3}{2}O_2 = Cr_2O_3$. The value of pO_2^* in **Figure 6.29** represents the oxygen partial pressure which is equal to the dissociation pressure of $CrTi_2O_5$. The distance x_n illustrates the point in which the gradient of pO_2 across the scale reaches pO_2^*. As can be observed in **Figure 6.29** the distance x_1 (which represents the stability range for $CrTi_2O_5$ for the atmosphere with $1\%O_2$) is larger than distance x_2 (for the atmosphere with $20\%O_2$). This can explain the formation of a continuous layer of $CrTi_2O_5$ near the oxide scale/superalloy interface on specimens oxidized in the atmospheres containing $1\%O_2$ while on the specimens oxidized in the atmospheres with $20\%O_2$ such a layer is not found after 50 hours at 1050°C. It seems that in the samples oxidized in the atmospheres containing $20\%O_2$ the $CrTi_2O_5$ layer was dissolved and Ti oxides start to be formed in the outer parts of the oxide scale, such as outer TiO_2 layer and/or Ti-oxides precipitates which are embedded in the middle of the Cr-oxide scale (**Figure 6.10**).

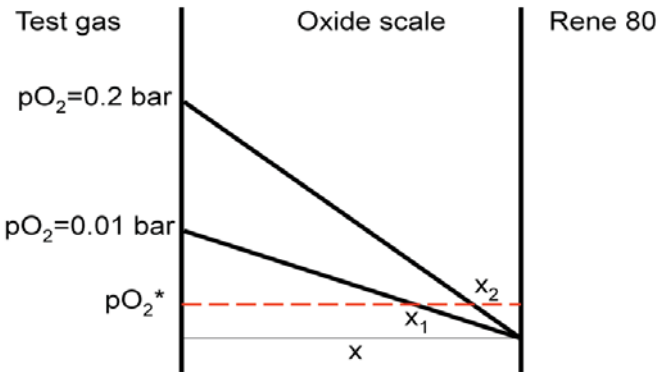

Figure 6.29 Schematic showing oxygen gradients in oxide scale depending on oxygen amount in oxidizing gas. pO_2^* - oxygen partial pressure which is equal to the dissociation pressure of $CrTi_2O_5$, x_1, x_2 - distances from metal/oxide interface representing the stability range for $CrTi_2O_5$ for the atmospheres with $1\%O_2$ and $20\%O_2$ respectively, x- oxide scale thickness.

After 50 hours of exposure the chromia scale thickness in Ar-$1\%O_2$ is smaller than that in Ar-$20\%O_2$ (**Figure 6.10**). A possible reason for this effect is the pO_2 dependence of scale growth

rate governed by cationic transport [120]. If one assumes, that Ti constantly diffuses out as described for Ar-20%O_2 and Ar-1%O_2 it might lead to a dissolution of the inner $CrTi_2O_5$-layer as well as for the formation of voids arranged in a line (**Figure 6.10**) if the Ti supply from the base alloy diminishes after longer exposure times e.g. due to Ti-depletion in sub-scale regions [109]. After 100 h of oxidation no continuous inner Cr, Ti-mixed oxide layer can be observed in any of the oxidized samples. In the gases containing 1%O_2 only remnants of this layer are locally present (see **Figure 6.27 a** and **b**). In the gases containing 20%O_2 only outer TiO_2 layer can be found and the particles of Ti-oxides which after 50 h oxidation were embedded in the middle of Cr-oxide scale, oxidation are after 100 h mostly concentrated very close to the outer TiO_2 layer.

In both atmospheres with lower pO_2 a more extensive spallation was found after oxidation for 100 h than in the high pO_2 gases (**Figures 6.11** and **6.12**). The SEM surface investigation showed that spallation also occurred locally after 50 h oxidation (**Figure 6.30**).

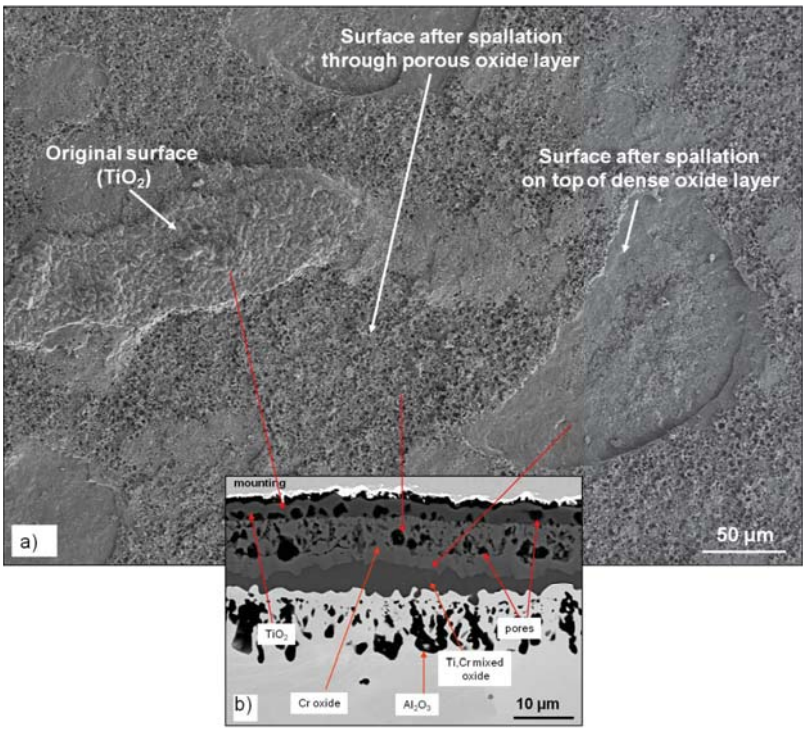

Figure 6.30 SEM surface image (a) and possible correlation of oxide scale spallation with oxide scale microstructure in cross section (b) of Rene 80 after oxidation at 1050°C in Ar-1%O_2-7%H_2O for 50 h. Figures a) and b) show different locations of the same specimen.

After oxidation up to 50 h formation of large pores in the outer part of the oxide scale (**Figures 6.9 a** and **b**) was observed in the samples oxidized in the Ar-1%O_2 gases. In the oxide scales formed in Ar- 20%O_2 based gases the pores are distributed more uniformly. This might be correlated with a more uniform distribution of Ti-oxides in the chromia scale (especially after exposure in Ar-20%O_2). After 50 hours oxidation short cracks were found at the inner region of this porous outer part of the oxide scale. After 100 h oxidation extensive spallation was found, initiated in the middle of the oxide scale; i.e. exactly in the inner region part of the porous oxide. This phenomenon was confirmed by SEM surface investigation (**Figure 6.30**).

The oxide scales during cooling are under compressive stress because of a lower CTE compared to the underlying metal. If the oxide scale reaches a critical thickness corresponding to a critical strain energy accumulation during cooling, scale spallation is likely to occur [121]. The exact spallation mechanism depends on the scale microstructure as well as the interfacial toughness. In many cases the spallation occurs at the oxide/metal interface. For this type of spallation two mechanisms, namely buckling and wedging, were proposed by H. Evans [121]. According to the buckling mechanism spallation occurs when the oxide scale is relatively strong (defect free), but the adherence of the oxide scale to the metal is weak. In this situation a crack nucleates at the oxide scale/metal interface during cooling and propagates along the interface eventually leading to spallation. Oxide scales spall according to the wedging mechanism if the oxide scale contains a large number of defects such as pores or microcracks but the oxide scale adherence to the underlying metal is relatively strong. In that case cracks originate and propagate over defects in the oxide scale during cooling eventually leading to spallation.

In the present study spallation was observed after isothermal exposures in Ar-O_2 based gases within the scale rather than at the oxide/metal interface. The observed more extensive scale spallation in Ar-1%O_2, might be correlated with the scale microstructure. After 50 hours exposure in Ar-1%O_2 porosity was accumulated in the outer part of the scale in form of large pores at a particular scale depth. This scale microstructure might explain the spallation within the scale, whereby the crack growth between the pores up to a critical size for onset of spallation most likely occurs by a mechanism similar to wedging [121]. **Figure 6.31** shows a schematic of the oxide scale development and spallation in Ar-1%O_2. The exact reason for the formation of the observed type of pores and the related spallation in the middle of the oxide scale are presently not known.

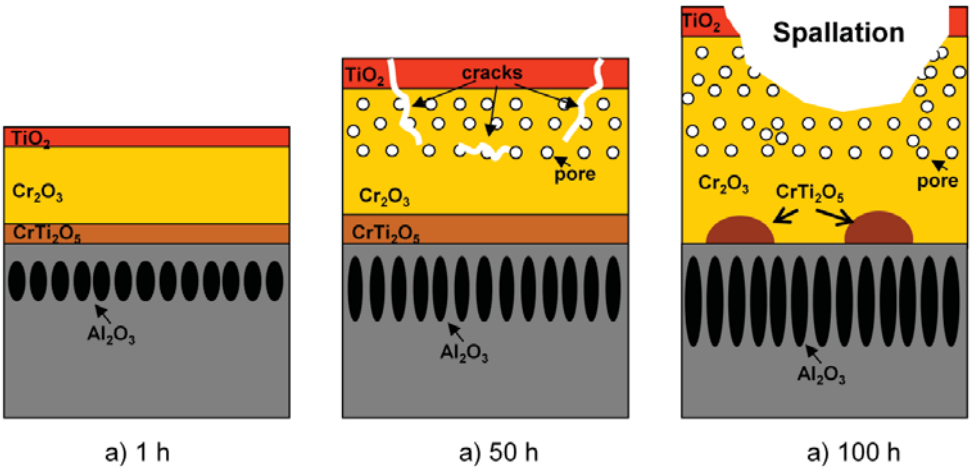

Figure 6.31 Schematic for development of oxide scale microstructure including pore formation and spallation for Rene 80 in test gases based on Ar-1%O_2.

6.3.3 Effect of water vapour on oxidation behaviour in Ar-O_2 based gases

A comparison of cross-sections of Rene 80 after 1 hour exposure at 1050°C (**Figure 6.6**) reveals that the depth of internal oxidation of Al is greater in both wet atmospheres by 30 to 50% than in the dry gas. In the EDX-elemental maps of the samples oxidized for 1 h internal oxidation of aluminium can be found in all test gases (**Figure 6.7**). However, in samples oxidized in wet atmospheres additionally internal oxidation of Ti on top of the aluminium oxide precipitates can be observed. This phenomenon is not observed in the specimens oxidized in the dry atmospheres.

Comparing the GD-OES results of the samples oxidized in the dry and wet gases (**Figure 6.5**) differences in the elemental depths profiles for oxidation in the different atmospheres can be observed. Following the B profile, it is apparent that in the outer part of the oxide scales the

boron concentration drops after oxidation in both wet gases while for the specimens oxidized in dry gases the boron concentration in the outer part of the scale slightly increases.

After longer exposure times also variations in the morphology of the outer TiO_2 layer were observed. In the cross sections of Rene 80 oxidized in both wet atmospheres the outer TiO_2 layer contains substantially more porosity than that oxidized in the dry atmospheres (**Figure 6.9**). Also the thickness of this Ti-oxide layer is larger in the wet gases. One of the probable reasons for this effect could be that porosity increased the effective volume of the TiO_2 layer. The porosity formation in the outer TiO_2 layer might be related to chromium evaporation as $CrO_2(OH)_2$ (reaction (3.2)) occurring in wet gas. Locally pressure caused by volatile Cr-species might develop at the TiO_2/Cr_2O_3 interface, which might lead to deformation of TiO_2 layer and porosity formation. One may speculate that a higher B-volatility in the water vapour rich gases is involved in the pore formation [107]. The latter argument might also explain a drop of the B concentration in the GD-OES depth profiles of Rene 80 oxidized in wet atmospheres (**Figure 6.5 a - d**).

6.3.4 Effect of water vapour on oxidation behaviour in air based gases

Rene 80 exposed in air based atmospheres formed oxide scales with similar growth rate as these observed in Ar-20%O_2. As shown in the mass change plot (**Figure 6.1**) no substantial differences in the mass changes are observed for the two types of atmospheres. However, from **Figure 6.17 b)** it can be seen that, in spite of similarities in the oxide scale compositions, substantial nitridation of Ti in synthetic air was found (compare with **Figure 6.10 c**). This effect was logically not found after exposure in Ar-O_2.

Considering the very low N-solubility in chromia, the N-penetration is related to molecular transport via defects in the oxide scale, such as pores or microcracks. In contrast, in case of chromia scales which are free of such defects, nitridation does not occur [41, 43]. Therefore it is obvious that the substantial porosity in the oxide scales on Rene 80 as a result of Ti-doping promotes the nitridation.

Contrary to the experiment in dry synthetic air no internal TiN formation is observed in the synthetic air + 7%H_2O. Suppression of internal nitridation by water vapour has been observed by Michalik et al. [122] during oxidation of pure chromium in N_2-1%O_2 with and without different amounts of water vapour. The authors explained this phenomenon by the fact that polar water vapour molecule absorbs on the surface of the oxide scale much more strongly than the non-polar molecule of N_2. It was also suggested that any contribution made by molecular water to oxygen mass transport within the chromia will also be enhanced.

Tying up Ti in the form of TiN results in suppression of Ti incorporation into the chromia scale. Therefore it can be expected that the adverse effect of Ti on the chromia scale growth rate described above might be to same extent suppressed during exposure in the dry synthetic air. Indications for the latter were found in the cross-sections: a thinner outer TiO_2 layer, a thinner Cr_2O_3 scale and coarser internal Al_2O_3 precipitates were found after exposure in synthetic air than in synthetic air + 7%H_2O (**Figure 6.17**). The results in the present work thus indicate that the effect of water vapour depends on the base gas composition, i.e. can be different between Ar-O_2 and N_2-O_2 atmospheres.

Specimens of Rene 80 with an HVOF MCrAlY-overlay coating after 100 hours of discontinuous exposure in synthetic air and synthetic air + 20% H_2O showed very similar mass gains (**Figure 6.18**). Also cross sections (**Figures 6.19** and **6.20**) of the overlay coated

Rene 80 showed that in average, the oxide scale thickness in both atmospheres was similar. However, the cross sections also showed that spallation of the oxide scale after 100 hours in synthetic air occurred, while on the specimen oxidized in wet atmosphere the oxide scale after 100 hours was adherent. In both atmospheres the fast growing Cr_2O_3 scales can be expected to spall during cyclic oxidation. Indications for this effect were found after 100 h of discontinuous exposure as well as in the TG test for 100 h. Based on the prevailing results it is not possible to unequivocally derive whether Cr-evaporation in the form of CrO_3 and/or e.g. $CrO_2(OH)_2$ played an important role in the material degradation. However, the differences between the mass changes after longer exposure time (2000 h) indicate a mass loss increase by about 20%due to the presence of water vapour in the test gas. These differences become important after about approximately 1000 h oxidation at 1050°C.

6.3.5 Boron incorporation into the scale and its depletion from the bulk alloy

B-enrichment in the inner part of the oxide scale was observed in all studied atmospheres in the GD-OES depth profiles (**Figures 6.5** and **6.16**). **Figure 6.32** shows a cross section of Rene 80 after oxidation at 1050°C for 20 hours in synthetic air. The morphology of the formed oxide scale is similar to that described in the beginning of chapter 6.3 (**Figure 6.26**). B-enrichment in the inner part of the oxide scale on Rene 80 was observed recently by Jałowicka [96], however, no quantitative analysis of the chemical composition and crystallographic structure of the B-containing oxide was provided.

The composition of the B-rich phase in the oxide scale was analysed by SEM/WDX (**Figures 6.32, 6.33**). The WDX analysis indicates formation of a Cr-B-mixed oxide, containing small amounts of Al and Ti.

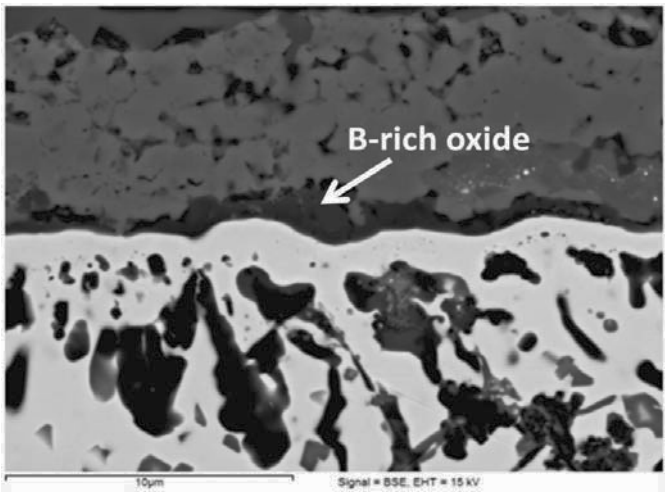

Figure 6.32 Cross sections of Rene 80 (SEM BSE images) after exposure at 1050°C for 20 hours in synthetic air.

Table 6.1 SEM/WDX quantitative point analysis of boron containing oxide precipitates such as that shown in **Figure 6.32**

All results in atomic%

Location	B	O	Al	Ti	Cr
1	22.4	58.2	0.3	4.5	14.6
2	20.9	58.4	2.5	5.9	12.3
3	21.2	59.1	0.3	4.9	14.5

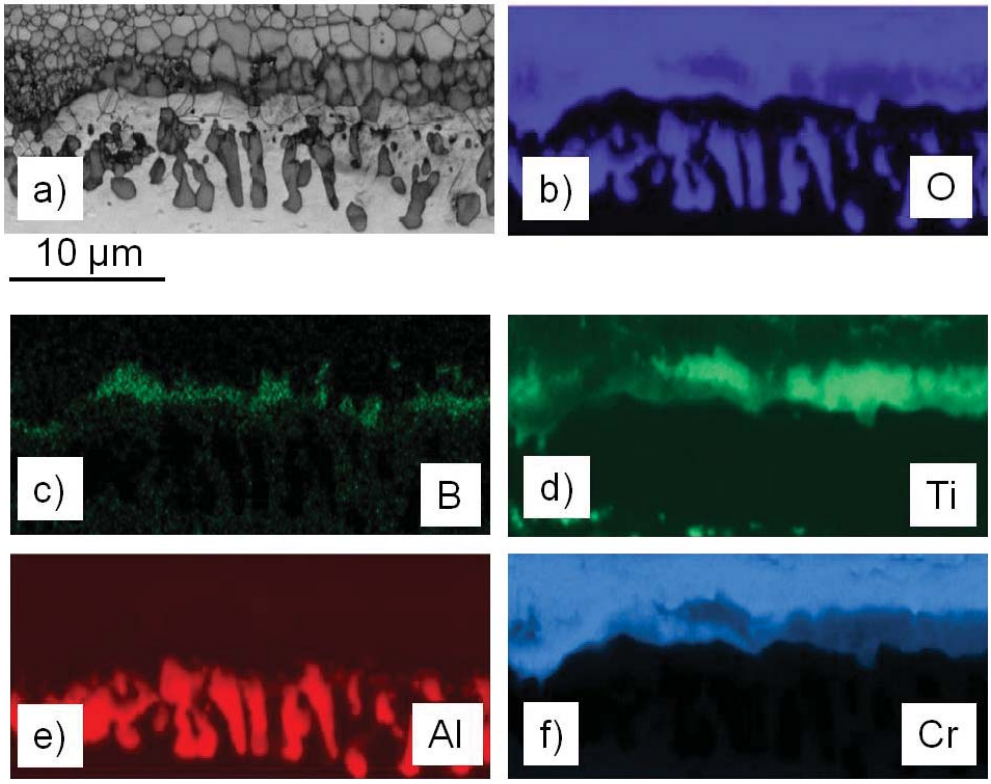

Figure 6.33 EDX elemental mapping of the oxide scale formed on Rene 80 during exposure at 1050°C for 20 hours in synthetic air: a) EBSD pattern quality map, b) – f) corresponding EDX elemental maps

To identify the crystallographic nature of the B-containing phase, EBSD patterns were collected from the phases found in the inner part of the oxide scale as well as in the alloy regions near to the interface with the oxide scale. These patterns were compared with those from various oxide compounds from the Inorganic Crystal Structure Database (ICSD) and National Institute of Standards and Technology (NIST) databases having a composition in agreement with the EDX/WDX measurement of the respective constituents. In this way the boron containing oxide phase could be unequivocally identified as $BCrO_3$ with the calcite crystallographic structure (**Figure 6.34**).

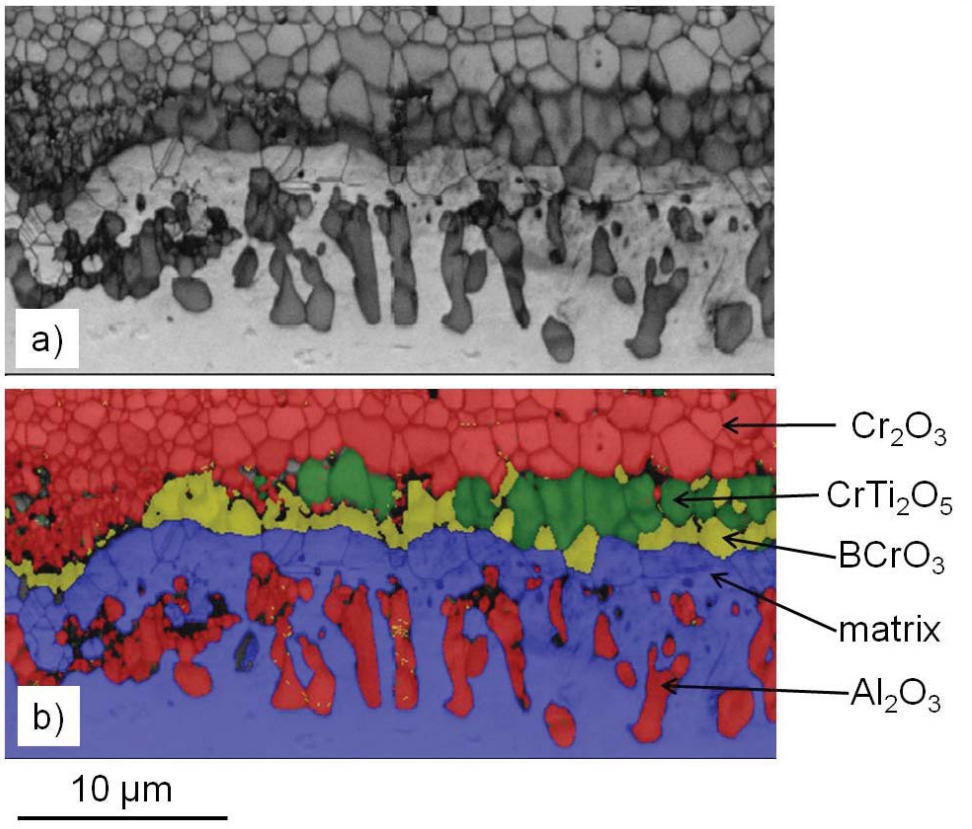

Figure 6.34 EBSD phase map near the scale/alloy interface of Rene 80 after exposure at 1050°C for 20 hours in synthetic air. Phase description: blue – Ni-matrix, red – Cr_2O_3/Al_2O_3, green – $CrTi_2O_5$, yellow – $BCrO_3$.

The WDX analysis (**Figure 6.32**) shows that the formed B-rich oxide is not pure $BCrO_3$, but also contains minor amounts of Ti and Al. Comparing the WDX and the EBSD results it may be speculated that Ti and Al ions can substitute Cr ions in the respective cation sub-lattice.

Based on the GD-OES depth profiles the enrichment of B in the oxide scale is apparently associated with a substantial B depletion from the base material (**Figure 6.35**).

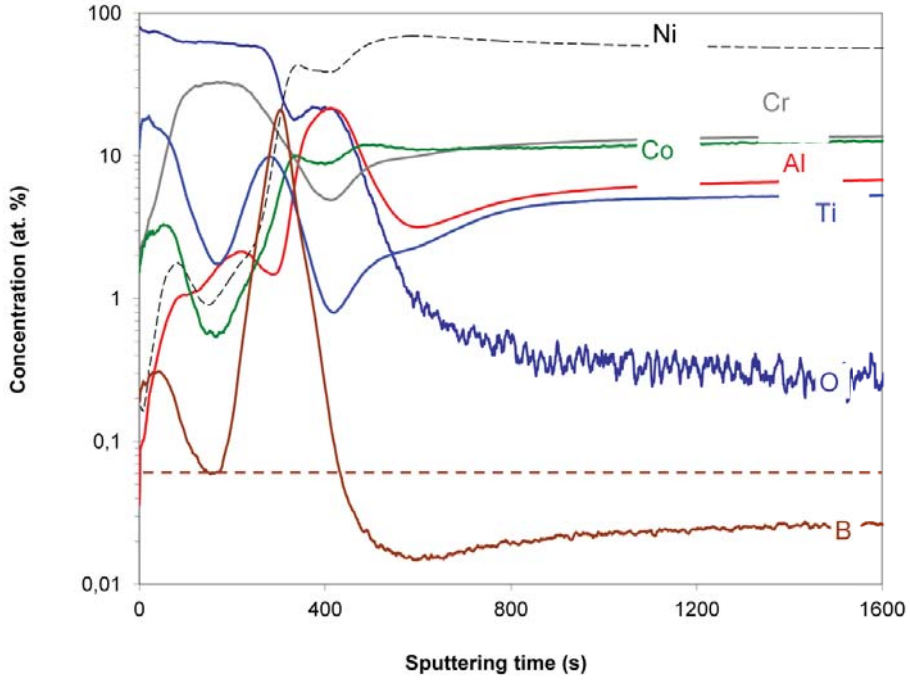

Figure 6.35 GD-OES depth profile of Rene 80 after oxidation at 1050°C for 20 hours in synthetic air. Horizontal brown dashed line shows B-concentration in non-exposed material.

Chemical analysis by ICP-MS of the non-exposed studied Rene 80 batch revealed a B content of 92 wt. ppm (about 490 at. ppm). The B-content in the non-exposed Rene 80 is marked on **Figure 6.35** as brown dashed line. The B concentration in the GD-OES depth profile was quantified using RSF's determined from the original B content in non-exposed material according to the procedure described in [97, 98]. The relative sensitivity factors (RSF's) were determined for the elements Ni, Cr, Co, Al, Ti, B from the known alloy composition in the following way:

$$RSF_X = \left(\frac{C_X}{C_{Ni}}\right)\left(\frac{I_{Ni}}{I_X}\right) \tag{6.3}$$

where: C – atomic concentration of element X and Ni, I_i – Ion intensity of the measured elements, respectively.

The RSF for oxygen was calculated using the following equation:

$$\frac{I_{Cr} \times RSF_{Cr}}{I_O \times RSF_O} = \frac{2}{3} \quad (6.4)$$

The RSF's are calculated using Ni as a reference i.e. setting $RSF_{Ni} = 1$. Using these RSF's, the concentration profiles can be calculated in the oxide scales of the alloys.

The GD-OES was found to be an ideal analytical method for detection of B enrichment in the oxide scale. The GD-OES depth profiles of Rene 80 exposed at 1050°C for 20 hours in synthetic air show, that the B content in the alloy below the oxide scale region after 1600 seconds of sputtering is in the range of about 250 at. ppm (see **Figure 6.35**). This might suggest that either the material is depleted from B to this amount or (more probably) that during sputtering the material depth not affected by B-depletion was not yet reached. To verify which of the two possibilities is correct, coupons of Rene 80 were exposed at 1050°C for various times in laboratory air. After exposure the oxide scales were removed and the bulk boron content was analysed by ICP-MS. The results presented in **Figure 6.36** indicate a rapid B depletion during oxidation at 1050°C, in agreement with the GD-OES profiles. The depletion occurs mainly in the first 20 hours of exposure. The obtained results are in very good agreement with the predictions by Jałowicka [96], who calculated that the time for complete B depletion from a 2 mm thick specimens of a similar material is 44 hours.

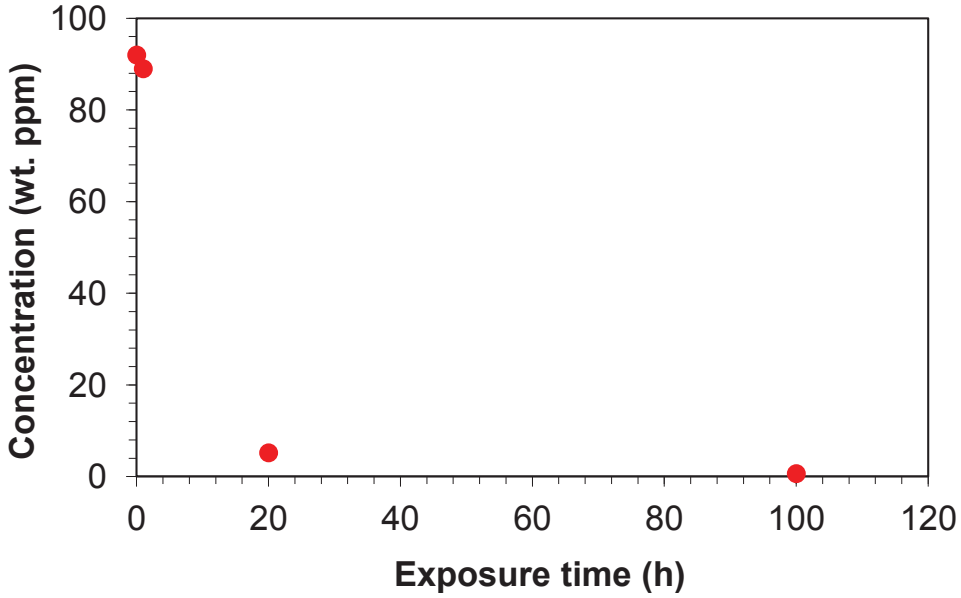

Figure 6.36 Bulk Boron concentration in Rene 80 as a function of time during air exposure at 1050°C (measured by ICP-MS)

It is known that polycrystalline alloys contain minor amounts of strengthening elements such as B and Zr, which segregate to the alloy grain boundaries [9]. The resulting reduction in grain boundary energy is associated with increased creep strength and ductility if the mechanism of failure involves grain decohesion. Therefore, depletion of the B reservoir during exposure at high temperature found in the present work might in principle have an adverse effect on the alloy creep strength and consequently the creep limited lifetime of the Ni-base alloy components. This should be verified in further studies.

7 Free standing MCrAlY coatings

7.1 General remarks

In the present section free standing MCrAlY coating after vacuum heat treatment (described in **chapter 5.2.2**) was investigated to obtain the oxidation kinetics at various temperatures in dry and wet air. The exposed MCrAlY-coatings had two surface finish conditions (ground surfaces and rough as-sprayed HVOF surface (see **chapter 5.2.2**)). The MCrAlY coatings were tested in both discontinuous and thermogravimetric tests according to the procedures described in **chapters 5.3.1** and **5.3.3** respectively.

7.2 As-received conditions

Figure 7.1 shows cross section SEM BSE images of the HVOF coating in the as-sprayed conditions before (**Figure 7.1 a)**) and after treatment (**Figure 7.1 b)**). The coating without heat treatment exhibits substantial porosity and non-uniform distribution of phases. Also boundaries between sprayed powder particles are visible. After the heat treatment only closed porosity remains and a uniform phase distribution over the coating can be observed.

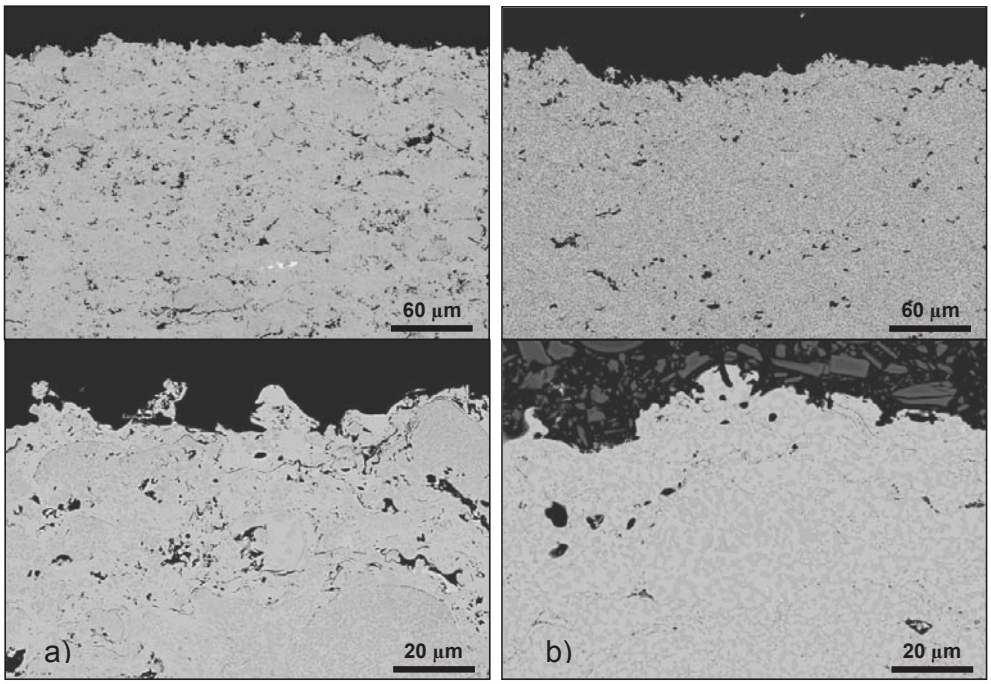

Figure 7.1 Cross sections images (SEM BSE) showing microstructure of free standing MCrAlY coatings in as-sprayed condition: a) prior to vacuum heat treatment, b) after heat treatment for 1 hour at 1080°C and 12 hours at 870°C in vacuum of 10^{-5} mbar.

7.3 Thermogravimetric tests of ground MCrAlY coatings

7.3.1 Oxidation kinetics

Figure 7.2 shows mass changes of the free standing MCrAlY coatings during isothermal oxidation for 100 hours in a thermobalance. The coating shows the highest mass change at 1120°C (0.44 mg/cm^2) after 100 hours, smaller at 1080°C (0.32 mg/cm^2) and the smallest mass changes for coatings oxidized at 1050°C. It appeared that the mass gain obtained for the wet gas exposure (0.20 mg/cm^2) was smaller compared to that in dry gas (0.27 mg/cm^2). Also, the shape of the mass change curves clearly indicates different oxidation kinetics between the wet and dry atmospheres. **Figure 7.3** shows that values of the instantaneous k_w (defined by

the equation (2.11) in **chapter 2.2**) for the coating oxidized in dry atmosphere is higher than that obtained for wet atmosphere.

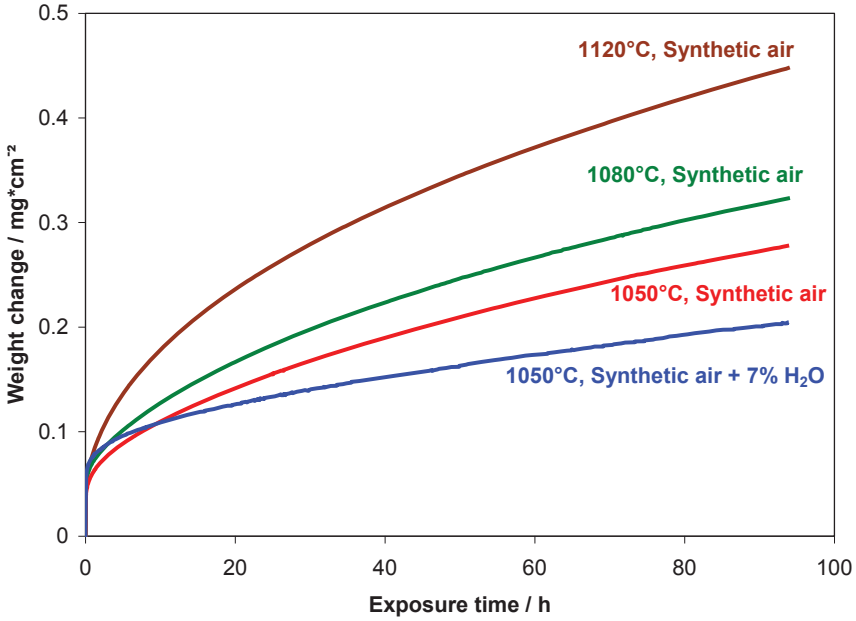

Figure 7.2 Mass changes of free standing MCrAlY specimens by HVOF (ground surfaces) during thermogravimetric test up to 100 h in dry and wet synthetic air

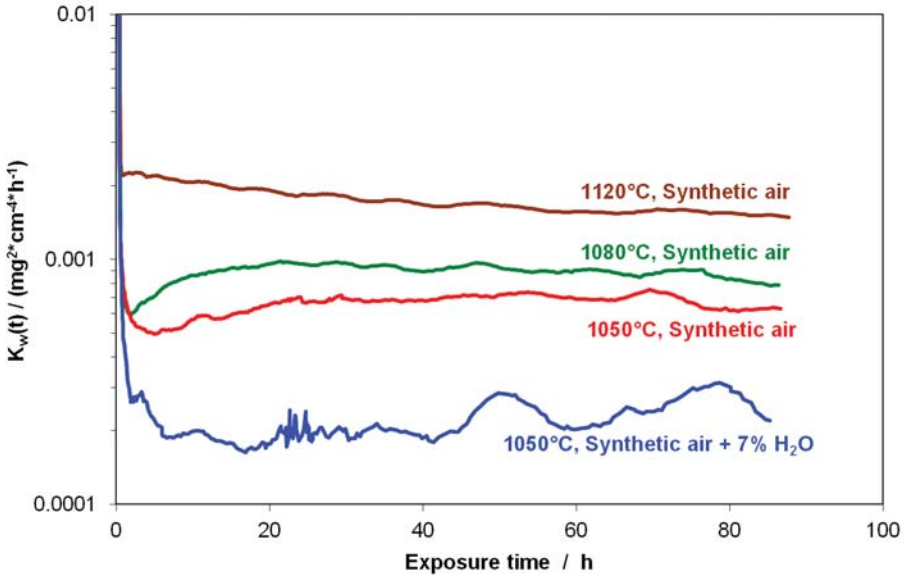

Figure 7.3 Instantaneous apparent k_w as a function of exposure time obtained during thermogravimetric test of free standing MCrAlY specimens by HVOF (ground surfaces) up to 100 h in dry and wet synthetic air

7.3.2 Analytical studies of free-standing MCrAlY coating

Figure 7.4 shows SNMS depth profiles for the free standing MCrAlY specimens discussed in **section 7.2.1**. All the samples show similar oxide scale composition with only minor differences. The SNMS profiles suggest that the oxide scale formed on the coatings at different temperatures in the two atmospheres have different thicknesses. This is in good agreement with the mass change curves in **Figure 7.2**. Additionally, the oxide on the coating oxidized in dry atmosphere at 1050°C is slightly thicker compared to that in the water vapour containing gas. Also the Cr content in the outer part of the scale is higher in the oxide of the coating oxidized in dry air; in the outer part of the scale the Cr content is about 1 at. % (**Figure 7.4 c)**) while for the coating oxidized in water vapour containing gas the amount of Cr in the outer part of the oxide scale is less than 0.4 at.% (**Figure 7.4 d)**).

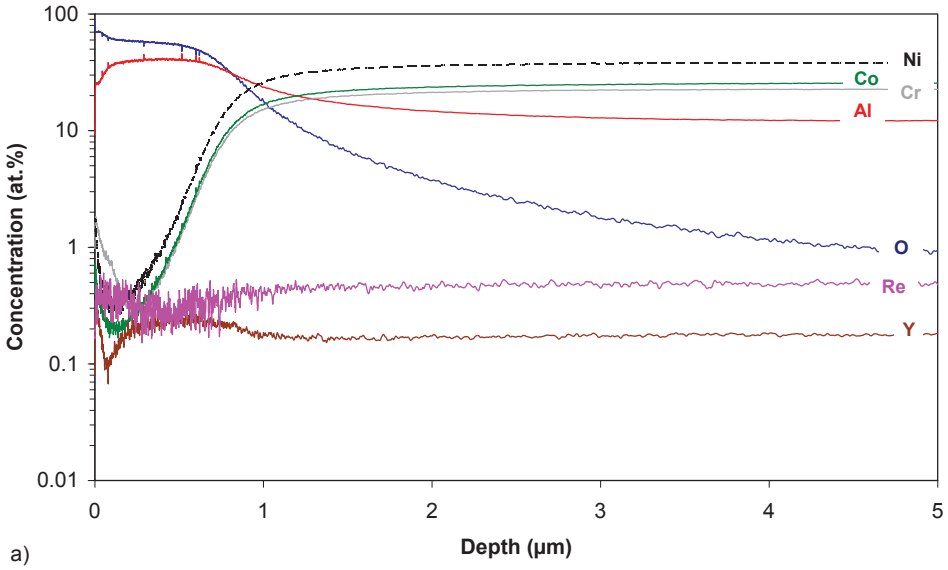

a)

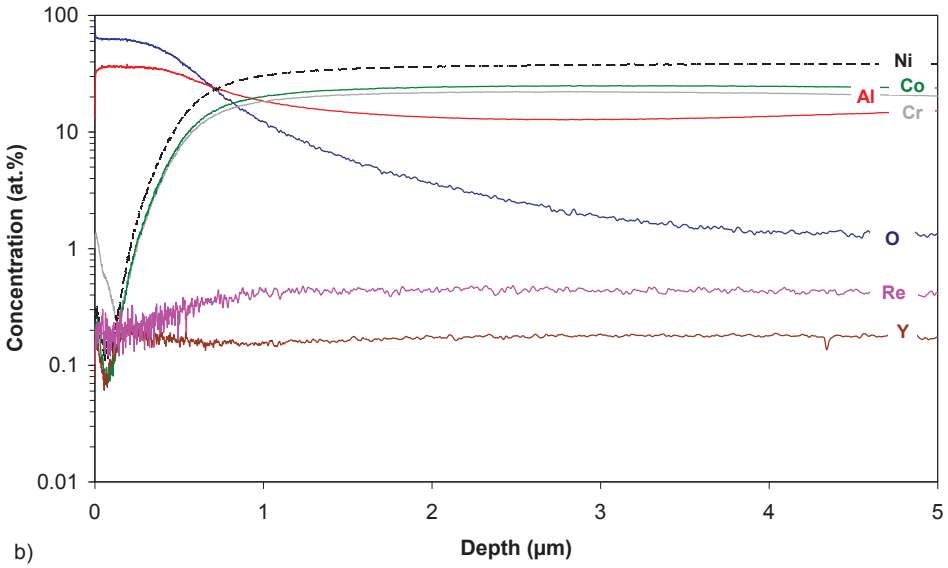

b)

Figure 7.4 SNMS depth profiles of free standing MCrAlY coating after thermogravimetric test for 100 h at: a) 1120°C in synthetic air, b) 1080°C in synthetic air, c) 1050°C in synthetic air and d) 1050°C in synthetic air + 7% H_2O

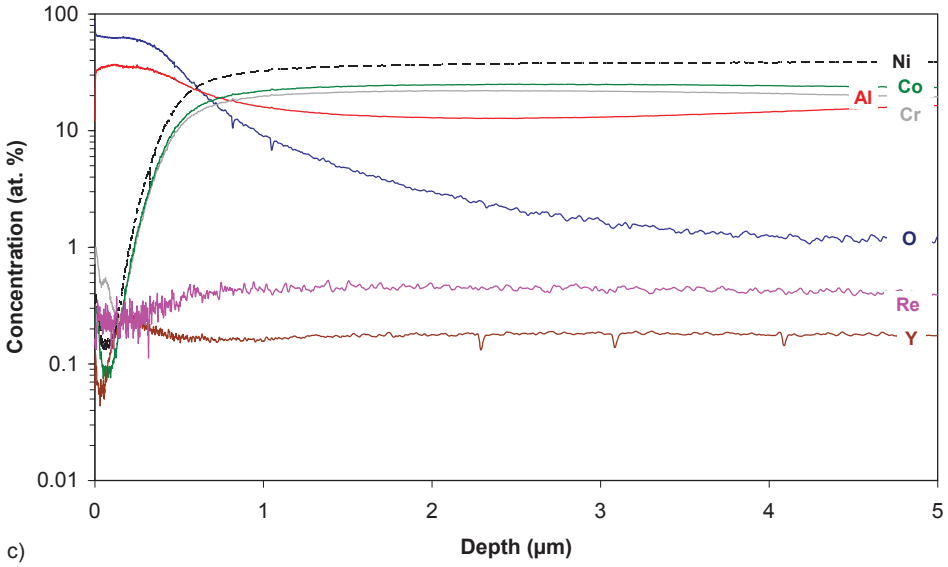

c)

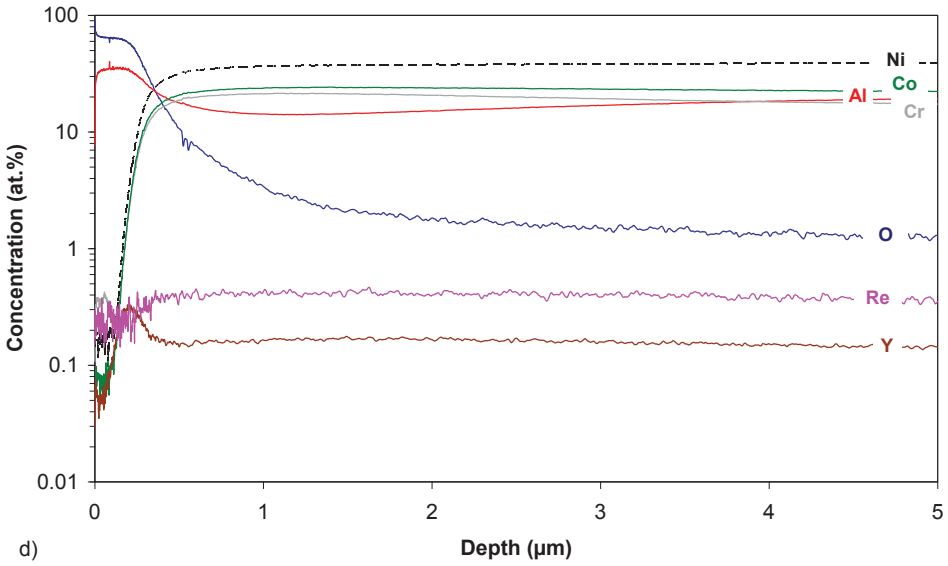

d)

Figure 7.4 Continued

SEM analyses of the coatings after the thermogravimetric exposures at 1050°C for 100 hours confirm the differences in the oxide scales thicknesses found by the thermogravimetric tests and the SNMS analyses (**Figure 7.5**).

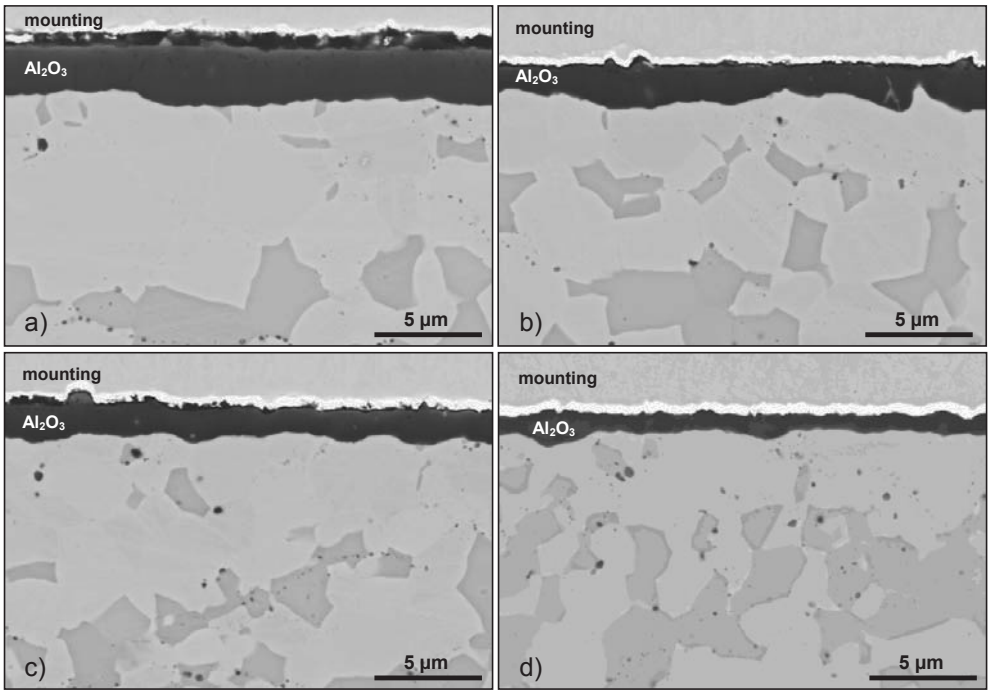

Figure 7.5 SEM images of cross sections of the free standing MCrAlY specimens after thermogravimetric test for 100 hours at: a) 1120°C in synthetic air, b) 1080°C in synthetic air, c) 1050°C in synthetic air and d) 1050°C in synthetic air + 7% H_2O

7.4 Discontinuous oxidation of the ground free standing MCrAlY coatings

7.4.1 Oxidation kinetics

Figure 7.6 shows mass change data obtained during discontinuous oxidation of ground free standing specimens of MCrAlY at 1050°C up to 2000 hours in dry and wet gas. The mass changes obtained for dry and wet atmosphere do not show significant differences.

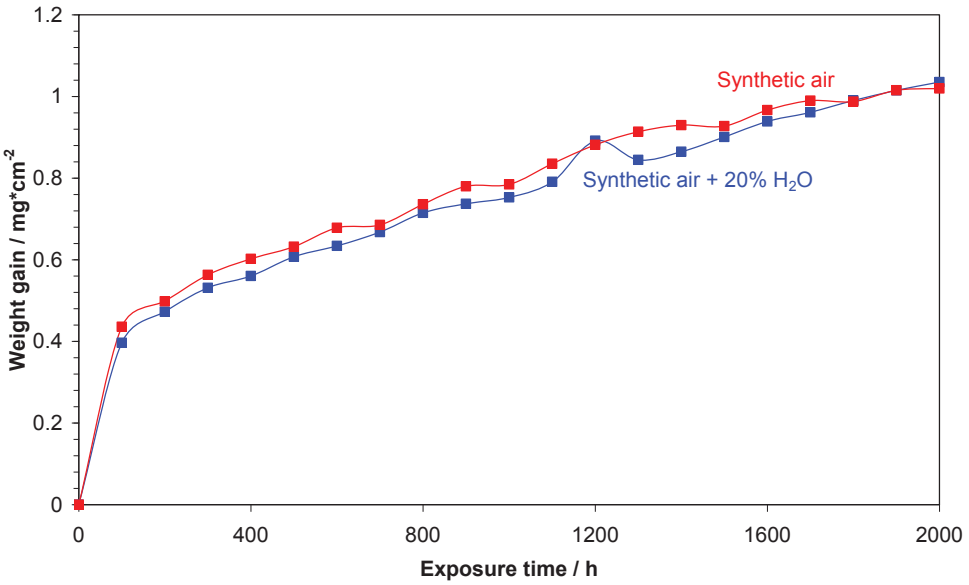

Figure 7.6 Mass changes of ground to 1200 grit free standing MCrAlY specimens during discontinuous oxidation at 1050°C up to 2000 h in dry and wet synthetic air

7.4.2 Analytical studies

SEM analyses of the ground coating specimens after discontinuous oxidation for 100 hours (**Figure 7.7**) reveal a small difference of the oxide scale thicknesses between the two gases, however, the difference is far less significant as in the case of the isothermal oxidation. The measured values of the oxide scale thickness after 100 hours are: 2.05 +/- 0.55 µm for the

coating oxidized in the dry atmosphere and 1.74 +/- 0.16 for the wet gas. Also a difference in the oxide scale morphology is apparent. On top of both oxide scales "spiky" shaped oxides are visible, however, on the oxide scale formed in wet atmosphere the number of spikes is larger. Probably this is remnant of θ-alumina from the early stages of exposure. In the outer part of the scale formed in dry atmosphere minor porosity can be observed.

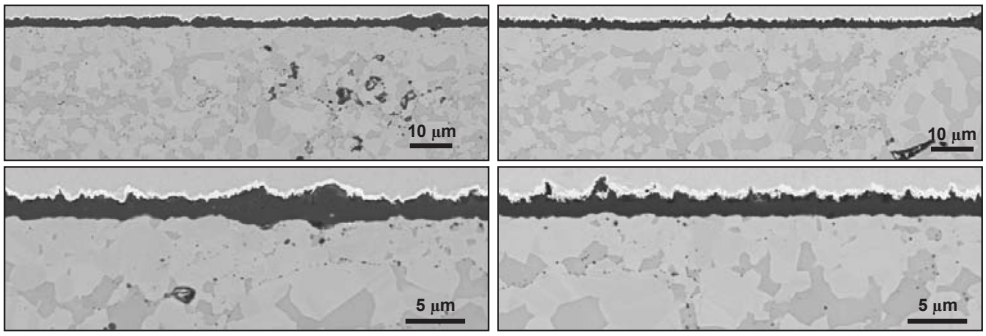

Figure 7.7 SEM images of cross sections of ground free standing MCrAlY coating after discontinuous oxidation at 1050°C for 100 hours in: a) synthetic air, b) synthetic air + 20%H_2O

After 2000 hours of exposure (**Figure 7.8**) presence of spikes can be observed on top of the oxide scale of coatings oxidized in dry atmosphere. Also pores in the outer part of the scale can be found. Coatings oxidized in wet gas formed mainly alumina scale with Co/Cr-rich oxide on top of the oxide scale.

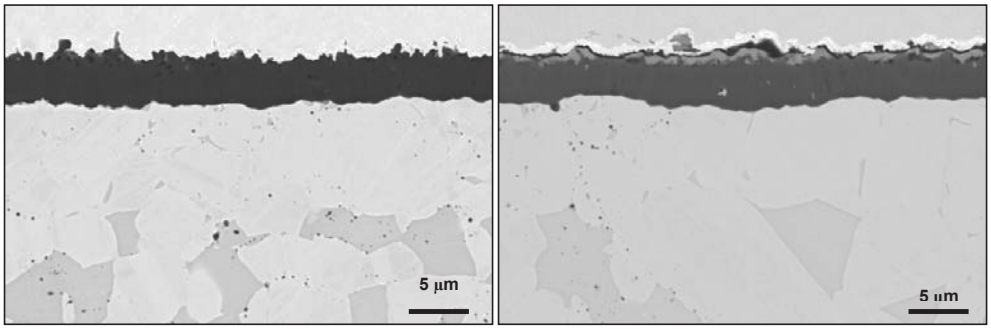

Figure 7.8 SEM images of cross sections of ground free standing MCrAlY coating after discontinuous oxidation at 1050°C for 2000 hours in: a) Synthetic air, b) Synthetic air + 20% H_2O

7.5 Discontinuous oxidation of as-sprayed HVOF MCrAlY coating surfaces

7.5.1 Analytical studies

Figures 7.9 and **7.10** show SEM images of cross-sections of rough, free-standing MCrAlY coating surfaces (as-sprayed condition) exposed at 1050°C for 100 hours in dry and wet synthetic air. Free-standing MCrAlY coatings exposed in dry and wet synthetic air formed an alumina surface scale. Based on **Figure 7.9** one can conclude that the thickness of the alumina scale formed in dry and wet test gases is similar, however the cross-sections (**Figure 7.10**) in higher magnification show that the alumina scale thickness varies depending on location.

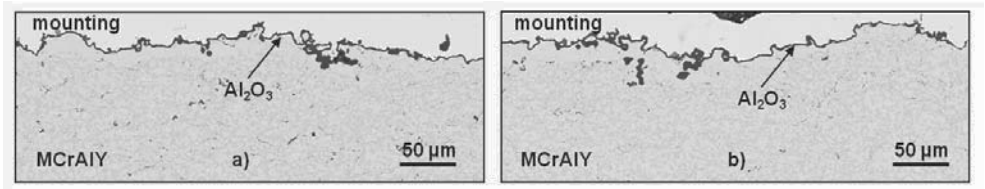

Figure 7.9 Overview SEM cross-sections of free-standing rough MCrAlY coatings (as-sprayed) exposed at 1050°C for 100 hours in: a) synthetic air and b) synthetic air + 20% H_2O

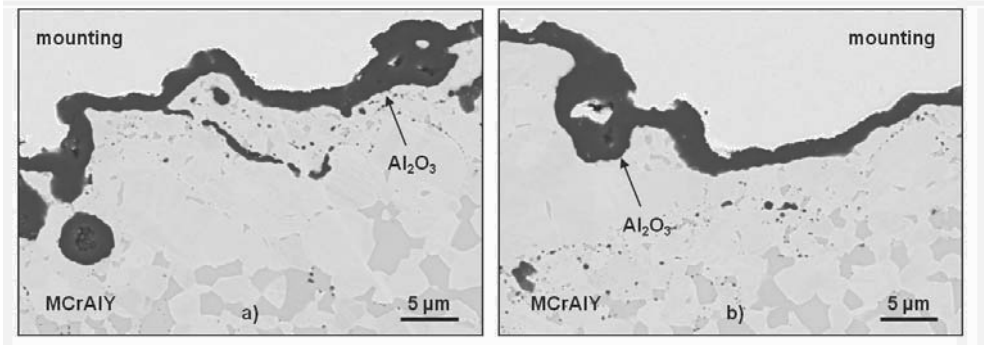

Figure 7.10 Detailed SEM cross-sections of free-standing rough MCrAlY coatings (as-sprayed) exposed at 1050°C for 100 hours in: a) synthetic air and b) synthetic air + 20% H_2O

7.6 Discussion on coating oxidation:

Figure 7.1 shows coating microstructures before and after heat treatment. Differences in the microstructure and morphology are clearly visible. The coating in the as-sprayed condition contains a large number of pores (**Figure 7.1 a)**). The high velocity oxy-fuel (HVOF) spraying is performed under the conditions at which the MCrAlY powder particles are incompletely melted; as the result the separated particles along the coating are visible. In order to improve the coatings oxidation resistance a vacuum heat treatment is necessary. As visible in **Figure 7.1 b)** the heat treatment results in substantial reduction of porosity. Also the γ and β precipitates present in the coating are homogenously distributed. In addition, tiny oxide particles were found within the coating. These oxides contain yttrium and aluminium and are most probably formed during deposition. The effect of vacuum heat treatment on the oxidation behaviour of the coating was investigated by Saeidi et al. [123]. The authors found that for coatings without heat treatment k_w was higher than for the same coating after heat treatment.

The present thermogravimetric measurements show that coatings oxidized at different temperatures in synthetic air formed mainly an alumina scale with minor amounts of chromium oxide in the outer part of the scales (**Figure 7.4 a) – c)**). The oxide scale thickness measurements after exposure of the ground MCrAlY for 100 hours shows that the oxide scale thickness increases with increasing exposure temperature (**Figure 7.11**).

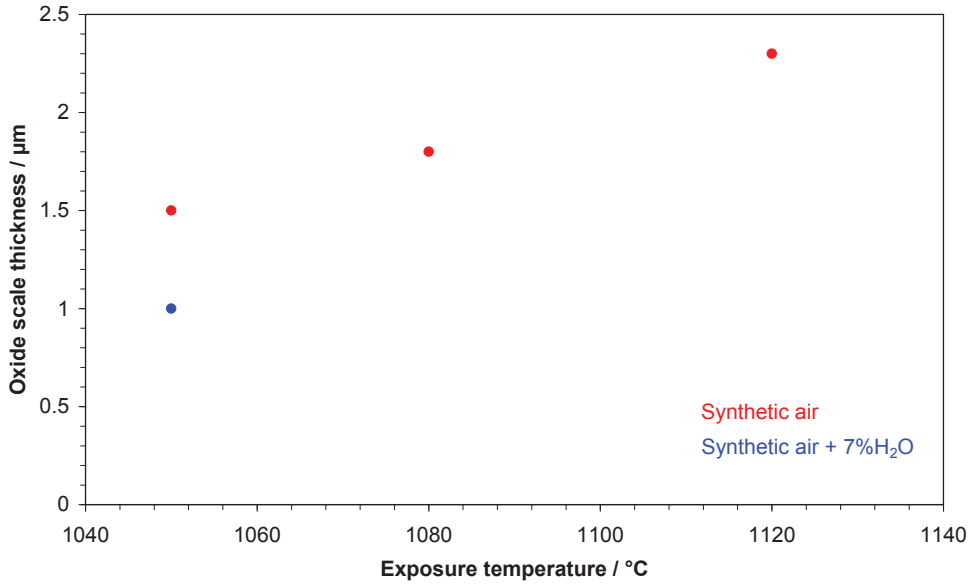

Figure 7.11 Thickness of formed alumina as a function of exposure temperature for ground HVOF MCrAlY coatings for 100 hours in dry and wet gas.

However, it should be noticed that the oxide scale thickness on ground coatings isothermally oxidized at 1050°C in synthetic air is larger than the thickness of the oxide scale formed in wet atmosphere (good agreement between the mass change curves (**Figure 7.2**), SNMS profiles (**Figure 7.4**) and SEM analyses (**Figure 7.5**). The evaluation of oxidation kinetics (**Figure 7.3**) reveals that the coating oxidized at 1050°C showed the lowest value of k_w, moreover this value has been reached already after relatively short time. It suggests, that the coating almost immediately formed a protective α-alumina layer. Also comparison of the SNMS depth profiles of the coatings oxidized in synthetic air without and with water vapour (**Figure 7.4**) showed, that in dry synthetic air the oxide scale contains more chromium in the outer part of the scale. This indicates that at the beginning of oxidation the coating formed transient chromia and after a given period of time formation of a protective α-alumina scale occurred. It is known, that oxygen transport through the chromia scale is much faster than through the alumina, and therefore formation of the transient chromia scale could be one of the possible explanations for the obtained higher mass change in synthetic air. The obtained

results indicates, that water vapour promotes formation of a “purer” and therefore more protective α-alumina scale.

A significant effect of water vapour on the oxide scale thickness was observed only during the TG test, in which relatively high heating rate prevails: 90 K/min. During discontinuous oxidation in tube furnaces, with a heating rate of 10 K/min, the effect of water vapour on the thickness of the formed oxide scale is far less pronounced. The measured oxide scales thicknesses for the coating oxidized in dry and wet air were 2.1 µm and 1.7 µm respectively. Additionally, on top of the formed oxide scale in wet air “spiky” shaped oxides are visible. These oxides are probably remnants of metastable alumina. One of the possible explanations for the discrepancy in the effect of water vapour on the oxidation kinetics can be differences in heating rate between the discontinuous and TG oxidation tests. α-Al_2O_3 is known to grow very slowly, however also other metastable crystal structures of aluminium oxide exist, including cubic-spinel γ-Al_2O_3, tetragonal δ-Al_2O_3, and monoclinic θ-Al_2O_3. These transient metastable aluminas grow significantly faster than α-Al_2O_3 (**Figure 7.12**) due to rapid outward cation transport, which usually results in formation of oxide scale with typical whiskers/needle type morphologies [98].

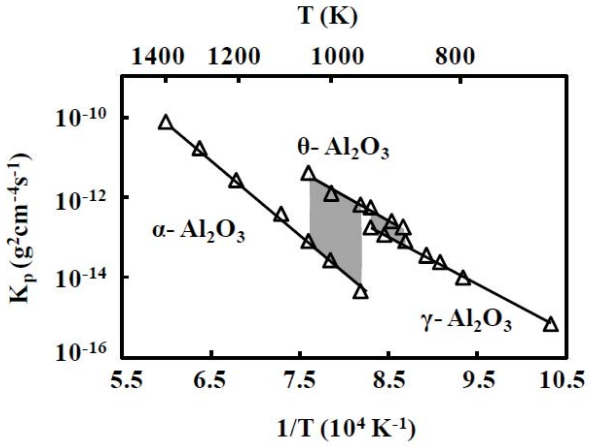

Figure 7.12 Arrhenius plot of parabolic rate constant (k_p) for the oxidation of pure NiAl [124]

Literature studies indicate [125] that water vapour can stabilize metastable alumina by dissociated water covering the oxide surface. The presence of OH^- groups stabilizes the surface of metastable alumina which will stay hydroxylated even at high temperatures. Götlind et al. [126] for FeCrAlY alloys found that water vapour stabilizes metastable alumina, especially during the early stages of oxidation. They also observed a higher oxidation rate of the material in the early stages of oxidation and correlate this with stabilization of metastable alumina.

For the coatings oxidized in the TG tests in the present studies mass change curves as well as k_w plots (**Figures 7.2** and **7.3**) clearly indicate a much higher mass gain at the very early stages of oxidation for the coating oxidized in the water vapour containing gas which may be correlated with the formation of fast growing metastable alumina. However, after less than one hour (**Figure 7.2**) the mass gain kinetics of the coating oxidized in wet atmosphere rapidly slowed down, which could be an indication for transformation from metastable alumina to protective α-Al_2O_3. The thinner oxide scale formed in the wet air after 100 h TG test could be explained by assuming that during the very early stages of oxidation water vapour promotes formation of metastable alumina which is very quickly transformed to protective, stable coarse-grained α-alumina after relatively short time. Taniguchi et al. [127] found that grains of an α-Al_2O_3 scale formed on a FeCrAlY alloy by transformation from metastable alumina are much coarser than when α-Al_2O_3 was initially nucleated on the metal surface. Thus, the grain boundary density was reduced in the case of the alumina scale formed by θ to α transition. The latter effect might explain why in the present study the thickening of the oxide scale after longer time in the wet gas is slower than in dry. On the coating oxidized in dry air in the outer part of the oxide scale a higher amount of chromium has been found

(**Figure 7.4 c)**). This may suggest that the coating formed initially a Cr-rich oxide, which could provide numerous sites for nucleation of a fine-grained α-Al_2O_3 [128]. Considering the major growth mechanism of α-Al_2O_3 scales to be oxygen grain boundary diffusion the latter observation can explain the formation of a thicker oxide scale on the coating oxidized in dry air during the thermogravimetric test.

Figure 7.13 shows schematic temperature curves as a function of time for the TG (**Figure 7.13 a)**) and the discontinuous oxidation test (**Figure 7.13 b)**). The temperature range in which the metastable alumina is commonly observed in the respective oxide scales on high-temperature alloys and coatings (from about 900°C up to 1050°C) is marked. It is clearly visible that the time during which the coatings are exposed in this temperature range in the TG furnace with the higher heating rate is significantly shorter than in the tube furnace with the lower heating rate. This might allow the coating exposed in the tube furnace to form in both atmospheres a thick metastable alumina scale before the furnace reaches the oxidation temperature of 1050°C at which the metastable alumina transforms after some time to stable α-alumina. The latter argument may explain why during exposure in the tube furnace in dry and wet atmospheres a difference between the oxide scale thicknesses is not as pronounced as in the case of the same coating in the TG experiments. Also the different amounts of water vapour in these two types of experiments (for TG test 7%, for tube furnace test 20%), might play a role.

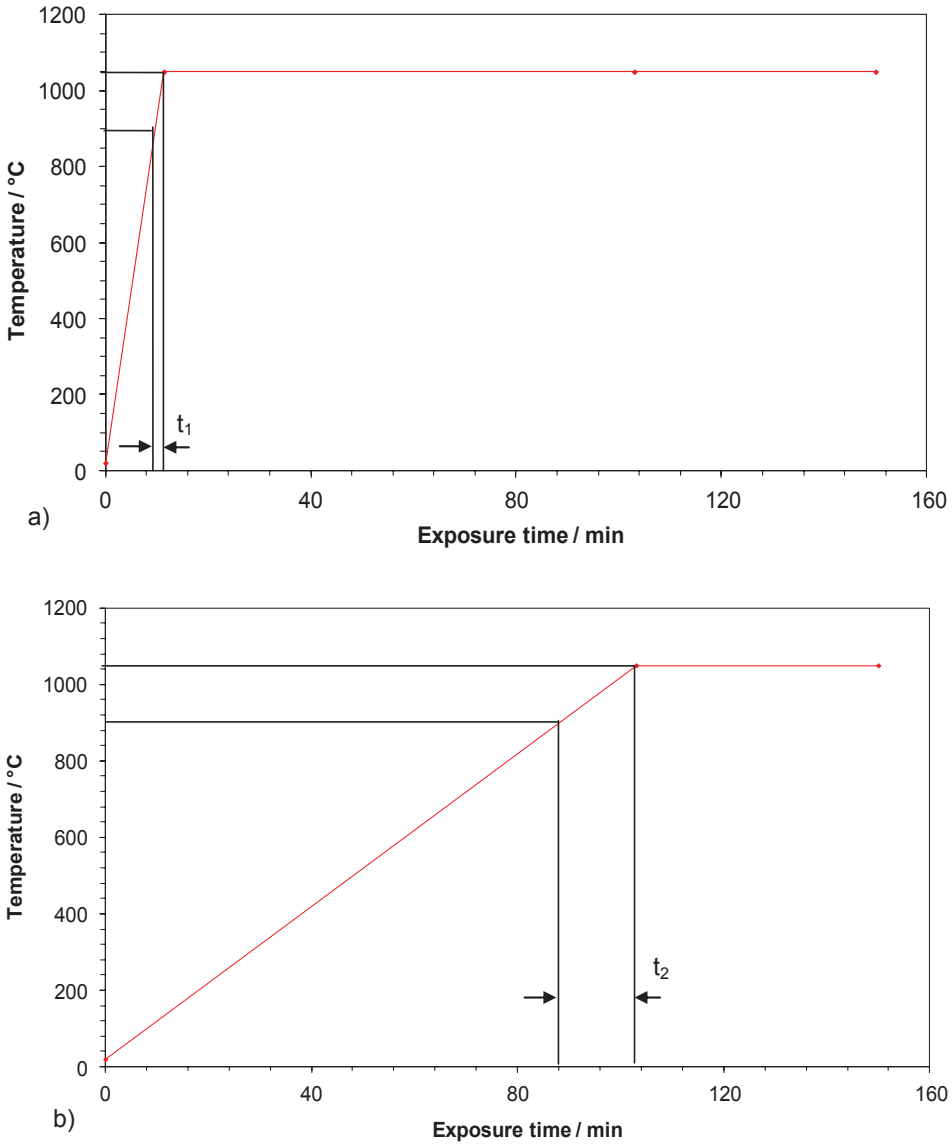

Figure 7.13 Sample temperature as a function of time during thermogravimetric test with heating rate of 90 K/min (a) and discontinuous oxidation test with heating rate 10 K/min (b)

Another possible explanation for the differences between the thickness and morphology of the oxide scales formed on free standing MCrAlY coatings exposed at 1050C for 100 hours in dry and wet synthetic air in TG experiment and in tube furnace test may be the following explanation. During early stage of oxidation (heating plus/or isothermal stage) MCrAlY

coating forms Cr-rich transient oxide. As described in **chapter 3.2** in gases containing O_2+H_2O, chromia tends to form volatile oxyhydroxides $Cr_2(OH)_2$. It is known that volatilization of chromia species depends inter alia on the gas flow rate, which in previously mentioned tests (TG and tube furnace test) is different. The SNMS depth profiles of ground free standing MCrAlY coatings after thermogravimetric exposure at 1050°C in dry and wet synthetic air (**Figure 7.4 c)** and **d)** respectively) revealed higher amount of chromium in the outer part of the oxide scale for the coating exposed in dry air. This may suggest that volatilization of transient Cr-rich oxide might took place for the coating exposed in wet air.

For free standing MCrAlY coatings exposed in tube furnace test at 1050°C for 100 hours slightly more "spiky" shaped oxides on ground free standing MCrAlY coating exposed in wet air can be observed (**Figure 7.7**). It was shown in literature that transient Cr-oxide promotes transition from metastable transition from metastable to stable α-Al_2O_3. Considering latter fact and more extensive presence of "spiky" shaped remnants of metastable alumina in wet air (**Figure 7.7**) one can speculate Cr-rich transient oxide evaporation.

Based on the results obtained in the present studies for free standing MCrAlY coating it is impossible to unambiguously show a single reason for differences in thickness and morphologies of the oxide scales formed on MCrAlY coatings. Most probably oxide nucleation during transient (heating) stages and volatilization of Cr species from Cr-rich transient oxide affect the oxide scale formation on free standing MCrAlY coatings.

8 APS-TBC systems

In this chapter several APS-TBC systems described in more details in Table 8.1 have been tested in two test types. The first type was a furnace cyclic test at 1120°C in laboratory air to investigate the effects of bondcoat surface roughness profile and topcoat porosity on the TBC-lifetime. To investigate the influence of water vapour on the APS-TBC-lifetime discontinuous tests with 100h cycles at 1050°C in synthetic air and synthetic air + 20 % H_2O were performed. The exact procedures of both test types were described in detail in **chapters 5.3.1** and **5.3.2.** For the accelerated test systems designated as System 1, System 3, System 4 and System 6 have been chosen. In the discontinuous test at 1050°C all of the APS-TBC systems described in **Table 8.1** except System 4 have been examined.

Table 8.1 Description of tested APS-TBC systems

Nr	Basic material	MCrAlY Production	TBC type	TBC-system designation
1	Rene 80	HVOF	porous	System 1
2	Rene 80	HVOF	dense	System 2
3	Rene 80	VPS	dense	System 3
4	Rene 80	VPS	porous	System 4
5	Rene 80	HVOF+APS-flashcoat spraying parameter set I	porous	System 5
6	Rene 80	HVOF+APS-flashcoat spraying parameter set II	porous	System 6
7	Rene 80	HVOF+APS-flashcoat spraying parameter set II overaluminized	porous	System 7

8.1 As-sprayed conditions

Figure 8.1 shows metallographic cross sections of TBC systems with HVOF and VPS bondcoats tested in the frame of the present work. The systems with HVOF bondcoat showed different roughness profiles compared to the systems with VPS bondcoats. The systems differ also in topcoat porosity. Additionally the systems shown in **Figure 8.1 c)** and **d)** have slightly thinner bondcoat than the systems shown in **Figure 8.1 a)** and **b)**. All the advanced TBC systems have a porous APS-sprayed topcoat as well as an APS-flashcoat (which is sprayed using the same MCrAlY powder as used for the VPS coatings). The system shown in **Figure 8.1 e)** has an APS-flashcoat deposited with spraying parameter set I. The system shown in **Figure 8.1 f)** has an APS-flashcoat deposited using spraying parameter set II; the structure obtained for this layer is much more dense than that of the coating shown in **Figure 8.1 e)**. Finally the system shown in **Figure 8.1 g)** has the same APS-flashcoat as the system shown in **Figure 8.1 f)**, however this flashcoat has been additionally aluminized using a slurry coating method.

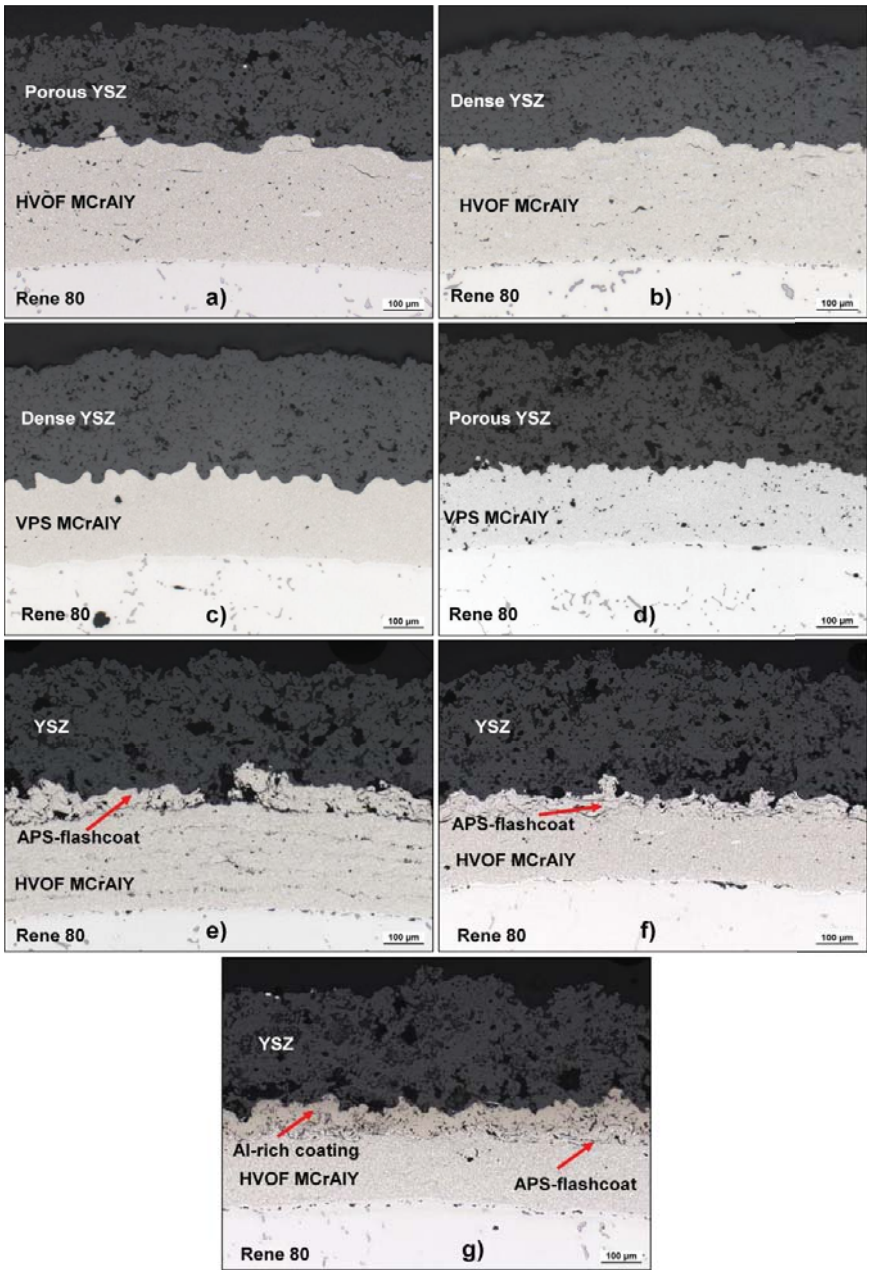

Figure 8.1 Metallographic images of the cross sections of TBC systems in as-sprayed conditions: a) HVOF BC + porous YSZ, b) HVOF BC + dense YSZ, c) VPS BC + dense YSZ, d) VPS BC + porous YSZ, e) APS-flashcoat spraying parameters set I, f) APS-flashcoat spraying parameters set II and g) overaluminized APS-flashcoat

8.2 Accelerated cyclic oxidation tests at 1120°C

8.2.1 Lifetime data

The TBC-systems described in **section 8.1** were tested in accelerated cyclic oxidation at 1120°C in laboratory air. **Figure 8.2** shows lifetimes obtained for the various TBC systems. It is visible that the TBC systems with increased bondcoat roughness by applying an APS-flashcoat showed the longest lifetime i.e. by a factor of up to 3 compared to the other coating systems. An exception is the system with APS-flashcoat sprayed with parameter set I.

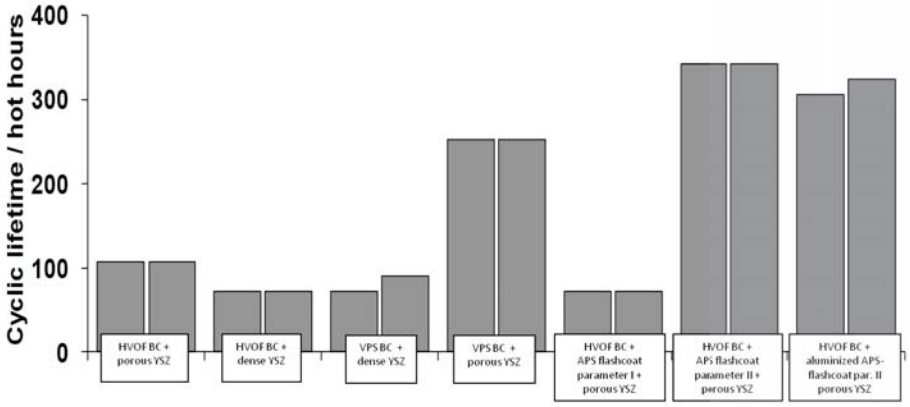

Figure 8.2 Lifetime barchart of TBC systems obtained during accelerated cyclic oxidation testing at 1120°C in laboratory air

8.2.2 Microstructural characterisation of TBC systems after failure

Figures 8.3 and 8.4 show cross sections of the TBC systems with the HVOF and VPS bondcoats after failure. In systems with HVOF bondcoat crack propagation occurs near the topcoat/bondcoat interface (**Figure 8.3 a)** and **b)**). For those systems also a slightly more pronounced pore formation at the bondcoat/base alloy interface is observed than for the system with VPS bondcoat and dense topcoat. For the system with VPS bondcoat and dense topcoat cracks are visible on the top of the convex bondcoat areas and they propagate through the dense topcoat above the concave areas. Finally, in the system with VPS bondcoat and porous YSZ topcoat cracks in some places propagate at the topcoat/bondcoat interface and in some places through the topcoat. Comparing the bondcoat/base alloy interfaces reveals for systems shown in **Figure 8.1 c)** and **d)** substantially porosity for the system with the porous topcoat (**Figure 8.1 d)**). For the systems with increased bondcoat roughness obtained by applying an APS-flashcoat the cracks tend to propagate through the YSZ topcoat. The system with the APS-flashcoat applied with spraying parameter set I showed a smaller amount of pores at the bondcoat/base alloy interface. It should however be mentioned that the lifetime of this coating is only 72 hours while for the systems with an APS-flashcoat it is more than 300 hours (**Figure 8.2**). Also formation of voluminous spinel oxide was found at the bondcoat surface in the TBC system with APS-flashcoat applied with spraying parameter set I (**Figure 8.4 e)**).

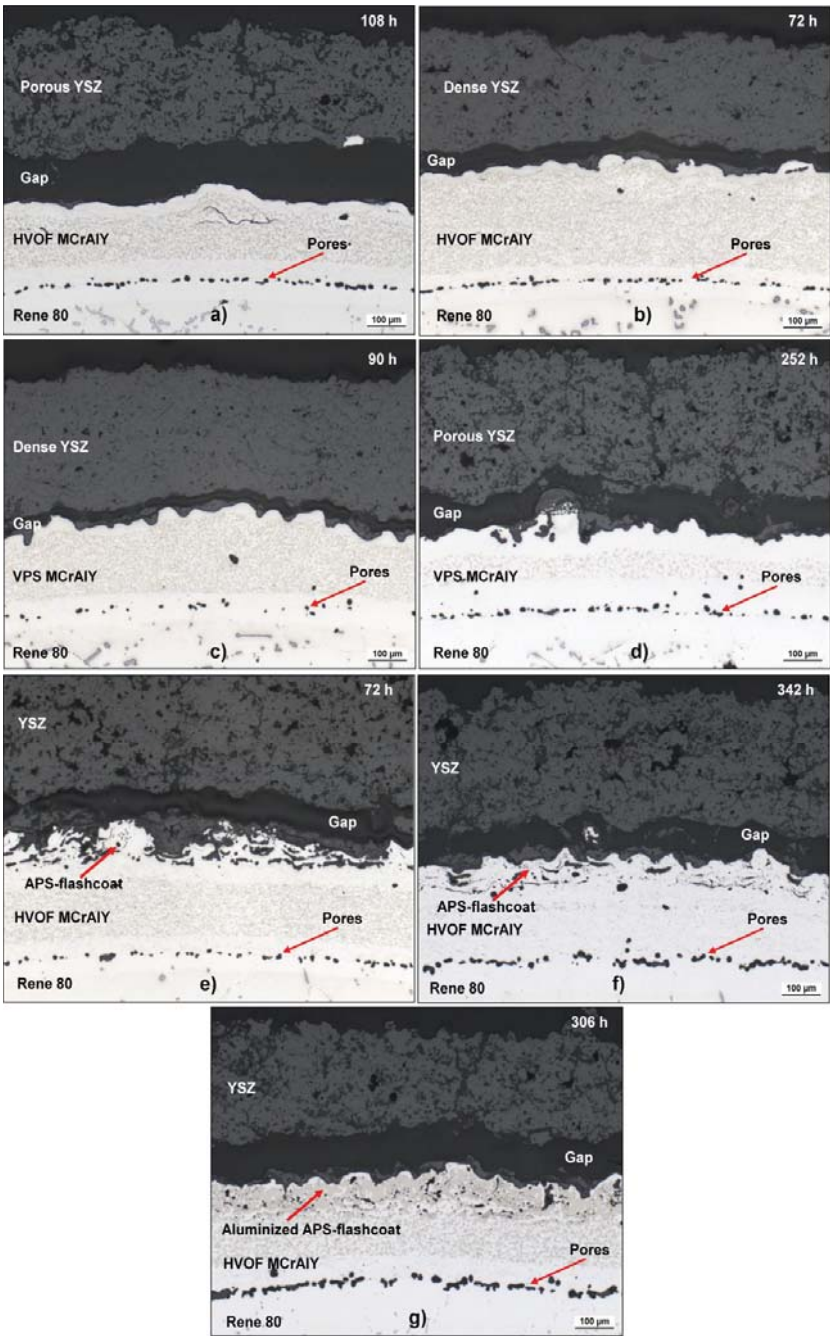

Figure 8.3 Metallographic cross sections of the TBC systems after oxidation till TBC failure in accelerated cyclic oxidation testing at 1120°C: a) HVOF BC + porous YSZ, b) HVOF BC + dense YSZ, c) VPS BC + dense YSZ, d) VPS BC + porous YSZ, e) APS-flashcoat spraying parameters set I, f) APS-flashcoat spraying parameters set II and g) overaluminized APS-flashcoat

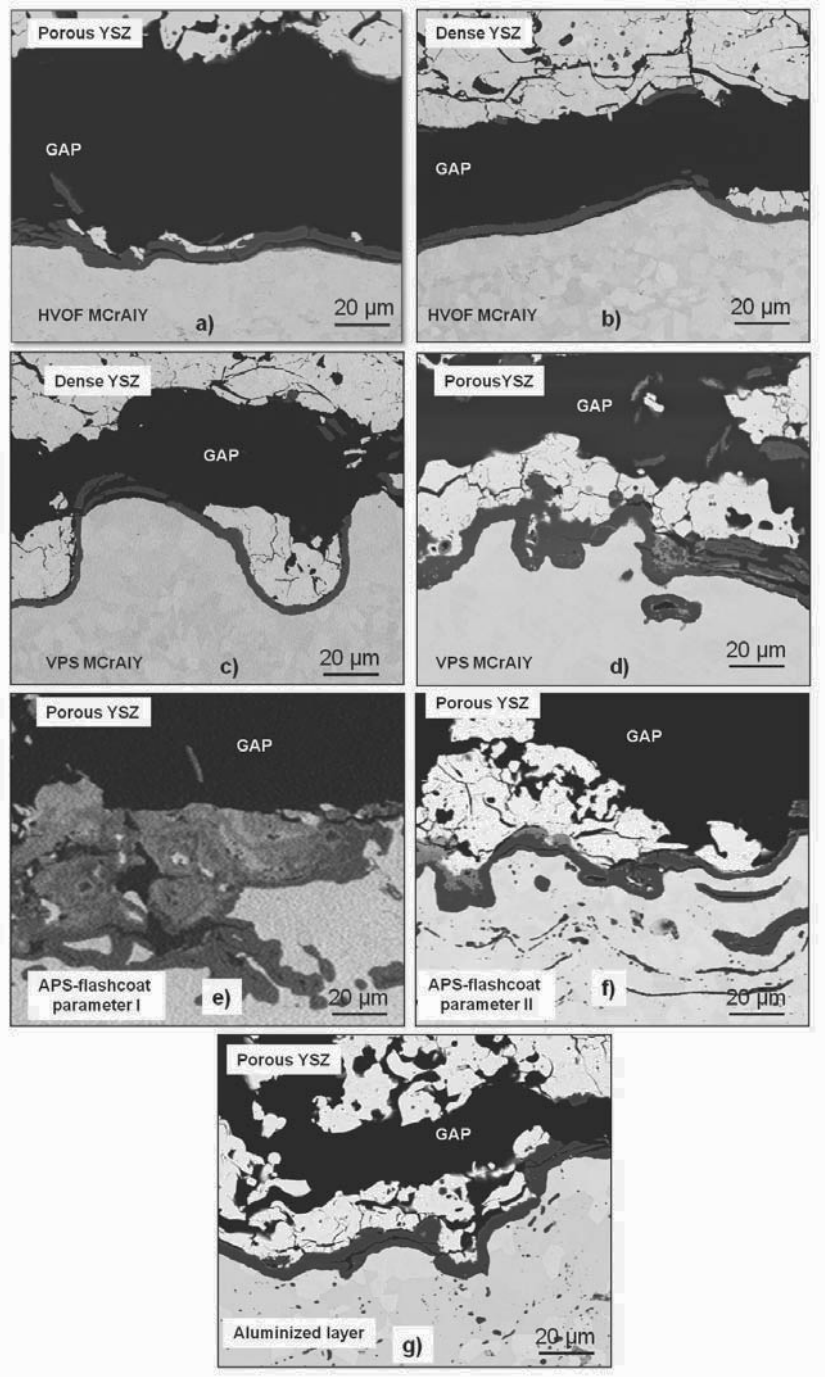

Figure 8.4 Cross section images (SEM) of the TBC systems after cyclic oxidation testing at 1120°C till TBC failure in accelerated test: a) HVOF BC + porous YSZ, b) HVOF BC + dense YSZ, c) VPS BC + dense YSZ, d) VPS BC + porous YSZ, e) APS-flashcoat spraying parameters set I, f) APS-flashcoat spraying parameters set II and g) overaluminized APS-flashcoat

8.2.3 Discussion of results obtained in accelerated cyclic oxidation testing

A comparison of the results obtained during cyclic oxidation tests at 1120°C indicate that the lifetime of the APS-TBC systems is mainly determined by two factors: topcoat porosity and bondcoat roughness profiles. The systems which have relatively flat bondcoats showed short lifetimes, independent of topcoat porosities (**Figures 8.3** and **8.4 a)** and **b)**).

The lifetime of APS-TBC systems with a higher bondcoat roughness profile strongly depends on topcoat porosity (comparison of **Figures 8.2**, and **8.3, 8.4 c)** and **d)**). In previous studies it was shown that topcoat porosity can hinder crack propagation by a crack tip blunting mechanism [129]. **Figure 8.5** schematically shows the crack propagation path in dense and porous ceramics. It is claimed [129] that the ratio between the stress intensity factors for a blunt and a sharp crack tip can be described by equation:

$$\frac{K_{IC,blunt}}{K_{IC}} = \left(1 + \frac{\sigma_0}{2r_0}\right)^{1/2} \quad (8.1)$$

where:

r_0 – characteristic zone at the crack tip considered to calculate average stress,

K_{IC}, $K_{IC,blunt}$ - is the toughness for the sharp and blunt crack tip respectively.

σ_0 - is the critical stress

The relationship in equation **(8.1)** is depicted in **Figure 8.6** which shows that crack tip blunting effectively increases the fracture toughness of the porous ceramic, to an extent depending on the pore morphology: the larger the pore size at the crack front, the higher the fracture toughness of the porous ceramic relative to its fracture strength [129].

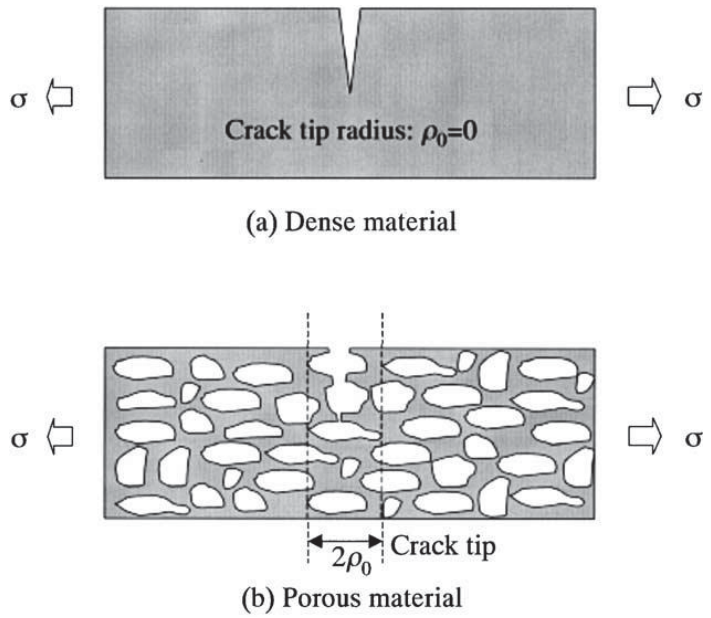

Figure 8.5 Schematic representation of a crack propagated in (a) a dense ceramic material and (b) a porous ceramic material, showing a sharp crack-tip in the dense material and a blunt crack-tip in the porous material (reproduced from Reference [129]).

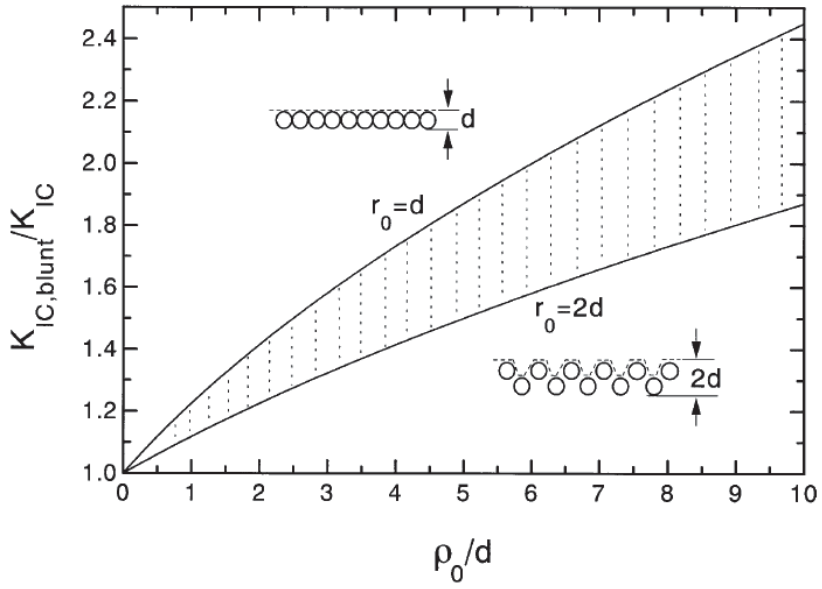

Figure 8.6 Relationship between the toughness ratio of a blunt crack to a sharp crack and the ratio of the blunt crack-tip radius to the effective grain width, where the hatched region

represents the results for different characteristic zone size. The dashed lines in the insets are the crack front of different grain arrangements (reproduced from Reference [129]).

The results obtained for the TBC systems in **Figure 8.4 e, f, g** indicate that the lifetime of APS-TBC systems with porous topcoats can be increased by further optimization of the bondcoat roughness profile, e.g. by applying an APS-flashcoat on top of the HVOF bondcoat. Apart from longer lifetime, the systems with HVOF bondcoat and APS-flashcoat would have an advantage of lower production costs than APS-TBC systems using VPS bondcoats.

However, the results in **Figure 8.4** also show that lifetime of the systems with APS-flashcoats is strongly affected by APS-flashcoat spraying parameters (compare lifetime obtained for advanced systems with APS-flashcoat sprayed with parameter set I and II, **Figures 8.3 e), f)** and **8.4 e) f)**) respectively. The quality of the applied APS-flashcoats appeared to be highly dependent on the spraying parameters. In **Figure 8.1 e)** the microstructure of the TBC system with APS-flashcoat applied with spraying parameters set I is shown. The microstructure of the TBC system with APS-flashcoat applied using spray parameter set I indicates that apparently not all MCrAlY powder particles were completely molten during spraying. Therefore the APS-flashcoat layer is not continuous and the adherence of larger powder particles to the HVOF base coating is poor. This microstructure leads to extensive local spinel formation upon cyclic exposure at 1120°C (**Figure 8.4 e)**). During exposure because of poor contact between such particles and the base HVOF bondcoat oxidation occurs at the HVOF/Flashcoat interface. Thereby, the flashcoat particles become effectively separated from the base HVOF coating. Each of the separated particles has as a relatively small aluminium reservoir and after depletion of this reservoir [92], no Al-supply from the underlaying HVOF coating is possible. Consequently, other elements like Cr, Ni, Co start to be oxidized. Nickel and cobalt based oxides (spinels, such as $NiCr_2O_4$, $CoCr_2O_4$) have a substantially higher growth rate than Al_2O_3 [130] and also relatively large Pilling-Bedtworth Ratios (PBR, which is the volume ratio of the formed oxide to the metal consumed). Therefore, oxidation of flashcoat particles leads to a large volume increase, which in turn

results in local stress generation leading to crack initiation, propagation and finally to the macroscopic failure of the topcoat. Formation of voluminous spinels is visible in **Figure 8.4 e)**. A similar observation was made with respect to the effect of bondcoat microstructure (porosity) on the lifetime of APS-TBC systems in reference [92]. The hindered Al supply within the bondcoat by formation of Al_2O_3 at intersplat boundaries of an APS bondcoat was in [92] called "the diffusion cell effect".

In contrast, when the APS-flashcoat was applied using the set of spraying parameter II, the lifetime of the APS TBC system significantly increased compared to the systems with HVOF or VPS bondcoats, apparently due to an improved bondcoat roughness profile. For the latter system, spinel formation can be also observed, locally however the amount of spinels is far less pronounced compared to the system with APS-flashcoat sprayed with parameter set I (compare **Figure 8.4 e)** and **f)**).

8.2.4 Parameters determining APS TBC's lifetime

As mentioned above, the lifetime of APS TBC systems is mainly determined by two factors: topcoat porosity and bondcoat roughness profile.

There are several methods which in an unambiguous way describe topcoat porosity, e.g. mercury porosimetry, X-ray tomography or two dimensional cross-sections evaluation. These methods are commonly used to determine topcoats porosity [131, 132, 133].

8.2.5 Standard methods for bondcoats roughness evaluation

Bondcoat roughness is commonly described by R_a and R_y values [134] as well as by tortuosity. These parameters are derived from bondcoat roughness profile measurements using a profilometer. **Figure 8.7** shows a description of R_a and R_y values for roughness evaluation of surface. **Figure 8.8** shows the methodology for tortuosity calculation. **Figure 8.9** shows bondcoats for which values describing surface roughness were evaluated in the present studies. **Table 8.2** shows the values of R_a and R_y and tortuosity as well as lifetimes obtained for the studied TBC systems with bondcoats deposited by HVOF, VPS and APS-flashcoat parameter set II, respectively.

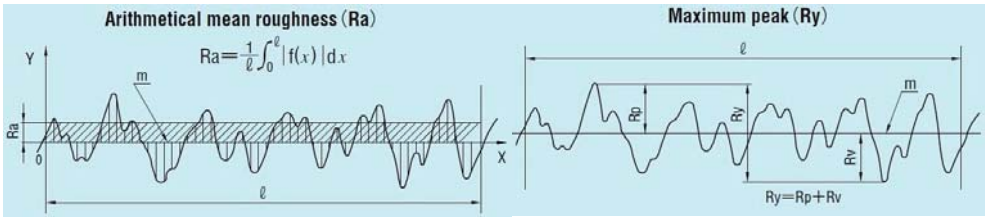

Figure 8.7 Procedure of R_a and R_y calculation

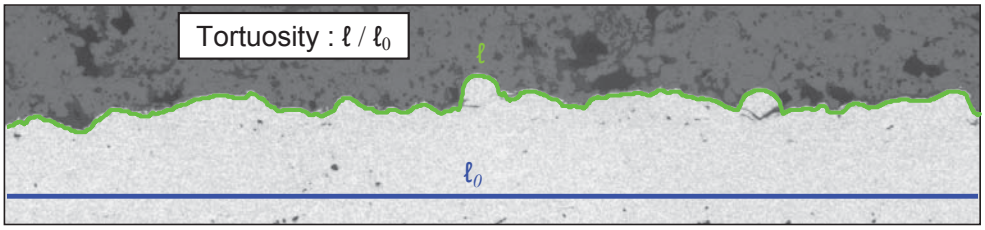

Figure 8.8 Procedure of tortuosity calculation

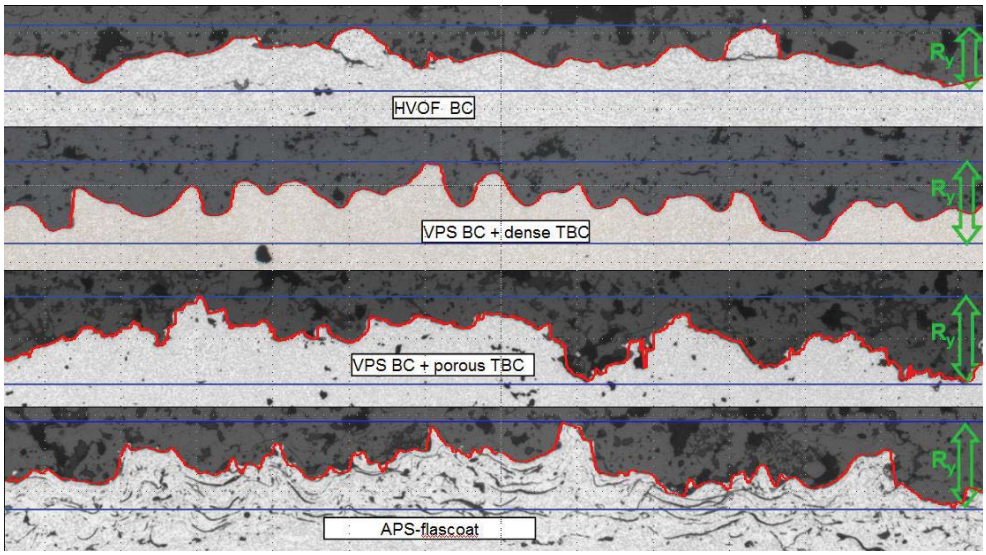

Figure 8.9 Bondcoat types evaluated in the present studies

Table 8.2 The measured roughness parameter values of different bondcoats compared with measured lifetimes of APS TBC systems

TBC type	HVOF BC + porous TBC	VPS BC + dense TBC	VPS BC + porous TBC	APS-flashcoat + porous TBC
R_a	11.3	13.4	12.9	13.2
R_y	65	85	91	90
ℓ / ℓ_0	1.2	1.3	1.3	1.4
Lifetime at 1120°C	108	72	252	344

The results show that the roughness description values commonly used for roughness characterization do not differ dramatically for the evaluated TBC systems. The obtained R_a, R_y values and the tortuosities for all studied systems are quite similar for TBC systems with VPS bondcoats (both: wit dense and porous TBC) and with APS flashcoat. Only the system with HVOF bondcoat showed a slightly lower R_a and R_y as well as tortuosity value than the other studied systems. Therefore, no direct correlation exist between roughness described by the commonly used methods and the lifetimes obtained for TBC systems with the various bondcoats types.

8.2.6 Results of bondcoat roughness evaluation using fractal analysis

The results presented in the previous chapter clearly showed that the conventional description of bondcoats roughness profiles using R_a and R_y does not allow a straightforward correlation with the cyclic oxidation lifetimes of the studied TBC systems. Therefore, another method is needed for bondcoat roughness profile evaluation. In the frame of the present work the suitability of fractal analysis for bondcoat roughness characterization was estimated.

The results of bondcoat roughness profiles evaluation obtained by using fractal analysis are summarized in **Table 8.2. Figure 8.10** shows the measured values for the relative length (L_R) as a function of scale (r) for the four studied bondcoat types.

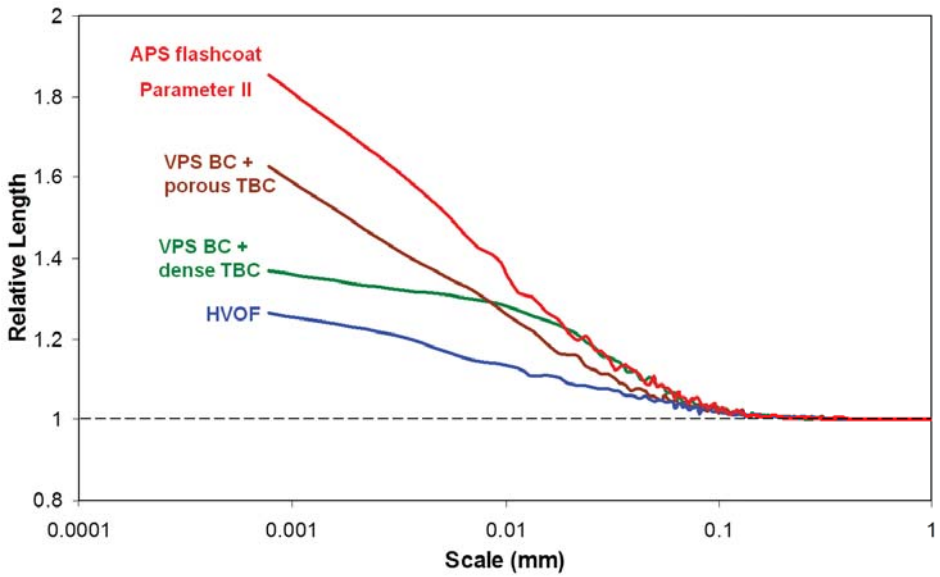

Figure 8.10 Relative length as a function of scale length obtained for evaluated types of TBC systems

Table 8.2 Characteristic parameters obtained during fractal analysis of bondcoat surfaces for studied TBC systems

	HVOF	VPS BC + dense topcoat	VPS BC + porous topcoat	APS-flashcoat Parameter II
Fractal dimension D	1.05	1.13	1.14	1.31
Length scale fractal complexity, LSFC	53	127	141	310
Smooth-Rough Crossover, SRC (µm)	130	110	70	40
Relative length at 20 µm	1.09	1.22	1.16	1.20
Relative length at 10 µm	1.13	1.29	1.28	1.41
Relative length at 5 µm	1.17	1.30	1.36	1.61
TBC lifetime at 1120°C (hot hours)	108	72	252	344

8.2.7 Discussion of results obtained by fractal analysis

The evaluation of the different bondcoat roughness profiles in **Figure 8.10** allows differentiation not only between the relatively flat HVOF and rough plasma sprayed bondcoats (as it was the case for standard R_a and R_y values described in **chapter 8.2.5**) but also between the two plasma sprayed bondcoat types. The relative length – scale plots in **Figure 8.10** for the VPS bondcoats are clearly different from that for the APS-flashcoat. Also differences between the two VPS bondcoats can be observed: the system with the dense topcoat showed lower L_R values for scales at 5 µm compared to the system with porous topcoat. The latter observation indicates, that the bondcoat in the system with porous topcoat possess a higher "microroughness".

Although further studies are definitely required to establish a quantitative correlation between the parameters, such as *D*, *SRC*, *LSFC* and TBC-lifetime for various bondcoat roughness profiles in the present work shows a clear trend the TBC-lifetime dependence on the bondcoat morphology characterized by fractal analysis.

8.2.8 Proposed failure mechanisms

Based on the cross-sections in the as-sprayed conditions (**Figure 8.1**) as well as after failure (**Figures 8.3** and **8.4**) and the results obtained by roughness evaluation using fractal analysis (**section 8.2.6.1**) the following failure mechanisms occurring during cyclic oxidation, are proposed in **Figure 8.11**. Stage I represents the situation when the TBC systems forms a TGO during high temperature exposure, however no substantial cracking has occurred yet. Stage II describes the moment of crack nucleation. The preferential crack nucleation sites are the convex bondcoat regions, where out of plane tensile stresses at the TGO/bondcoat interface are generated upon cooling due to CTE mismatch between the bondcoat and the TGO [68]. Stage III shows the situation during crack propagation.

For the TBC system with the HVOF bondcoat, cracks nucleated at the TGO/bondcoat interface propagate relatively fast along the flat topcoat/bondcoat interface (**Figure 8.11 a)**). Thereby, the failure mechanism of the studied APS TBC system with HVOF bondcoat is similar to that observed for EB-PVD TBC systems [135]. In systems with VPS bondcoat and dense topcoat the crack propagation mechanism is fundamentally different. Cracks start to form on top of the convex bondcoat sites and, because of the dense topcoat, they propagate relatively fast within the topcoat. As visible in **Figure 8.11 b)** propagation of cracks within the topcoat and above the concave regions of bondcoats leads to easy crack linking, and

therefore relatively early macroscopic TBC failure. For the TBC systems with the VPS bondcoats and the HVOF+APS-flashcoat sprayed with parameter set II, the cracking mechanism is different from that of the HVOF bondcoat due to the differences in bondcoat roughness. This is because in case of the first mentioned coating the cracks need to propagate through the porous, tough ceramic topcoat above the concave bondcoat regions. It was shown by Chang et al. [91], Freborg et al. [136] and Arens et al. [137] that initially in these topcoat areas a compressive out of plane stress prevails, which hinders the crack propagation. In addition, topcoat porosity can hinder the crack propagation by a crack tip blunting mechanism [129].

The fact that first delamination of the TGO from the convex bondcoat areas does not necessarily lead to rapid TBC-failure of the systems with plasma sprayed bondcoats can be derived from detailed examination of the TGO-morphologies, (**Figure 8.12**) which show the so-called "repeated cracking" phenomenon [81]. During oxidation the TGO grows, thickens and after reaching a critical thickness a local delamination occurs in the convex sites of the bondcoat during cooling between the TGO and bondcoat. These initial cracks, however, cannot link together because of a compressive stress [91], above the bondcoat concave areas, as described above. After delamination, oxygen gets access to the bondcoat below the delamination during continued exposure, and a new layer of the TGO forms on the bondcoat surface. After the second TGO layer reaches a critical thickness, a delamination at the TGO/bondcoat interface occurs again. This process repeats several times thereby effectively shifting the crack propagation closer to the bondcoat/topcoat interface. At some point the increased TGO-thickness in the concave areas of the bondcoat leads to stress conversion from compressive into tensile [91, 136, 137], which promotes crack linking finally leading to macroscopic topcoat failure.

Considering the above discussion of the crack initiation and growth on rough bondcoat surfaces it is likely that in the system with APS-flashcoat much more sites for cracks nucleation are available due to the higher "microroughness" (**Figure 8.11 d)**). The multiple crack initiation at different heights of the bondcoat surface profile leads to local stress relaxation resulting in an extended TBC lifetime. Further studies are required to verify this assumption by following the crack growth in the studied TBC systems as a function of exposure time, prior to failure.

In addition to roughness increase by applying of APS-flashcoat, another factor can play a role in extending the lifetime of the TBC systems with APS-flashcoat. It is visible in the cross section in **Figure 8.1 f)**, that APS-flashcoat contains intersplat porosity, which during exposure became oxidized (**Figure 8.3 f)**). This might provide a "composite" layer with an intermediate CTE between the CTE for metallic bondcoat and ceramic topcoat. This can reduce the stress in the topcoat during cooling, which in turn reduce the driving force for crack propagation. Studies by Ajdelsztajn et al. [138], claimed greatly improved lifetime for the TBC systems with cryomilled NiCrAlY bondcoat compared to the TBC systems with conventional NiCrAlY bondcoat, which was attributed to a reduction in bondcoat CTE and/or increased mechanical strength.

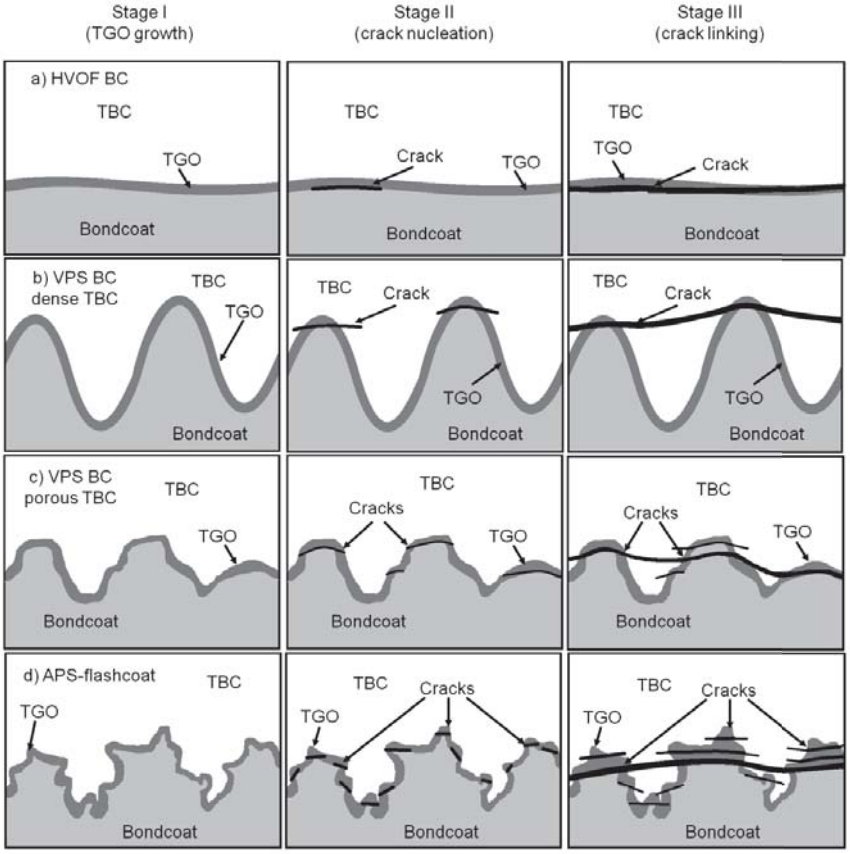

Figure 8.11 Proposed cracking mechanisms for TBC systems with: a) HVOF bondcoat, b) VPS bondcoat with dense TBC and c) VPS bondcoat with porous TBC, d) APS-flashcoat spraying parameter set II

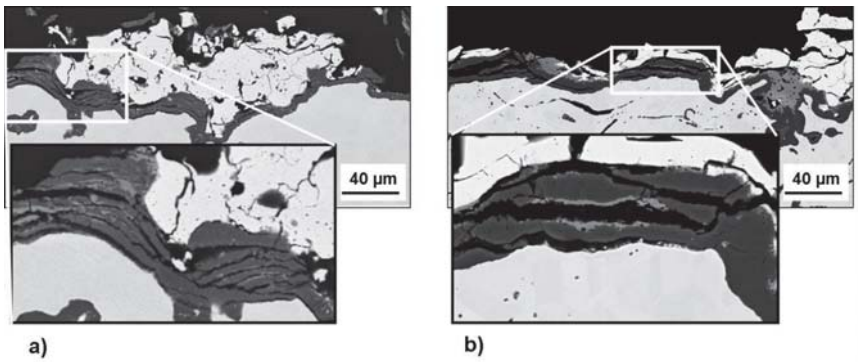

Figure 8.12 Cross sections images (SEM) showing examples of repeated cracking of TGO for TBC systems with: a) VPS bondcoat and porous TBC b) HVOF+APS-flashcoat sprayed with parameter set II after discontinuous oxidation at 1050°C till failure.

8.3 Lifetime oxidation tests at 1050°C in dry and wet atmospheres

8.3.1 Lifetime results

The results of accelerated test at 1120°C showed better lifetimes for advanced TBC systems. Extension of lifetime was correlated with improvement of the bondcoat roughness profile by applying an APS-flashcoat. It was illustrated that the quality of the APS-flashcoat strongly depends on the used spraying parameters. Additionally intersplat porosity within the flashcoat has been found in the cross sections of the TBC systems with APS-flashcoats. Considering all these facts and the envisaged application of the tested APS TBC systems (material will be used in gas turbines using hydrogen rich syngas) tests at 1050°C in dry air and air with 20%H_2O were performed to investigate the effect of water vapour on the lifetime and oxidation behaviour of the TBC systems. **Figures 8.13** and **8.14** show the lifetimes obtained for APS-TBC systems in synthetic air and synthetic air + 20% H_2O respectively. The test results showed that water vapour shortened the lifetime of some of the TBC systems. The results show that in both atmospheres the lifetime of TBC systems with APS-flashcoat applied on top of a HVOF bondcoat was longer than the other coating systems. In two systems exposed in dry air (with APS-flashcoat, sprayed with parameter set II and with aluminized layer) one specimen of each system was removed for microstructure investigation before actual macroscopic failure of the TBC.

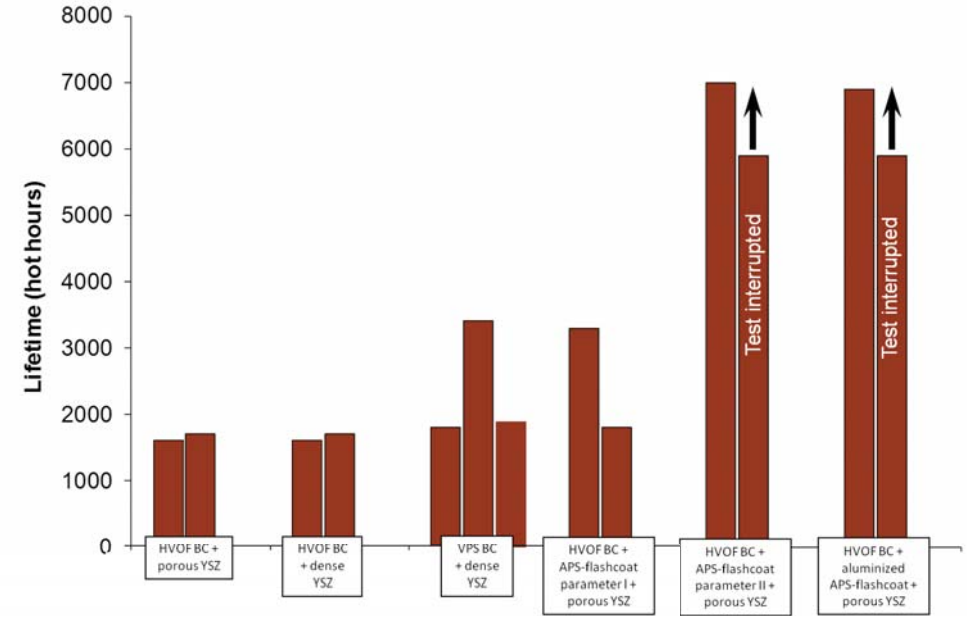

Figure 8.13 Lifetimes of different TBC systems obtained during discontinuous oxidation at 1050°C in synthetic air. Bar marked with an arrow represents specimens which were removed from the test at the given times prior to macroscopically visible TBC failure for microstructure characterisation.

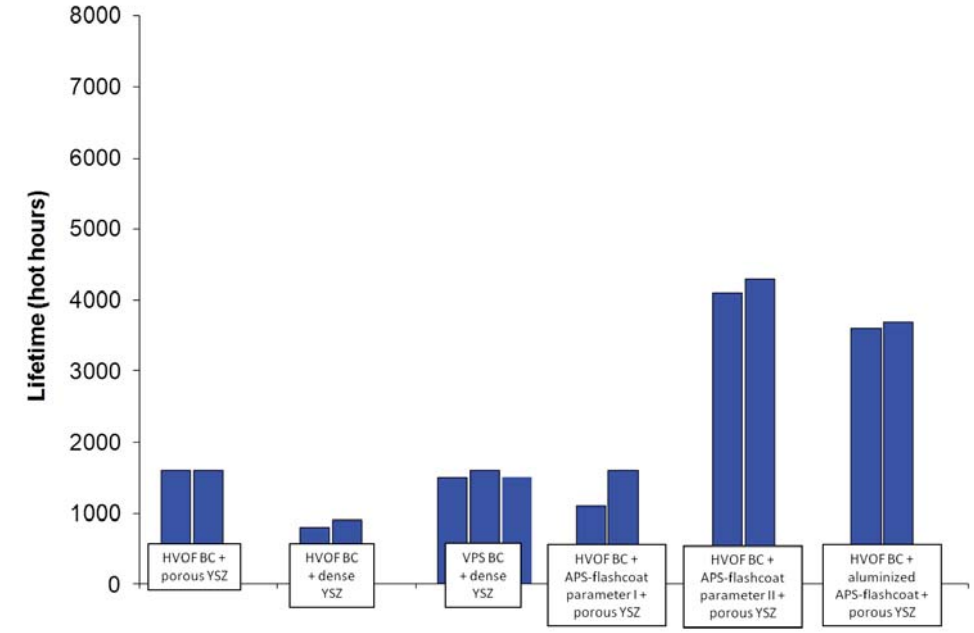

Figure 8.14 Lifetimes of different TBC systems obtained during discontinuous oxidation at 1050°C in synthetic air + 20% H_2O

8.3.2 Microstructural characterisation

Figures 8.15 and **8.16** show the SEM cross-sections of the tested APS-TBC systems after 100 hours discontinuous exposure i.e., prior to failures at 1050°C in the two test atmospheres. It can be seen that the TGO formed on bondcoats in wet air is in average thinner or has about the same thickness compared to that formed in the dry gas (**Figures 8.17** and **8.18**).

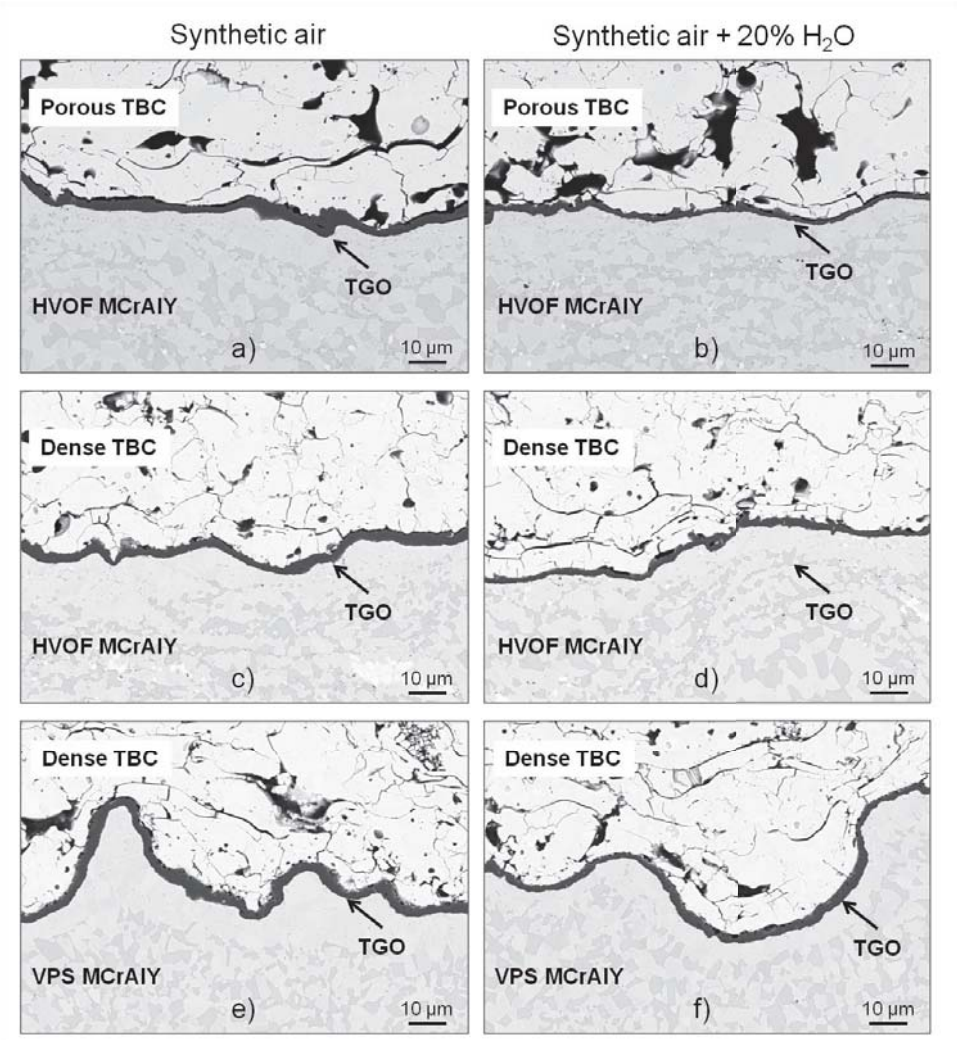

Figure 8.15 Overview cross sections images (SEM) of APS TBC systems with: HVOF bondcoat + porous TBC (a and b), HVOF bondcoat + dense TBC (c and d) and VPS bondcoat + dense TBC (e and f), after discontinuous exposure at 1050°C in: dry synthetic air a), c), e) and synthetic air + 20%H_2O b), d), f) for 100 hours

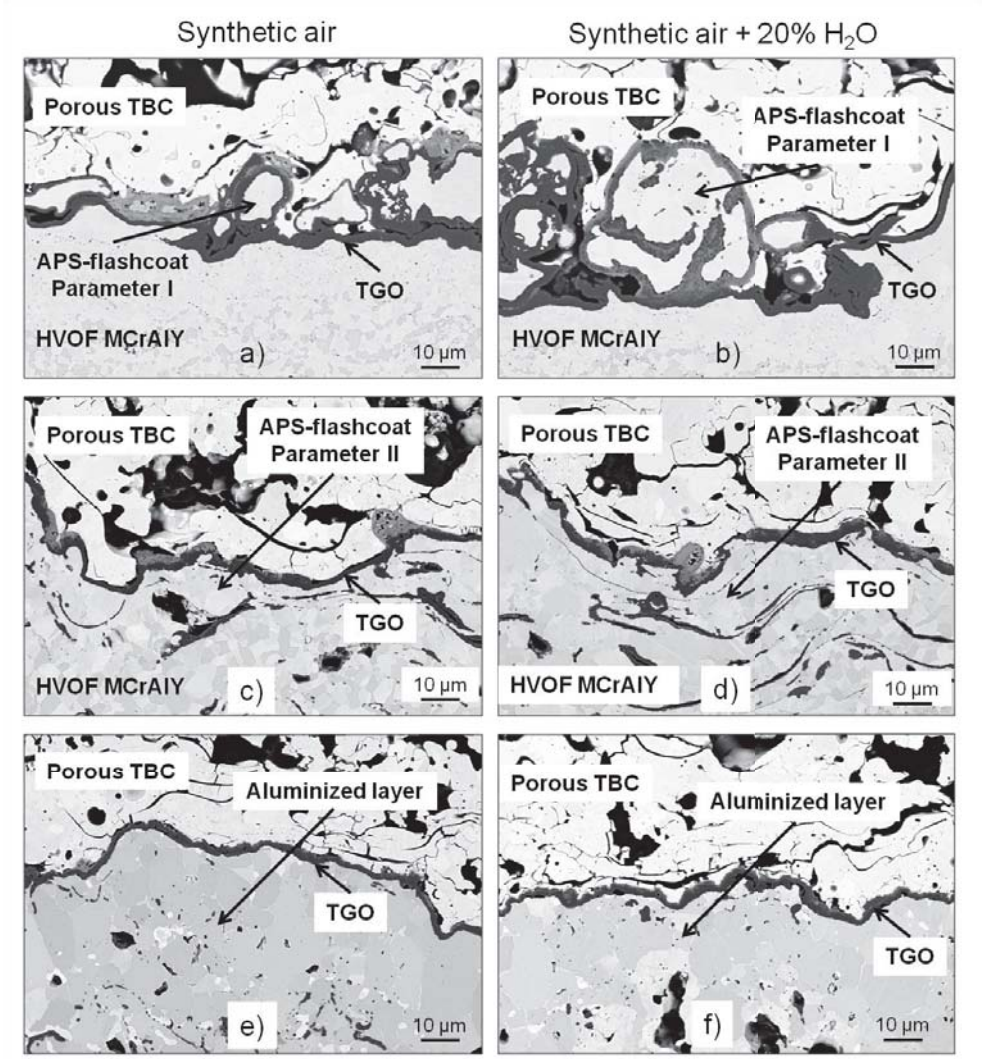

Figure 8.16 Overview cross sections images (SEM) of APS TBC systems with: HVOF BC + APS-flashcoat parameter set I + porous TBC (a and b), HVOF BC + APS-flashcoat parameter set II + porous TBC (c and d) and HVOF BC + aluminized APS-flashcoat + porous TBC (e and f), after discontinuous exposure at 1050°C in: dry synthetic air a), c), e) and synthetic air + 20%H_2O b), d), f) for 100 hours

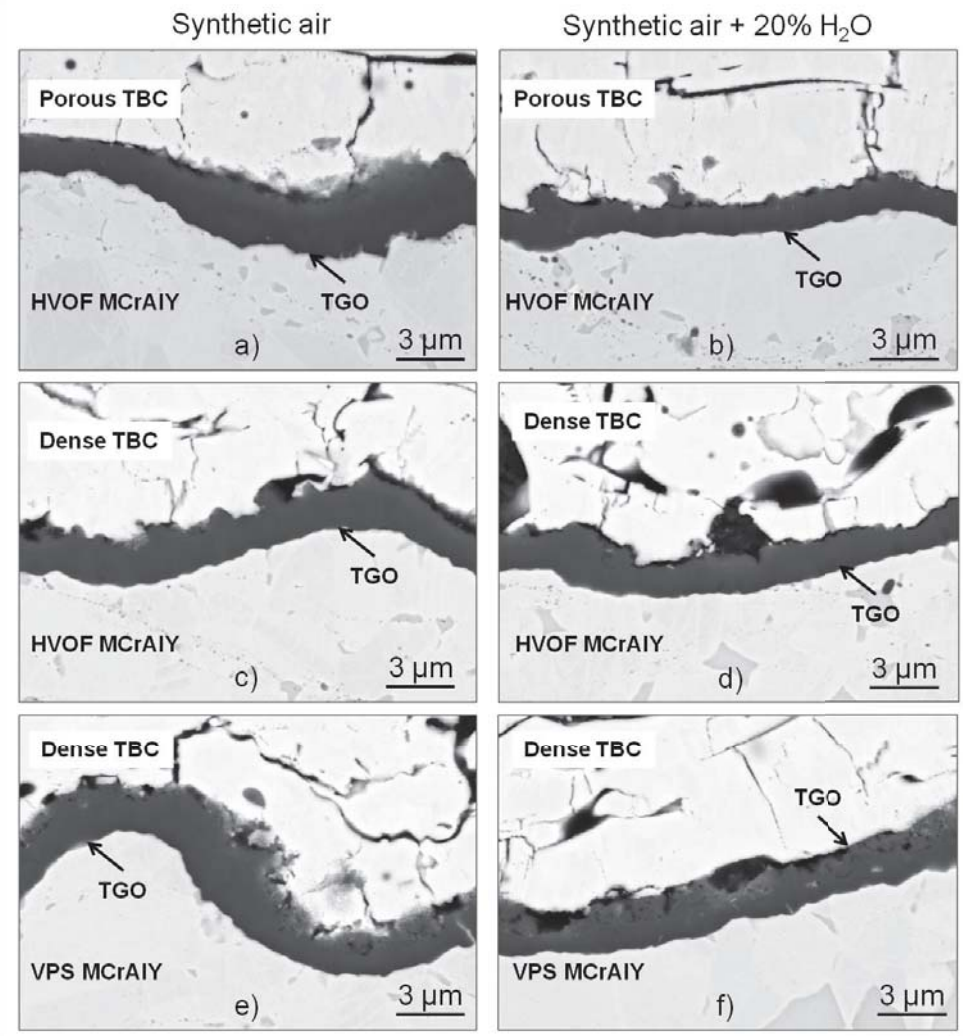

Figure 8.17 High magnification (SEM images) for cross sections of APS TBC systems with: HVOF bondcoat + porous TBC (a and b), HVOF bondcoat + dense TBC (c and d) and VPS bondcoat + dense TBC (e and f), after discontinuous exposure at 1050°C in dry synthetic air a), c), e) and synthetic air + 20%H_2O b), d), f) for 100 hours

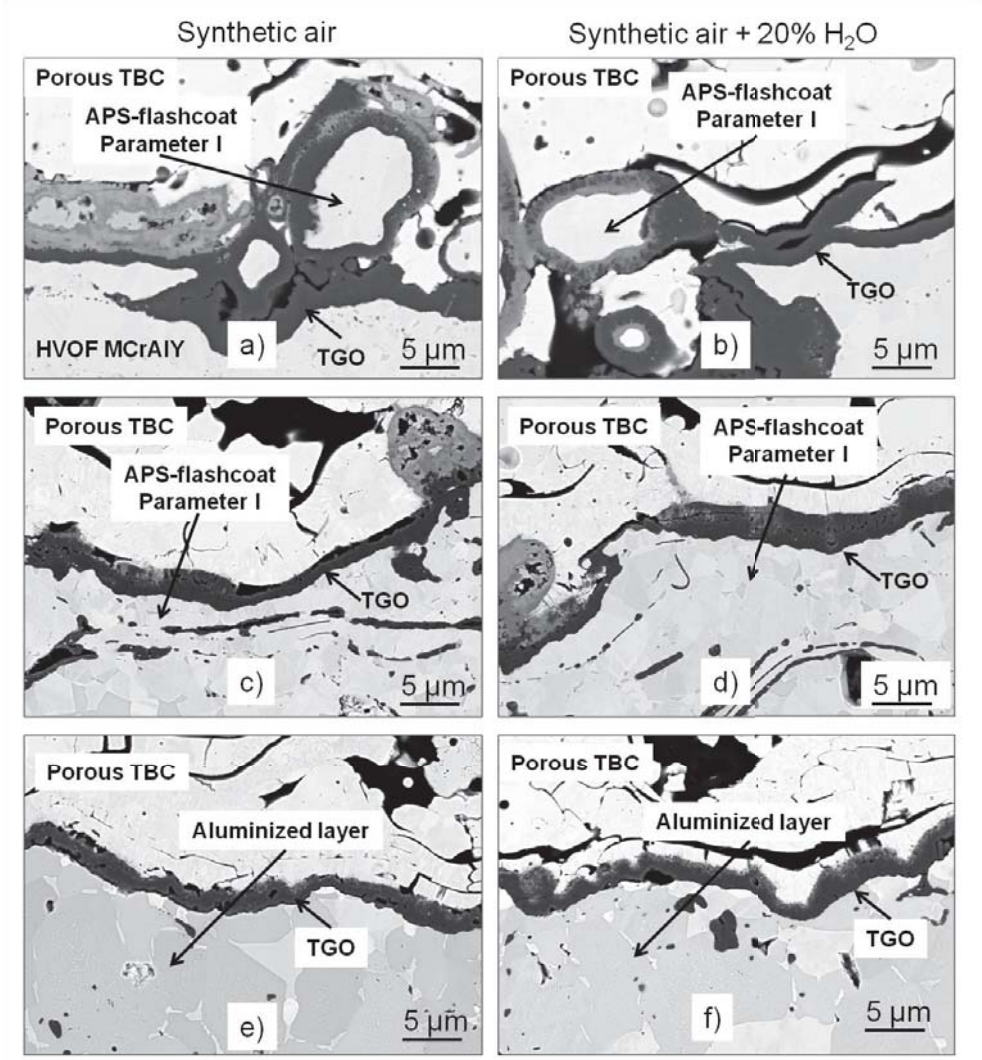

Figure 8.18 High magnification (SEM images) for cross-sections of APS TBC systems with: HVOF BC + APS-flashcoat parameter set I + porous TBC (a and b), HVOF BC + APS-flashcoat parameter set II + porous TBC (c and d) and HVOF BC + aluminized APS-flashcoat + porous TBC (e and f), after discontinuous exposure at 1050°C in: dry synthetic air a), c), e) and synthetic air + 20%H_2O b), d), f) for 100 hours

Figures 8.19 and **8.20** show metallographic cross sections of the various APS TBC systems after TBC failure obtained during discontinuous oxidation at 1050°C in synthetic air and synthetic air + 20% H_2O comparing TBC systems with HVOF and VPS bondcoats and TBC

systems with HVOF + APS-flashcoat (with and without aluminizing layer) systems. The cross sections show that the TBC systems failed according to the mechanisms proposed in **chapter 8.2.7**. Based on **Figures 8.21** and **8.22** showing SEM-BSE cross sections of the tested APS-TBC systems one can observe similar thickness of TGO formed in dry and wet atmospheres. Only the system with VPS bondcoat seems to form a slightly thicker TGO in the wet than in the dry gas (**Figure 8.21 e)** and **f)**). However it needs to be emphasized that comparison of the exact TGO thickness after failure is difficult, because the formed TGO is cracked and in many places no longer attached to the bondcoat.

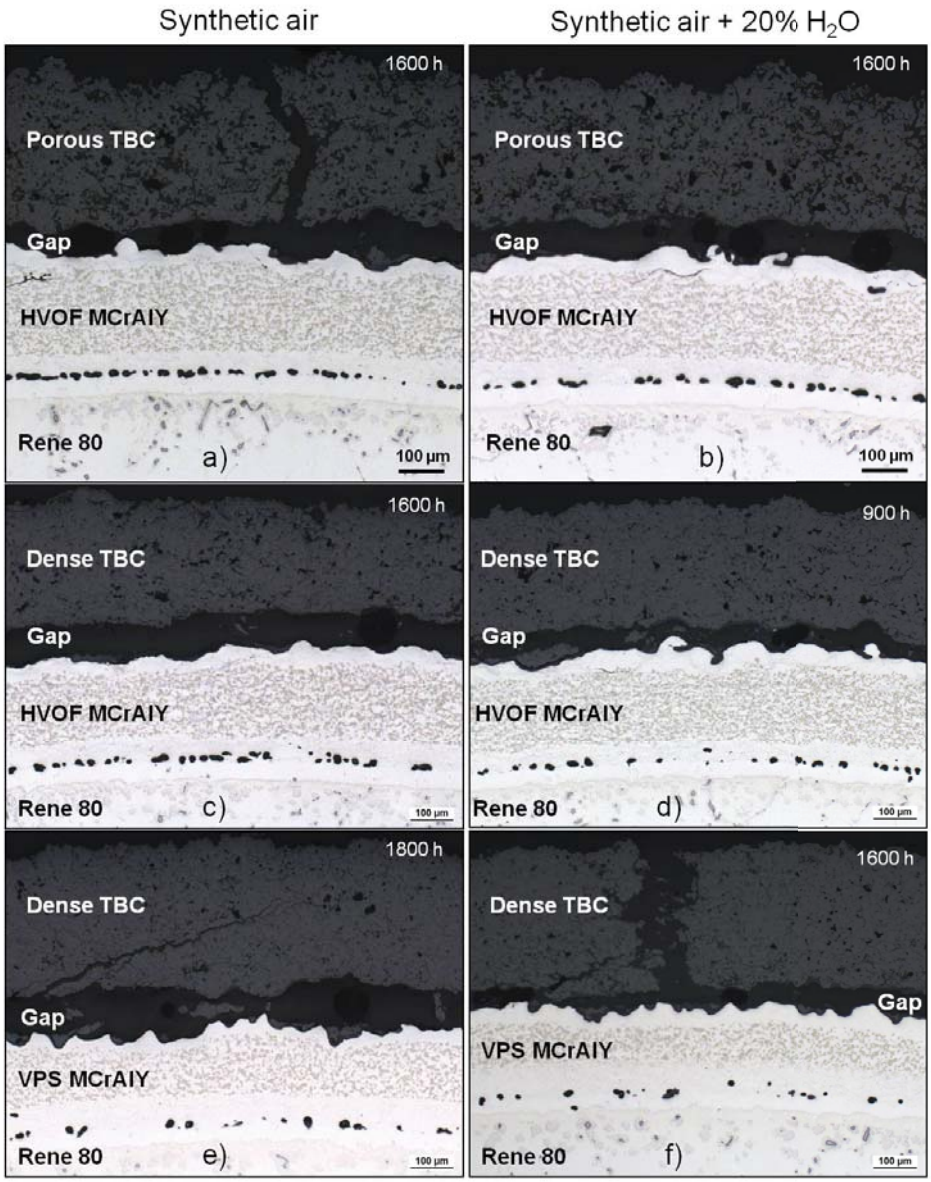

Figure 8.19 Metallographic cross sections of APS TBC systems with: HVOF bondcoat + porous TBC (a and b), HVOF bondcoat + dense TBC (c and d) and VPS bondcoat + dense TBC (e and f), after discontinuous exposure at 1050°C in: dry synthetic air a), c), e) and synthetic air + 20%H_2O b), d), f) till TBC failure

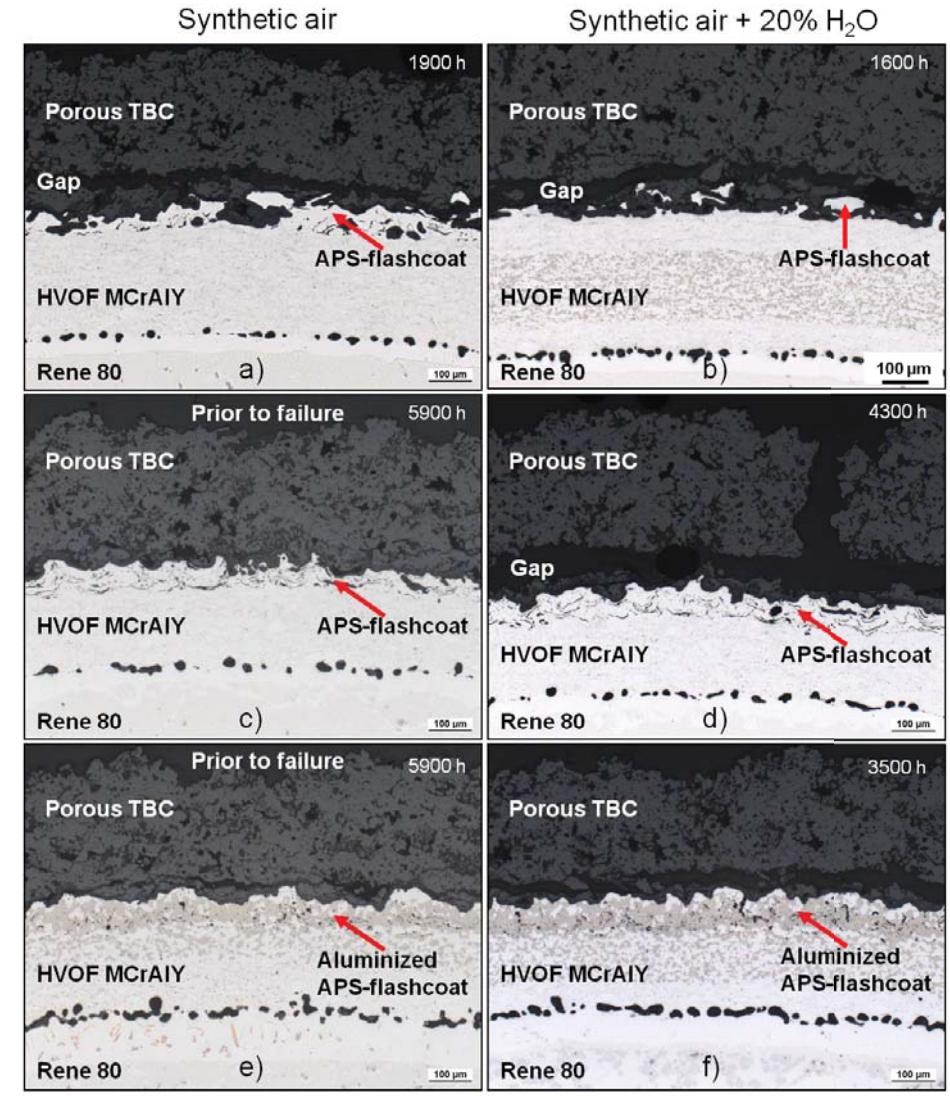

Figure 8.20 Metallographic cross-sections of APS TBC systems with: HVOF BC + APS-flashcoat parameter set I + porous TBC (a and b), HVOF BC + APS-flashcoat parameter set II + porous TBC (c and d) and HVOF BC + aluminized APS-flashcoat + porous TBC (e and f), after discontinuous exposure at 1050°C in: dry synthetic air a), c), e) and synthetic air + 20%H_2O b), d), f) till TBC failure

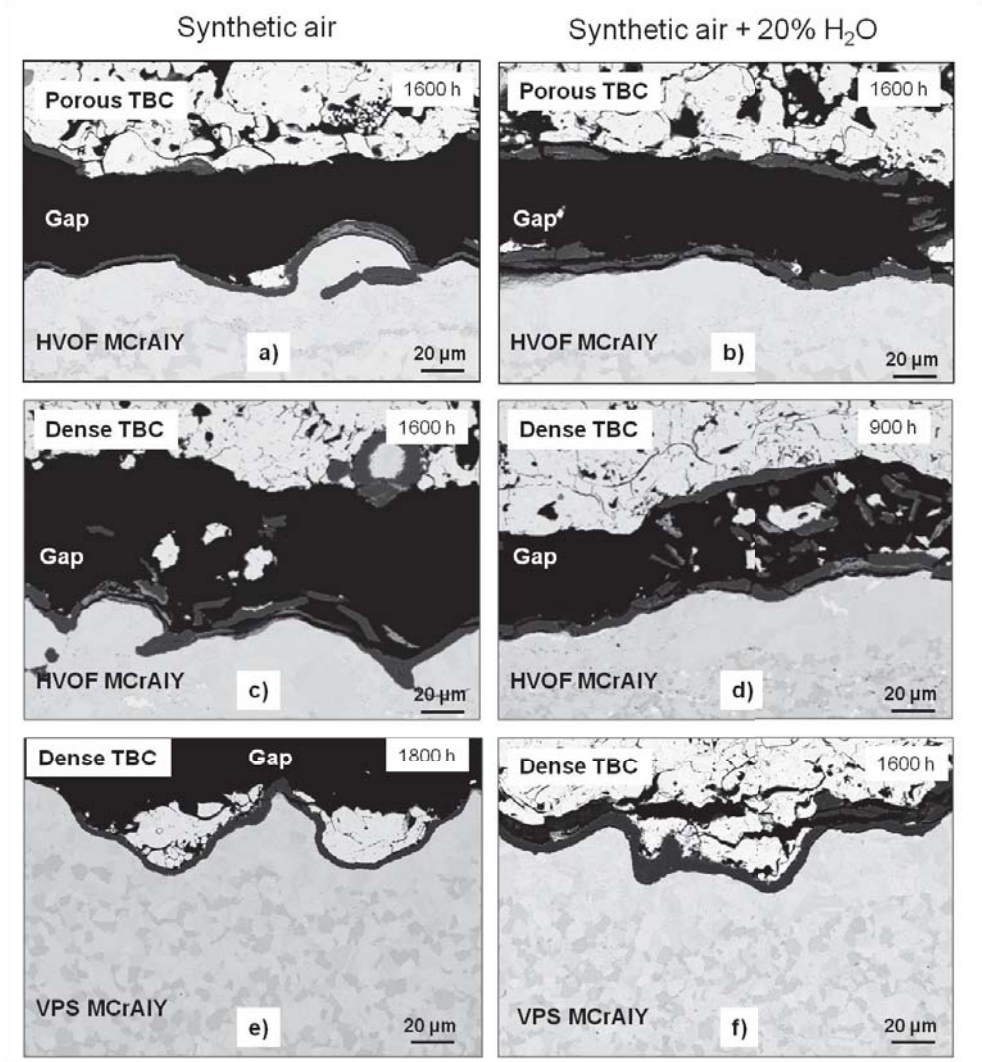

Figure 8.21 Cross sections images (SEM) of APS TBC systems with: HVOF bondcoat + porous TBC (a and b), HVOF bondcoat + dense TBC (c and d) and VPS bondcoat + dense TBC (e and f), after discontinuous exposure at 1050°C in: dry synthetic air a), c), e) and synthetic air + 20%H_2O b), d), f) till TBC failure

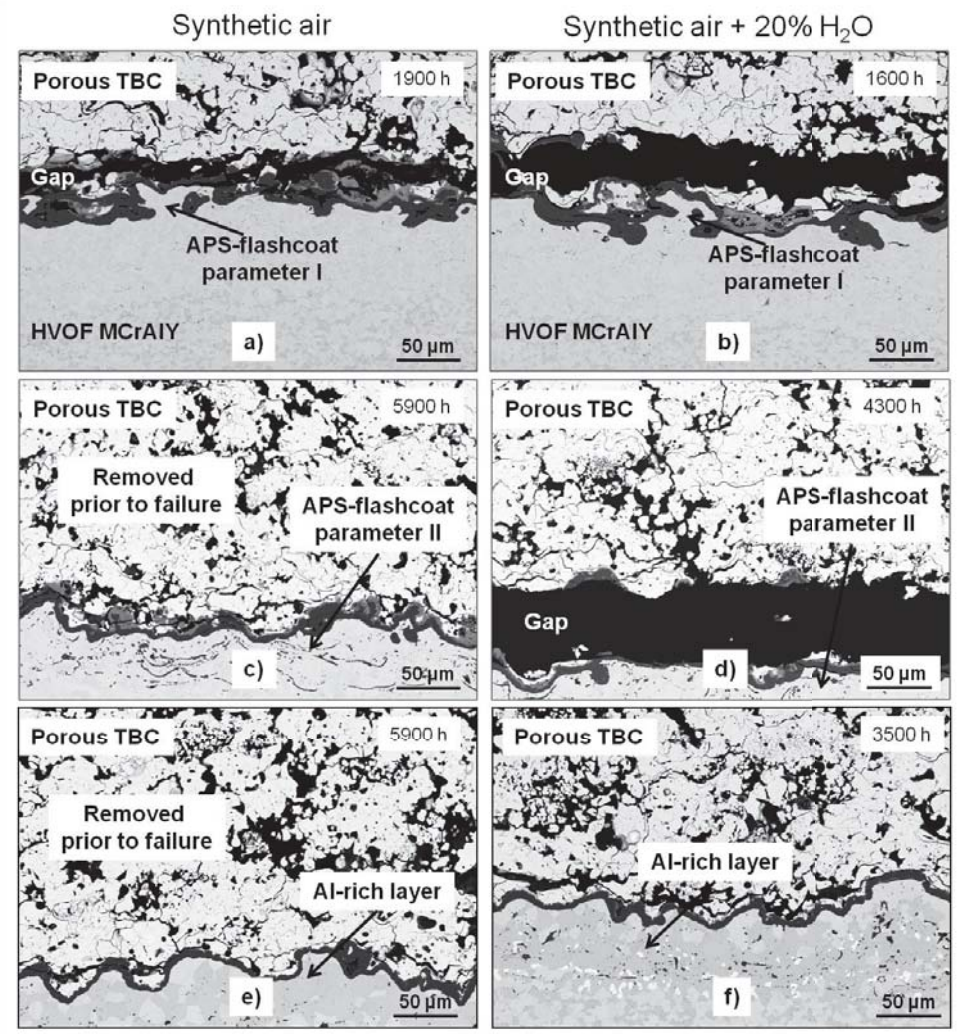

Figure 8.22 Cross sections images (SEM) of APS TBC systems with: HVOF BC + APS-flashcoat parameter set I + porous TBC (a and b), HVOF BC + APS-flashcoat parameter set II + porous TBC (c and d) and HVOF BC + aluminized APS-flashcoat + porous TBC (e and f), after discontinuous exposure at 1050°C in: dry synthetic air a), c), e) and synthetic air + 20%H_2O b), d), f) till TBC failure

8.3.3 Effect of water vapour on failure mechanisms of TBC-systems

8.3.3.1 General remarks

The results obtained during 1120°C cyclic exposure and 1050°C discontinues exposure showed that in both atmospheres the lifetimes of APS-TBC systems with APS-flashcoat are longer than those of the other tested TBC systems. All TBC-systems with APS-flashcoats and one TBC system with HVOF bondcoat and dense TBC showed shorter lifetime in water vapour containing atmospheres. Additionally, the system with APS-flashcoat applied with spraying parameter set I showed shorter lifetime than the other systems with APS-flashcoat. The reason for this shortened lifetime is a very poor oxidation resistance of the system with APS-flashcoat sprayed using parameter set I as was discussed in the **chapter 8.2.3**.

The TBC system containing an HVOF bondcoat and porous TBC does not show lifetime shortening in the presence of water vapour. The TBC system with relatively flat HVOF bondcoat and dense TBC showed a lifetime which is shorter by a factor of two in wet air. The TBC system containing VPS bondcoat and dense topcoat exposed in dry synthetic air showed a substantial scatter in TBC lifetime between two specimens (1800 h and 3400 h **Figure 8.13**). Therefore a third specimen from this system was exposed in both atmospheres. The lifetime results showed that on average also for this system lifetime shortening by water vapour is observed.

The lifetimes obtained for TBC systems with APS-flashcoat sprayed with parameter set II and with aluminized APS-flashcoat were shorter when exposed in wet air than in dry air.

However, the lifetime obtained in the wet gas were still longer than the TBC systems with HVOF and VPS bondcoats.

To elucidate the reasons for the lifetime reduction by water vapour more detailed investigations have been performed including investigations of bondcoat as well as topcoat properties.

8.3.3.2 Discussion of TGO formation and failure in dry and wet air

8.3.3.2.1 State of the art TBC systems with HVOF and VPS bondcoats

As mentioned before three TBC systems with conventionally manufactured bondcoats have been tested:

a) HVOF MCrAlY + porous YSZ (Amperit)
b) HVOF MCrAlY + dense YSZ (METCO)
c) VPS MCrAlY + dense YSZ (METCO)

Lifetime shortening after exposure in wet air has been found for the systems b) and c). This might be an effect of a combination of two facts: easier way of water vapour penetration through the porous ceramic topcoat and a relatively flat bondcoat roughness profile. In **section 8.2.6.3** a failure mechanism for TBC systems with different types of bondcoat roughness profiles was proposed. For systems with a relatively flat bondcoat it was proposed that the failure mechanism is very similar to that observed for EB-PVD TBC systems. An effect of water vapour on the lifetime of EB-PVD systems was observed previously [80, 95]

and explained by hydrogen embrittlement of the TGO/bondcoat interface. Smialek [63] described the hydrogen embrittlement phenomenon according to the following reactions:

$$Al_{alloy} + 3H_2O_{ambient} = Al(OH)_3 + 3H_{ads} \quad (8.2)$$

or

$$2Al_{alloy} + 3H_2O_{ambient} = Al_2O_3 + 6H_{ads} \quad (8.3)$$

Both reactions have a result that adhesion of the alumina scale is decreased which leads to crack formation and, in case of a flat bondcoat, to very rapid crack propagation and finally failure.

In system c) the increased roughness of the VPS-bondcoat, according to failure mechanisms proposed in **section 8.2.6.3**, forces the crack to propagate through the ceramic. The effect of the wet atmosphere on the TBC life thus differs from that found for the system with the flat HVOF bondcoat, however, as mentioned before, on average the lifetime of the TBC-system with the VPS bondcoat exposed in wet gas was slightly shortened.

SEM cross-sections of the APS-TBC systems with conventionally applied bondcoats (**Figure 8.15**) show that for all of these systems the TGO formed in the water vapour containing atmosphere are in average slightly thinner than, or possess the same thickness (**Figure 8.17**) compared to that formed in dry atmosphere.

An exact definition of TGO thickness after TBC failure (**Figure 8.21**) is very difficult, because of TGO delamination and TGO damage. However, the cross-sections shown in **Figure 8.21** confirm the failure mechanisms proposed in the **section 8.2.7**. The system with

VPS bondcoat **(Figure 8.21 e)** and **f)** forms a slightly thicker TGO in wet atmosphere (compare places where TGO is still intact despite a slightly shorter exposure time).

8.3.3.2.2 TBC systems with HVOF bondcoat roughness improved by APS-flashcoat

Figures 8.16 and **8.18** show SEM cross-sections of systems containing APS-flashcoats applied with spraying parameter set I (a, b), set II (c, d) and with an aluminized layer (e, f). For the system with APS-flashcoat applied with spraying parameter I, separated particles of MCrAlY flashcoat in intermediate stage of oxidation (prior to breakaway oxidation) according to a "diffusion cell" mechanism (described in reference [92]). Also, formation of voluminous spinel can be locally observed after exposure in both atmospheres (**Figures 8.16** and **8.18 a** and **b**). Spinel formation can also be observed in the system with APS-flashcoat applied with spraying parameter set II in both atmospheres. However, the size and amount of spinels is far less that found for the system with APS-flashcoat applied using spraying parameter set I. The thickness of the TGO formed in both atmospheres showed substantial variation depending on location, however in average the thickness of the TGO formed in dry and wet atmosphere is quite similar (**Figures 8.16** and **8.17 c** and **d**). The system with aluminized flashcoat does not exhibit spinels formation; the formed TGO consist mainly of alumina. For this system indication of thin "mixed zone" [139] on top of the alumina can be observed for the specimen exposed in wet atmosphere (**Figure 8.18 f)**). The thickness of the formed TGO is comparable in both atmospheres.

For the TBC system with APS-flashcoat applied using spraying parameter set I, the lifetime in both atmospheres show substantial scatter between the specimens exposed in the

same atmosphere. Moreover, a slight shortening of the lifetime was observed after exposure in wet atmosphere. This fact might be explained by the presence of a poorly adherent, partly discontinuous APS-flashcoat, which (as explained in **section 8.2.3**) exhibits oxidation in separate cells which leads to formation of voluminous transient oxides and consequently to early TBC failure (**Figure 8.23**). Comparing **Figure 8.23** with **Figure 8.16** it can be observed, that in many areas the APS-flashcoat was almost completely oxidized.

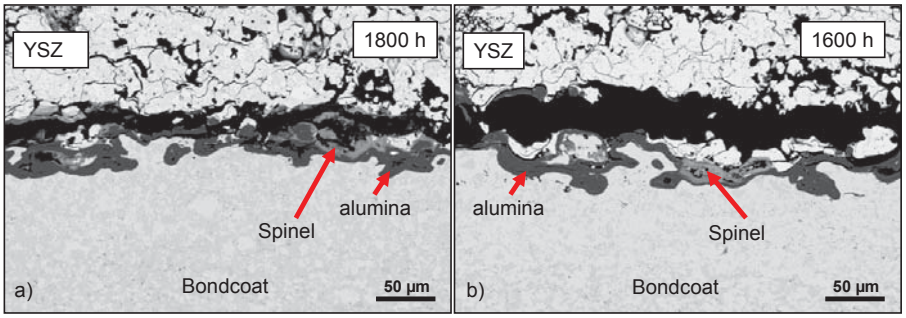

Figure 8.23 SEM cross sections of APS-TBC systems with APS-flashcoat sprayed with spraying parameter I after discontinuous exposure at 1050°C till TBC failure in: a) Synthetic air, b) Synthetic air + 20% H_2O

The APS-TBC system with APS-flashcoat applied with spraying parameter set II showed much better performance compared to the system sprayed with parameter set I. The parameter II system exhibited the longest lifetime of all studied systems in both atmospheres: dry (7000 hours) and wet (about 4200 hours). For interpreting the lifetime shortening by the presence of water vapour **Figure 8.24** shows cross sections of the TBC system with flashcoat applied with parameter set II after exposure at 1050°C till failure in dry and wet air. For the specimen oxidized in dry air, which was removed from the furnace after 5900 hours, i.e. prior to failure, one can observe a rather uniform, thin TGO. Only locally formation of a thicker oxide scale is observed. In these places also formation of spinel can be found. Also, occurrence of repeated cracking can be observed. The latter observation was found in earlier studies e.g. by Naumenko et.al. [81] for systems with various types of VPS bondcoat. The authors explained

this effect by assuming that the TGO during cycling oxidation cracked and re-grows after local delamination. For the specimen oxidized in wet air increased spinel formation has been observed (**Figure 8.24 b)**). Also, the overall thickness of the TGO is at least comparable with that found in dry air, despite the shorter exposure time. Formation of this spinel could be a possible parameter for explaining the earlier failure in the water vapour containing air.

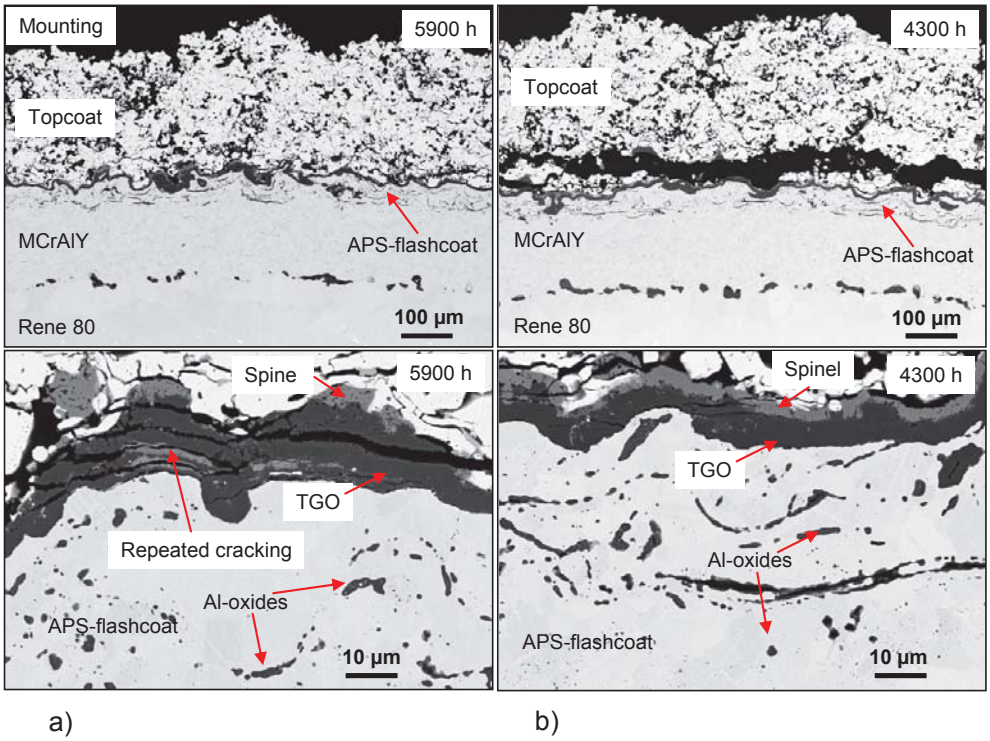

Figure 8.24 Cross sections images (SEM) of APS-TBC systems with APS-flashcoat deposited with spraying parameter set II after discontinuous exposure at 1050°C in: a) synthetic air for 5900 h (prior to failure), b) synthetic air + 20% H_2O for 4300 h (after failure).

The system with overaluminized APS-flashcoat also showed lifetime shortening in the water vapour containing gas. **Figure 8.25** shows SEM cross sections of specimens after discontinuous exposure till TBC failure at 1050°C in dry and wet gas. Similarly as in the previous case, one specimen oxidized in dry atmosphere has been removed from the furnace prior to failure to get a more insight into TGO growth and cracking mechanism. It can be observed that the TGO thickness is comparable in both atmospheres despite almost doubled

exposure time in dry air. In this TBC system the coating consists mainly of γ- and β-phase. However, formation of a Cr-rich phase is observed in the TBC system exposed in wet air. The Cr-rich phases were identified by SEM-EDX as Cr-carbides. Formation of Cr-rich phases in MCrAlY coating was also observed by Toscano et al. [140]. In the as-received condition the MCrAlY coating used in the present studies, the carbon content is relatively low, however because of the aluminizing method, which is a "slurry coating" process, additional carbon might be introduced into the coating.

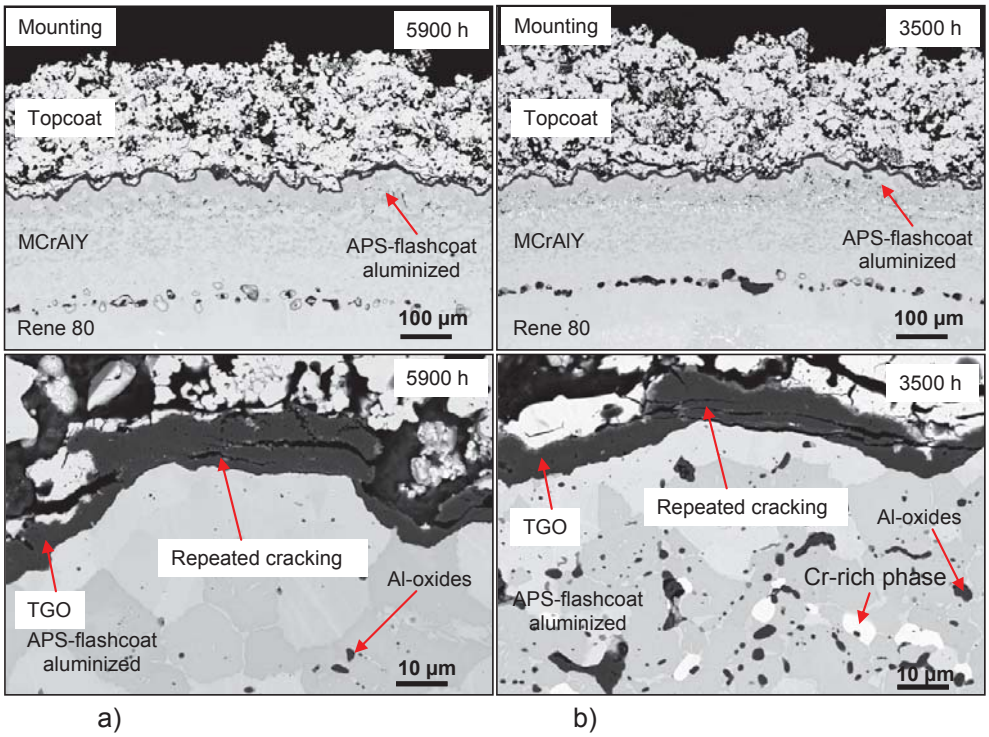

Figure 8.25 Cross sections images (SEM) of APS-TBC with overalualuminized APS-flashcoat after discontinuous exposure at 1050°C in: a) synthetic air for 5900 h (prior to failure), b) synthetic air + 20% H_2O for 3500 h (after failure).

Figure 8.26 shows the microstructure of the TGO formed on the APS-TBC systems with aluminized layer on top of the bondcoat with APS-flashcoat. A difference in total thickness of the TGO is visible, however it is not very pronounced, despite the almost two times longer exposure time in dry atmosphere. Also, the microstructure of the TGO formed in dry and wet

conditions seems to be similar; in both cases formation of fine grained oxide scale in the outer part of the TGO and a coarser grained alumina scale beneath is observed. However, comparing **Figures 8.26 c)** and **d)** it can be concluded that more substantial porosity is formed in case of the TBC exposed in wet atmosphere.

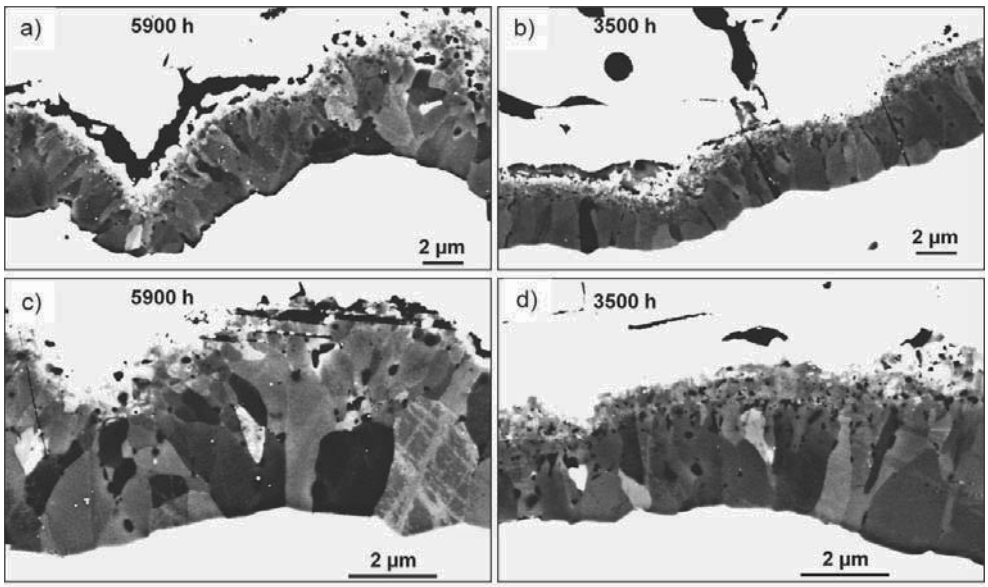

Figure 8.26 SEM in-lens images at low a), b) and high c), d) magnification showing microstructure of TGO formed on APS-TBC systems with aluminized flashcoat layer after discontinuous exposure at 1050°C in: Synthetic air for 5900 h a), c), and Synthetic air + 20%H_2O for 3500 h.

8.3.3.2.3 Summary of water vapour effects on TGO formation

- For all of the APS-TBC systems, similar TGO-morphologies were observed for specimens exposed in dry and wet synthetic air. However, the amount of spinel was slightly larger after exposure in synthetic air containing 20% H_2O than in dry air. The only exception was the TBC system with APS-flashcoat applied with spraying parameter set I, which showed equally extensive spinel formation in both atmospheres because of the "diffusion cell" effect.

- An exact comparison of the TGO-growth kinetics between the dry and wet atmosphere is difficult because of intrinsic TGO-morphology/thickness variation on rough bondcoat surfaces [16].
- The shorter lifetime of some of the studied systems in the wet test gas cannot be straightforwardly correlated with increased TGO growth rate, especially considering the frequently observed near-cubic TGO-growth kinetics [38]. If the lifetime of TBC is related only to TGO-growth kinetic differences variation, then, according to near-cubic kinetics, the difference in lifetime by a factor of two can result in TGO thickness difference of only about 25 %, whereas the variation in TGO-thickness within the same APS-TBC specimen is much greater than 25%. On free standing coatings exposed at 1050°C in dry and wet synthetic air for 100 hours no significant effect of H_2O addition on TGO growth kinetics was observed (**section 7.4.1**).
- Similar alumina TGO grain microstructure after oxidation for 100 hours was observed on APS-TBC systems exposed in dry and wet synthetic air (**Figure 8.26**).
- Considering the failure mechanisms of the studied TBC-systems with rough plasma sprayed bondcoats in **Figure 8.11** the lifetime is to a large extent determined by crack propagation through the ceramic topcoat. Therefore, a possibility exists that water vapour can affect crack growth in the topcoat. The various aspects of the topcoat microstructure, crack propagation and the environmental effects on both of these parameters will be discussed in the following chapter.

8.3.3.3 Water vapour interaction with the topcoats

8.3.3.3.1 Investigation of ceramic YSZ powders used for topcoat spraying

As mentioned previously, all the TBC systems in the present investigation are based on superalloy Rene 80 with MCrAlY (**Table 5.2**) as a bondcoat and with zirconia stabilized by 8% yttria as a top layer. The systems differ in bondcoat deposition method, powders used for manufacturing of the topcoats and also topcoat porosity. As mentioned in the previous chapters three TBC systems with conventional bondcoats were tested as shown in **Figure 8.27.**

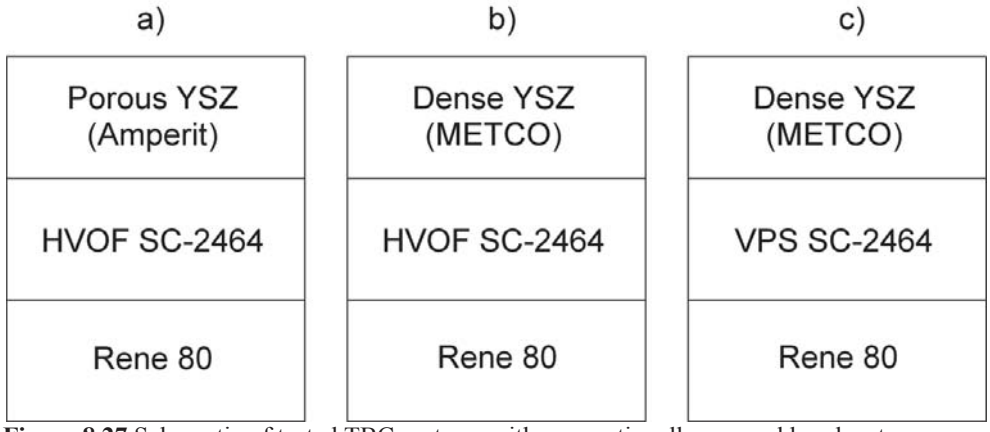

Figure 8.27 Schematic of tested TBC systems with conventionally sprayed bondcoats

The lifetime results confirmed that combination of the two parameters, topcoat porosity and bondcoat roughness profiles, are of great importance for the obtained lifetime. However, the tests in dry and wet air revealed that the lifetimes of the systems shown in **Figure 8.27 b)** and **c)** were shorter in the water vapour containing atmosphere. Systems designated in **Figure 8.27** a) differs from systems b) and c) in topcoat porosity as well as in the powder source for topcoat manufacturing. The topcoat in system a) was sprayed using Amperit powder while in systems b) and c) from **Figure 8.27** Metco powder has been used. Therefore, an investigation

of powders before spraying as well as investigation of deposited ceramic coating has been performed.

Figure 8.28 shows images of YSZ powder particles of Amperit and Metco respectively. It is clearly visible that the Amperit powder particles are much more uniform in size and additionally are larger in site that the compared to Metco powder. The latter powder showed substantial scatter in powder particle size and, in addition, those particles seems to be denser than is the case for the Amperit powder (**Figure 8.29**). Cross section investigation of both powders confirmed the differences in powder sizes as well as densities (**Figure 8.30**). Apart from the fact that the particles of the METCO powder are denser they have additionally a different structure. Many particles of this powder are spherical while particles of the Amperit powders are agglomerates. EDX measurement of the elements within the powder particles showed that in the METCO powder the distribution of yttrium is not uniform (**Figure 8.31**), while in Amperit the yttrium is rather uniformly distributed (**Figure 8.32**). This might have a result that formation of monoclinic phase in case of METCO could be locally promoted in the Y-poor areas[141].

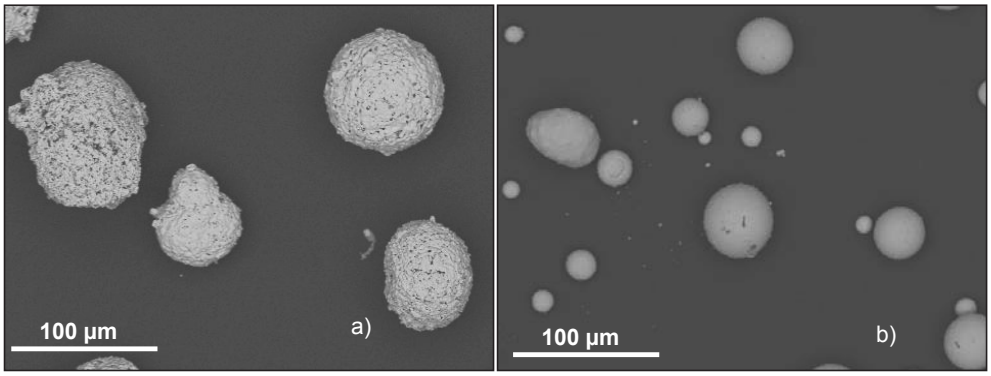

Figure 8.28 BSE SEM images of ceramic YSZ powder surfaces: a) Amperit and b) METCO used for the spraying ceramic TBC topcoat

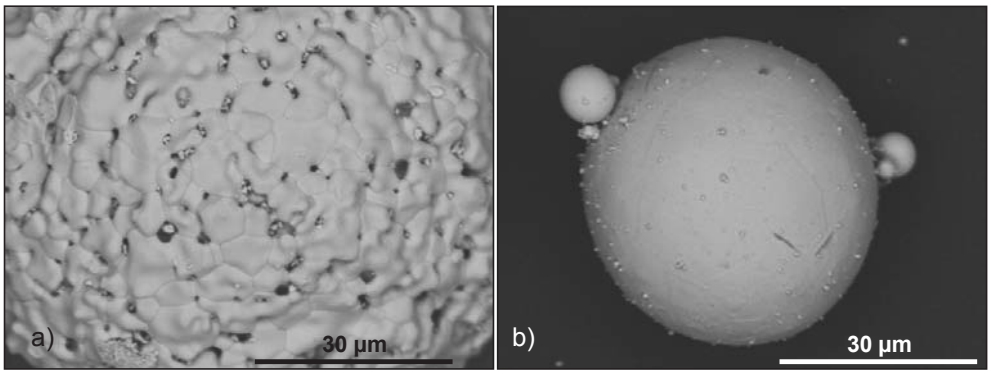

Figure 8.29 BSE SEM images of ceramic YSZ powder particles: a) Amperit and b) METCO used for the spraying ceramic TBC topcoat

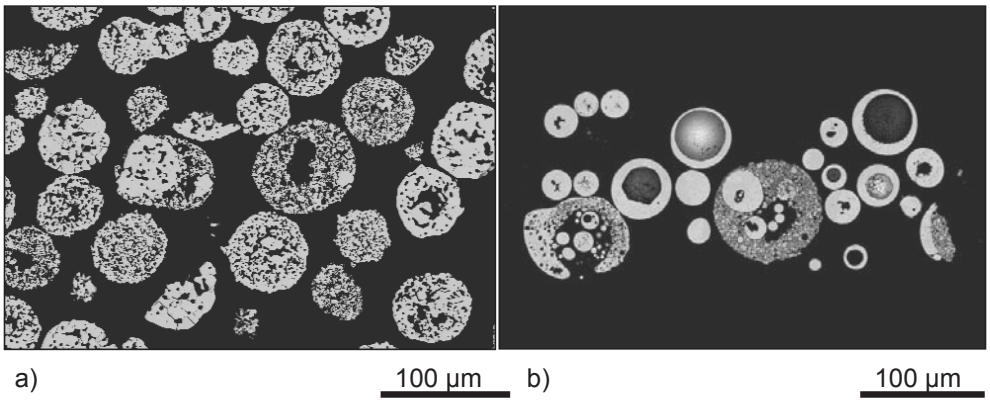

Figure 8.30 Cross section images (SEM) of YSZ powders: a) Amperit and b) METCO

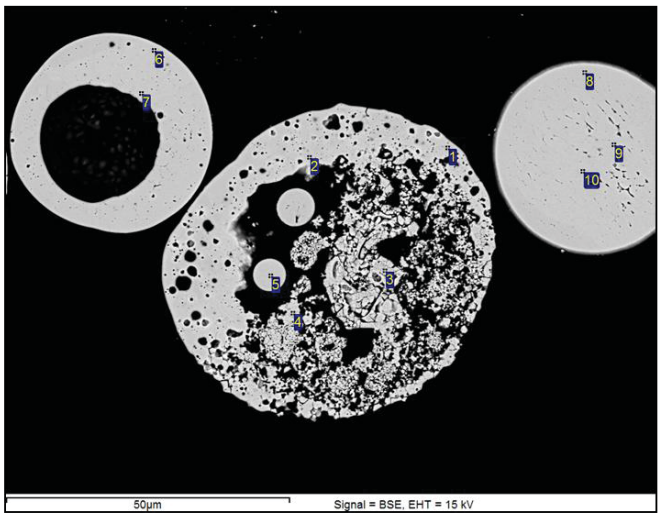

Spectrum	Na	Si	Ti	Y	Zr	Hf	O
1	0.0	0.0	0.0	4.2	68.9	1.4	*25.5*
2	0.0	0.0	0.0	0.0	72.9	1.3	*25.8*
3	0.1	0.0	0.0	0.0	72.8	1.4	*25.8*
4	0.0	0.3	0.0	13.2	60.3	1.1	*25.2*
5	0.0	0.0	0.0	4.3	69.0	1.2	*25.6*
6	0.0	0.0	0.0	4.2	69.0	1.2	*25.6*
7	0.0	0.0	0.0	5.0	68.1	1.3	*25.5*
8	0.0	0.0	0.0	4.1	69.1	1.3	*25.6*
9	0.0	0.0	0.0	4.2	68.9	1.4	*25.5*
10	0.0	0.0	0.0	4.6	68.5	1.3	*25.5*

Figure 8.31 Cross section image (SEM) of METCO YSZ powder particles and EDX point analyses showing non-uniform yttrium distribution

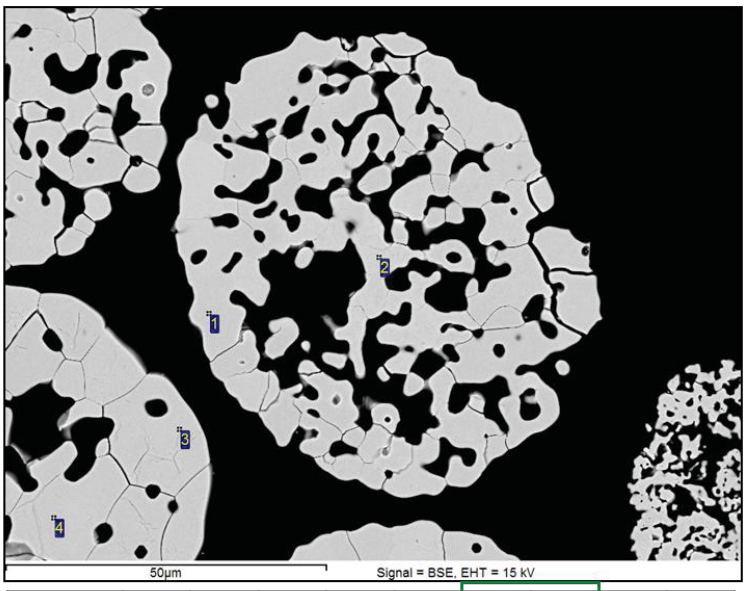

Spectrum	Al	Si	Ca	Ti	Fe	Y	Zr	Hf	O
1	0.1	0.0	0.0	0.0	0.0	5.1	68.0	1.3	*25.5*
2	0.1	0.0	0.0	0.0	0.0	3.9	69.1	1.3	*25.6*
3	0.0	0.0	0.1	0.0	0.0	5.2	67.9	1.3	*25.5*
4	0.0	0.0	0.0	0.1	0.0	5.1	68.0	1.3	*25.5*

Figure 8.32 Cross section image (SEM) of Amperit YSZ powder particles and EDX point analyses showing uniform yttrium distribution

Also the chemical composition of the powders as investigated by ICP-OES and ICP-MS (**Table 5.3**) revealed slight differences in chemistry of both powders: for METCO a minor amount of Na was found to be present (approximately 0.02 wt. %), while in Amperit Na was not detected by ICP-OES. Moreover, in Amperit small amounts of Ca, Al and Fe were present contrary to the METCO powder.

The amounts of the monoclinic phase in the powders were measured using X-ray diffraction. It was found that the Amperit powder batch contains 6 wt. % monoclinic phase while the METCO powder contains 15 wt. % of the monoclinic zirconia (**Figure 8.33**).

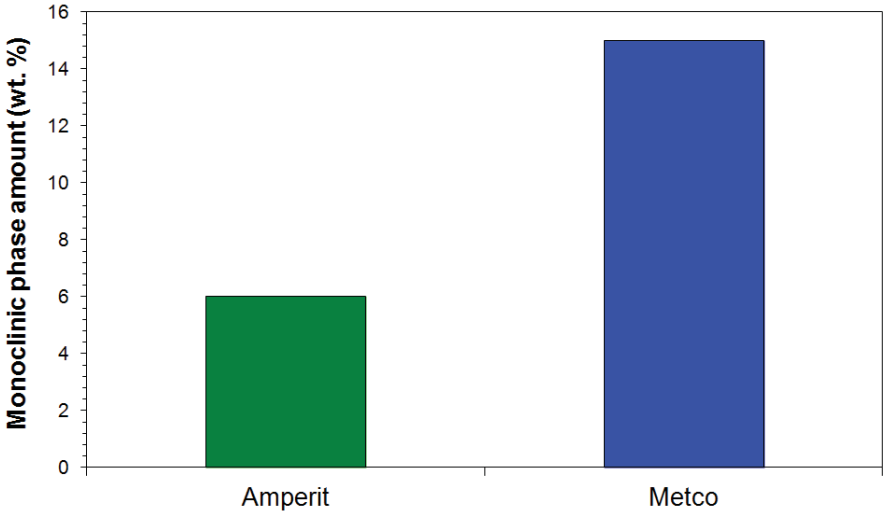

Figure 8.33 Amount of monoclinic zirconia determined from X-ray diffraction patterns for different powder feedstock in as-received condition

8.3.3.3.2 Investigation of sprayed topcoats

Pure zirconia is stable in the following crystallographic structures [142]:

$$Ortorombic \longleftrightarrow monoclinic \xleftrightarrow{1170^{o}C} tetragonal \xleftrightarrow{2370^{o}C} cubic \xleftrightarrow{2680^{o}C} liquid \ .$$

Pure zirconia sintered above 1170°C transforms during cooling from tetragonal to monoclinic phase. This martensitic transformation is accompanied by a large shear strain and a big volume change, which leads to large internal stresses [142]. These stresses are so large that pure zirconia may disintegrate by cracking during cooling. Therefore calcium, magnesium, yttrium or cerium oxides are added to stabilize tetragonal zirconia below 1170°C. The presence of the tetragonal zirconia phase is desired because of its ability to toughening by martensitic transformation. The most widely used stabilizer of tetragonal zirconia is yttrium oxide and it was estimated that for application in TBC systems the best material is partially stabilized YSZ containing 6-8 wt.% Y_2O_3 [142, 143, 144]. Many researchers believe that stabilization is a direct consequence of the oxygen vacancies introduced by the aliovalent

alloying element rather than the aliovalent dopant itself [145, 146]. It is known that, upon increasing dopant concentration (e.g. Y_2O_3), the material transforms to a tetragonal form, called partially stabilized, and then to a cubic one, called fully stabilized. The electrostatic neutrality of this rather ionic material is maintained by oxygen vacancies. In case of fully stabilized zirconia one vacancy is produced by addition of every two yttrium ions [147]. It is believed that dopant cations do not take an active part in the stabilization mechanism, which is dominated by the crystal distortions around the oxygen vacancies. However, this form of stabilization alone is unlikely to be the complete explanation because the solubility of the tetragonal and cubic phases at different temperatures depends on the alloying dopants [147].

Figure 8.34 shows the most recent zirconia-yttria phase diagram in which the metastable phases are considered. The necessity of considering the metastable phase diagrams is that cation diffusion in zirconia is exceptionally slow at all but the highest temperatures. In reference [141] it is claimed that the estimated time for full compositional YSZ homogenization at 1500°C (common temperature used for zirconia sintering) may be several weeks.

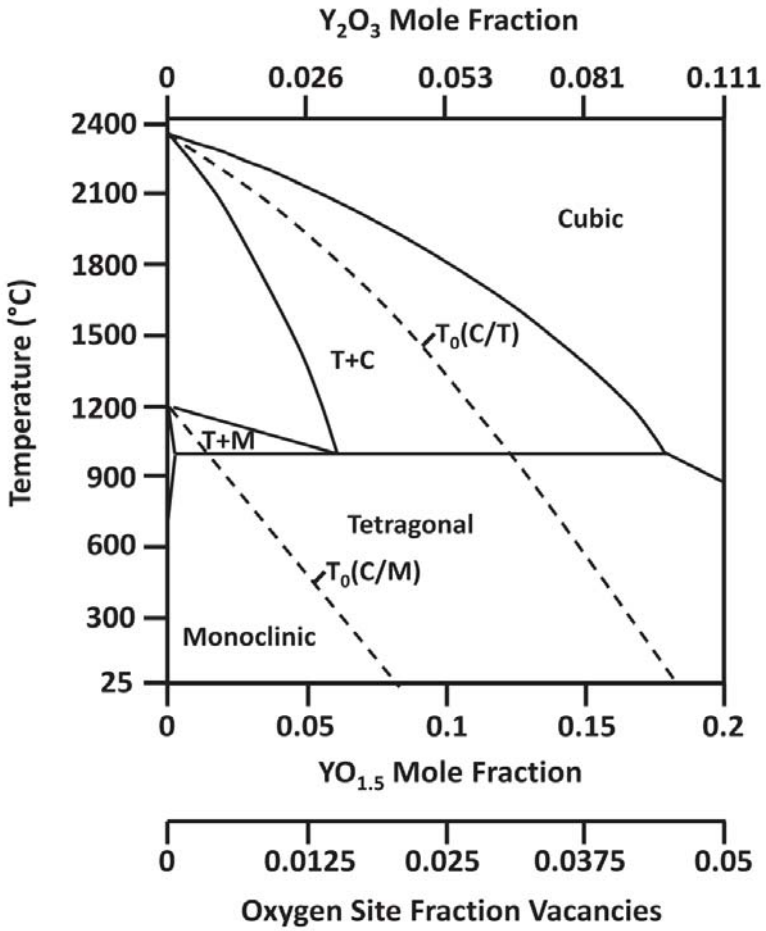

Figure 8.34 Metastable zirconia-yttria phase diagram (reproduced from reference [141])

It is known that during air plasma spraying powder particles become molten and, upon reaching the substrate, solidify very rapidly, whereas after solidification the tetragonal phase of zirconia is retained. From this point of view it is favourable to reach a high temperature to melt the powder particles completely and spray them using a distance as short as possible. However, in the TBC systems, certain porosity is required for obtaining the desired parameters (high strain tolerance, fracture toughness) for practical application [141]. This porosity is achieved either by lowering the spraying temperature or by increasing the distance

between the spraying gun and the substrate as was shown for bondcoat spraying in reference [148]. Both parameter variations lead to increasing amount of monoclinic zirconia, either by not complete melting of the powder particles or by cooling of molten particles during the flight between the spraying gun and reaching of the substrate surface. Therefore amounts of the monoclinic phase in the powder feedstock could in principle result in larger amount of the monoclinic zirconia in sprayed ceramic topcoat layer.

Figure 8.35 shows the SEM (left column) and SEM/CL (right column) images of TBC systems with ceramic topcoat sprayed using a) Amperit and b) METCO powder feedstock. The white spots on the right hand sides of the SEM/CL images (right column) show the monoclinic phase in the ceramic coating. It is clearly visible, that in the coatings produced from different powders the amount, distribution and morphology of the monoclinic zirconia are different. In the coating produced from Amperit powder the amount of monoclinic zirconia visually seems to be less and also this monoclinic zirconia agglomerates are finer and more homogenously distributed compared to the coating produced from the METCO powder. For the latter monoclinic phases formed big agglomerates and are not homogenously distributed over the coating. Similar differences in the monoclinic phase's distribution over the ceramic coating after exposure till TBC failure are visible in **Figure 8.36**.

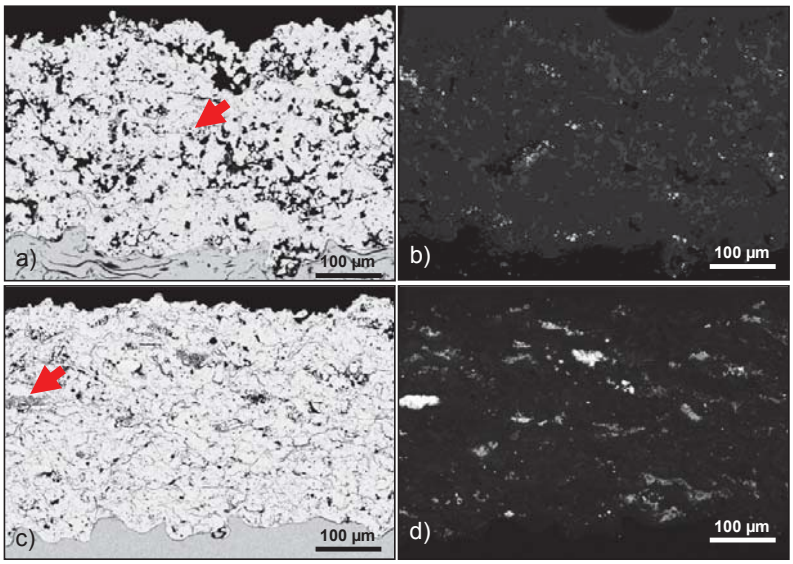

Figure 8.35 SEM a), c) and SEM/CL b), e) images of ceramic topcoats in as sprayed conditions showing monoclinic phase distributions in coatings manufactured using Amperit a), b) and METCO c), d) powders. Arrows indicate monoclinic phase location.

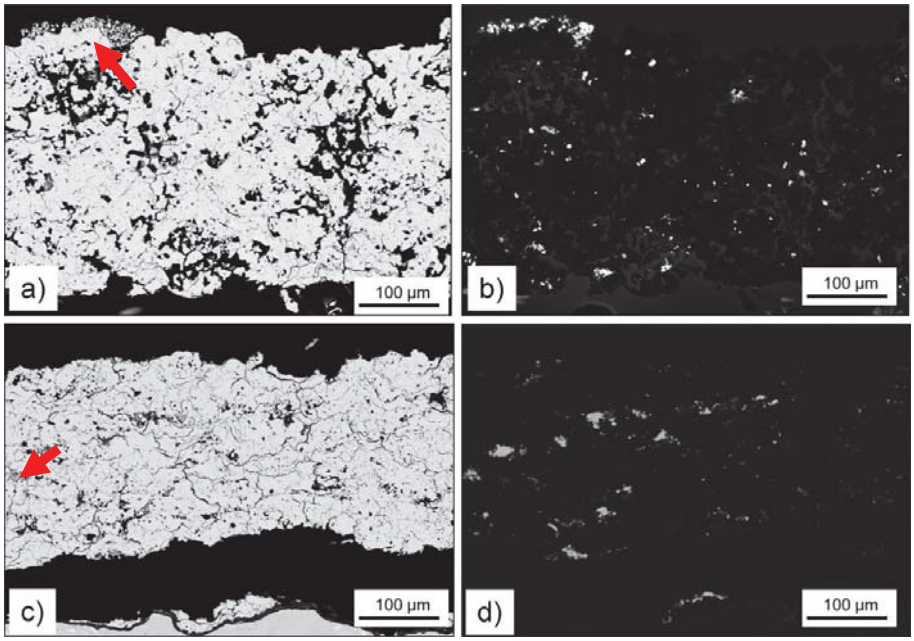

Figure 8.36 SEM a), c) and SEM/CL b), e) images of ceramic topcoats after exposure till TBC failure showing monoclinic phase distributions in coatings manufactured using Amperit a), b) and METCO c), d) powders. Arrows indicate monoclinic phase location.

In **Figure 8.37** SEM and SEM/CL images of single monoclinic zirconia is depicted. Again, the white area in the SEM/CL image shows the monoclinic zirconia region. It is clearly visible that the monoclinic zirconia is very porous and "disintegrated". One may speculate that monoclinic zirconia agglomeration might be an easy point/area for crack nucleation during cyclic TBC lifetime testing.

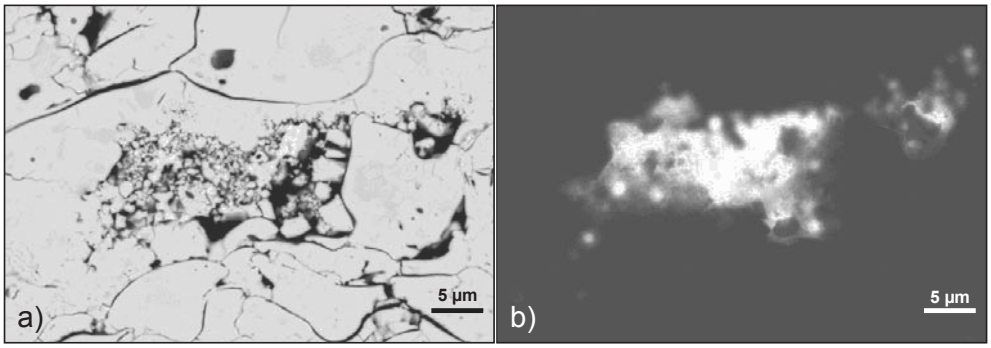

Figure 8.37 SEM a) and SEM/CL b) image of monoclinic zirconia in the as-sprayed YSZ coating (coating sprayed using METCO powder)

To quantitatively confirm the observation of monoclinic zirconia in the coating, X-ray diffraction analyses were performed on the coatings from the TBC systems in the as-sprayed conditions. The obtained results show that in the coating produced from the Amperit powder only 0.7 wt.% of monoclinic zirconia was found while in the coating produced from the METCO powder the amount of monoclinic zirconia was 1.4 wt.% (**Figure 8.38**).

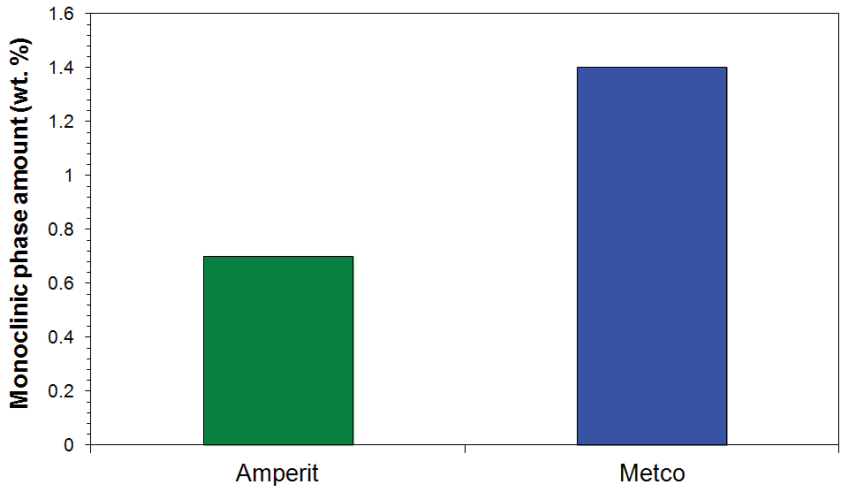

Figure 8.38 Amount of monoclinic zirconia determined from X-ray diffraction patterns of as-sprayed TBC coatings using different powder feedstock

As described in **section 8.3.3.3**, possible explanations for lifetime shortening of APS-TBC systems as a result of changing test conditions might be related to the ceramic topcoats properties (amount of monoclinic zirconia), hydrogen embrittlement affecting alumina adhesion leading to failure or different bondcoat oxidation in dry and wet gases (comparable TGO thicknesses in spite of two times shorter exposure time for systems exposed in dry and wet atmospheres). However, other possible explanations for the shorter TBC lifetime in water vapour containing gases may be derived from various recent publications.

Ingo et al. [149] investigated segregation phenomena at the fracture surfaces of 8 wt. % Y_2O_3-ZrO_2 TBC. The authors found that elements like Si, Na and Al tend to segregate thereby forming a silicate-segregated film thus providing sites at which fracture could originate. In bulk ceramics the adverse effect of impurities such as Na on fracture in the presence of water vapour is a well known phenomenon called static fatigue [150].

Chemical analysis of the ceramic powders used to produce the topcoats in the present studies show that the METCO powder contains about 0.06 wt.% Na and 0.03 wt.% Si while the

Amperit powder contains 0.04 wt.% Si, 0.02 wt.% Ca and 0.06 wt.% Al. Therefore, segregation of these elements may affect overall TBC performance during long term exposure. Moreover, Si was identified to be present in the sprayed coatings in the monoclinic phase (**Figure 8.39**).

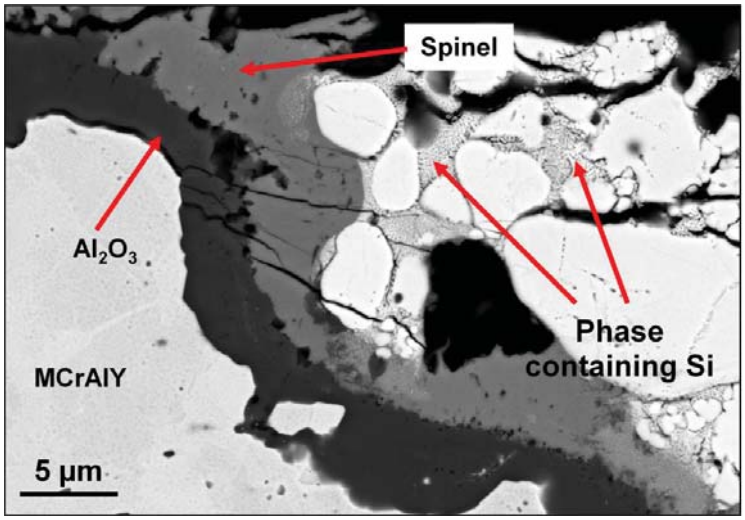

Figure 8.39 Cross section image (SEM) of the TBC with HVOF + APS-flashcoat sprayied using parameter set II after exposure for 5900 hours at 1050°C showing phases containing Si

Stabilization of the tetragonal zirconia by yttrium not only enables fabrication of crack free ceramic, but also allows preparation of the sintered bodies of polycrystalline tetragonal zirconia phase which is retained down to room temperature contrary to the fact that the thermodynamically equilibrium phase is monoclinic. This tetragonal phase exhibits exceptional fracture toughness [143]. This toughening could be achieved by a so-called Transformation Toughening mechanism [151]. Phase transformation toughening starts in the presence of large tensile stresses around the crack, which can destabilize the tetragonal phase in the vicinity of the crack, forming a transformation zone. McMeeking and Evans [152] developed a model of phase transformation in which the stress induced transformation leads

to a shielding (K_{Ish}) of the applied stress intensity factor (K_I). This means that the real stress intensity factor at the crack tip (K_{Itip}) is lower than that applied by the external forces, according to:

$$K_{Itip} = K_I - K_{Ish} \tag{8.4}$$

This model and experimental data show that, the higher the applied stress intensity factor, the larger the transformation zone and the larger the shielding effect. This is expressed by the equation [141]:

$$K_{Ish} = C_{sh} K_I \tag{8.5}$$

with

$$C_{sh} = \frac{0.214 E V_f e^T (1+\nu)}{(1-\nu)\sigma_m^c} \left(\frac{\sqrt{3}}{12\pi}\right) \tag{8.6}$$

where:

E – Young's modulus,

V_f - volume fraction of transformable particles,

e^T - volume dilatation associated with the transformation,

ν – Poisson ratio,

σ_m^c - critical local stress leading to phase transformation.

In the present studies indications were found, that the crack propagation velocity in the topcoat depend on the type of testing environment. **Figure 8.40** shows the crack velocity as a function of stress intensity for zirconia in different environments. The data clearly show that the stress intensity obtained for zirconia exposed in water is the lowest among all other studied atmospheres. Thereby, the curve obtained at 25°C in water shows a slightly higher

stress intensity than that obtained in water at 75°C. These results suggest that a so-called Low Temperature Degradation process may occur [141].

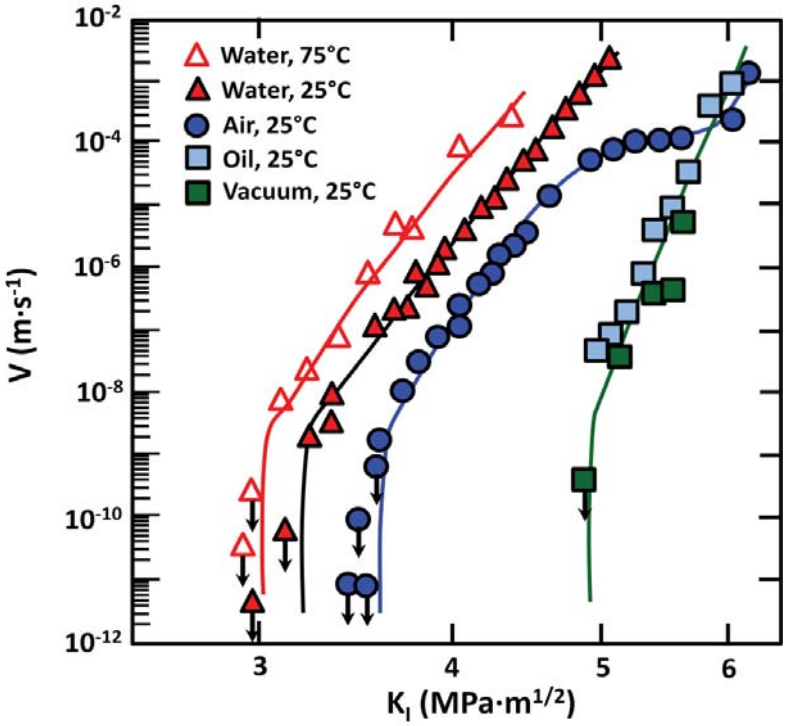

Figure 8.40 Crack velocity V as a function of stress intensity K_I obtained for zirconia in different environments (reproduced from reference [141])

The Low Temperature Degradation (LTD) process is very widely investigated in the field of dental ceramics [141, 142] and it is described as a kinetic phenomenon in which polycrystalline, tetragonal material slowly transforms to monoclinic zirconia over a relatively narrow but important temperature range, typically room temperature to around 400°C in the presence of water vapour [141]. It is worth noticing that in this process the transformation of tetragonal into the monoclinic phase occurs without presence of cracks. The nucleation and growth process can be described by the following equation [141]:

$$\alpha = 1 - exp(-(bt)^n) \tag{8.7}$$

where:

α - the fraction of tetragonal phase that has transformed into monoclinic phase,

t - time of exposure to moisture,

b - value of the constant,

n – exponent depending on temperature.

Experimental data and simulations show that the exponent has a value between 0.5 and 4 [141].

Figure 8.41 shows a time-temperature transformation plot obtained for a 5-YSZ (2.8 % Y_2O_3) thermal barrier coating proposed by Lughi et al. [153]. It is apparent that the fastest monoclinic phase formation in zirconia exposed in water vapour containing environment takes place in the temperature range between 200°C and 350°C (**Figure 8.41**). As described in **chapter 5.3.1** the specimens in the present studies were after exposure cooled in the test atmosphere till 70°C and held at this temperature for 2 hours. This means that APS-TBC specimens were held in synthetic air containing 20 % H_2O also in the temperature range in which Low Temperature Degradation process is likely to occur. Additionally, after cooling down, specimens are taken out from the furnace, therefore water vapour may condensate on the surface of the topcoat. **Figure 8.42** shows a measured cooling curve for a discontinuous test. It can be seen that the exposure time in the temperature range between 200°C and 350°C is approximately 1.2 hour (about 4400 s). Comparing the derived data with **Figure 8.41** one can conclude that the temperature region in which relatively extensive monoclinic phase formation may occur has been reached. However, it needs to be mentioned that the data presented in **Figure 8.41** concern TBC's with 5% Y_2O_3 stabilized zirconia, while in the present work 8% Y_2O_3 stabilized zirconia was investigated Therefore less extensive monoclinic phase formation might be expected.

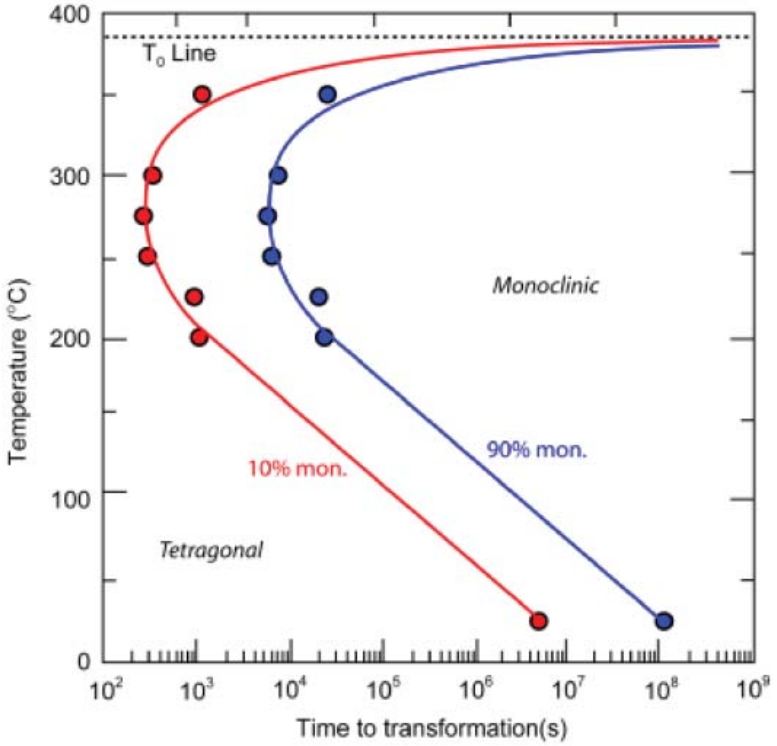

Figure 8.41 Time-temperature transformation (TTT) plot obtained for 5-YSZ TBC exposed in laboratory air (average humidity approximately 60%), (reproduced from reference [141])

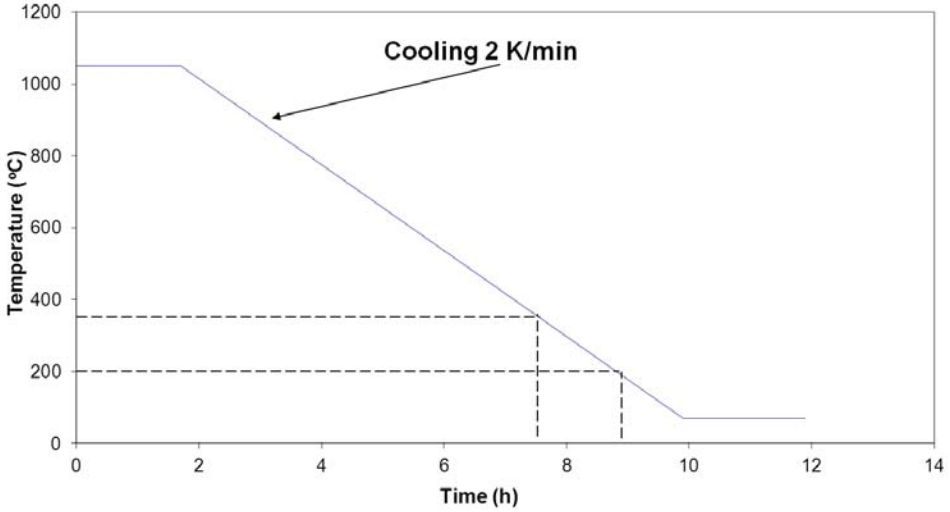

Figure 8.42 Schematic showing cooling curve obtained for discontinuous exposure at 1050°C in the present studies. Dashed line illustrate the temperature region in which LTD [141] is likely to occur and the period of time in which the phenomenon may occur.

The mechanism of LTD proposed in reference [141] is shown in **Figure 8.43**. The low temperature degradation process occurs by diffusion of water species into the lattice via oxygen vacancies (**Figure 8.43 a)**) and results in an increase of the lattice parameters. This leads to a transformation of tetragonal to monoclinic and the corresponding disintegration and finally failure of the ceramic coating.

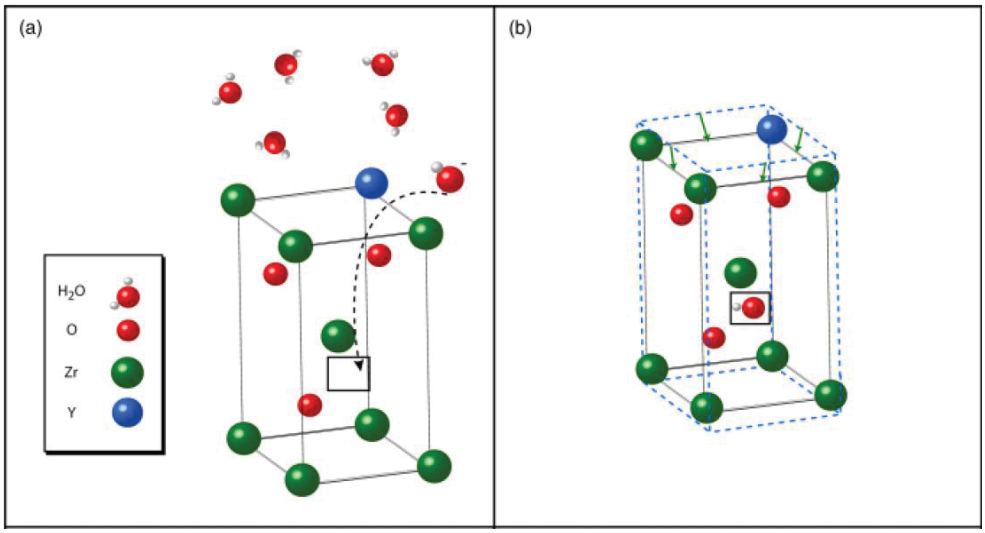

Figure 8.43 Schematic mechanism of low temperature degradation of YSZ in the presence of water vapour (reproduced from Chevalier et.al. [141])

In the present studies all TBC systems were cooled down within the furnace in ambient atmospheres to room temperature and the same TBC systems were exposed to water vapour in the whole temperature range between room temperature and 1050°C. Therefore, low temperature degradation processes might have taken place.

8.3.3.3.3 Discussion of possible water vapour effects on topcoat properties

Considering the failure mechanisms (**Figure 8.11**) for the APS-TBC systems with rough bondcoats it was recognized that cracks originate from the top of convex areas of the

bondcoats when the TGO delaminates and, after delamination, the crack propagates through the YSZ ceramic. For the system with VPS bondcoat and dense ceramic topcoat crack propagation through the dense ceramic topcoat is rapid (considering findings in [129]). Therefore the TBC lifetime is determined to a large extent by the TGO delamination. However, also the topcoat properties can have an impact on the TBC lifetime shortening by the water vapour addition. For the ceramic powder batch METCO a less uniform Y-distribution was found which, according to [154], results in a larger fraction of monoclinic phase. For powder batch METCO many areas with low Y-content were locally found (see **Figure 8.31**). According to **Figure 8.33**, this means that transformation from tetragonal to monoclinic phase starts locally in the latter areas at higher temperatures than in the case of more uniform Y-distribution (compare **Figure 8.32**).

It has been described in literature [141] that transformation from tetragonal to monoclinic phase is promoted by water vapour in a certain temperature region (typically between 200°C and 400°C). This phenomenon can be critical especially at slow cooling rates such as in the prevailing discontinuous exposures.

Impurities such as Si, Al and especially Na were found in the METCO YSZ powder batch. Na was claimed to decrease the fracture toughness of YSZ by segregating to the grain boundaries [150]. In bulk ceramics the adverse effect of Na on fracture is a well-known phenomenon called static fatigue.

For the same atmospheres longer lifetime of TBC systems containing a porous topcoat sprayed using the Amperit YSZ powder batch was observed (**Figures 8.13** and **8.14**). It was proposed in **section 8.2.3** that the latter TBC systems showed higher fracture toughness due to higher porosity. Also, a more uniform Y-distribution in the powder and in the ceramic coating

may contribute to an extension of the TBC lifetime. However, the lifetime obtained in wet atmosphere is generally shorter than that for the same APS-TBC systems obtained in dry gas. One of the possible reasons for this finding might be the low temperature degradation phenomenon [141]. Comparison of **Figures 8.35 b)** and **8.36 b)** indicates that the amount of monoclinic phase is increased after exposure. However, the comparison is not unequivocal, because cathodoluminescence is not an accurate quantitative analytical method.

In the present studies the tests were performed at relatively slow heating/cooling rates. Therefore LTD might have played a more important role than would be the case if the experiments were performed under rapid temperature cycling conditions and/or cooling in dry gas [7].

Further studies are required to investigate the effect of cooling rate in wet environments on the lifetime of TBC systems with various topcoat properties and bondcoats roughness profiles, thereby taking into account the environment in which the cooling takes place.
It was not possible to identify one single parameter responsible for the shortening of the lifetime in wet atmospheres. It might be that not a single, but a combination of parameters is responsible for shorter lifetime in water vapour containing gases.

In spite of the lifetime shortening by water vapour, it can be stated that the absolute lifetime values of the APS-TBC-systems with optimized topcoat microstructure and bondcoat roughness profile/microstructure appeared to be a factor of 3 longer than those of the systems with dense topcoats and flatter bondcoat surfaces (**Figures 8.13** and **8.14**).

9 Summary and conclusions

In the present studies the effect of water vapour on the oxidation behaviour of three material groups used in stationary gas turbines was investigated.

The materials are:

4. The polycrystalline Ni-base superalloy Rene 80, which is representative of a chromia forming alloy;
5. An alumina forming Re-containing MCrAlY coating, and
6. A TBC systems applied on Rene 80 and having the same MCrAlY as the bondcoat.

The three material types were investigated mainly at 1050°C, however, some tests were also performed at higher temperatures: 1080°C and 1120°C. The oxidation behaviour of all studied materials was found to be affected by water vapour.

The SEM results in combination with the GD-OES depth profiles obtained on oxidized superalloy Rene 80 showed, that the alloy forms a complex oxide scale, which contains an outer TiO_2 layer in the outer part of the oxide scale in which boron enrichment was found. Below the TiO_2 layer, Cr_2O_3 with substantial porosity was found, which develops with increasing exposure time. In the inner part of the oxide scale a layer of $CrTi_2O_5$ precipitates were observed, below which, B-containing phases, identified in the present studies as $BCrO_3$, are present. The alloy formed also internally oxidized Al_2O_3 precipitates.

The Rene 80 formed the above described oxide scale in all test atmospheres, which were Ar-O_2 based atmospheres with various O_2 content: 1% and 20% as well as synthetic air (N_2-20%O_2) with and without addition of 7%H_2O.

Addition of 7% water vapour to Ar-1% O_2 and Ar-20% O_2 promotes internal oxidation of Ti which after 1 hour of exposure forms a mixed oxide compound with Al. The presence of water vapour also causes porosity in the outer TiO_2 layer, which might be correlated with the enhancement of Cr evaporation by water vapour addition. The thickness of this outer Ti oxide layer increased with addition of water vapour in the gas.

Decreasing of pO_2 in the atmosphere from 0.2 to 0.01 bar results in formation of continuous $CrTi_2O_5$ layer in the inner part of the oxide scale which is still present after longer exposure (50 h). This continuous layer cannot be observed on Rene 80 exposed in Ar-20%O_2 gas. Also presence of a large number of pores aligned in a line in the outer part of the chromia scale was found on Rene 80 exposed in low pO_2 gas. After longer exposure time (100 h) spallation within the oxide scale was found to be more pronounced in low pO_2 gas, which might be correlated with $CrTi_2O_5$ layer dissolution.

In the Rene 80 exposed in dry synthetic air formation of TiN below the internally oxidized Al_2O_3 precipitates was found. Formation of coarser Al_2O_3 precipitates which locally forms virtually continuous sub-scale of Al_2O_3 out of the growing precipitates, which might be correlated with less Ti incorporation into the oxide scale due to formation of TiN.

Addition of water vapour (7%) resulted in suppression of TiN formation. This was explained by preferential adsorption of polar water vapour molecules or H-associated species in the oxide scale than non-polar N_2 molecules.

Addition of 20% H_2O into synthetic air during discontinuous, long term test was found to affect the oxidation behaviour of Rene 80. It is important to mention, that the oxide scale composition/morphology obtained on Rene 80 after discontinuous test is substantially

different from short exposure times: large amounts of refractory elements e.g. W, Mo in the oxide scale is present. Moreover, repeated scale spallation occurred. The latter phenomenon was found as a major reason for mass loss in both test gases. However, 20% higher mass loss in water vapour containing environment was observed. Possible reason for the higher mass loss might be evaporation of oxyhydroxides of Cr, Co and W.

The results obtained for Rene 80 during short term exposures showed enrichment of B in the inner part of the oxide scale. The formation of B-rich phase in the form of mixed oxide compound with Cr was observed by EBSD after 20 h at 1050°C. This phase was identified as $BCrO_3$ with calcite crystallographic structure. Formation of this phase resulted in B-depletion from the bulk alloy from 100 wt. ppm to below 5 wt. ppm during 20 h of exposure. After 100 hours of exposure the B was depleted below 1 wt. ppm, which might be correlated with a very fast diffusivity of B in the alloy matrix. Also B distribution in the oxide scale was found to be affected by water vapour addition: smaller enrichment in the outer part of the oxide scale was found for Rene 80 exposed in water vapour containing gases than that exposed in dry atmospheres. This might be correlated with the evaporation of B-oxyhydroxide species which is expected to be stronger in water vapour containing compared to dry atmospheres.

Free standing HVOF MCrAlY coatings were oxidized in two types of experiments: thermogravimetric isothermal and discontinuous oxidation exposures.

In the TG tests up to 100 hours it was found that, depending on the exposure temperature, the coatings oxidized in synthetic air formed an aluminium oxide scale with small amounts of Cr near the outer part of the scale. The oxide scales thickness measurement after exposure of the ground MCrAlY for 100 hours shows that the oxide scale thickness increases with increasing exposure temperature from 1.5 µm for coating exposed at 1050°C to 2.3 µm for coating

exposed at 1120°C (**Figure 7.11**). It was also found that the coating exposed at 1050°C in dry gas formed a thicker oxide scale compared to that formed on the coating exposed in wet air. Moreover, the oxide scale formed in the wet gas was "purer" alumina compared to that formed in the dry gas. This fact might be explained by initial stabilization of fast growing metastable alumina in the wet environment, which then transformed into stable α-alumina with a larger grain size and consequently slower growth rate after longer exposure times.

During discontinuous oxidation in a tube furnaces the differences in the formed oxide scale thickness were far less pronounced than those observed in the samples after TG tests. This might be related to the lower heating rate and consequently a longer period of time at which the coating could form metastable alumina so that the effect of H_2O on the stabilization of θ-Al_2O_3 could play a less important role.

For the lifetime tests of APS-TBC systems two set-ups were used:

1. Accelerated oxidation in cyclic oxidation rig at 1120°C in laboratory air with 2 h heating and 15 min cooling using pressurized air, and
2. Discontinuous oxidation test in a horizontal tube furnace at 1050°C in synthetic air and synthetic air + 20 wt.% H_2O with 100 h cycles and furnace cooling in the test gas.

APS-TBC systems on Rene 80 with nominally the same bondcoat chemical composition produced by High Velocity Oxyfuel (HVOF), Vacuum Plasma Spraying (VPS) and High Velocity Oxyfuel + Air Plasma Spraying-flashcoats (HVOF+APS-flashcoats) (two sample sets) respectively and two types of topcoats were studied regarding the influence of the bondcoat and topcoat microstructure on the lifetime of the APS-TBC systems in a cyclic oxidation test. It was found that the TBC system with the bondcoat applied by HVOF showed a relatively short lifetime. This could be correlated with a flat bondcoat surface which allowed

easy crack growth and linking upon crack nucleation. In contrast in the TBC-systems with the plasma sprayed bondcoats the crack propagation occurred to a large extent within the tough, porous topcoat. Consequently, the lifetime of the TBC systems with VPS bondcoat and APS-flashcoat (set II) appeared to be around a factor of 2.5 and 3.5 respectively longer than that with the HVOF bondcoat.

Considerable variations of lifetime observed between the systems with VPS bondcoat and optimized APS-flashcoat could not be explained by comparing their bondcoat roughness profiles on the basis of commonly used R_a and R_y values. Therefore an alternative approach, using fractal analysis, was tested for the bondcoat roughness evaluation. The latter showed that the APS-flashcoat exhibited a more "microrough" surface than the VPS bondcoat which results in a more distributed microcracking and delayed crack linking thereby effectively extending the lifetime of the system with the APS-flashcoat.

Another (additional) explanation for longer lifetime of TBC systems with APS-flashcoat could be, that oxidized intersplat porosity in the flashcoat might provide a layer with a lower CTE compared to metallic bondcoat, which might reduce the stress in the topcoat, thereby reducing the driving force for crack propagation and extending the lifetime during cyclic oxidation.

It was also found that the lifetime of the TBC systems with the APS-flashcoat strongly depends on the parameters used for the flashcoat spraying. The APS-flashcoat applied with a slightly different set of spraying parameters was a porous and not perfectly continuous layer. This resulted in a much shorter lifetime of the respective TBC-system (even shorter than that of the system with flat HVOF bondcoat) as a result of rapid breakaway oxidation of the flashcoat.

Finally, the effect of water vapour on the TBC life at 1050°C in air was investigated. It was found that addition of water vapour decreases the lifetime by about 30% to 50%, depending on the prevailing system. The failure mechanisms appeared to be the same as in the accelerated test. Moreover, the ranking of the TBC lifetime was essentially the same in both test types, although the absolute lifetime values were much greater at 1050°C than at 1120°C. Therefore, the advanced TBC systems containing an optimized APS-flashcoat on a HVOF-MCrAlY showed the longest lifetime, also in the water vapour containing gas.

Various parameters were considered which might be responsible for the lifetime shortening of the TBC-systems due to presence of H_2O in the test gas. In the present studies no indications were found which could suggest that the TGO-growth in the APS-TBC systems might be strongly affected by the water vapour. The exact comparison of TGO thickness is difficult because of non-uniform TGO-formation on rough surfaces resulting in a large variations of the TGO-thickness on one specimen. Considering the failure mechanism of the tested APS-TBC systems with rough bondcoats whereby the crack propagates to a large extent through the ceramic topcoat, detailed investigations of the sprayed topcoats as well as ceramic YSZ powders used for their spraying were carried out.

The two studied batches of YSZ powders by METCO and Amperit showed different sizes and morphology of the particles. For the batch of METCO, powder particles were spherical shaped and far denser than particles of the Amperit powder. Also differences in chemistry of the ceramic powders were found. The studied METCO powder batch contained minor amounts of Na. Moreover, for the latter powder, non-uniform Y distribution across the powder particles was found in the cross sections. Finally, the amount of monoclinic phase in the METCO powder batch was higher (15 wt. %) than that in the Amperit powder (6 wt.%).

Investigation of the sprayed YSZ coatings revealed, that the amount of the monoclinic phase was much lower than that in the powders. For the coating sprayed using METCO powder the amount of the monoclinic phase was higher (1.4 wt. %) compared to the coating sprayed using Amperit (0.7 wt.%). It is important to mention that different spray guns and spraying parameters were used for the production of the two ceramic coatings which might also affect the amount of the monoclinic phase.

In the present oxidation tests on the effect of water vapour on TBC-life the cooling at a relatively slow rate was performed in the test gas i.e. in dry and wet air respectively, contrary to the earlier studies, where the cooling was in dry or laboratory air (e.g. [7]). Considering the fact, that for the TBC systems with rough bondcoats the failure path lies within the ceramic topcoat, it might be that water vapour can affect the crack velocity in the YSZ during cooling. A possible mechanism for the latter effect can be the so-called Low Temperature Degradation (LTD) i.e. H_2O induced tetragonal to monoclinic transformation of the YSZ at temperatures below approximately 400°C, but further studies are required to verify this assumption.

10 References:

[1] IEA, *World Energy Outlook 2013, International Energy Agency*, Paris, France, **2013**.

[2] VGB PowerTech,*VGB Facts and Figures - Electricity Generation,*www.vgb.org, **2013/2014**.

[3] EIA, *Electric Power Monthly with Data for September 2013- U.S. Energy Information Administration,* www.eia.gov, November **2013.**

[4] V. Poloczek, H. Hermsmeyer, Modern Gas Turbines with High Fuel Flexibility, Siemens AG, Energy Sector, Germany, Power Generation –Asia, **2008** .

[5] B. Becker, B. Prade, M. Karg, Siemens gas turbine featuring low caloric gas applications, Power Generation, Asia **2004.**

[6] H2-IGCC Update – First Year – Nov 2009 – Oct 2010,

http://www.h2-igcc.eu/Pages/Publications_reports.aspx

[7] P. Song, Influence of Material and Testing Parameters on the Lifetime of TBC Systems with MCrAlY and NiPtAl Bondcoats, PhD Thesis, RWTH Aachen, **2011**

[8] P. Dowson, D. Bauer, S. Laney, Selection of the materilas and material related processes for centrifugal compressors and steam turbines in the oil and petrochemical industry, Proceedings of the 37th turbomachinery symposium, **2008.**

[9] J.R.Davis, ASM Specialty Handbook, Heat Resistant Materials, ASM International, Materials Park, OH, **1997**

[10] H. Harada, J. Gas Turbine Soc. of Japan **2000**, 28, 278-284

[11] M.Lamm, R.F. Singer, Metall. Mat. Trans. A, **2007**, 38A,

[12] D.J. Young, *High Temperature Oxidation and Corrosion of Metals*, **2008**, Elsevier: Cambridge,UK.

[13] R. Darolia, International Materials Reviews, vol. 58, No 6, 315-348, **2013.**

[14] D.R.G. Achar, R. Munoz-Arroyo, L. Singheiser, and W.J. Quadakkers, *Modelling of phase equilibria in MCrAlY coating systems*, Surface and Coatings Technology, **2004**. 187(2-3): p. 272-283.

[15] A. Hesnawi, H. Li, Z. Zhou, S. Gong, and H. Xu, *Isothermal oxidation behaviour of EB-PVDMCrAlY bond coat*, Surface & Coatings Technology, **2007**. 81(8): p. 947-952.

[16] A. Gil, V. Shemet, R. Vassen, M. Subanovic, J. Toscano, D. Naumenko, L. Singheiser, and W.J. Quadakkers, *Effect of surface condition on the oxidation behaviour of MCrAlY coatings*, Surface & Coatings Technology, **2006**. 201(7): p. 3824-3828.

[17] B.K. Pant, V. Arya, and B.S. Mann, *Development of Low-Oxide MCrAlY Coatings for Gas Turbine Applications*, Journal of Thermal Spray Technology, **2007**. 16(2): p. 275-280.

[18] P. Richer, M. Yandouzi, L. Beauvais, and B. Jodoin, *Oxidation behaviour of CoNiCrAlY bond coats produced by plasma, HVOF and cold gas dynamic spraying*, Surface & Coatings Technology, **2010**. 204(24): p. 3962-3974.

[19] W.R. Chen, X. Wu, B.R. Marple, D.R. Nagy, and P.C. Patnaik, *TGO growth behaviour in TBCs with APS and HVOF bond coats*, Surface & Coatings Technology, **2008**. 202: p. 2677-2683.

[20] M. Peters, C. Leyens, U. Schulz, W. Kaysser, EB-PVD thermal barrier coatings for aeroengines and gas turbines, Advanced Engineering Materials, 3 (**2001**) pp. 193-204

[21] M. Donachie, S. Donachie, Superalloys – a technical guide, ASM international technical books committee, 2nd Edition, Materials Park, USA (**2002**)

[22] M. Peters, B. Saruhan-Brings, U. Schultz, Proc. CEAS 2009 European Air and Space Conf., Manchester, UK, October 2009, CEAS, 1-9.

[23] D. Zhu and R.A. Miller, "Sintering and Creep Behavior of Plasma-Sprayed Zirconia- and Hafnia-Based Thermal Barrier Coatings", Surf. Coat. Technol., 108-109, 114-120 (**1998**).

[24] M.D. Gorman, I. Spitsberg, B.A. Boutwell, R. Darolia, R.W. Bruce, V.S. Venkataramani, A.M. Thompson and A. MogroCampera, "Ceramic compositions for low conductivity thermal barrier coatings", US Patent, 6,858,334, 2005.

[25] J. Singh, D.E. Wolfe, R.A. Miller and D.M. Zhu, "Tailored Microstructure of zirconia and hafnia-based thermal barrier coatings with low thermal conductivity and high hemispherical reflectance by EB-PVD" J. Mater. Sci. 2004, 39, 1975-1985.

[26] R.A.Miller, *Current status of thermal barrier coatings — An overview*, Surface & Coatings Technology, **1987**. 30(1): p. 1-11.

[27] R.G. Wellman and J.R. Nicholls, *A review of the erosion of thermal barrier coatings*, Journal of Physics D: Applied Physics, **2007**. 40(16): p. 293-305.

[28] T.E. Strangman, *Thermal barrier coatings for turbine airfoils*, Thin Solid Films, **1985**. 127(1-2): p. 93-106.

[29] H. Guo, H. Xu, X. Bi, and S. Gong, *Preparation of Al2O3–YSZ composite coating by EBPVD*, Materials Science and Engineering A, **2002**. 325: p. 389-393.

[30] D. Chen, M. Gell, E.H. Jordan, E. Cao, and X. Ma, *Thermal Stability of Air Plasma Spray and Solution Precursor Plasma Spray Thermal Barrier Coatings*, Journal of the American Ceramic Society, **2007**. 90(10): p. 3160-3165.

[31] J.H. Zaat, *A Quarter of a Century of Plasma Spraying*, Annual Review of Materials Science, **1983**. 13: p. 9-42.

[32] J.R. Nicholls, K.J. Lawson, A. Johnstone, and D.S. Rickerby, *Methods to reduce the thermal conductivity of EB-PVD TBCs*, Surface and Coatings Technology, **2002**. 151-152: p. 383-391.

[33] P. Kofstad, High Temperature Corrosion, Elsevier Applied Science Publisher Ltd, **1998**

[34] N.Birks, G.H.Meier, and F.S.Pettit, *High-temperature oxidation of metals (2nd Edition)*, Cambridge Univeristy Press, England, **2006**.

[35] C. Wagner, *Z. Phys. Chem.*, 21 (**1933**), 25

[36] W.J. Quadakkers, *Growth mechanisms of oxide scales on ODS alloys in the temperature range 1000–1100°C*, Materials and Corrosion, **1990**. 41(12): p. 659-668.

[37] K.P.R. Reddy, J.L. Smialek, and A.R. Cooper, *18O Tracer Studies of A1203 Scale Formation on NiCrAI Alloys*, Oxidation of metals, **1982**. 17(5/6): p. 429-449.

[38] W.J. Quadakkers, D. Naumenko, E. Wessel, V. Kochubey, and L. Singheiser, *Growth Rates of Alumina Scales on Fe–Cr–Al Alloys*, Oxidation of Metals, **2004**. 61(1/2): p. 17-37.

[39] C.S. Giggins, F.S. Pettit, Trnas. Met. **1968**, AIME 245, 2495.

[40] W. J. Quaddakers, J. F. Norton, S. Canetoli, K. Schuster, A. Gil, In 3rd International Conference on Microscopy of Oxidation; S. B. Newcomb, J. A. Little, Eds,; The Institute of Materials: Cambridge, **1996**, pp 609-619.

[41] M. Michalik, M. Hänsel, J. Zurek, L. Singheiser, W.J. Quadakkers, Mater. High Temp. 22 (**2005**) 213-221.

[42] Hänsel, M.; Quadakkers, W. J.; Singheiser, L.; Nickel, H. Report Forschungszentrum Julich, Jul-3583,**1998**; ISSN 0944-2952.

[43] Hänsel, M.; Quadakkers, W. J.; Young, D. J. Oxid. Met. **2003**, 59(3/4), 285–301.

[44] Essuman, E.; Meier, G. H.; Zurek, J.; Hänsel, M.; Norby, T.; Singheiser, L.; Quadakkers, W. J. Corros. Sci. **2008**, 50(6), 1753–1760.

[45] Zurek, J.; Young, D.J.; Essuman, E.; Hänsel, M.; Penkalla, H.J.; Niewolak, L.; Quadakkers, W.J., "Growth and adherence of chromia based surface scales on ni-base alloys in high- and low-pO_2 gases", Materials Science and Engineering, A, 477, (2008), 259-270.

[46] Essuman, E.; Meier, G.; Zurek, J.; Hänsel, M.; Quadakkers, W. J. Oxid. Met. **2008**, 69(3), 143–162.

[47] Essuman, E.; Meier, G.; Zurek, J.; Hänsel, M.; Singheiser, L.; Quadakkers, W. J. „Enhanced internal oxidation as trigger for breakaway oxidation of Fe-Cr alloys in gases containing water vapor“, Scripta Materialia, (2007), 57, 845-848.

[48] England, D. M.; Virkar, A. V. J. Electrochem. Soc. **1999**, 146(9), 3196–3202.

[49] England, D. M.; Virkar, A. V. J. Electrochem. Soc. **2001**, 148(4), A330–A338.

[50] S. Henry, J. Mougin, Y. Wouters, J.-P. Pettit, A. Galerie, Mater. High Temp. 17 (**2000**) 231.

[51] G. Hultquist, B. Tveten, E. Hörnlund, Oxid. Met. 54 (1/2) (**2000**) 1.

[52] N. K. Othman, J. Zhang, D. J. Young, "Water Vapour Effects on Fe-Cr Alloy Oxidation", Oxidation of Metals, **2010**, 73:337-352

[53] M. H. Bin Ani, T. Kodama, M. Ueda, K. Kawamura, T. Maruyama, „The Effect of Water Vapor In high Temperature Oxidation of Fe-Cr Alloys at 1073 K", Material Transactions, Vol. 50, No. 11 (2009), pp. 2656 to 2663.

[54] E. J. Opila, D. L. Mayers, N. S. Jacobson, I. M. B. Nielsen, D. F. Johnson, J. K. Olminsky and M. D. Allendorf, Journal of Physical Chemistry A 2007, (111), 1971 (2007).

[55] M. Stanislowski, J. Froitzheim, L. Niewolak, W.J. Quadakkers, K. Hilpert, T. Markus, L. Singheiser, "Reduction of chromium vaporisation from SOFC interconnectors by highly effective coatings", Journal of Power Sources, 164, (2007), 578-589

[56] V.P. Deodeshmukh, "Long-Term Performance of High-Temperature Foil Alloys in Water Vapor Containing Environment. Part I: Oxidation Behavior" Oxid. Met., 79, 2013, 567-578

[57] V.P. Deodeshmukh, "Long-Term Performance of High-Temperature Foil Alloys in Water Vapor Containing Environment. Part II: Chromia Vaporization Behavior" Oxid. Met., 79, 2013, 579-588

[58] G.R. Holcomb, “Calculation of Reactive-evaporation Rates of Chromia”, Oxid. Met. (2008), 69: 163-180.

[59] B. Pujilaksono, T. Jonsson, M. Halvarsson, I. Panas, J. E. Svensson, L. G. Johansson, Oxidation of Metals, **2008**, 70: 163-188

[60] M. C. Maris-Sida, G.H. Meier, F.S. Petit, Metallurgical and Materials Transactions, **2003**, vol. 34A, 2609-2619.

[61] K. Onal, M.C. Maris-Sida, G.H. Meier, F.S. Pettit, Superalloys, 2004, 607-615.

[62] R. Janakiraman, G.H. Meier, F.S.Petit, Metalurgical and Materials Transactions, **1999**, vol. 30A, 2905-2913.

[63] J. L. Smialek, Report NASA/TM-2010-216260 (**2010**), pp.36

[64] J.L. Smialek, Report NASA/TM-2005-214030 (**2005**), pp.36

[65] D.R.G. Achar, R. Munoz-Arroyo, L. Singheiser, W.J. Quadakkers, “Modelling of phase equilibria in MCrAlZ coating systems”, Surface & Coating Technology, 187, (2004), 272-283.

[66] U. Täck, “The Influence of Cobalt and Rhenium on the Behaviour of MCrAlY Coatings”, Technische Universitat Bergakademie Freiberg, 2004.

[67] J. Toscano, A. Gil, T. Hüttel, E. Wessel, D. Naumenko, L. Singheiser, W.J. Quadakkers, “Temperature dependence of phase relationships in different types of MCrAlY-coatings” Surface and Coating Technology 202, (2007), 603-607.

[68] W. J. Quadakkers, A. K. Tyagi, D. Clemens, R. Anton, L. Singheiser, “The Significance of Bond Coat Oxidation for the Life of TBC Coatings”, The Minerals, Metals & Materials Society, 1999, 119-130

[69] H. Lan, P.Y. Hou, Z.G. Yang, Y.D. Zhang, C. Zhang, Oxidation of Metals, **2011**, 75:77-92

[70] A. Gil, D. Naumenko, R. Vassen, J. Toscano, M. Subanovic, L Singheiser, W.J. Quadakkers, "Y-rich oxide distribution in plasma sprayed MCrAlY-coating studied by SEM with a cathodoluminescence detector and Raman spectroscopy", Surface & Coatings Technology, 204, (2009), 531-538.

[71] B. Gudmundsson and B.E. Jacobson, Thin Solid Films, **1989**. 173(1): p. 99-107.

[72] T.J. Nijdam and W.G. Sloof, Acta Materialia, **2007**. 55(17): p. 5980-5987.

[73] W. Braue, K. Fritscher, U. Schulz, C. Leyens, and R. Wirth, Materials Science Forum, **2004**. 61-464: p. 899-906.

[74] M. Subanovic, D. Sebold, R. Vassen, E. Wessel, D. Naumenko, L. Singheiser and W.J. Quadakkers, "Effect of manufacturing related parameters on oxidation properties of MCrAlY-bondcoats", Materials and Corrosion 59, 2008, No. 6, 463-470.

[75] J. Toscano, R. Vassen, A. Gil, M. Subanovic, D. Naumenko, L. Singheiser, W.J. Quadakkers, "Parameters affecting TGO growth and adherence on MCrAlY-bond coats for TBC's", Surface & Coatings Technology, 201, (2006), 3906-3910.

[76] D. Toma, W. Brandl, U. Köster, Oxidation of Metals, 2000, vol. 53:125-137.

[77] M. Subanovic, D. Naumenko, M. Kamruddin, G. Meier, L. Singheiser, W.J. Quadakkers, "Blistering of MCrAlY-coatings in H_2/H_2O-atmospheres", Corrosion Science 51, 2009, 446-450.

[78] D. Naumenko, W.J. Quadakkers, Effects of Metallurgical Chemistry and Service Conditions on the Oxidation Limited Life Time of FeCrAl-Based Alloys, Report Forschungszentrum Jülich, Jül-3948, ISSN 0944-2952, Jülich, Germany (2002)

[79] J. Toscano, D. Naumenko, A. Gil, L. Singheiser, and W.J. Quadakkers, Materials and Corrosion, **2008**. 59(6): p. 501-507.

[80] V. Deneux, Y. Carodet, S. Hervier, D. Monceau, “Effect of Water Vapor on the Spallation of Thermal Barrier Coating Systems During Laboratory Cyclic Oxidation Testing” Oxidation of Metals, 2010, 73:83-93.

[81] D. Naumenko, V. Shemet, L. Singheiser and W.J. Quadakkers, “Failure mechanisms of thermal barrier coatings on MCrAlY-type bondcoats associated with the formation the thermally grown oxide”, Journal of Material Science, 2009. 44: p. 1687-1703.

[82] F. Tang, J.M. Schoenung, Scripta Materialia, **2005** 52:905-909

[83] Y. Yamazaki, H. Fukanuma, N. Ohno, Journal of Solid Mechanics and Materials Engineering, vol.4, No2, **2010**, 196-207.

[84] O. Bernardi, “Mikrostrukturelle Untersuchungen zu Lebensdauer und Ausfallmechanismen von EB-PVD Warmedammschichten auf plasmagespritzen Haftvermittlerschichten”, Diploma work, Technical University of Darmstadt, Germany, 2005

[85] T.J. Nijdam, W.G. Sloof, “Combined pre-annealing and pre-oxidation treatment for the processing of thermal barrier coatings on NiCoCrAlY bond coatings”, Surf. Coat. Technol., 201, (2006), 3894

[86] U. Schulz, M. Menzebach, C. Leyens, Y.Q. Yang, “Influence of substrate material on oxidation behavior and cyclic lifetime of EB-PVD TBC systems”, Surf. Coat. Technol., 146-147, (2001), 117-123

[87] N.M. Yanar, F.S. Pettit, G.H. Meier, “Failure characteristics during cycling oxidation of yttria stabilized zirconia thermal barrier coatings deposited via electron beam physical vapor deposition on platinum aluminide and on NiCoCrAlY bond coats with processing modifications for improved performances”, Metall. Mat. Trans. 37A (2006), 1563.

[88] D.Renusch, H.Echsler, and M.Schütze, Materials at High Temperatures, **2004**. 21(2): p. 65-76.

[89] J.T. DeMasi-Marcin, K.D. Sheffler, and S. Bose, Journal of Engineering for Gas Turbines and Power, **1990**. 112(4): p. 521-526.

[90] R. Vaßen, G. Kerkhoff, and D. Stover, Materials Science and Engineering A, **2001**. 303: p. 100-109.

[91] G.C. Chang, W. Phuchareon, R.A. Miller, "BEHAVIOR OF THERMAL BARRIER COATINGS FOR ADVANCED GAS TURBINE BLADES", Surf. Coat. Technol., 30, 1987, 13-28

[92] H.E. Evans and M.P. Taylor, Oxidation of metals, **2001**. 55(1-2): p. 17-34.

[93] M.A. Helminiak, N.M. Yanar, F.S. Petit, T.A. Taylor, G.H. Meier, Surface and Coating Technology, 2009, doi:10.1016/j.surfcoat.2009.09.065

[94] K. Yasuda, Y. Goto, and H. Takeda, Journal of the American Ceramic Society, **2001**. 84(5): p. 1037-1042.

[95] M. Rudolphi, D, Renusch, H.E. Zchau, M. Schütze, Microscopy of Oxidation, **2009**, 347-351

[96] A. Jałowicka, "Effect of Strengtening Additions on the Oxidation and Sulfidation Resistance of Cast Ni-Base Superalloys", PhD Thesis, RWTH Aachen, 2013.

[97] J.-P. Pfeifer, H. Holzbrecher, W.J. Quadakkers, W. Speier, „Quantitative analysis of oxide films on ODS-alloys using MCs^+-SIMS and e-beam SNMS", J. Anal.Chem., 346, **1993**, 186 – 191.

[98] W.J. Quadakkers, A. Elschner, W. Speier, H. Nickel, „Composition and growth mechanisms of alumina scales on FeCrAl-based alloys determined by SNMS", App. Surf. Sci., 52, **1991,** 271 – 287

[99] C.A. Brown, G. Savary, Wear, 141 (**1991**), 211-226.

[100] C.A. Brown, W.A. Johnsen, R.M. Butland, Annals of the CIRP, Vol. 45/1/**1996**.

[101] S. Siegmann, C.A. Brown, Published: 1st United Thermal Spray Conference – Thermal Spray: A United Forum for Scientific and Technological Advances, Indianapolis, Indiana, **1997**, ISBN/ISSN: 0-87170-618-0, pp: 665-670.

[102] S. Siegmann, C.A. Brown, Published: 2nd United Thermal Spray Conference, Düsseldorf, D, **1999**, ISBN/ISSN: 3-87155-653-X, pp: 355-360.

[103] C.A. Brown, S. Siegmann, International Journal of Machine Tools & Manufacture, Vol. 41 (**2001**) 1927-1993

[104] R.S. Scott, P.S. Ungar, T.S. Bergstrom, C.A. Brown, F.E. Grine, M.F. Teaford, A. Walker, Nature, Vol. 436/4 August **2005**/doi:10.1038/nature03822.

[105] V. Briones, C.A. Brown, J.M. Aguilera, Journal of the American Oil Chemists' Society, Vol. 83. no. 3 (2006), 193-199.

[106] http://www.surfract.com/sfrax.html

[107] P.J Meschter, E.J. Opila, N.S. Jacobson, "Water Vapor-Mediated Volatilization of High-Temperature Materials", Annu. Rev. Mater. Res. 2013, 43:559-88.

[108] A. Jałowicka, W. Nowak, D. Naumenko, L. Singheiser and W.J. Quadakkers, "Effect of nickel base superalloy composition on oxidation resistance in SO_2 containing, high pO_2 environments" Materials & Corrosion, 2013, In press

[109] S. Cruchley, H.E. Evans, M.P. Taylor, M.C. Hardy, S. Stekovic, "Chromia layer growth on a Ni-based superalloy: Sub-parabolic kinetics and the role of titanium", Corrosion Science 75 (2013), 58-66.

[110] Piron-Abellan, J.; Quadakkers, W. J. Development of ferritic steels for application as interconnect materials for intermediate temperature solid oxide fuel cells (SOFCs), Report Forschungszentrum Julich, Jul-4170, March 2005; ISSN 0944-2952.

[111] Huczkowski, P.; Ertl, S.; Piron-Abellan, J.; Christiansen, N.; Hoefler, T.; Shemet, V.; Singheiser, L.; Quadakkers, W.J. Mater. High Temp. 2005, 22(3/4), 253–262.

[112] B.A. Pint, A.J. Garrat-Reed, L.W. Hoobs, "Possible Role of the Oxygen Potential Gradient in Enhancing Diffusion of Foreign Ions on α-Al_2O_3 Grain Boundaries", J. Am. Ceram. Soc., 81 [2], 305-14 (1998)

[113] Megusar J., Meier G.H., (1976) Metal Trans 7A:1133

[114] U. Krupp and H.-J. Christ, Oxid. Met. 52, 1999, 277-298.

[115] U. Krupp and H.-J. Christ, Oxid. Met. 52, 1999, 299-320.

[116] S. Guriswamy, S. M. Park, J. P. Hirth, and R. A. Rapp, Oxid. Met. 26, 77 (1986)

[117] J. Litz, A. Rahmel, and M. Schorr, Oxid. Met. 30 1987, 95-105

[118] Naoumidis, A.; Schulze, H. A.; Jungen, W.; Lersch, P. J. Eur. Ceram. Soc. 1991, 7, 55–63.

[119] Essuman, E.; Meier, G.; Zurek, J.; Hänsel, M.; Singheiser, L.; Norby, T.; Quadakkers, W. J. Mater. Scie. 2008, 43:5591–5598.

[120] D.J. Young, D. Naumenko, L. Niewolak, E. Wessel, L. Singheiser, W.J. Quadakkers, "Oxidation kinetics of Y-doped FeCrAl-alloys in low and high pO_2 gases", Materials and Corrosion, 2010, 61, No. 10, 838-844.

[121] Evans, H. E.; International Materials Reviews 1995, Vol.40 No. 1

[122] M. Michalik, S.L. Tobing, M. Hänsel, V. Shemet, W.J. Quadakkers, D.J. Young, Materials and Corrosion, 2013

[123] S. Saeidi, K.T. Voisey, D.G. McCartney, Journal of Thermal Spray Technology, vol. 18(2), 2009, 209-216.

[124] H.J.Grabke, *Oxidation of NiAl and FeAl*, Intermetallics, **1999**. 7(10): p. 1153-1158.

[125] Z. Lodziana, N-Y, Topsoe, J.K. Norskov, Nature Materials, Vol. 3, **2004**, p-p: 289-293.

[126] H. Götlind, F. Liu, J.-E. Svensson, M. Halvarsson, L.-G. Johansson, Oxidation of Metals, **2007**, 67:251-266.

[127] S. Taniguchi, T. Shibata, A. Andoch, “Phase Transformation of Alumina Scales Formed on Al-deposited Stainless Steel Foils”, Metal-Supported Automotive Catalytic Converters, ISBN 3-88355-254-2, (1997) 179-189

[128] H.J. Grabke, “Oxidation of NiAl and FeAl”, Intermetallics, 7, (1999), 1153-1158

[129] Z.Y. Deng, J. She, J.F. Yang, T. Ohji, and Y. Tanaka, (2004), Journal of the European Ceramic Society, 24(7), 2055

[130]D. J. Young, High Temperature Oxidation and Corrosion of Metals, Elsevier Ltd., ISSN: 1875-9491, 2008

[131] J. Ilavsky, C. C. Berndt, J. Karthikeyan, “Mercury intrusion porosimetry of plasma-sprayed ceramic”, Journal of Materials Science, 32 (1997), 3925-3932

[132] H. Taud, R. Martinez-Angeles, J.F. Parrot, L. Hernandez-Escobedo, “Porosity estimation method by X-ray computed tomography”, Journal of Petroleum Science and Engineering, 47 (2005), 209-217

[133] T. George, M.S. Anderson, W.T. Pike, T.L. Lin, R.W. Rathauer, K.H. Jung, D.L. Kwong, “Microstructural investigations of light-emitting porous Si layers”, Appl. Phys. Lett. 60 (19), (1992), 2359-2361

[134] E.S. Gademwla, M.M. Koura, T.M.A. Maksoud, I.M. Elewa, H.H. Soliman, Journal of Material Processing Technology, 123 (2002), 133-145

[135] P. Song, D. Naumenko, R. Vassen, L. Singheiser, W.J. Quadakkers, Surface and Coatings Technology, 2013, 221, p. 207-213

[136]A.M. Freborg, B.L. Ferguson, W.J. Brindley, G.J. Petrus, Mat. Sci. Eng. A245, 1998, 182-190

[137] M. Ahrens, R. Vassen, D. Stover, Surf. Coat. Technol. 161, 2002, 26-35

[138] L. Ajdelsztajn, D. Hulbert, A. Mukherjee, J.M. Schoenung, “Creep deformation mechanism of cryomilled NiCrAlY bond coat material”, Surface and Coating Technology, 201, (2007), 9462-9467,

[139] K. Fritscher, W. Braue, U. Schulz, “Assessment of Cyclic Lifetime of NiCoCrAlY/Zr O2-based EB-PVD TBC Systems via Reactive Element Enrichment in the Mixed Zone of the TGO Scale”, Metallurgical and Materials Transactions A, 44A, 2013, DOI: 10.1007/s11661-012-1561-2

[140] J. Toscano, A. Gil, T. Hüttel, E. Wessel, D. Naumenko, L. Singheiser, W.J. Quadakkers, Surface and Coating Technology 202, (2007), 603-607.

[141] J. Chevalier, L. Gremillard, A.V. Virkar, D.R. Clarke, “The Tetragonal-Monoclinic Transformation in Zirconia: Lessons Learned and Future Trends”, J. Am. Ceram. Soc. 92 [9], (2009), 1901-1920.

[142] V. Lughi, V. Sergo, Dental Materials 26 (2010), 807-820.

[143] R. Darolia, International Materials Reviews, vol. 58, No. 6 (2013), 315-348.

[144] N.M. Yanar, M. Helminiak, G.H. Meier, F.S. Pettit, Metallurgical and Materials Transactions A, Vol. 42A, (April 2011), 905-921.

[145] P. Li, I. W. Chen, and J. E. Penner-Hahn, ‘‘Effect of Dopants on Zirconia Stabilization—An X-Ray Absorption Study: I, Trivalent Dopants,’’ J. Am. Ceram. Soc., 77 [1] 118–28 (1994).

[146] X. Guo, ‘‘Property Degradation of Tetragonal Zirconia Induced by Low-Temperature Defect Reaction with Water Molecules,’’ Chem. Mater., 16 [21] 3988–94 (2004).

[147] S. Fabris, A. T. Paxton, and M. W. Finnis, ‘‘A Stabilization Mechanism of Zirconia Based on Oxygen Vacancies Only,’’ Acta Mater., 50 [20] 5171–8 (2002).

[148] B. Rajasekaran, G. Mauer, R. Vassen, “Enhanced Characteristic of HVOF-sprayed MCrAlY Bond Coats for TBC Applications”, Journal of Thermal Spray Technology, 206, 2011, 1209-1216

[149] G. M. Ingo, G. Padeletti, Surface and Interface Analysis, Vol. 21, 450-454 (1994).

[150] G. Choi, S. Horibe, “Static fatigue in ceramic materials: influences of an intergranular glassy phase and fracture toughness”, Journal of Material Science, 28, (1993), 5931-5936

[151] J.W. Hutchinson, “Mechanisms of toughening in ceramics”, Theoretical and Applied Mechanics, (1989), 139-144

[152] R. M. McMeeking and A. G. Evans, ‘‘Mechanics of Transformation-Toughening in Brittle Materials,’’ J. Am. Ceram. Soc., 65 [5] 242–6 (1982).

[153] V. Lughi, D.R. Clarke, “Low-temperature transformation kinetics of electron-beam deposited 5 wt.% yttria-stabilized zirconia” Acta Materialia, 55 (2007), 2049-2055

[154] K. Yasuda, M. Itoh, S. Arai, T. Suzuki, M. Nakahashi, „Phase transformation of yttria-stabilized zirconia plasma-sprayed coatings in a humid atmosphere”, Journal of Material Science, 32 (1997), 6291-6297

Band / Volume 225
Sorption, Transformation and Transport of Sulfadiazine in a loess and a sandy Soil
S. Sittig (2014), v, 121 pp
ISBN: 978-3-89336-982-9

Band / Volume 226
A Lagrangian transport core for the simulation of stratospheric trace species in a Chemistry Climate Model
C. M. Hoppe (2014), vi, 112 pp
ISBN: 978-3-89336-984-3

Band / Volume 227
Einfluss der Probengröße und der Kornorientierung auf die Lebensdauer einer polykristallinen Ni-Basislegierung bei LCF- Beanspruchung
T. Seibel (2014), II, 131 pp
ISBN: 978-3-89336-986-7

Band / Volume 228
Implementation of capillary electromigrative separation techniques coupled to mass spectrometry in forensic and biological science
T. N. Posch (2014), 264 pp
ISBN: 978-3-89336-987-4

Band / Volume 229
Mobile Messungen - Messung und Bewertung von Verkehrsemissionen
C. Ehlers (2014), VII, 136 pp
ISBN: 978-3-89336-989-8

Band / Volume 230
Data Processing and Trace Gas Retrievals for the GLORIA Limb Sounder
T. Guggenmoser (2014), xi, 111, XXVI
ISBN: 978-3-89336-993-5

Band / Volume 231
Assessment of Laser Induced Ablation Spectroscopy (LIAS) as a method for quantitative in situ surface diagnostic in plasma environments
N. Gierse (2014), 199 pp
ISBN: 978-3-89336-994-2

Band / Volume 232
Lattice-Boltzmann-Simulation in faserbasierten Mikrostrukturen
J. P. Brinkmann (2014), viii, 129 pp
ISBN: 978-3-89336-995-9

Band / Volume 233
Numerische Simulationen von Abfallgebinden aus der Wiederaufarbeitung von Kernbrennstoffen
S. Schneider (2014), 201 pp
ISBN: 978-3-89336-998-0

Band / Volume 234
Materials for Advanced Power Engineering 2014
J. Lecomte-Beckers, O. Dedry, J. Oakey, B. Kuhn (Ed.)
(2014), xxi, 930, viii pp
ISBN: 978-3-95806-000-5

Band / Volume 235
Untersuchungen zur Abtrennung, Konversion und Transmutation von langlebigen Radionukliden
Ein Beitrag zur fortschrittlichen Entsorgung von hochradioaktiven Abfällen
G. Modolo (2014), 291 pp
ISBN: 978-3-95806-005-0

Band / Volume 236
Keramische Membranen für die H_2-Abtrennung in CO-Shift-Reaktoren
D. van Holt (2014), IV, 169 pp
ISBN: 978-3-95806-007-4

Band / Volume 237
Entwicklung von porösen Silica-Membranen zur CO_2-Abtrennung aus dem Rauchgas fossil befeuerter Kraftwerke
J. S. Eiberger (2014), II, 163 pp
ISBN: 978-3-95806-008-1

Band / Volume 238
Development of a highly sensitive and versatile mass spectrometer system for laboratory and atmospheric measurements
S. Albrecht (2014), iv, 171 pp
ISBN: 978-3-95806-009-8

Band / Volume 239
High Temperature Corrosion of Alloys and Coatings in Gas-Turbines Fired with Hydrogen-Rich Syngas Fuels
W. Nowak (2014), 201 pp
ISBN: 978-3-95806-012-8

Weitere ***Schriften des Verlags im Forschungszentrum Jülich*** unter
http://wwwzb1.fz-juelich.de/verlagextern1/index.asp

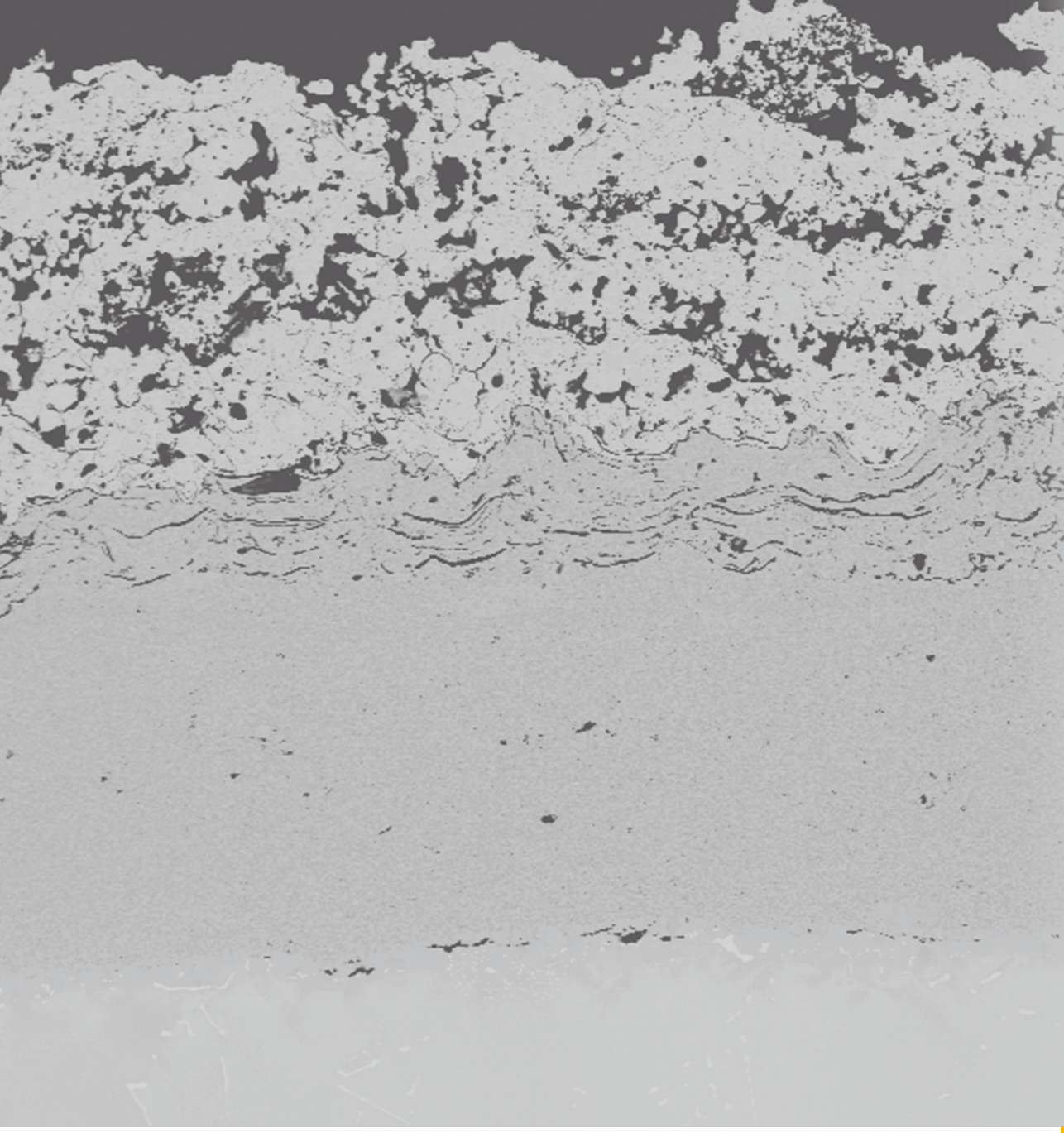

Energie & Umwelt / Energy & Environment
Band / Volume 239
ISBN 978-3-95806-012-8

JÜLICH
FORSCHUNGSZENTRUM